

THE WINDS OF LOW-MASS STARS AND SOLAR WIND EVOLUTION

DÚALTA Ó FIONNAGÁIN

A THESIS SUBMITTED FOR THE DEGREE OF

DOCTOR OF PHILOSOPHY



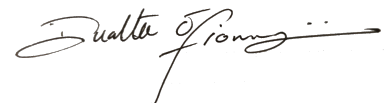
SCHOOL OF PHYSICS
TRINITY COLLEGE DUBLIN

2020

DECLARATION

I, Dúalta Aodh Ó Fionnagáin, hereby declare: This thesis has not been submitted as an exercise for a degree at this or any other university; That it comprises work performed entirely by myself during the course of my Ph.D. studies at Trinity College Dublin; That I was involved in a number of collaborations, and where it is appropriate my collaborators are acknowledged for their contributions.

I agree to deposit this thesis in the University's open access institutional repository or allow the Library to do so on my behalf, subject to Irish Copyright Legislation and Trinity College Library conditions of use and acknowledgement.



Dúalta Ó Fionnagáin

August 14, 2020

SYNOPSIS

Stellar winds affect the evolution of stars (as well as impacting the planets orbiting these stars) through the removal of angular momentum and mass over time. This process changes the rotation rate of the host star, which in turn affects the stellar wind. The Sun is the only star for which there are *in situ* wind measurements, and those present day values do not reflect the past and future states of the solar wind. Throughout this thesis, I research the evolution of the solar wind using numerical simulations (in 1D, 3D, HD, and MHD) of the winds of similar low-mass stars. I focus on examining the evolution of these winds and the effects these winds can have on the exoplanets that are embedded within them. The temporal trends of solar-mass stars along the main sequence is quantified in terms of mass-loss rate and angular momentum-loss rate, with both quantities decreasing as the star ages. This is important as it provides information on the evolutionary stage of the star and the age-rotation relationship. From the simulations in this thesis, I was able to examine the environments of orbiting exoplanets, by studying the effects the local wind conditions would cause on the orbiting planet. These quantities can have significant impacts on the evolution of the planet and in particular the planetary atmosphere. I examine the wind of λ Andromedae, a solar-mass star which has evolved off the main sequence to become a sub-giant star. This is the first 3D MHD study into an evolved solar-mass stellar wind, and I do so using both polytropic and Alfvén wave-driven winds. I show that a thermal, thermally-driven wind driven from a hot corona best replicates the radio observations of this star.

As stellar winds permeate the entire region from the star to the interstellar medium, orbiting planets experience the direct impact of evolving stellar winds. This causes the planets' magnetospheres and atmospheres to change over long timescales, leading to significant effects on our understanding of planetary evolution and their atmospheres. The presence, removal, or lack of an atmosphere will drastically change the surface conditions on a planet. My research provides the astronomy community with wind condi-

tions to estimate the effects of stellar winds on any planets orbiting these low-mass stars, as well as the evolution of conditions around the Earth and Mars. I show that in the past the magnetosphere of the Earth would have been much smaller than the present day size. For more extreme exoplanetary systems, close-in exoplanets can directly interact with their host stars through magnetic processes in their winds or magnetospheres. Although not a new concept, the study of star-planet interactions is evolving due to advances in instrumentation leading to exciting new discoveries and supporting evidence for this phenomenon. I simulate the wind of 55 Cancri, which possesses a system of 5 exoplanets, and show that magnetic star-planet interactions are not only possible, but probable in the case of the closest planet, 55 Cancri e. I quantify the phenomenon using the wind conditions between the planet and star and show any emission is likely to be quite transient and difficult to observe with complex temporal signatures, but possible given long observational monitoring or serendipitous observations.

Stellar winds emit radiation in the form of thermal bremsstrahlung in the radio regime as expected from an ionised plasma. This emission could be an indicator for important wind quantities such as mass-loss rate and density. Unfortunately, to date, no low-mass stellar winds have been detected in the radio regime due to their tenuous nature, however non-detections and upper limits still provide meaningful constraints on the same wind parameters. However, disentangling this emission from other radio sources in the stellar system can be difficult. To aid in the detection of radio emission from low-mass stellar winds I analytically and numerically calculate the thermal radio flux densities expected from the stellar winds I simulated, at frequencies where they are expected to possess the strongest flux density. Currently, only upper-limits exist for the observations of these stellar winds. I predict the flux density expected from a number of solar-mass stars, showing that within the next generation of radio telescopes, the additional sensitivity should allow the community to detect some of these winds directly. These studies are also relevant when searching for any other radio emissions from star-planet systems, as it is important to quantify emission from the stellar wind so it can be properly accounted for.

The novel research carried out in this thesis has explored the long-term evolution of the solar wind using numerical simulations, and analysed the significant changes experienced by the host star and orbiting planets. The various results presented here have succeeded in quantifying this relationship between wind evolution, the host star, and orbiting planets. Future research into the winds of low-mass stars spans a wide-range of possible avenues including star-planet interactions, wind radiation, temporal events (CMEs, flares), and planetary atmospheric and magnetospheric evolutionary trends.

ACKNOWLEDGEMENTS

I have been fortunate to work and collaborate with some incredible colleagues during my PhD. However clichéd, the highlight of the past four years was the exceptional people I have met and befriended along the way, all of whom helped me get to this point.

First and foremost, I would like to express my sincere gratitude to my supervisor, Aline Vidotto. Your enthusiasm and inspirational words kept me motivated and focused throughout the entirety of my PhD. Your support, patience, and guidance whenever I needed it was extraordinarily helpful, I could not have had a better supervisor.

I would like to thank all of my colleagues I have worked with in TCD. I am grateful to the members of the astrophysics research group (old and new) for keeping me sane, be it through coffee breaks, ice-cream trips, pints, or even the heated debates, all of you are amazing colleagues and friends. In particular thanks goes out to my two PhD co-conspirators, Ioana, who was always up for a geography quiz or two to break up the day, and Sean, for those philosophical discussions during our podcasting obsession! I would like to express my thanks to the postdocs in our group—Carolina, Donna, and Gopal—

for their guidance, expertise, proof-reading abilities, and most of all, not getting fed up of my endless questions. I would also like to acknowledge the BCool collaboration, without which, much of the research in this thesis would not be possible.

To *all* of my friends, thank you for the continuous support, laughs, distractions, podcasts, and chats. To my parents, who always encouraged me to do my best, and without whom I would not be where I am today, you have my utmost thanks, love, and respect. To my siblings, grandparents, cousins, aunts and uncles, thank you for all of your moral support. Finally, to Aoibhín, your love and support throughout the past four years has been absolutely vital. You were always there to encourage, listen, and laugh with me (or at me!) when I needed it most, despite my foibles and constant threats to quit my PhD to drink coffee professionally. This work would not be possible without you.

PUBLICATIONS

Publications resulting, partially or wholly, from this work:

REFEREED:

1st Author

- **D. Ó Fionnagáin**, A. A. Vidotto, P. Petit, C. Neiner, W. Manchester IV., C. P. Folsom
“ λ Andromedae: The solar wind post main sequence”, under review, 2020.
- **D. Ó Fionnagáin**, A. A. Vidotto, P. Petit, C. P. Folsom, S. V. Jeffers, S. C. Marsden, J. Morin, J. D. do Nascimento Jr, and BCool Collaboration.
"The solar wind in time-II. 3D stellar wind structure and radio emission." *Monthly Notices of the Royal Astronomical Society*, 483, no. 1 (2018): 873-886.
- **D. Ó Fionnagáin**, and A. A. Vidotto.
“The solar wind in time: a change in the behaviour of older winds?.”, *Monthly Notices of the Royal Astronomical Society*, 476.2 (2018): 2465-2475.

Co-Author

- C. P. Folsom, **D. Ó Fionnagáin**, L. Fossati, A. A. Vidotto
“The circumstellar environment of 55 Cnc: the super-Earth 55 Cnc e as a primary target for star-planet interactions”, *Astronomy & Astrophysics*, 633, A48, 2020
- R. D. Kavanagh, A. A. Vidotto, **D. Ó Fionnagáin**, V. Bourrier, R. Fares, M. Jardine, Ch Helling, C. Moutou, J. Llama, and P. J. Wheatley.
“MOVES-II. Tuning in to the radio environment of HD189733b.” *Monthly Notices of the Royal Astronomical Society*, 485, no. 4 (2019): 4529-4538.

NON-REFEREED:

- **D. Ó Fionnagáin**, and A. A. Vidotto. “The Aging Solar Wind: a Break in Wind Evolution at Older Ages?” Proceedings of the IAU 13, no. S335 (2017): 98-101.
- **D. Ó Fionnagáin**, Vidotto, A., Petit, P., Folsom, C., Jeffers, S., Marsden, S., Morin, J., do Nascimento Jr., J. (2018). “The Solar Wind in Time II: can we detect radio emission from young solar analogues?”, Zenodo.
<http://doi.org/10.5281/zenodo.1487988>
- **D. Ó Fionnagáin**. (2019, April 30). ofionnad/radiowinds: Calculating Thermal Bremsstrahlung Emission from Stellar Winds (Version v1.1.0). Zenodo.
<http://doi.org/10.5281/zenodo.2654877>

CONTENTS

List of Figures	xiii
List of Tables	xvi
Acronyms	xvii

I FUNDAMENTAL CONCEPTS	1
1 WINDS OF LOW-MASS STARS	3
1.1 An introduction to stellar winds	5
1.2 Evolution of stellar activity	11
1.3 Stellar surface magnetic fields	17
1.4 Star-planet interactions (SPI)	22
1.5 Thesis Outline	25
2 MODELLING WINDS OF SOLAR ANALOGUES	27
2.1 1-Dimensional Parker wind	31
2.2 1-Dimensional Polytropic Winds	36
2.3 3-Dimensional Magnetohydrodynamical Model	41
2.4 3-Dimensional Magnetohydrodynamical Wave Model	47

3	RADIO PROCESSES FROM IONISED PLASMA	50
3.1	Mechanical and radiative processes in thermal plasmas	51
3.2	Analytical radio emission	55
3.3	Numerical radio emission	60
II	THE SOLAR WIND IN TIME	63
4	MAIN SEQUENCE SOLAR WIND EVOLUTION	65
4.1	Introduction	65
4.1.1	Calibrating our simulations to the solar case	67
4.2	Solar wind in time sample	68
4.3	Stellar wind parameters at the wind base	70
4.3.1	Temperature-rotation relation	70
4.3.2	Density-rotation relation	72
4.4	Evolution of global properties of the Solar Wind	73
4.4.1	Mass-loss rate	73
4.5	Radio emissions from stellar winds	75
4.5.1	Radio emission from our simulations	76
4.6	Discussion	78
4.6.1	Consequences for the ageing Sun	78
4.6.2	$T_{\text{cor}} - \Omega$: Goodness of fit	81
5	THE SOLAR WIND IN TIME - 3D MHD SIMULATIONS	84
5.1	Stellar sample	87
5.2	Mass-loss rates, angular momentum-loss rates & open magnetic flux . .	90
5.3	Evolution of the radio emission with age	95
5.4	Evolution with magnetic cycle	100
5.5	Wind detectability in radio	100
6	LAMBDA ANDROMEDAE	104
6.1	λ Andromedae in context	105
6.2	Observed surface magnetic fields	108

6.3	The wind of λ Andromedae	113
6.3.1	Hot wind model	115
6.3.2	Cold wind model	115
6.4	Post-MS winds from MHD simulations	117
6.5	Radio emission from the wind of λ And	122
6.5.1	Other sources of radio emission	126
III EFFECTS OF WIND EVOLUTION ON PLANETS		128
7	PLANETARY ENVIRONMENTS EMBEDDED IN STELLAR WINDS	130
7.1	Evolution of the local properties of the wind on solar system planets . . .	132
7.2	Planetary magnetosphere effects	135
7.3	Local wind parameters in 3D	138
7.3.1	Wind derived properties at typical hot-Jupiter distances	139
8	THE CIRCUMSTELLAR ENVIRONMENT OF 55 CANCRI	144
8.1	The system of 55 Cancri	145
8.1.1	The surface magnetic field of 55 Cancri	147
8.2	The stellar wind around the planets orbiting 55 Cnc	150
8.3	Star-planet interactions?	154
8.3.1	Energy budget for SPI	156
9	CONCLUSIONS & FUTURE WORK	161
9.1	The solar wind in time: a change in the behaviour of older winds?	162
9.2	The Solar Wind in Time II: 3D stellar wind structure and radio emission	164
9.3	λ Andromedae: A solar wind proxy post-main sequence	166
9.4	The circumstellar environment of 55 Cnc: the super-Earth 55 Cnc e as a primary target for star-planet interactions	168
9.5	Future Work	169
9.5.1	Winds of solar-mass stars off the main sequence	170
9.5.2	Investigating wind effects on exoplanets	171
9.5.3	Transient events in low-mass stellar systems	172

9.5.4	Cosmic rays & solar wind evolution	174
9.5.5	Understanding the solar wind driving mechanisms	175
	Bibliography	178

LIST OF FIGURES

Figure 1.1	H-R diagram - Stellar Evolution	4
Figure 1.2	The Astrosphere	6
Figure 1.3	Mass-loss rates vs. X-ray fluxes for low-mass stars	7
Figure 1.4	Charge Exchange at the wind-ISM boundary	8
Figure 1.5	Cyclical complexity in stellar winds and stellar rotation	11
Figure 1.6	Stellar rotational evolution	13
Figure 1.7	Stellar rotational evolution anomaly	14
Figure 1.8	X-ray Flux and Rotation	15
Figure 1.9	High energy irradiance from solar analogues	16
Figure 1.10	$T_{\text{cor}}-F_X$ low-mass stars	17
Figure 1.11	The Zeeman effect and polarisation	19
Figure 1.12	Stokes V-ZDI schematic	21
Figure 1.13	Example of Stokes V and surface magnetic field observations	22
Figure 2.1	Parker wind solution	36
Figure 2.2	Polytropic wind structure vs. Temperature	39

Figure 2.3	Polytropic wind structure vs. Γ	40
Figure 2.4	Simulation grid example	44
Figure 3.1	The path of an electron through a plasma	53
Figure 3.2	Schematic for analytical thermal bremsstrahlung coordinates	57
Figure 3.3	Trend of I_β for different α	59
Figure 3.4	A schematic of a 3D wind and the method for calculating the radio flux density.	61
Figure 4.1	Coronal temperature vs. stellar rotation for solar mass stars	71
Figure 4.2	Mass-loss rates from 1D simulations	75
Figure 4.3	Stellar mass loss rate - single fit	81
Figure 4.4	Wind temperature vs. stellar rotation - single fit	82
Figure 5.1	Stellar surface magnetic fields from ZDI observations	90
Figure 5.2	3D MHD stellar wind simulation solutions for solar analogues	91
Figure 5.2	previous figure continued	92
Figure 5.3	Global wind trends from 3D MHD simulations vs. rotation	94
Figure 5.4	Specific radio intensity from stellar winds	98
Figure 5.5	Radio spectra calculated from simulated stellar winds	99
Figure 5.6	Radio spectra normalised to 10 pc	101
Figure 5.7	Radio flux density vs. stellar rotation	102
Figure 6.1	λ And evolution on the H-R diagram	106
Figure 6.2	Lambda Andromedae surface magnetic field	110
Figure 6.3	Observed stokes I and V profiles for λ And	111
Figure 6.4	Lambda And: Hot wind model	119
Figure 6.5	Lambda And: Cold wind model	122
Figure 6.6	Lambda And: Cold wind model — dipole	123
Figure 6.7	Lambda And: Radio specific intensity	124
Figure 6.8	Lambda And: density structure	125
Figure 6.9	Gudel-Benz & λ And	127
Figure 7.1	Local planet-wind parameters from 1D wind simulations	133

Figure 7.2	Magnetosphere schematic	134
Figure 7.3	Planetary magnetosphere radius vs. stellar rotation	135
Figure 7.4	Polar opening angle	136
Figure 7.5	Orbital wind density, velocity, and ram pressure for a HJ	141
Figure 7.6	Velocity histogram for 3D MHD stellar winds	142
Figure 8.1	Surface magnetic field of 55 Cnc	148
Figure 8.2	Stokes V profiles of 55 Cnc	149
Figure 8.3	3D MHD wind simulations of 55 Cancri	151
Figure 8.4	55 Cnc wind parameters around planets e and b	152
Figure 8.5	Magnetic structure of 55 Cnc wind and SPI	154
Figure 8.6	Erratic SPI behaviour	158
Figure 8.7	Alfvén velocities in the stellar wind of 55 Cnc	159
Figure 8.8	Alfvén wave travel times from planet e to stellar surface	159
Figure 8.9	Poynting flux energy in 55 Cnc system	160
Figure 9.1	Thermal radio emission from CME	173
Figure 9.2	Solar Orbiter EUV of the Sun	176

LIST OF TABLES

Table 4.1	Stellar sample for 1D wind simulations	69
Table 4.2	Mass-loss rates for 1D simulations	74
Table 4.3	Radio flux density calculated analytically from 1D stellar wind simulations	77
Table 5.1	Stellar sample for 3D MHD wind simulations	87
Table 5.2	Numerically calculated radio emission from 3D MHD stellar winds	96
Table 6.1	Physical parameters of λ And	107
Table 6.2	Summary of Lambda Andromedae simulations	114
Table 6.3	Radio observations for Lambda And	120
Table 8.1	Local wind properties for planets orbiting 55 Cancri	153

COMMON ACRONYMS

3D	3-dimensional
1D	1-dimensional
AMR	Adaptive Mesh Refinement
AW	Alfvén Wave
AWSOM	Alfvén Wave Solar Model
BATS-R-US	Block Adaptive Tree Solarwind Roe Upwind Scheme
ISM	Interstellar Medium
LSD	Least Squares Deconvolution
MHD	Magnetohydrodynamics
MS	Main Sequence
SKA	Square Kilometre Array
SPI	Star-Planet Interactions
VLA	Very Large Array
ZDI	Zeeman Doppler Imaging

*The wonder is, not that the field of stars is so vast,
but that man has measured it.*

ANATOLE FRANCE

I

FUNDAMENTAL CONCEPTS

In this part, I outline the fundamental concepts important to understanding the research conducted in this thesis. I discuss the evolution of low-mass stars throughout their lifetime and how we can quantify this progression in terms of empirical evidence and simulations. The important stellar activity indicators are examined in relation to global stellar parameters such as rotation, X-ray luminosity, and chromospheric emissions. In particular, I consider the winds of solar-mass stars, as they are the focal point of this body of work. I lay out the necessary background theory and mathematical formalisms to understand how the solutions to the equations describing stellar winds are solved, and will be referred to throughout this thesis. I discuss the physical mechanisms through which stellar winds develop and are accelerated, and the multiple different methods for simulating this phenomenon. This chapter includes a description of the theory of radio emission from stellar winds and how we can calculate and attempt to detect this phenomenon.

WINDS OF LOW-MASS STARS

Stellar evolution is fundamentally defined by the changes a star exhibits over time and it can be quantified empirically in a number of ways. The inability to study individual stars over their exceptionally long lifetimes is circumvented by studying stellar populations, frequently described using plots such as the Hertzsprung-Russell (H-R) diagram (Figure 1.1). In its most basic form, the H-R plot displays the surface temperatures (or colour) of stars vs. their luminosity (or absolute magnitude). For example, the Sun has a relative luminosity of $1 L_{\odot}$ and an effective temperature of 5770 K (shown in Figure 1.1). It becomes possible to group stars of a similar nature together and study their counterparts at different evolutionary stages. Through this method one can derive indirectly the plausible scenarios of stellar evolution forward or backward in time for a particular stellar object.

Low-mass stars are defined here as stars with $M_{\star} \lesssim 1.5 M_{\odot}$ (where M_{\odot} is one solar mass) for which we can assume will end their lives as white dwarfs (the separate group of stars in the lower left corner of the H-R diagram in Figure 1.1). As low-mass stars are

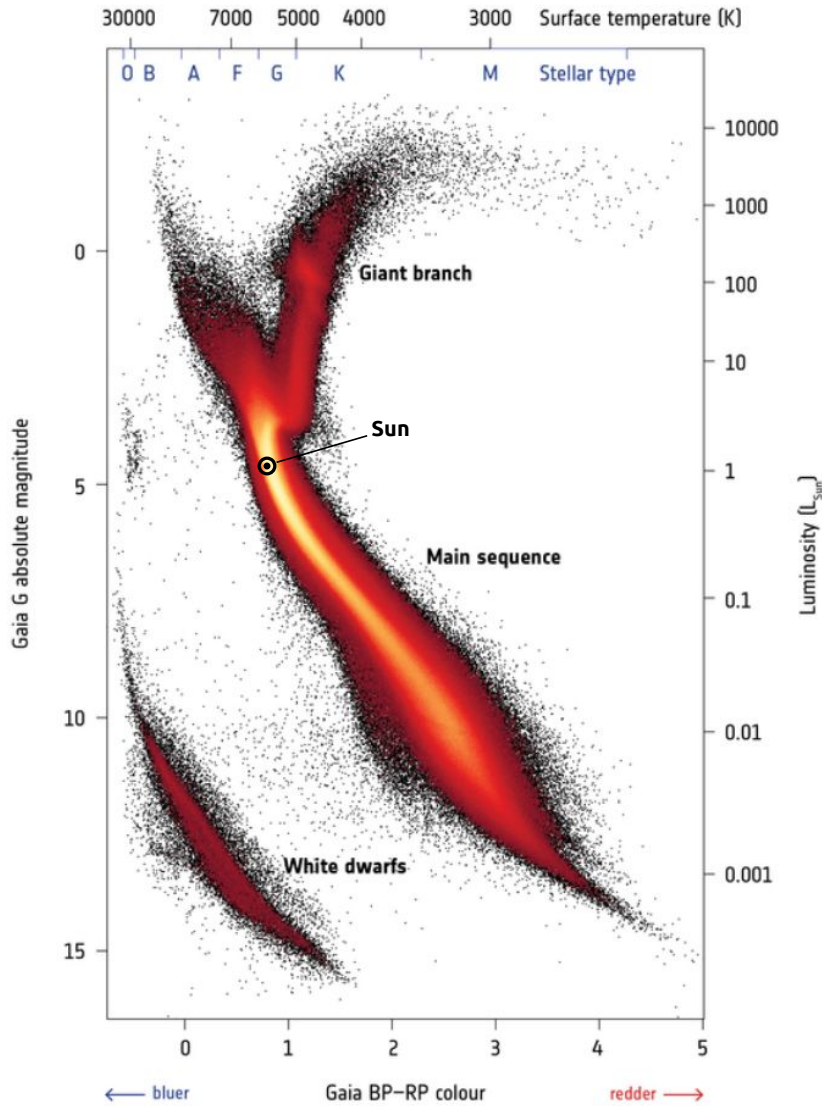


Figure 1.1: Hertzsprung-Russell diagram of over 4 million stars from the Gaia DR2 (Gaia Collaboration et al., 2018). We can see the approximate temperatures, stellar classifications and luminosities labelled on the top and right axes. The most populated areas are those of the main sequence (MS), the giant branch (composed of sub-giants, red giants, and asymptotic giants) and the white dwarfs. These regions are where stars spend most of their lives. For the research conducted in this these, we are most concerned with the MS and the giant branch.

the most ubiquitous type of star in our galaxy (Chabrier, 2003), they are expected to host the most exoplanets (Howard et al., 2012), and therefore are the most promising candidates in the search for habitable planets. It is important that we understand the mechanisms through which the majority of the stars in the universe evolve throughout their life, and how this affects their surrounding environments, including exoplanets. In this work, we will focus on stars that fall into this category, notably for those most similar to the Sun in mass.

1.1 AN INTRODUCTION TO STELLAR WINDS

In this thesis, our main focus is on stellar winds. These winds consist of ions, electrons, and neutrals that form an outflow from the surface of the star. Their composition typically consists of hydrogen (particularly for low-mass stars on the main sequence), but other species can be found in stellar winds (such as helium, carbon, oxygen, and neon). This wind permeates the environment around the star from the stellar surface up to the astropause¹, where the wind impacts upon the interstellar medium (ISM; see Figure 1.2). Missions like Voyager 1 and Voyager 2 have provided great insight into the structure of the solar wind from the Earth towards the outer heliosphere and the ISM, as both have now exited the solar system. The removal of material from the star significantly affects the evolution of the star throughout its lifetime, and therefore is an important area of research for an understanding of both stars and exoplanets.

Historically, the terms “solar wind” and “stellar wind” were both coined by E. Parker. In 1951, [Biermann \(1951\)](#) noticed that the tails of comets pointed radially away from the Sun, suggesting they were moving through some medium. This began the idea that there was some extended atmosphere from the Sun that should be easily detectable (at the time). [Chapman & Zirin \(1957\)](#) conjectured that this extended medium consisted of a static atmosphere that permeated the heliosphere. We now know that this is incorrect, and [Parker \(1958\)](#) was the first to show analytically that the medium consisted of a stationary supersonic outflow. Stationary here means that the wind structure remains constant, given a particular density and velocity profile. He managed to do this years previous to *Mariner 2* empirically confirming his theory ([Neugebauer & Snyder, 1962](#)), by comparing his predicted plasma values at Earth. From this point, the theoretical understanding and empirical evidence in the study of the solar wind grew rapidly. We now possess a broad range of theoretical and computational tools for the study of low-mass stellar winds, for a full discussion on these see [Gombosi et al. \(2018\)](#); [Cranmer & Winebarger \(2019\)](#) and references within.

¹ The astrosphere is the more general stellar equivalent of the heliosphere for the Sun.

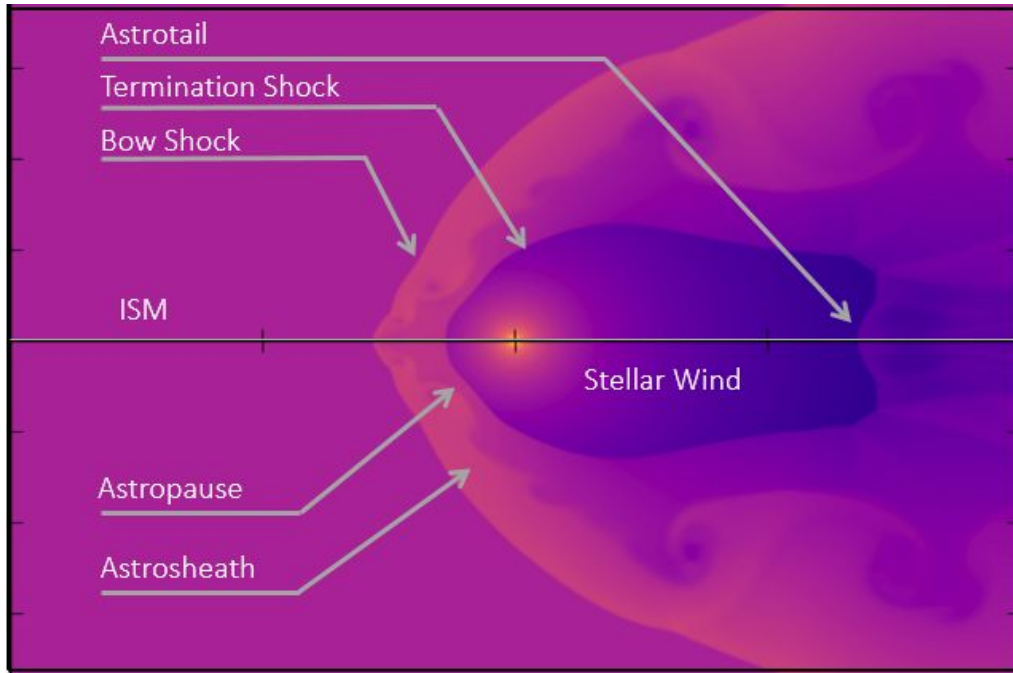


Figure 1.2: Example of an astrosphere of a star, moving in the interstellar medium (ISM). The astrosphere is produced by the stellar wind, originating from the central star. This produces an astropause and a bow shock upon interaction with the ISM. This is a snapshot of a hydrodynamic (HD) simulation I ran of a star-ISM interaction using the PLUTO code. The system is quite dynamic; all the phenomena labelled here change structure and position through time. The colours here represent density.

Observationally, these winds are difficult to detect—due to their rarefied nature—but there are some techniques which are bearing fruit and promising for the future. For example, Ly- α observations of the astrospheric absorption at the wind-ISM boundary provide an indirect way to determine mass-loss rates (Wood et al., 2014), shown here in Figure 1.3. As mentioned in the previous paragraph, the solar wind impacts the ISM at the heliopause. This occurs in other stellar systems too, leading to a physical phenomenon known as charge exchange (see Figure 1.4). The result is a change in the observed Ly- α spectra, due to the increase in the fast neutral H protons that will absorb in the line. The authors Wood et al. (2014) quantified the charge exchange between the neutral ISM and the ionised wind for many stars, calculating the additional Ly- α absorption at the astropause along the line of sight. Modelling this absorption with hydrodynamic (HD) models, the mass-loss rate can be calculated. However, wind density and velocity is also required within these HD models to calculate mass-loss rates, which is not known and must be assumed, further obscuring the true mass-loss rates. Cur-

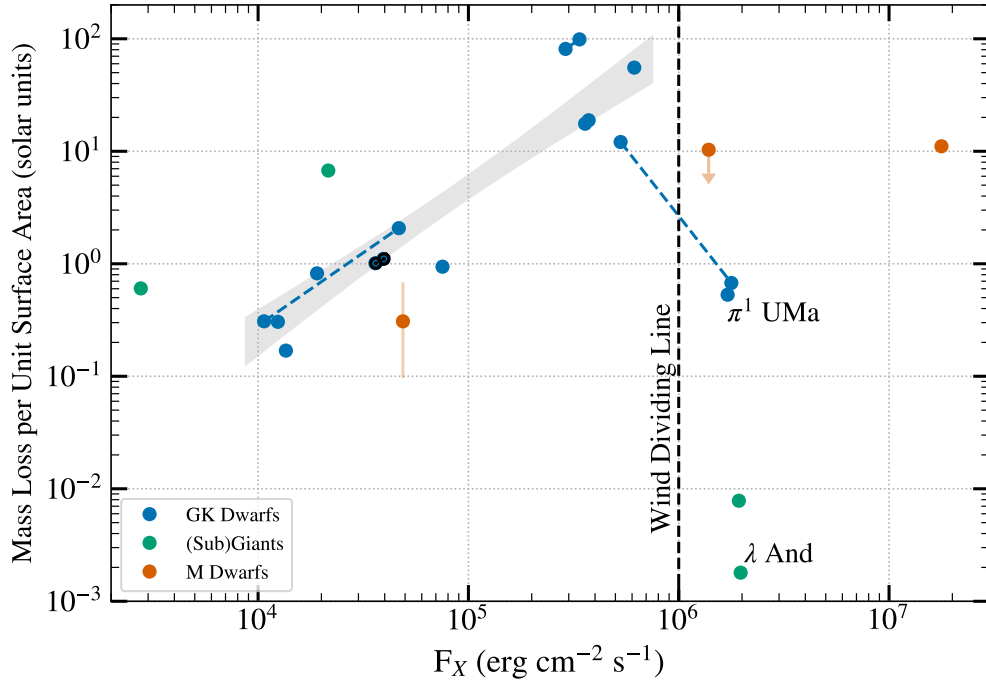


Figure 1.3: Comparison of X-ray fluxes from low-mass stars and their derived mass-loss rates using the Ly- α technique. Pre-wind dividing line, it seems there is a power law relationship between these two stellar parameters (fit shown in grey band). However, for stars with higher X-ray flux, this relationship breaks down and the distribution is somewhat more random, although more data points are needed here. *Adapted from Wood et al. (2014).*

rently, Ly- α observations are the most promising method of detecting low-mass stellar winds indirectly. This method can also be applied to stellar wind-planet interactions, and has been observed and modelled in the past for particular systems (Vidal-Madjar et al., 2003; Kulow et al., 2014; Ehrenreich et al., 2015; Bourrier et al., 2016; Vidotto & Bourrier, 2017). Figure 1.3 also shows the relationship between these derived mass-loss rates and the stellar X-ray flux, suggesting a power law relationship and hinting at a wind-dividing line.

Another encouraging method is thermal radio bremsstrahlung observations, the mechanism for which is discussed at length in Chapter 3. In this thesis we make many predictions on the thermal radio bremsstrahlung that particular stellar winds may emit, and whether this should be detectable or not (Chapter 5). This builds upon efforts previously made to detect low-mass stellar winds in the radio regime (Gaidos et al., 2000; Villadsen et al., 2014; Fichtinger et al., 2017). In the past, massive stars (roughly those that display $M_{star} \gtrsim 8 M_{\odot}$) have been readily detectable in the radio (Abbott et al., 1980).

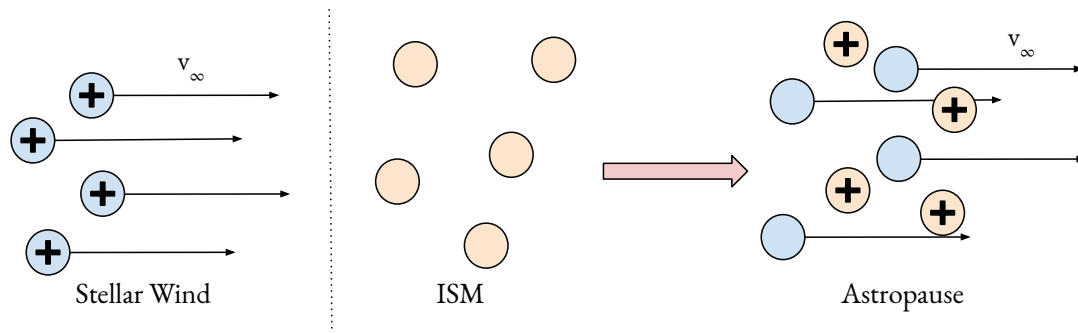


Figure 1.4: Basic schematic of charge exchange processes at the astropause. Stellar wind particles are shown in blue, ISM particles are shown in orange. The exchange of the electric charge between the particles as they interact causes a lot of fast neutralised protons to form, travelling at the terminal wind velocity (v_∞). This causes a change in the Ly- α absorption spectrum.

This is primarily due to their high density outflows, which produce a strong enough signal to be detected here on Earth. In spite of this, winds of low-mass stars have eluded direct detection in the radio so far. In addition to the lower expected radio fluxes, the thermal radio emission must be disentangled from any other source of radio emission from the star which can have many causes (e.g. gyro-synchrotron, cyclotron, chromospheric emission etc. Gary & Linsky 1981; Villadsen et al. 2014). Bowers & Kundu (1981) found that winds of low-mass stars are not easily detected. They observed 29 stars at 4.9 GHz using the Very Large Array¹ (VLA; which gave a flux sensitivity of between 0.5-2 mJy) and only one source provided a positive detection. Gaidos et al. (2000) attempted to observe 4 solar-type stars using the VLA at 3.6 GHz and found a similar result. However, these upper limits can provide important constraints on the density of the wind. More modern observations of solar-type stars have been conducted, Villadsen et al. (2014) found positive detections for thermal radio emission from three solar-type stars, but conclude that this emission is not from the wind, but from lower down in the stellar atmosphere. Fichtinger et al. (2017) observed four young MS solar-type stars and also found a non-detection for their stellar winds. However, in all of these works, non-detections provide important constraints on the possible densities in these winds, and therefore are essential to our understanding of the stellar winds. Improving the

¹<https://science.nrao.edu/facilities/vla>

sensitivity level of radio telescopes should lead to more positive detections in the future. These works are discussed throughout this thesis.

Due to their diverse nature, stars have many different mechanisms for forming winds (Lamers & Cassinelli, 1999). For low-mass stars however, there are two dominant mechanisms, as currently understood in the literature. These are *thermally driven winds*, and *magnetically driven winds* (or *wave driven winds*). Initially, Parker (1958) only considered the effects of gas pressures as the solar wind expands from a several million degree corona, making various assumptions: isothermal, isotropic, steady, non-rotating, no magnetic fields. This setup predicts the wind parameters at Earth very well and is still widely used today (Vidotto et al., 2019; Gaidos et al., 2020). Here the corona is the hot outer atmosphere of the Sun, between the transition region and the solar wind. The solar wind is accelerated low down in the solar atmosphere. Usually the wind is said to originate from the hot corona (although the fastest solar wind emanates from coronal holes), where the plasma is relatively dense, with slow velocities and high temperatures. This tends towards a faster terminal velocity as it approaches the heliopause. At Earth, we see typical values of 400–600 km s⁻¹, depending on solar activity. The density drops off with distance as $\sim r^{-2}$, although this decay index can vary close to the Sun. The density of the solar wind at 1 au is typically 5-15 particles cm⁻³ (Usmanov et al., 2000; McComas et al., 2008). Note that this is within the equatorial regions around the Sun. The polar regions show much faster wind velocities at the same distance (800 km s⁻¹), and is associated with lower densities (2-3 particles cm⁻³) and higher temperatures (3×10^5 K). Parker also examined how the solar magnetic field would be affected by the solar wind. Since the magnetic field is both embedded in the solar surface, and dragged out by the solar wind, the magnetic field is warped. Parker concluded that the effect of an constant solar outflow, combined with the solar rotation, would cause the magnetic field lines to become dragged out, leading to the “Parker spiral”.

The theory of *Alfvén wave driven winds* was developed shortly thereafter (Alfvén, 1957; Parker, 1965; Alazraki & Couturier, 1971; Hollweg, 1973). Observations from *Mariner 2* confirmed the existence of these waves (Coleman, 1967), giving support to

these wave-driven theories. These two mechanisms (thermal and magnetic) for forming winds are not necessarily independent of each other. In the solar case, the solar wind can be modelling reasonably well with thermally driven wind models, however, the hot solar corona is thought to mainly be heated through magnetic processes, such as Alfvén waves (Hollweg, 1978, 1986; Cranmer & Winebarger, 2019). Stellar winds models have become increasingly complex throughout the years, moving to more dimensions, including more physics, relaxing assumptions, and including different driving mechanisms to see which models can both efficiently and accurately represent low-mass stellar winds (e.g. Keppens & Goedbloed 1999a; Chandran et al. 2011; Suzuki et al. 2013; Sokolov et al. 2013; van der Holst et al. 2014; Gombosi et al. 2018; Cranmer & Winebarger 2019). It is also likely that a fully thermally driven wind is not adequate to describe the winds of all low-mass stars, especially those in different temperature regimes. A full discussion of stellar wind models that are used in this thesis is included in Chapter 2.

These stellar winds, mainly through embedded magnetic fields, remove angular momentum from the star (Weber & Davis Jr., 1967; Kawaler, 1988; Pinsonneault et al., 1990; Vidotto et al., 2014b). Although the ages of low-mass stars are not well constrained, they appear to evolve throughout their main sequence lifetime through the loss of angular momentum—i.e. they rotate more slowly as they age (Skumanich, 1972). The theory of how angular momentum could be removed from a star including the complex interplay of the stellar magnetic field and the stellar wind was developed initially by Weber & Davis Jr. (1967), known as the magnetic rotator theory. In this seminal work, the authors quantified the angular momentum and torque in the solar wind. Rotation has been linked to most of the other observable activity indicators for a star (discussed in Section 1.2). The activity indicators in turn can cause a change in the stellar wind properties of the star (which can have significant effects on any orbiting planets). Therefore this process is extremely complex and non-linear, but there are clear links that connect all of these fundamental stellar parameters, as shown in Figure 1.5.

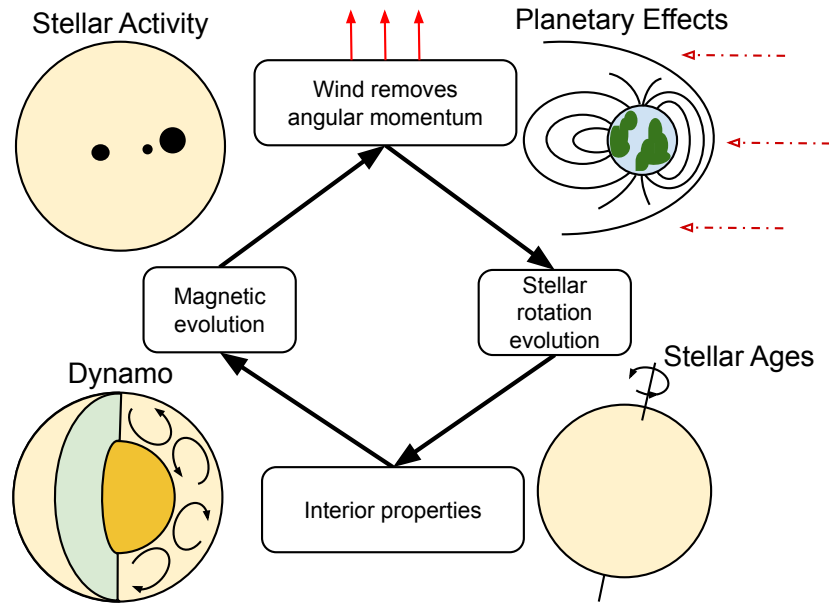


Figure 1.5: Schematic showing how each stellar parameter can effect the next, leading to a complex and cyclic dependency. In this thesis, we focus mostly on the top of this schematic, including stellar winds, planetary effects, and stellar rotational evolution. *Based on figure from Vidotto (2016a).*

1.2 EVOLUTION OF STELLAR ACTIVITY

Stellar activity can be thought of as a collective term for any observable marker that indicates presence of a stellar magnetic field. These include but are not limited to flaring, chromospheric activity (spectral lines, e.g. Ca II H&K), coronal activity (UV and X-ray emissions), starspots, etc. Initially the evolution of stellar activity was quantified by Schatzman (1962); Kraft (1967) and Skumanich (1972). Skumanich (1972) found that stellar rotation is inversely proportional to the age of the star ($\Omega_{\star} \propto t^{-1/2}$), i.e. older stars rotate slower than younger stars and this behaved in a very predictable manner. He achieved this by comparing stellar rotation (derived through a spectrogram) to the ages of stellar clusters (the Pleiades, Hyades, Ursa Major, and the Sun), with observations from Kraft (1967). This discovery from Skumanich (1972) agreed with stellar formation theory, namely the nebular hypothesis, which predicted a collapse of a nebula forming the central star with formation of orbiting planets. In this theory, the star would collapse to spin at its fastest rate, and slow down during its lifetime thereafter.

Additionally, this was the first empirical evidence confirming previous theoretical work by [Weber & Davis Jr. \(1967\)](#) that found the winds of stars should be extracting angular momentum, thereby slowing down stellar rotation. [Skumanich \(1972\)](#) also had shown that the stellar activity indicators Ca^+ and Li also declined in a similar fashion to the stellar rotation rate. This was the beginning of linking stellar rotation to other stellar activity indicators. Since then, it has been shown that the rotation rate of a star is an excellent indicator for X-ray activity ([Pallavicini et al., 1981](#); [Wright et al., 2011](#)), chromospheric activity ([Noyes et al., 1984](#)), flaring rate ([Davenport et al., 2019](#)), starspot number ([Davenport, 2015](#); [Nielsen et al., 2019](#)), and magnetic field strength ([Vidotto et al., 2014b](#); [See et al., 2017](#)), particularly along the MS.

Rotation and age has been studied in much greater depth since the work of [Skumanich \(1972\)](#), and it appears this relationship works very well for stars along the MS ([Mamajek & Hillenbrand, 2008](#)), but fails for very young and old stars ([Gallet & Bouvier, 2015](#); [Van Saders et al., 2016](#)). We see that young solar-type stars tend to show a large range of rotation rates, so this rotation-age relationship works for stars older than ≈ 1 Gyr, as shown in [Figure 1.6](#) ([Gallet & Bouvier, 2013](#)). Using a model of angular momentum loss incorporating stellar spin-up (interactions between star and stellar disk causing increase in rotation rate), differential core and envelope rotation and stellar spin-down at key ages, the authors modelled rotational evolutionary tracks that solar-type stars can follow throughout their lifetime. Three different percentile tracks (25th, 50th, and 90th) are shown in [Figure 1.6](#). These three tracks account for the wide spread in rotation rates that are present in young stellar clusters. In [Figure 1.6](#) the tracks follow the same trend (the Skumanich law) after ≈ 1 Gyr. This means that for our Sun the rotational evolution in the immediate future can be predicted. Although this presents the problem that we cannot say for certain what the rotation rate of the Sun was before ≈ 1 Gyr. More recently, works such as [Van Saders et al. \(2016\)](#); [Booth et al. \(2017\)](#) have presented evidence for more complex changes in stellar behaviour at older ages. [Van Saders et al. \(2016\)](#) have shown that some stars older than the Sun do not follow the accepted age-rotation relation explored by [Skumanich \(1972\)](#) ($\gtrsim 4$ Gyr). Dated using

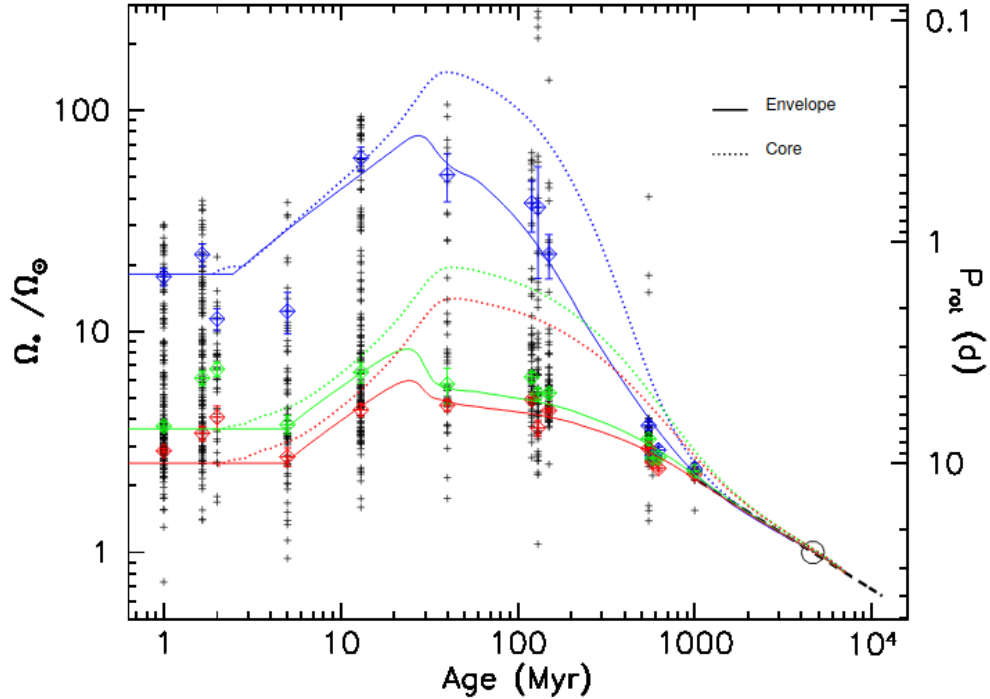


Figure 1.6: The rotational evolution of a $1 M_{\odot}$ star. The black crosses show rotational-age data from different young open clusters. Solid lines show the rotational rate of the stellar surface, relative to the Sun. Blue (fast), red (slow) and green (median) lines show the 90th, 25th, and median of the rotational distributions of the data. Source: *Gallet & Bouvier (2013)*.

asteroseismology, the authors found stars displayed higher rotation rates than expected, which suggests that solar-like stars decrease their rate of angular momentum loss after a certain age, shown in Figure 1.7. In contrast to this, *Booth et al. (2017)* found that solar-type stars show a sharp decrease in their X-ray fluxes past an age of approximately 1-2 Gyr, which they suggest is due to increased stellar spin-down. At first, this seems to contradict the work presented by *Van Saders et al. (2016)*, as stars with lower X-ray fluxes are expected to rotate slower, not faster. However, since the angular momentum loss of stars depends on the momentum that can be carried away per unit mass of their wind, the momentum lost would decrease if the mass lost also decreased. This provides a way to reconcile both works; A decrease in X-ray luminosity could suggest a weaker stellar wind, which in turn, removes less angular momentum, resulting in a faster spinning star. This process for removing stellar angular momentum is discussed further in Chapter 4.

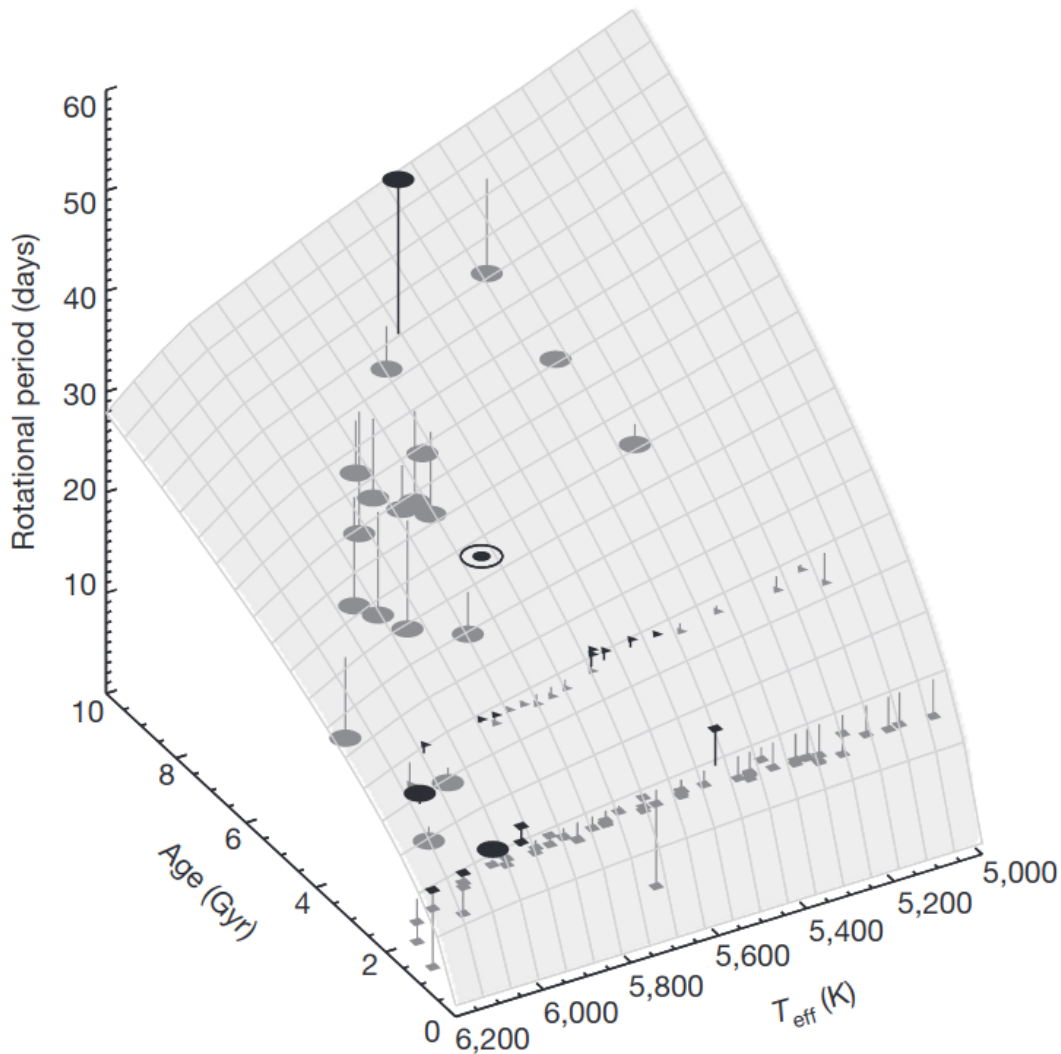


Figure 1.7: A 3D plot showing the rotational period of stars versus the stellar age and effective temperature. Grey points lie below the plane, black points above the plane. This plot shows old, evolved stars rotating much faster than expected from the standard model (grey plane). Source: *Van Saders et al. (2016)*.

X-ray emission is an empirical stellar trait that is frequently attributed to stellar activity. This is because strong surface magnetic activity is linked with flaring on the Sun, giving rise to hot non-thermal plasmas, which emit soft and hard X-rays. Figure 1.8 (from *Wright et al., 2011*) showed that X-ray fluxes are tightly correlated with Rossby number¹ (Ro), forming two regimes, see Figure 1.8. The authors show that after $\approx Ro = 0.2$, the stellar X-ray flux begins to decline. Interestingly, it is clear that for lower Ro —i.e. faster rotation rates, and hence younger ages through the age-rotation relationship—the X-ray flux saturates. even though younger stars show a large range of rotation periods.

¹ Rossby number is the ratio of stellar period to convective turnover time.

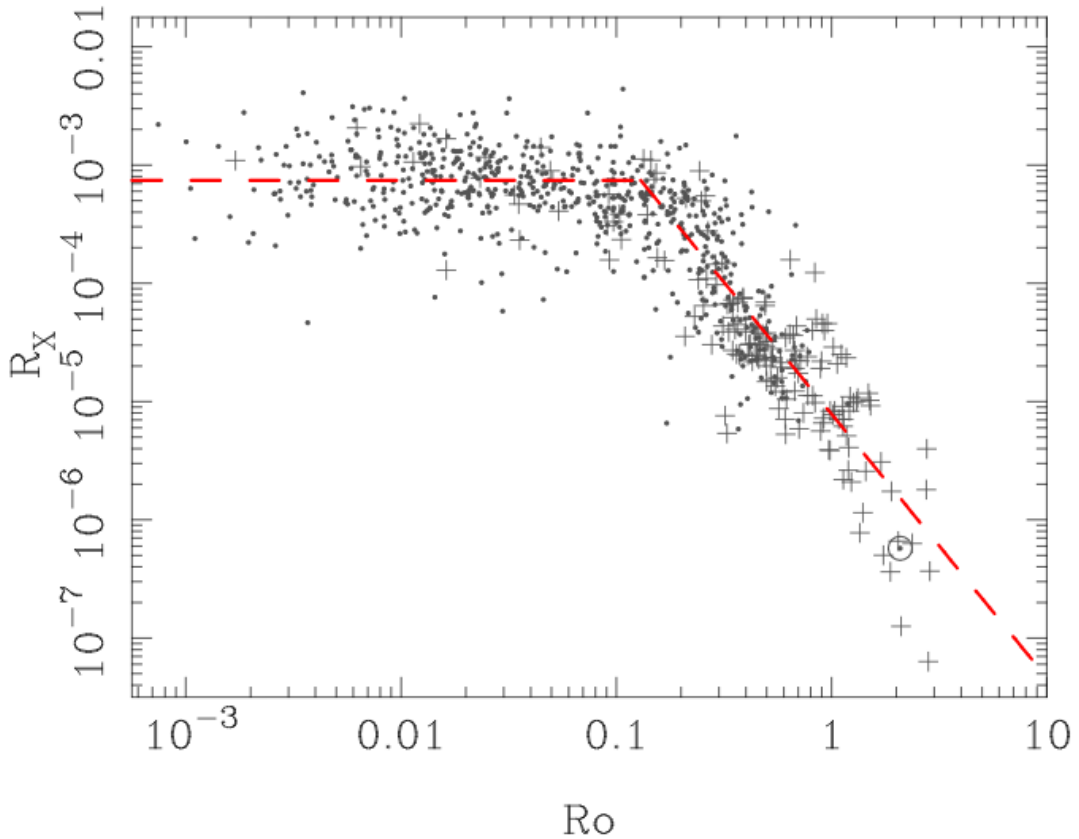


Figure 1.8: Wright et al. (2011) displays how the bolometrically normalised X-ray flux (R_X) of stars changes with their Rossby number. We can see that there is a saturated region for stars with low Ro number (faster rotators), implying younger stars also have saturated X-ray fluxes due to the age-rotation relations (Figure 1.6). The stars' X-ray flux drops off as stellar spin-down takes effect.

This saturation in X-ray flux suggests that there is a limit to the rotation-driven stellar activity, which could be due to a change in the interior dynamo, saturation of active regions on the surface (maximum filling factors), or a narrowing of the corotation radius, causing the region of X-ray emission to decrease. This would suggest that rotation can no longer effectively increase activity through X-ray emission above this cut-off.

Stellar X-ray luminosity has been shown many times to correlate with the average coronal temperature of stars (Pallavicini et al., 1981; Schrijver et al., 1984; Schmitt et al., 1990). This is somewhat expected as it is the hot plasma that is producing the soft X-ray emission, with the hard X-ray being produced in the small volumes around stellar flares. Studies of solar-mass stars specifically, and the evolution of their emitted high energy radiation, has provided the work in this thesis with a solid motivation for examining the evolution of the solar wind. Various authors usually use stars with a mass similar

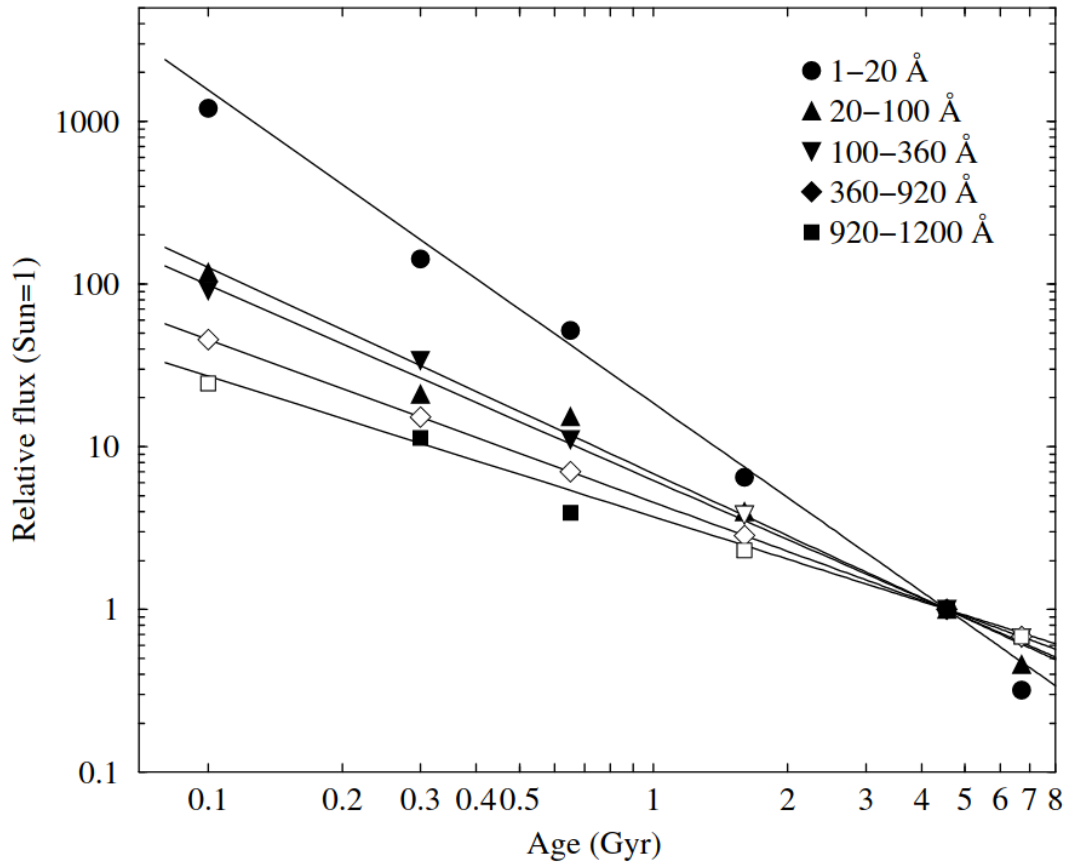


Figure 1.9: The high energy irradiances of solar analogues, categorised by five different energy bands, and their trends with stellar age. *From Ribas et al. (2005).*

to the Sun to infer the values the Sun could have displayed in the past or could display in the future (Güdel, 2007). Dorren & Guinan (1994) looked at stars in the optical and UV regimes, from which they inferred a decline in activity with stellar age. Güdel et al. (1997) examined how the high energy radiation (X-ray and ultraviolet) emitted from the Sun has evolved, by observing the coronae of nine solar-like G type stars. Since these high energy fluxes can be connected to coronal activity, they derived trends in coronal temperature and emission measure¹ with rotation and age of these solar analogues (see also Telleschi et al. 2005). More pointedly, Ribas et al. (2005) examined the high energy irradiance from solar-mass stars and split the emission into energy bands. The authors found there is evidence that the fastest rotators produce much more hard X-ray emission, which displays enhanced decay, more so than the soft X-ray emission as the stars spin down (Figure 1.9). Telleschi et al. (2005) focused on the evolution of these coronal

¹ Emission measure (EM) is the integral of plasma density along line-of-sight, usually used in UV or X-ray astronomy: $EM = \int n^2 dV$

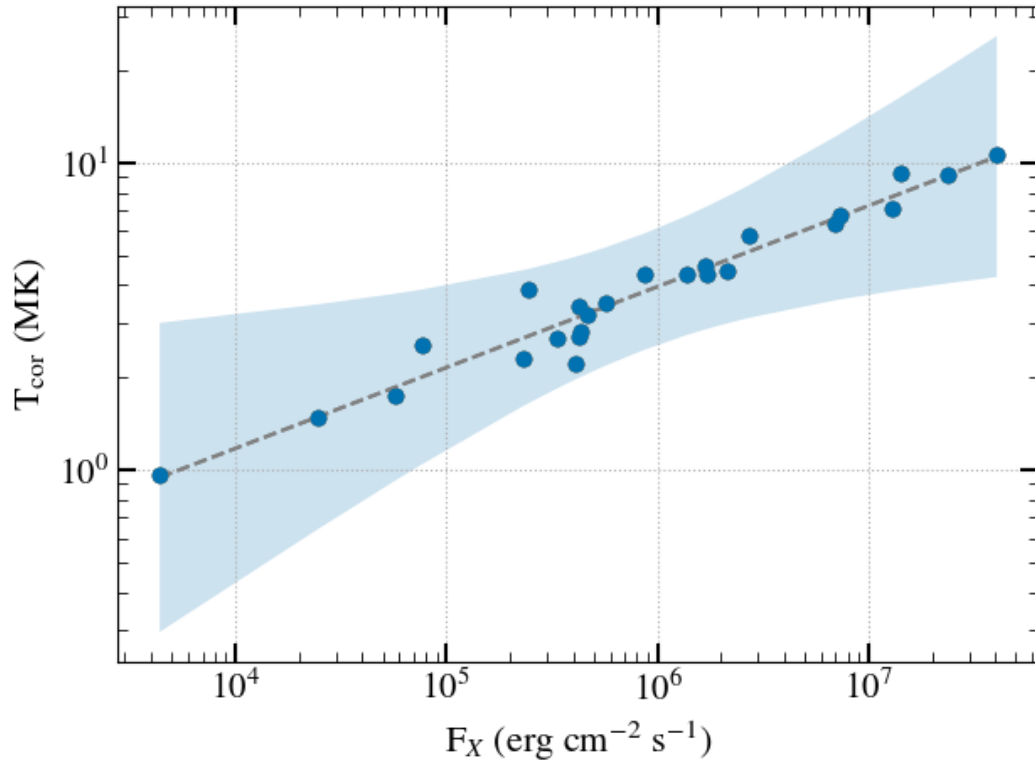


Figure 1.10: Stars with higher X-ray flux exhibit higher coronal temperatures. We include an independent fit giving the same relationship found by [Johnstone & Güdel \(2015\)](#): $T_{\text{cor}} \propto F_X^{0.26}$. Shaded area shows 95% confidence interval. *Adapted from [Johnstone & Güdel \(2015\)](#).*

temperatures in solar-type stars by studying the X-ray spectra of solar analogues. The authors showed how the X-ray luminosity varies with stellar rotation period. This was expanded upon by [Johnstone & Güdel \(2015\)](#), who showed how the average coronal temperature varies with the X-ray flux (Figure 1.10, see also [Ó Fionnagáin & Vidotto 2018](#)).

1.3 STELLAR SURFACE MAGNETIC FIELDS

My research begins with the use of surface magnetic field maps of stars. I will give a brief overview of the techniques used, so that the reader understands the origins of our stellar magnetic field observations. For more information on this topic there is much research that I point the reader to here: stellar magnetism overviews ([Mestel, 1999](#); [Reiners, 2012](#); [Brun & Browning, 2017](#)), magnetic field trends ([Morin et al., 2008](#),

2010; Donati & Landstreet, 2009; Vidotto et al., 2014b; Rosén et al., 2016; Folsom et al., 2016), magnetic field—stellar wind connection (Vidotto et al., 2014b; Vidotto, 2016b; Finley et al., 2018; See et al., 2019b), Zeeman Doppler Imaging (ZDI) (Donati et al., 1995, 1997; Folsom et al., 2016, 2018a; See et al., 2017; Lehmann et al., 2017, 2018), magnetic field cycles and activity relationships (Boro Saikia et al., 2015; Saikia et al., 2018; Jeffers et al., 2017, 2018).

The magnetic field strength in stars can be inferred using the Zeeman effect. An atomic emission or absorption line is excited if electrons transition from one energy level to another. The exact energy of these levels is altered in the presence of a magnetic field, which depends on the electron spin and angular momentum. The Zeeman effect is the physical phenomenon of splitting spectral lines into separate components due to the presence of a static magnetic field. It is a well studied effect in physics, first discovered by Pieter Zeeman in 1897 (Zeeman, 1897), with the anomalous Zeeman effect reported by Armagh man Thomas Preston¹ some years later (Preston, 1899). George Ellery Hale was the first to notice this effect in sunspots, thereby discovering that sunspots were magnetic in nature (Hale, 1908). This is the first example of somebody using this effect on a star, and is essentially the same method that is used today for the Sun, with some added mathematical complexity to deal with non-resolved surfaces in the case of stars.

Combining this magneto-radiation phenomenon with the Doppler effect, the surface magnetic fields of stars can be derived. This technique is relatively new compared to the previous research mentioned, but has existed long enough to be well-tested on observations of many different stars. Proposed by Marsh & Horne (1988), the technique was developed by Donati & Brown (1997) (cf. Piskunov & Kochukhov, 2002), who described a method for processing the spectropolarimetric observations of stars to produce a surface magnetic field. Observations of the stellar surface are conducted using a spectropolarimeter. This instrument records the polarisation as well as the total intensity as a function of wavelength. This is necessary for multiple reasons. Simple observations of unresolved stellar Zeeman effect would result a single disk averaged value

¹ Preston, incidentally, is a TCD alumnus that worked with G. F. Fitzgerald and conducted this research in UCD, but unfortunately died a year later at the age of 40 (Weaire & O'Connor, 1987)

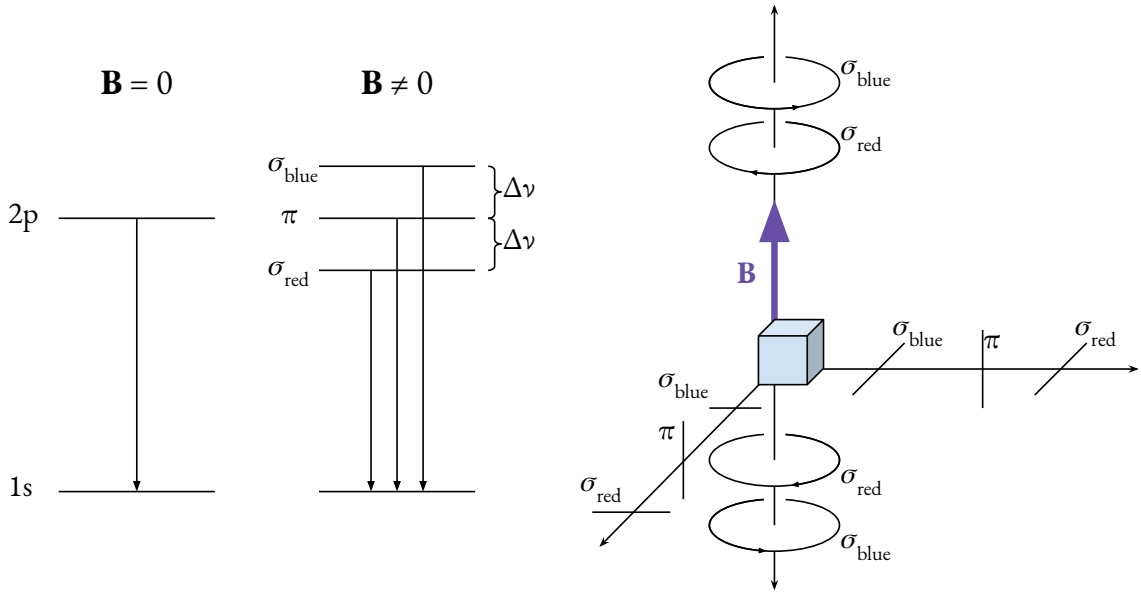


Figure 1.11: Schematic showing the splitting and polarisation effects of a spectral line under the influence of a magnetic field.

for magnetic field. The Zeeman components of a spectral line are typically unresolved in stellar spectroscopy, making it difficult to distinguish them from other line broadening processes such as thermal, turbulent and rotational broadening. However, few effects produce circular polarisation in lines, thus the Zeeman effect can be reliably detected in polarisation for much weaker magnetic fields. Since the polarisation of Zeeman components (often referred to as $\sigma_{\text{blue,red}}$ and π , denoting the shifts in wavelengths from line splitting) of an observed line depends on the orientation of the magnetic field to the line of sight, the polarisation also provides geometric information on the magnetic field. The dependence on orientation can be described by orbital theory of electrons as different orbital transitions will produce different polarisation signatures relative to the magnetic field, based on the change in electron angular momentum ($L_{\sigma} = \pm 1; L_{\pi} = 0$). Parallel to the magnetic field, σ transitions will be circularly polarised (right or left polarised for +1 and -1 changes in angular momentum respectively), and π transitions will be invisible. Perpendicular to the magnetic field, σ transitions will appear linearly polarised, while π transitions appear linearly polarised, perpendicular to the σ transitions. These effects are discussed in depth in [Landi Degl’Innocenti & Landolfi \(2004\)](#); [Reiners](#)

(2012), and shown schematically in Figure 1.11. Stokes parameters are frequently used as a measure of polarisation (Stokes, 1852), and schematically are defined as

$$\begin{aligned} \mathbf{I} &= \updownarrow + \leftrightarrow & \mathbf{Q} &= \updownarrow - \leftrightarrow \\ \mathbf{U} &= \nearrow - \nwarrow & \mathbf{V} &= \cup - \cup \end{aligned}$$

Stokes I is the integrated (unpolarised) light. Stokes Q and U measure the two directions of linear polarization, and Stokes V measures circular polarization.

Using a technique known as least squares deconvolution (LSD) the information from many spectral line profiles can be combined to create a pseudo-average profile with much less noise (Donati et al., 1997; Kochukhov et al., 2010). With observations provided using a spectropolarimeter, the Zeeman effect can be combined with LSD, therefore good resolution and a wide range of wavelengths is necessary to obtain accurate results. Combining both the Zeeman effect and LSD, interesting effects can be observed in the observed polarised line profiles. We show the effect of a magnetic spot on the circularly polarised Stokes V line in Figure 1.12. Given that we know the effect of a magnetic field on the spectra, it is then possible to work backwards to derive the total surface magnetic field. Zeeman Doppler Imaging (ZDI) is a technique in which we invert a time series of Stokes V profiles to infer a magnetic field (Figure 1.13a). Note that this technique does have degenerate solutions, so the magnetic field with the least total magnetic field energy is used. In reality this is the solution which maximises entropy (for definitions see Folsom et al., 2018a, ; e.g. Figure 1.13b).

There are some limitations to ZDI which we always make clear when using these results for stellar wind simulations. Surface magnetic field maps derived through ZDI favour large-scale magnetic fields over small-scale magnetic fields. This is due to resolution issues, as differences in Doppler shift depend on the velocity sensitivity of the instrument, making regions near each other on the stellar disk difficult to disentangle. The strongest magnetic fields also appear in the smallest regions—i.e. starspots, similar to sunspots on the Sun. This is further complicated by the tendency of starspots to come in pairs with an opposite sign to their radial magnetic field (at least in stars like the

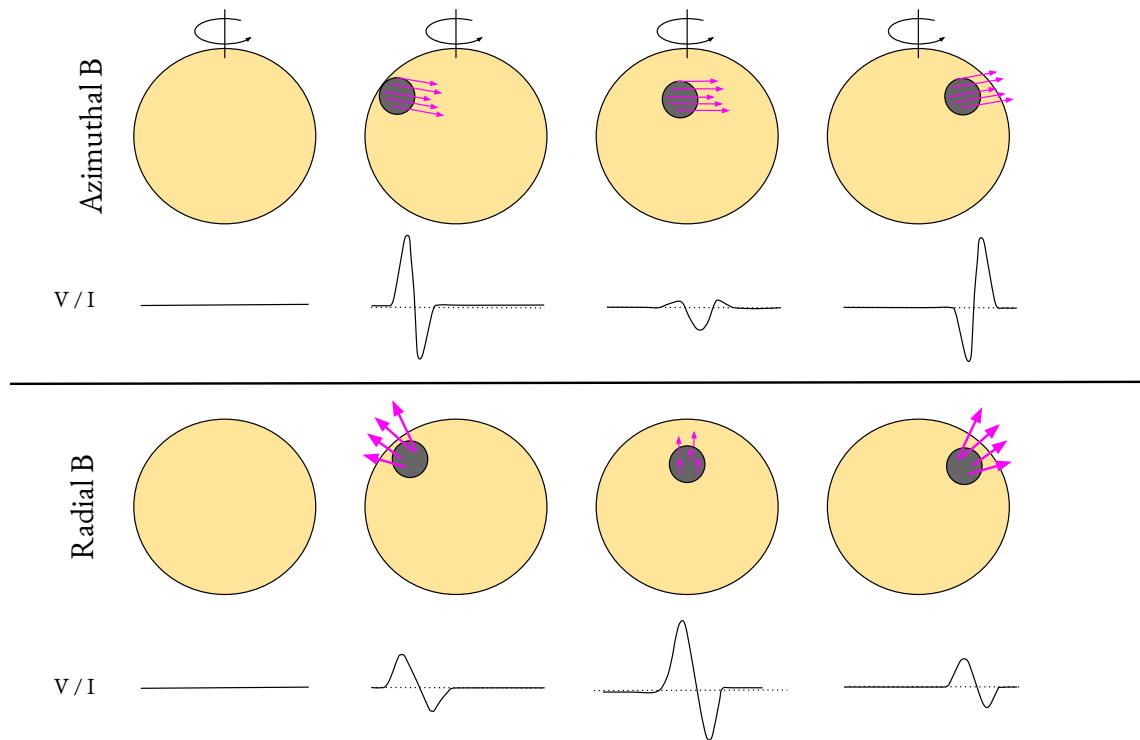


Figure 1.12: This schematic shows the effect of azimuthal and radial magnetic fields (magenta arrows) from a singular source (grey spot) on the stellar disk. We see how the circularly polarised (Stokes V) line profile changes as the star rotates about its axis.

Sun), which largely cancels out in Stokes V observations with limited spatial resolution. There has been much research into the validity of surface magnetic fields as described by the ZDI technique, which concludes that they are valid, especially for large-scale fields (Vidotto, 2016b; See et al., 2017; Lehmann et al., 2017, 2018; See et al., 2019b,a; Boro Saikia et al., 2020).

As we are dependent on the stellar rotation to obtain full coverage of the stellar surface, the rotation period of the star is important to consider. Slow rotators are harder to observe as they take much longer to get full surface coverage. They generally provide lower spatial resolution, since the rotational Doppler shift is the best way to distinguish different regions on the surface. Therefore, older stars take much more observational time due to their weak magnetic fields and slow rotation. If a star exhibits very weak large-scale magnetic field, this is difficult to observe in the Zeeman splitting and requires a higher signal to noise ratio in Stokes V. As a star ages, its large scale magnetic field will weaken (Vidotto et al., 2014b). Therefore surface magnetic field maps of evolved solar-mass giants can be difficult to derive.

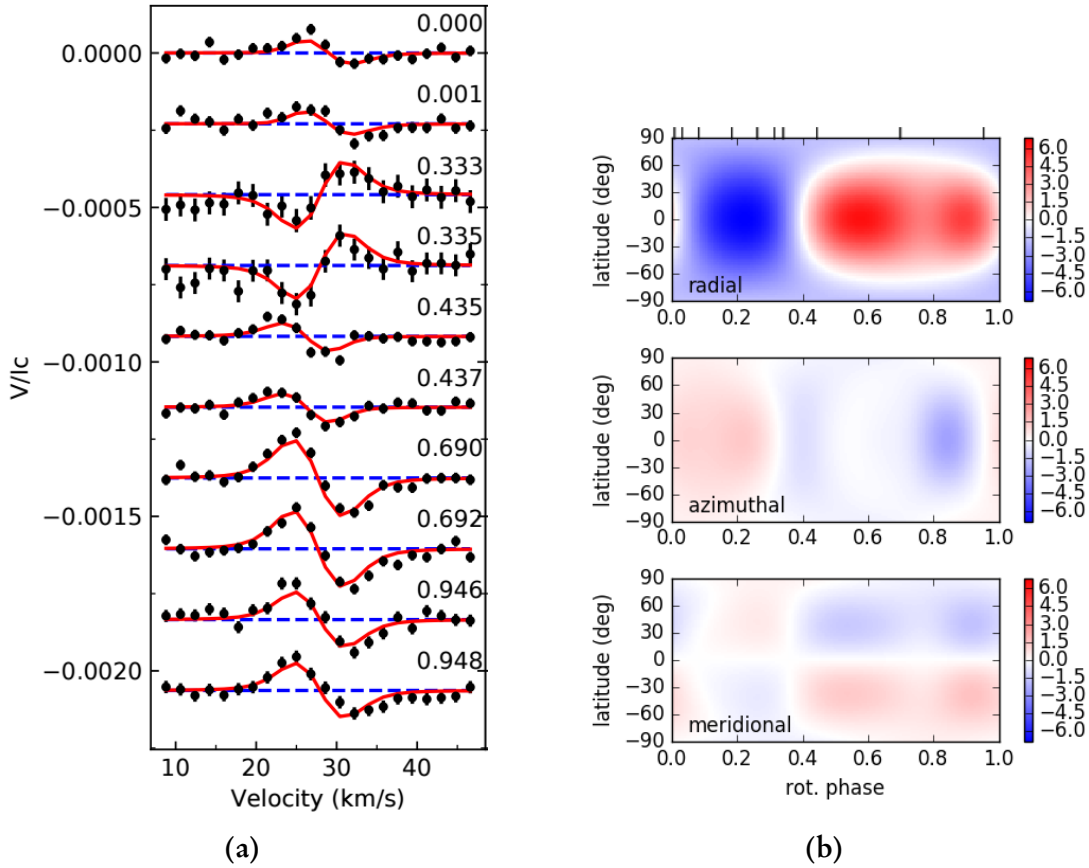


Figure 1.13: *Left:* An example of Stokes V profiles for different stellar phases are shown in this figure. *Right:* This is an example of the radial (top), azimuthal (middle) and meridional (bottom) magnetic fields for 55 Cancri, a slowly rotating star. This map was published in [Folsom et al. \(2020\)](#).

The resulting magnetic field is one that looks like Figure 1.13b, for a slowly rotating star with limited spatial resolution. This method provides us with the necessary surface magnetic fields to simulate the winds of solar-type stars. We can use these values and place them at the base of our simulations (discussed further in Chapter 2).

1.4 STAR-PLANET INTERACTIONS (SPI)

The map above (Figure 1.13b) shows the magnetic field of the solar-like star 55 Cnc, which was published in [Folsom et al. \(2020\)](#). This star hosts 5 exoplanets, one of which is orbiting very close to the star at 0.015 au. The close-proximity and the relatively strong magnetic field of the star led us to investigate possibilities of magnetic interactions

between the star and the planet. Thus, the final introductory topic that I discuss here concerns star-planet interactions.

Star-planet interactions (SPI) can be loosely defined as any interaction between a star and an orbiting planet, perhaps ignoring the implied gravitational interaction that keeps that planet in orbit. The main types of SPI can be split into 4 main categories: magnetic, wind, radiative, and tidal (Vidotto, 2019).

In this work we focus on two interactions, that of the wind and magnetism. Throughout Part III, we reference these two types of SPI frequently. The wind is the first interaction that we deal with and is probably the most intuitive. As the streaming particles from the stellar wind travel from the stellar surface to the edge of the astrosphere, they undoubtedly will impact upon the planet or the planetary magnetic field. These particles carry with them a mass, momentum, and charge. This impact pressure from these particles—commonly referred to as ram pressure—can affect the magnetosphere of a planet, changing its properties, such as size and shape. The exact way this happens depends on the strength of the stellar wind (faster and more dense winds produce larger ram pressures), and the strength and orientation of the planetary magnetic field. Planets without a magnetic field are also affected. These charged particles from the wind impact their atmospheres, mainly the upper layers such as the ionosphere. The interaction of the upper ionosphere and stellar wind form electromagnetic current and an induced magnetosphere forms, although usually this is much weaker than an intrinsic planetary magnetic field. As a consequence, this change in magnetic properties can change the atmosphere of the planet, as the atmospheric particles are ripped away from the planet. This is observed to occur within our own solar system. Understanding how the wind of the Sun has evolved is an important step in understanding the long-term evolution of the planets in the solar system, including the Earth and the development of life (see e.g. Chassefière & Leblanc 2004).

This effect can be exacerbated by radiative SPI. When stars emit high energy radiation (incl. the Sun), this can be absorbed in the planetary atmosphere. For close in exoplanets this can cause significant heating and expansion of the atmosphere, making

it easier to escape the gravitational potential well of the planet (Lammer et al., 2003). In this work we do not explicitly study the effects of this high energy radiation, but rather focus on the ram pressure changes as the stellar wind evolves. Even small changes, sustained over long periods of time can determine whether a planet will keep or lose its atmospheric envelope, producing vastly different evolutionary outcomes for the planet.

It can be assumed that stars always exhibit some magnetic fields. Many planets also exhibit intrinsic magnetic fields (e.g. Earth & Jupiter), although some are not magnetic (e.g. Venus). Under the correct conditions, this magnetised system can cause observational phenomena from the star or planet which would otherwise be absent. One idea is that anomalous activity can be observed on the star, which is induced by the presence of an exoplanet (Cuntz et al., 2000; Cranmer & Saar, 2007). This can occur through the propagation of particles along magnetic field lines connecting the planet and the star, induced by transient magnetic reconnection events (Ip et al., 2004). It can also occur through the formation of Alfvén wings, which channels particles from the planet to the star (Strugarek et al., 2015; Strugarek et al., 2019). The observability of this anomalous activity is strongly dependent on the magnetic field topologies of the star and planet, the exoplanetary orbits, and the stellar wind environment (McIvor et al., 2006; Shkolnik et al., 2008). Stars with orbiting exoplanets have been observed to show anomalous activity that can be attributed to magnetic interactions with exoplanets (Shkolnik et al., 2002; Shkolnik et al., 2005; Cauley et al., 2018). From this the authors were able to estimate the magnetic field of orbiting exoplanets. Exoplanetary magnetic fields have not been directly detected, but there is much recent evidence that they exist (Cauley et al., 2018, 2019; Vedantham et al., 2020). This alone is a strong motivating factor to understand these SPIs better, but it also enables us to place constraints on the wind. Given magnetic interactions with an exoplanet, we can say that the exoplanet must orbit within a certain distance (the Alfvén surface, discussed further in Chapter 2). In Chapter 8 I discuss the research we conducted into 55 Cancri and its exoplanets (namely planet e, a rocky planet very close to the star), using observations of the stellar magnetic

field and wind simulations to determine if SPI was capable of manifesting in this system through magnetic interactions.

1.5 THESIS OUTLINE

In this chapter, the underlying motivation to study the evolution of low-mass stars was introduced. I discussed the research over the past few decades that has linked stellar rotation to stellar activity markers, which allowed us to quantify the evolutionary state of stars. I briefly illustrate the few methods we possess to indirectly measure the mass-loss rates of low-mass stellar winds, considered essential for the evolution of these stars throughout their lifetimes.

Throughout the remainder of Part I of the thesis, I will describe the necessary theory for understanding the research conducted and results derived from my work. In Chapter 2, I will describe the mathematical models and governing equations of solar and stellar winds, from the most fundamental of wind models (the Parker wind), to full 3D ideal MHD winds, followed by wave-driven 3D MHD winds. Chapter 3 defines some relevant plasma physics equations and theory to understand the thermal emission we expect to see in the radio regime from stellar winds.

In Part II I will discuss the research carried out on the solar wind evolution by studying solar analogues—stars similar to our own Sun—across a range of ages. In Chapter 4 I will examine 1D hydrodynamic (HD) simulations of these stellar winds, allowing insights into the mass-loss rates of solar-type stars along the main sequence. To do this we will propose a novel wind temperature-stellar rotation relationship. Chapter 5 will examine the full 3D magnetohydrodynamic (MHD) simulations of solar analogue winds, using observed surface magnetic field maps. These 3D MHD simulations will allow me to investigate the mass-loss and angular-momentum lost through these winds at various stellar ages. Finally in Chapter 6, I examine the wind of a post-MS solar-mass star (λ An-

dromedae), allowing an examination of the effects an expanded stellar radius and wave driving mechanism has on the stellar wind.

In Part III I will explore the effects of these evolving stellar winds on (exo-)planets. The planets are embedded in the stellar winds, which consequently, directly affect the evolution of the planetary magnetosphere and atmosphere. Chapter 7 will examine this effect for all of the simulated winds (1D & 3D). Chapter 8 takes a look at the effects of closer in exoplanets, specifically in the case of the 55 Cancri planetary system, and its closest exoplanet, 55 Cnc e. I discuss the necessary environmental conditions for the production of star-planet interactions, and the effects of propagation conditions for waves in these winds. Finally, Chapter 9 concludes the research in this thesis, and outlines interesting future work that lies ahead.

MODELLING WINDS OF SOLAR ANALOGUES

The expulsion of material from the surface of stars through stellar winds is the process by which stars lose mass. This material forms a continuous outflow from the star, an interplanetary medium, which creates the astrosphere around a star, terminating as it reaches a pressure equilibrium with the ISM (Figure 1.2). The concept that the Sun and stars possess winds was precipitated by Biermann (1951), as he noted the directionality of comet tails was always pointed radially away from the Sun. Biermann himself suggested a particle flux from the Sun, but did not focus on the origins of such a flux. Chapman & Zirin (1957) suggested that this could be due to a static medium, one which does not change with time. However, this idea had a number of physical problems, namely the large pressure as the wind approaches the ISM which does not equate with the ISM pressure, outlined by Parker (1958, 1960). Parker (1958) built upon this idea from Chapman however, and investigated how a steady outward flow could be formed

from the Sun beginning with the solar corona. This outward flow he coined the solar wind (and in later work the stellar wind for other stars). He successfully showed that the Sun could possess an isotropic, non-rotating, isothermal, stationary wind, which is accelerated close to the Sun and terminates at the ISM. This theory for a stellar wind is the simplest approximation we can make, that can still predict values at the range of Earth quite accurately. Therefore it is still widely used today, as it is inexpensive for resources to compute. While considering a hydrodynamic flow, Parker did include some analysis on how this flow would effect the solar dipolar magnetic field, and produced what is now known as the Parker spiral. This spiral shows how radial inter-planetary magnetic field lines get dragged behind the solar rotation, forming Archimedean spirals. Since this pivotal leap by Parker, models have begun to evolve and became more complex as time went on. Additional physics and mechanisms were included in wind models, as both our understanding of the physics and computational power increased.

The first numerical solutions to the solar wind were simulated by [Noble & Scarf \(1963\)](#), using the wind surrounding the Earth as a constraining condition for their simulations. With advances including heat conduction, viscosity, and two-fluid models appearing not much longer afterwards ([Scarf & Noble, 1965](#); [Sturrock & Hartle, 1966](#)). [Weber & Davis Jr. \(1967\)](#) included the solar magnetic field and rotation in their models, providing another leap in advances. At this point more complex magnetic field models were appearing for the solar corona (potential field models; [Altschuler & Newkirk 1969](#)), allowing extrapolation of magnetic fields above the solar surface. Concurrently, models were being developed that included expansion of plasma from the coronal field lines into the solar wind ([Pneuman & Kopp, 1971](#)). By the 70s, 2D models of the solar corona began to appear ([Steinolfson et al., 1975, 1982](#)), with 3D wind models being developed alongside them ([Pizzo, 1978, 1980](#)). A theme throughout this development is the difficulty in connecting different regions of the solar atmosphere, the transition region to the chromosphere, to the corona and then to the large-scale solar wind and heliosphere.

The development of the BATS-R-US code began shortly thereafter, which is used throughout this work (Powell et al., 1999). From here, there are many different codes developed using 3D MHD formulations for simulating the solar wind and heliosphere, constantly adding additional physical processes (Usmanov et al., 2000; ud-Doula & Owocki, 2002; Sokolov et al., 2013; van der Holst et al., 2014; Strugarek et al., 2015; Xia et al., 2018; Daley-Yates & Stevens, 2019). 1-, 2-, and 3D models are all still frequently used, focusing on different physical processes (Suzuki, 2002; Suzuki et al., 2013; Suzuki, 2018; Hayashi, 2005; Cranmer et al., 2007; Johnstone et al., 2015a; Shoda et al., 2018a,b). There is an abundance of research into this area, for which I direct the reader to Gombosi et al. (2018) for a full review of the current state of MHD modelling of the solar corona and the solar wind.

The physical process of accelerating and forming winds, which is quite complicated and still not fully understood, can have different origins depending on the properties of the star. All stars have pressure gradients that cause the outflow of particles from their surfaces. Young, active stars have winds that are driven due to thermal expansion from hot coronae, which in turn is suspected to originate due to magnetic activity on the star (Hollweg, 1976; Cranmer et al., 2007). This is thought to be the case for many low-mass stars. For high-mass stars or stars that have evolved past their MS lifetime with large luminosities, the process is mostly driven by radiation pressure through continuum and line opacities in the wind (Castor et al., 1975). The expulsion of particles as a wind from the star can affect the life-cycle of a star, particularly for massive stars, which possess much higher mass-loss rates than low-mass stars. In this work, we focus on low-mass, solar-type stars, with our main wind simulations taking into account the most important physical process, namely the thermal expansion of these stellar winds.

Obtaining measurements of stellar wind properties is challenging, with some remote (i.e. *ex situ*) observations providing tenuous connections to real physical parameters, as discussed in Chapter 1. Our Sun is the only case where *in situ* measurements allow us to place tight constraints on the wind parameters. At the Earth, the solar wind holds a velocity around 400-600 km s⁻¹ and a density of 5-15 protons per cm⁻³ (Mc-

Comas et al., 2008; Usmanov et al., 2014; Bagenal, 2013). The Sun has a mass-loss rate of $\sim 10^{-14} M_{\odot}\text{yr}^{-1}$ (Wang, 1998; Cranmer & Saar, 2011; Cranmer, 2017). Mass-loss rate is considered to be the most important and influential parameter when studying stellar winds. In the case of massive stars, their extreme mass-loss rates (approx. $10^{-8} - 1 M_{\odot} \text{yr}^{-1}$, depending on the evolutionary stage and mechanism) can change their evolutionary pathway and how they die, while the main effect on low-mass stars is the angular-momentum loss evolution of the star. Since *in situ* measurements are not possible for distant stars, we must rely on more indirect methods. The first method one can use to study stellar winds is through indirect observations. These include, but are not exclusive to, Ly- α observations of the astrosphere-interstellar medium interaction, and observations of thermal radio emission from their stellar winds, both described in the previous chapter.

The other indirect method used for studying stellar winds is through modelling. By constructing models of the plasma accelerated from the stellar surfaces, we can begin to constrain the physics at play in these dynamic environments. These simulations can be compared to the observations outlined in Chapter 1, which guides the formulation of these models. A symbiotic relationship between observations and simulations is essential to progress the research that sits at the very edge of our knowledge. Observations help design simulations, and simulations help guide the observations.

With this in mind, we describe the models that are used throughout this thesis to give the reader an understanding of the mechanics working behind our results.

2.1 1-DIMENSIONAL PARKER WIND

In [Parker \(1958\)](#), the author assumed that the solar wind was not in a state of hydrostatic equilibrium, as previous works had assumed, but rather in a stationary state of constant expansion. Equation 2.1 shows the equation of hydrostatic equilibrium for a static wind.

$$\frac{dP}{dr} + \frac{GM_{\star}\rho}{r^2} = 0 \quad (2.1)$$

Here, P is the pressure, r is the radial distance from the star, G is the gravitational constant, ρ is the mass density, and M_{\star} is the stellar mass. To form a stationary expanding wind the hydrostatic equation (Equation 2.1) needs to include a term to shift the equilibrium balance in favour of the outward acting forces. The first term denotes the pressure gradient, while the second term denotes the gravitational force. In the case of a static fluid, these are equal and opposite, therefore sum to zero. Throughout this chapter we will use the concept of mass conservation, and mass-loss rate from a stellar wind. To illustrate this imagine you have a volume element dV which holds a certain mass, m

$$m = \int_V \rho dV \quad (2.2)$$

The rate of changing mass of the fluid in the volume element dV is

$$\frac{dm}{dt} = \frac{\partial}{\partial t} \int_V \rho dV \quad (2.3)$$

We can also quantify the rate of mass leaving the surface S , which defines the volume V using the divergence theorem

$$\oint_S \rho \mathbf{v} d\mathbf{S} = \int_V \nabla \cdot (\rho \mathbf{v}) dV \quad (2.4)$$

Therefore the change in mass of volume V is equal to the mass that left the volume through surface S

$$\frac{\partial}{\partial t} \int_V \rho dV = - \int_V \vec{\nabla} \cdot (\rho \mathbf{v}) dV \quad (2.5)$$

$$\therefore \frac{\partial \rho}{\partial t} + \nabla \cdot (\rho \mathbf{v}) = 0 \quad (2.6)$$

Equation 2.6 is known as the continuity equation. It states that the change in density within a volume equates with the mass diverging from that volume, therefore conserving mass. In the case of a stationary wind $\partial/\partial t = 0$, and so

$$\nabla \cdot (\rho \mathbf{v}) = 0 \quad (2.7)$$

$$\frac{1}{r^2} \frac{\partial}{\partial r} (r^2 \rho v_r) = 0 \quad (2.8)$$

$$\rho v_r r^2 = \text{const} \quad (2.9)$$

where we use spherical coordinates, v_r is the radial velocity. If we consider a sphere, the change in mass within the sphere (or the mass-loss rate, \dot{M}) is

$$\dot{M} = 4\pi r^2 \rho v_r \quad (2.10)$$

To derive the momentum equation of the wind, we can use Newton's 2nd law of motion in Lagrangian form.

$$\rho \frac{D(v)}{Dt} = \sum \frac{\mathbf{F}}{V} \quad (2.11)$$

where \mathbf{F} represents the forces in the system. In the case of an expanding wind there are two forces at play: the outward force from pressure and the inward force from gravity, shown in Equation 2.12.

$$\rho \frac{D(v)}{Dt} = - \frac{dP}{dr} - \frac{GM_\star \rho}{r^2} \quad (2.12)$$

where the second term is the pressure gradient and the third term is the gravity acting against the wind expansion. This is the momentum equation in Lagrangian coordinates. However, the Lagrangian derivative of the fluid is in the frame of the fluid, which can

be expressed in terms of the Eulerian derivative (the rest frame or observers frame) and convective derivative as

$$\frac{D}{Dt} = \frac{\partial}{\partial t} + \mathbf{v} \cdot \nabla \quad (2.13)$$

$$\rho \frac{D(\mathbf{v})}{Dt} = \rho \left(\frac{\partial \mathbf{v}}{\partial t} + \mathbf{v} \nabla \cdot \mathbf{v} \right) \quad (2.14)$$

Since a Parker wind is stationary in Eulerian coordinates—not changing in time—the Eulerian derivative on the right can be eliminated ($\partial \mathbf{v} / \partial t = 0$). In the case of a constantly expanding wind we can equate Equation 2.14 with the outward forces that causes the wind to expand. By substituting Equation 2.12 into Equation 2.14 and dividing across by density. Written in radial coordinates we find

$$v \frac{dv}{dr} = -\frac{1}{\rho} \frac{dP}{dr} - \frac{GM_{\star}}{r^2} \quad (2.15)$$

In this case, the first term describes the acceleration of the wind due to the imbalance between the second and third terms (pressure and gravity respectively). It can be useful to examine the wind in terms of energy per unit mass

$$e(r) = \frac{v^2}{2} - \frac{GM_{\star}}{r} + \frac{5}{2} \frac{\mathcal{R}T}{\mu} \quad (2.16)$$

where the terms represent kinetic energy, potential energy and enthalpy respectively. \mathcal{R} is the gas constant and μ is the permeability of free space. Note that $\mathcal{R}/\mu = k_B$. Taking the energy at the base of the wind to be $e(r_0)$ we can write the following equation to show explicitly how the energy changes with r , assuming an isothermal wind

$$e(r) = e(r_0) + \frac{v^2 - v_0^2}{2} + \frac{GM_{\star}}{r_0} \left(1 - \frac{r_0}{r} \right) \quad (2.17)$$

where r_0 and v_0 are the values of radial distance and velocity at the base of the wind respectively. From this equation it then becomes clear that we are constantly adding energy, which is how isothermal winds remain at the same temperature for their entire

profile, that is $T(r) = T_0$. In Equation 2.17 there are no loss terms. It begins with the base energy $e(r_0)$ and both the second and third terms on the right hand side are always positive distance and velocity are always increasing.

We can derive the Parker momentum equation used to numerically solve for the stellar wind solution. Beginning with the momentum equation (Equation 2.15), the second term can be re-written, assuming an isothermal ideal gas,

$$P = nk_B T = \mathcal{R}\rho T / \mu$$

$$\frac{1}{\rho} \frac{dP}{dr} = \frac{\mathcal{R}}{\mu} \frac{dT}{dr} + \frac{\mathcal{R}T}{\mu\rho} \frac{d\rho}{dr} = \left(\frac{\mathcal{R}T}{\mu} \right) \frac{1}{\rho} \frac{d\rho}{dr}$$

where n here is the number density. Assuming a stationary wind, the mass-loss rate is constant

$$\rho v r^2 = \text{constant}$$

$$\frac{1}{\rho} \frac{d\rho}{dr} = -\frac{1}{v} \frac{dv}{dr} - \frac{2}{r}$$

From manipulating the momentum equation in Equation 2.15, assuming an isothermal stationary wind, we arrive at the standard Parker wind equation (Lamers & Cassinelli, 1999)

$$v \frac{dv}{dr} + \frac{\mathcal{R}T}{\mu} \left\{ -\frac{1}{v} \frac{dv}{dr} - \frac{2}{r} \right\} + \frac{GM_\star}{r^2} = 0 \quad (2.18)$$

which is sometimes displayed as

$$\frac{1}{v} \frac{dv}{dr} = \left\{ \frac{2a^2}{r} - \frac{GM_\star}{r^2} \right\} / \{v^2 - a^2\} \quad (2.19)$$

where a is the isothermal sound speed

$$a = (\mathcal{R}T/\mu)^{1/2} \quad (2.20)$$

This equation has many solutions but only one is the correct wind solution. This solution is the only physical solution which begins subsonically and passes through a critical

point, becoming supersonic at large distances. From this equation (Equation 2.19) we can see that there exists a critical point in the wind. This happens where the wind velocity equals the sound speed of the wind, $v = a$. We can find the location of this critical point by examining when the numerator of Equation 2.19 goes to zero

$$\begin{aligned}\frac{2a^2}{r_c} &= \frac{GM_\star}{r_c^2} \\ r_c &= \frac{GM_\star}{2a^2}\end{aligned}$$

In an isothermal wind, this critical point coincides with the sonic point. This is not necessarily true for other types of winds however. If a solution does not pass through the critical point, the result is an unphysical wind solution (see Fig. 3.1 in Lamers & Cassinelli 1999). A typical transonic solution to the Parker wind equation is shown in Figure 2.1. This is a 1D wind solution for the solar wind with a temperature of 1 MK, and a velocity of 480 km s^{-1} at 1 au. The density in Figure 2.1 is arbitrary and can be scaled based on the base density (which is approximately the same as the corona density). Assuming a base density of 10^9 cm^{-3} (similar to observations; Warren & Brooks 2009) this results in a wind density of 7.7 cm^{-3} at 1 au. Both the velocity and density from the Parker wind solution agree with the values observed at Earth. While isothermal Parker winds are sufficiently good at estimating the overall profile of stellar winds there are areas where they can be improved. Namely they overestimate the temperature throughout the wind, and due to the added energy they overestimate the wind velocity. Nonetheless, they are a powerful and useful tool for the study of stellar winds. Polytropic winds alleviate some of these issues, by changing the energy deposition in the wind (Keppens & Goedbloed, 1999a) and allowing the temperature to change through the wind, which is what happens in reality.

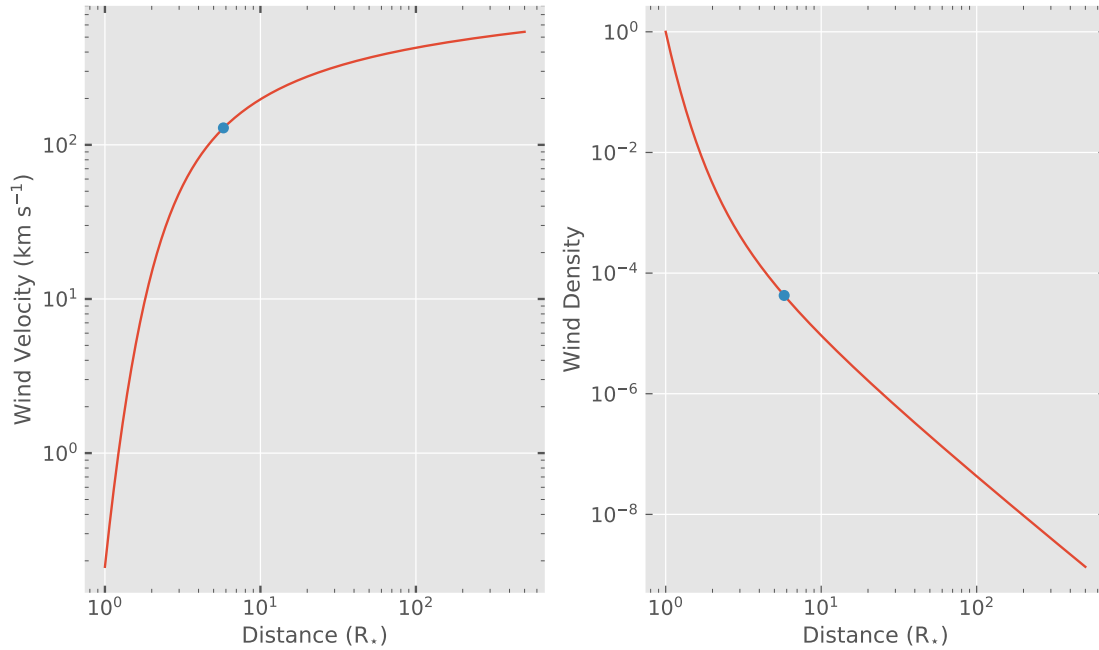


Figure 2.1: A solution of the Parker wind for the case of the Sun. Velocity (left) and density (right) profiles are shown. The blue point indicates the position of the critical point in the wind. Here the temperature of the wind is 1 MK. As the wind reaches terminal velocity, the density will decay $\propto r^{-2}$.

2.2 1-DIMENSIONAL POLYTROPIC WINDS

In Chapter 4 I use the polytropic wind model to investigate the evolution of the solar wind by simulating the winds of many solar-like stars. In this section I derive the equations which describe the polytropic wind model. In this scenario, the wind is no longer isothermal, but the energy deposition is controlled and set somewhere between adiabatic and isothermal. The introduction of temperature gradients means that there will now be additional pressure gradients in the wind, and also the sonic and critical points will change, changing the mass-loss rate of the wind. Temperature gradients are achieved through the polytropic index, which is usually denoted as Γ . Note that the lowercase

γ usually denotes the adiabatic index¹, but these get mixed up in the literature. The generalised energy of the wind is

$$e(r) = \frac{v^2}{2} - \frac{GM_*}{r} + \frac{\gamma}{\gamma-1} \frac{\mathcal{R}T}{\mu} = \frac{v^2}{2} - \frac{GM_*}{r} + \frac{5\mathcal{R}T}{2\mu}. \quad (2.21)$$

where in the case of an ideal monotomic adiabatic gas, $\gamma = 5/3$, resulting in an enthalpy of $5\mathcal{R}T/2\mu$. Polytopic winds are defined by the relationship

$$T(r) = T_0 \left(\frac{\rho(r)}{\rho_0} \right)^{\Gamma-1}, \quad P(r) = P_0 \left(\frac{\rho(r)}{\rho_0} \right)^{\Gamma}, \quad (2.22)$$

where Γ is the polytropic index, and represents the energy deposition in the wind (when $\Gamma = 1$ the wind is isothermal). T_0 , p_0 and ρ_0 represent the base temperature, pressure and density of the wind respectively. Smaller Γ denote larger energy deposition, and larger Γ represent smaller energy deposition. For an adiabatic wind $\Gamma = \gamma = 5/3$ and if there is no additional energy input, which is the case of no other acceleration terms, a wind will not be produced. However, this is frequently used when other forms of energy deposition are included, such as Alfvén waves. The Γ term can be viewed as a representation of all energy sources that are not being explicitly solved in the wind. However, there is some research that has used more explicit energy deposition mechanisms (Cranmer et al., 2007; Verdini et al., 2010; Suzuki et al., 2013; van der Holst et al., 2014). In my work throughout this thesis I use a Γ that is constant throughout the wind, but Γ can also be a function of r (Van Doorselaere et al., 2011; Johnstone & Güdel, 2015). We can describe the momentum equation of these polytropic winds as

$$v \frac{dv}{dr} + \frac{1}{\rho} \frac{dP}{dr} + \frac{GM_*}{r^2} = 0. \quad (2.23)$$

¹ Usually the adiabatic index is the ratio of the specific heat capacities at constant pressure and volume $\gamma = c_p/c_v$, and in the case of a monoatomically ideal gas this is $5/3$. The polytropic index, on the other hand, is the parameter used to replicate the energy deposition in the wind and can be anywhere from isothermal ($\Gamma = 1$) to adiabatic ($\Gamma = 5/3$).

This is similar to Equation 2.15, however the wind pressure is now described by Equation 2.22. We can rearrange the pressure term by assuming again the ideal gas law, however, now the pressure depends on the wind density as

$$\frac{P}{P_0} = \left(\frac{\rho}{\rho_0}\right)^\Gamma$$

$$\ln\left(\frac{P}{P_0}\right) = \Gamma \ln\left(\frac{\rho}{\rho_0}\right)$$

$$\ln P - \ln P_0 = \Gamma(\ln \rho - \ln \rho_0)$$

$$\therefore d \ln P = \Gamma d \ln \rho$$

In this case we need to use the identity that $d \ln(x)/dr = 1/x dx/dr$, which is just that the derivative of a logarithm is an asymptote, but rearranged to include dr .

$$\frac{1}{\rho} \frac{dP}{dr} = \frac{P}{\rho} \frac{d \ln P}{dr} = \frac{\Gamma \mathcal{R}T}{\mu} \frac{d \ln \rho}{dr} = \frac{\Gamma \mathcal{R}T}{\mu} \left\{ -\frac{1}{v} \frac{dv}{dr} - \frac{2}{r} \right\}$$

This results in the momentum equation for polytropic winds

$$v \frac{dv}{dr} + \frac{\Gamma \mathcal{R}T}{\mu} \left\{ -\frac{1}{v} \frac{dv}{dr} - \frac{2}{r} \right\} + \frac{GM_*}{r^2} = 0 \quad (2.24)$$

$$\frac{1}{v} \frac{dv}{dr} = \left\{ \frac{2\Gamma a^2}{r} - \frac{GM_*}{r^2} \right\} / \{v^2 - \Gamma a^2\} \quad (2.25)$$

In the particular case of $\Gamma = 1$, it is clear that we will recover the isothermal Parker wind. We can solve Equation 2.25 using a numerical method known as the ‘shooting method’, it is a trial and error method by using a range of guesses for the base velocity, to check which solution passes through the critical point, where both the numerator and the denominator of the above equation are zero. The wind profile has the same form as the Parker wind, beginning subsonically, passing through the critical point, becoming supersonic and terminating at the ISM (see Figure 2.1 and Figure 2.2). For each guess the wind is solved using Equation 2.25 until either the numerator or denominator reach zero, then the guess is adjusted and trialled again. The adjustment for initial velocity

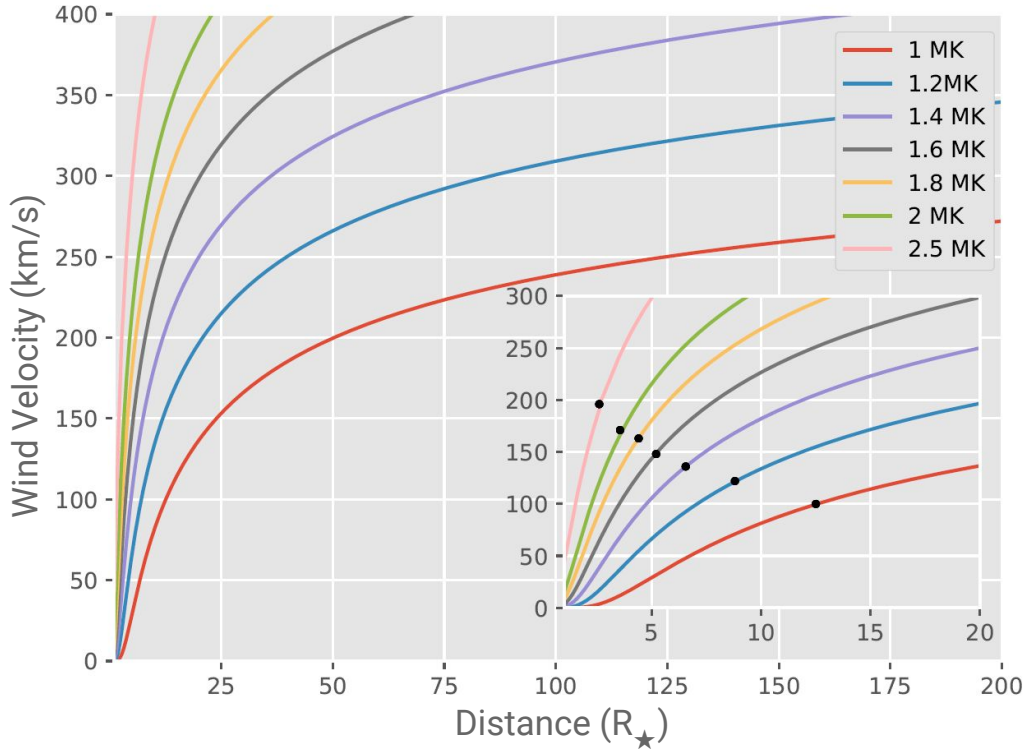


Figure 2.2: Example of the effect of base temperature on thermally driven polytropic winds. Velocity profiles of the winds using different base temperatures are plotted above. Critical points are shown as black points on each wind profile. $\Gamma = 1.05$ for each of these winds.

can be made by checking which reached zero first, the denominator or the numerator of Equation 2.25. The solution is achieved when both the numerator and denominator reach zero simultaneously (in reality this is restricted by the resolution of initial velocity guesses). Any standard numerical scheme can be used to integrate this equation, we employ a 4th order Runge-Kutta scheme (Süli & Mayers, 2003). As we can see, the critical point depends on the stellar mass, wind temperature, and polytropic index used, which will vary from star to star. The critical point will now change as the velocity of the wind depends on the polytropic index. We can find this critical distance in a similar manner as before

$$r_c = \frac{GM_\star}{2\Gamma a^2} \quad (2.26)$$

In the case of the Parker isothermal winds ($\Gamma = 1$), the position of the critical point can be determined *a priori* analytically. In the case of the polytropic winds this can not be achieved as the sound speed changes with r because the wind is no longer isothermal. Figure 2.2 shows solutions to polytropic wind equations using a solar mass star, varying

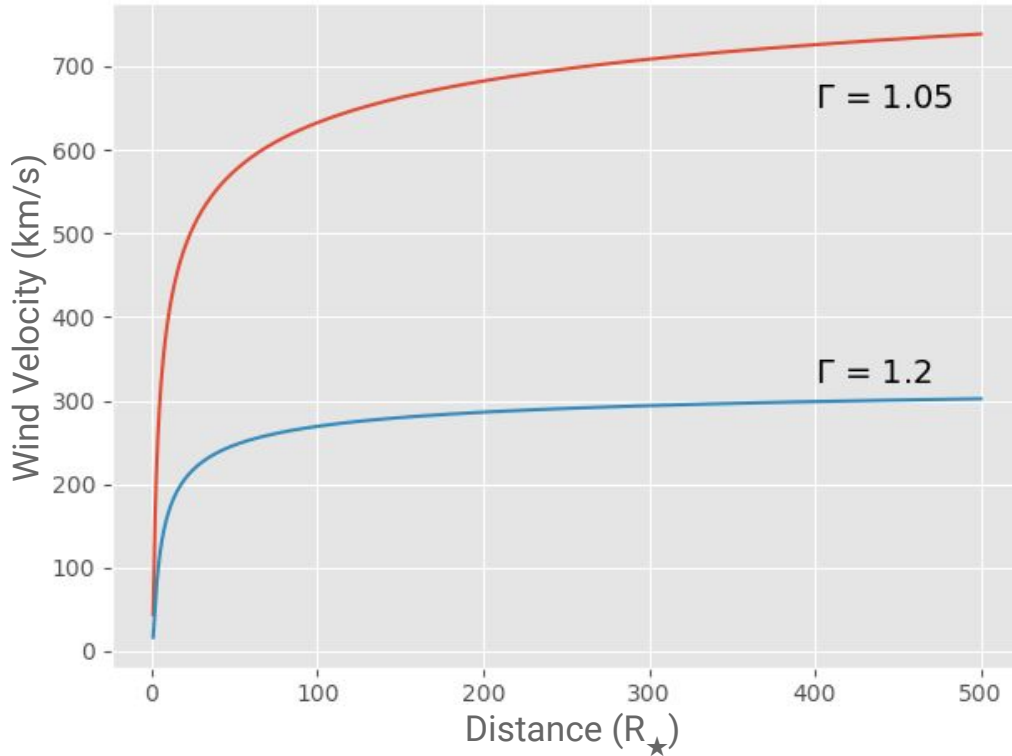


Figure 2.3: The effect of different Γ values on thermally driven polytropic winds. Velocity profiles are shown for two values of Γ . All other stellar parameters are kept the same in this scenario.

the base temperature of the stellar wind. The black points represent the position of the critical point in the wind. We can see the position of this point changes with different wind temperatures and velocities.

Figure 2.3 shows what happens when we vary the polytropic index for the wind of a solar mass star. The polytropic index effectively represents a number of unresolved physical processes in the wind, which act to accelerate the wind from the star. In the case of the Sun this parameter has been constrained through observations of the solar corona (see [Van Doorselaere et al. 2011](#), who derive a value of $\Gamma = 1.10 \pm 0.02$). In our simulations, we keep assume the polytropic index is constant, which is a reasonable approximation when simulating other stellar winds. Constraining this value for other stellar winds is difficult, as we do not have direct observations or information on their wind profiles. [Johnstone et al. \(2015a,b\)](#) examined stellar winds for low-mass stars, and determined that there are little constraints we can place on the polytropic index in stellar winds other than extending solar wind physics to these scenarios. The authors conclude

more stringent observations of low-mass stellar winds are necessary to constrain stellar wind parameters further. In our wind simulations we assume a polytropic index of $\Gamma = 1.05$, which results in values agreeable with solar wind observations at Earth. It is also similar to values adopted in [Johnstone et al. \(2015a,b\)](#) and is similar to that found in the solar corona ([Van Doorselaere et al., 2011](#)). The wind models discussed in this section are used to describe the stellar winds of solar-like stars in Chapter 4. These models therefore allow us to derive trends in solar wind evolution over the main sequence lifetime of the Sun ([Ó Fionnagáin & Vidotto, 2018](#)).

Polytropic winds address the non-physical aspect of the constant temperature in Parker winds. However, like the previously discussed Parker winds, these polytropic winds are 1D approximations of an actual stellar wind. They lack the 3 spatial dimensions and magnetic fields of realistic stellar winds. To rectify this I use the BATS-R-US code discussed in the following section.

2.3 3-DIMENSIONAL MAGNETOHYDRODYNAMICAL MODEL

Numerically simulating 3D MHD plasmas is complex and can be expensive computationally. However, they provide valuable information on the stellar wind structure (velocity, density, magnetic field, and temperature), which I use in Chapter 5 to extend my research of solar-like stellar wind evolution.

There are many methods to solve the ideal MHD equations, such as the finite volume method, smoothed particle hydrodynamics, and spectral numerical methods. In this work we use the most common of these for studying stellar winds, the finite volume method. This is whereby a domain in space is defined, which is then divided into many self-similar blocks or cells. The discretised conserved variables are defined by the cell-averaged values. For each time step, the cell-averaged value is updated using the sum of cell boundary fluxes and source terms at each iteration. Riemann solvers are used

to pass information between discretised cell walls. These are necessary due to the Riemann problem, which is an initial value problem in finite volume computational fluid dynamics. It arises by the creation of discontinuities in a continuous function, at the cell walls, and is inherent in finite volume methods. In our simulations we use the Roe solver (Roe, 1981). To solve the ideal MHD equations in this framework we need to write them in conservative form

$$\frac{d\mathbf{U}}{dt} + \nabla \cdot \mathbf{F}(\mathbf{U}) = \mathbf{S}(\mathbf{U}) \quad (2.27)$$

Equation 2.27 shows the conserved quantities \mathbf{U} , flux vectors \mathbf{F} , and source vectors \mathbf{S} . Note that flux and source terms are explicitly functions of the conserved quantities \mathbf{U} . In the ideal MHD case these terms can be expressed as

$$\mathbf{U} = \begin{bmatrix} \rho \\ \rho \mathbf{v} \\ \mathbf{B} \\ \varepsilon \end{bmatrix}, \quad \mathbf{F} = \begin{bmatrix} \rho \mathbf{v} \\ \mathbf{P} \\ \mathbf{v}\mathbf{B} - \mathbf{B}\mathbf{v} \\ \mathbf{E} \end{bmatrix}, \quad \mathbf{S} = \begin{bmatrix} 0 \\ \rho \mathbf{g} \\ 0 \\ \rho \mathbf{g} \cdot \mathbf{v} \end{bmatrix} \quad (2.28)$$

where each row in these matrices in combination with Equation 2.27 represents a different conservation equation. Here \mathbf{P} is a pressure tensor,

$$\mathbf{P} = \rho \mathbf{v}\mathbf{v} + \left(P + \frac{B^2}{8\pi} \right) \mathbf{I} - \frac{\mathbf{B}\mathbf{B}}{4\pi}, \quad (2.29)$$

and \mathbf{E} is the energy vector

$$\mathbf{E} = \mathbf{v} \left(\varepsilon + P + \frac{B^2}{8\pi} \right) - \frac{(\mathbf{v} \cdot \mathbf{B})\mathbf{B}}{4\pi}. \quad (2.30)$$

\mathbf{g} represents gravitational acceleration, ρ is density, \mathbf{v} is the velocity vector, \mathbf{B} is the magnetic field vector, \mathbf{I} is the identity matrix, and ε represents the energy

$$\varepsilon = \frac{\rho v^2}{2} + \frac{P}{\Gamma - 1} + \frac{B^2}{8\pi}. \quad (2.31)$$

where the first term is kinetic energy, the second term is internal enthalpy and the third term is magnetic energy. These equations are discussed below in primitive form (Equations 2.33 to 2.36). See Toro (2013) for a comprehensive discussion on hyperbolic fluid equations, Riemann solvers, and numerical methods for fluid dynamics.

The grids can be chosen to be uniform or irregular. In this work we utilise both. The fineness of the grid structure, otherwise known as the resolution, has a great impact on the simulation. Resolution is usually required to be high in places with large gradients in density and velocity, as well as locations of low plasma β . Plasma β is defined as the ratio of magnetic pressure to thermal pressure and is defined as

$$\beta = \frac{P_{\text{th}}}{P_{\text{mag}}} = \frac{nk_B T}{B^2/8\pi} \quad (2.32)$$

where B is the magnetic field strength, n is the number density, k_B is the Boltzmann constant, and T is temperature. We show an example of the grids we use in the BATS-R-US code in Figure 2.4. Here the star would be at the centre with the wind emanating from the centre outwards. Grids can be changed using adaptive mesh refinement (AMR) which allows the grid resolution to change during simulation time (I use this in simulations in Chapter 6). This is an extremely useful feature for saving computational resources and time. We use both Cartesian and spherical grids in this work. For each simulation in the subsequent chapters we describe each individual grid structure.

The addition of two dimensions and a magnetic field from the 1D polytropic HD model means that we must adopt a different code to solve these equations and produce a 3D grid. For the work presented in this thesis, we use the widely adopted BATS-R-US tool (Powell et al., 1999). This code has been used frequently in the past to study many magnetic astrophysical plasma environments (Powell et al., 1999; Tóth et al., 2005; Manchester IV et al., 2008; Vidotto et al., 2015; Vidotto, 2017; Alvarado-Gómez et al., 2018). Here we use it to solve for 8 parameters: mass density (ρ), wind velocity ($\mathbf{v} = \{v_x, v_y, v_z\}$), magnetic field ($\mathbf{B} = \{B_x, B_y, B_z\}$), and gas pressure P . The code numerically solves the set of closed ideal MHD equations representing the mass continuity, momentum continuity, induction and energy equation. The induction equa-

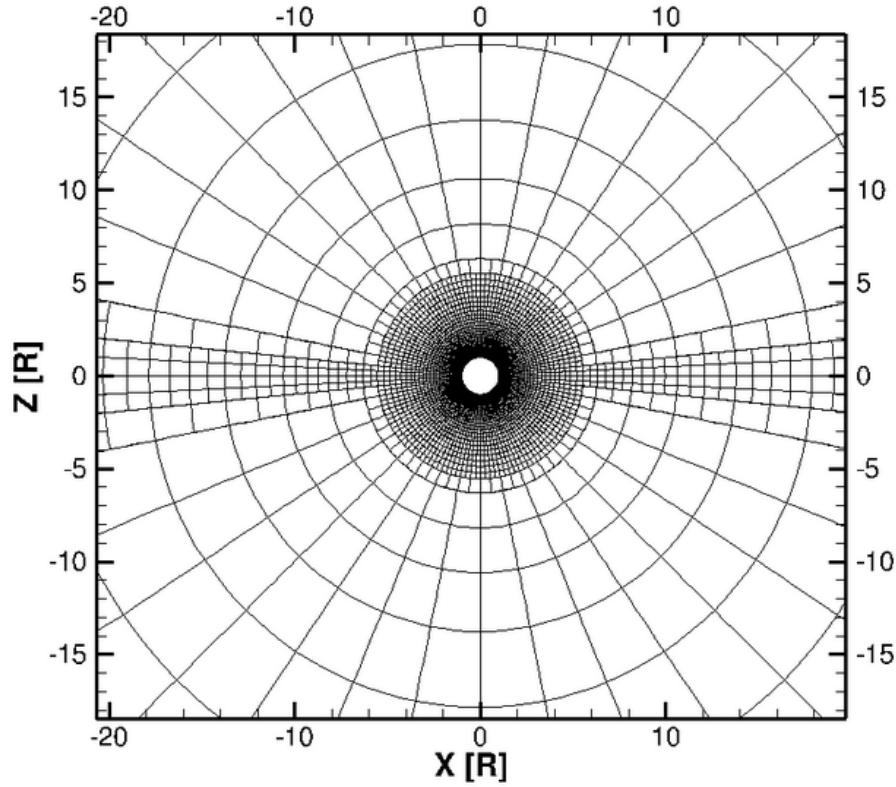


Figure 2.4: Example of spherical grid used in solar wind simulation. The star is positioned at 0,0. The x-z plane of the simulation is shown, with radial stretching and increased resolution near the star, and AMR to resolve the current sheet.

tion defines the relationship between the magnetic field and velocity of the plasma. As we know from Maxwell's equations, moving charged particles will produce a magnetic field. In the ideal MHD case, the induction equation assumes negligible resistivity. The expanded form of Equation 2.28 is

$$\frac{\partial \rho}{\partial t} + \nabla \cdot (\rho \mathbf{v}) = 0, \quad (2.33)$$

$$\frac{\partial (\rho \mathbf{v})}{\partial t} + \nabla \cdot \left[\rho \mathbf{v} \mathbf{v} + \left(P + \frac{B^2}{8\pi} \right) \mathbf{I} - \frac{\mathbf{B} \mathbf{B}}{4\pi} \right] = \rho \mathbf{g}, \quad (2.34)$$

$$\frac{\partial \mathbf{B}}{\partial t} + \nabla \cdot (\mathbf{v} \mathbf{B} - \mathbf{B} \mathbf{v}) = 0 \quad (2.35)$$

$$\frac{\partial \varepsilon}{\partial t} + \nabla \cdot \left[\mathbf{v} \left(\varepsilon + P + \frac{B^2}{8\pi} \right) - \frac{(\mathbf{v} \cdot \mathbf{B}) \mathbf{B}}{4\pi} \right] = \rho \mathbf{g} \cdot \mathbf{v}, \quad (2.36)$$

where the total energy density is given by Equation 2.31. We assume that the plasma behaves as an ideal gas, such that $P = nk_B T$, where $n = \rho/(\mu m_p)$ is the total number density of the wind, ρ represents the mass density and μm_p denotes the average particle mass. We take $\mu = 0.5$, which represents a fully ionised hydrogen wind. We can also relate the pressure to the density, by assuming the wind is polytropic in nature, which follows the relationship: $P \propto \rho^\Gamma$. As discussed previously, this polytropic index implicitly adds heat to the wind as it expands, meaning we do not require an explicit heating equation in our model. We adopt $\Gamma = 1.05$ for all our polytropic simulations, which is similar to effective index found by Van Doorselaere et al. (2011) for the solar corona, and to values used in the literature for simulating winds (Vidotto et al., 2015; Pantolmos & Matt, 2017; Ó Fionnagáin & Vidotto, 2018). The polytropic index most likely changes throughout the wind with distance from the solar surface—i.e. the energy deposition in the wind changes with r . However, as in the 1D polytropic model, we neglect this in our simulations as an overall effective polytropic index achieves a similar result.

Output parameters of our simulation include the velocity, density, and pressure of the plasma. We also retrieve the magnetic fields and electrical currents in the wind. From these parameters, we can derive many other important quantities which are influential in stellar evolution. An important quantity that we use frequently is the mass-loss rate. This was introduced and defined above in Equation 2.10. This can be calculated numerically from our simulations by integrating the mass flux ($\rho \mathbf{v}$) over surfaces within the simulation,

$$\dot{M} = \oint_S \rho \mathbf{v} \cdot d\mathbf{S}, \quad (2.37)$$

where S denotes the surface over which we are integrating (usually concentric spherical shells). As mass loss is such an important evolutionary parameter for stars and their winds, we utilise this formula frequently. This mass also carries away angular momentum (\dot{J}), which we can quantify from our simulations using the following equation

$$\dot{J} = \oint_S \left[-\frac{\varpi B_\phi B_r}{4\pi} + \varpi v_\phi \rho v_r \right] dS \quad (2.38)$$

where $\varpi = (x^2 + y^2)^{1/2}$ is the cylindrical radius, B and v are the magnetic field and velocity components of the wind, and r and ϕ denote the radial and azimuthal components respectively (Mestel, 1999; Vidotto et al., 2014a). The first term in Equation 2.38 represents the angular momentum-loss through magnetic stresses in the wind, and the second term represents the angular momentum carried away by the particles in the wind. Usually the magnetic stresses dominate in removing angular momentum from the star, as shown by Weber & Davis Jr. (1967).

Similar to Parker winds, these 3D MHD winds have important critical points. There are 3 in magnetic winds, known as the fast, slow, and Alfvén points. The Alfvén point is the most important of these critical points for our research. In 3D this becomes the Alfvén surface. It is the distance at which any Alfvén waves that propagates through the wind do so at the same velocity as the wind itself ($V_A = v_r$). Alfvén waves, first theorised by H. Alfvén (Alfvén, 1942), are types of MHD waves. They form in plasmas due to perturbations where the magnetic field acts as a restoring force on the particles, which have inertia, causing a wave oscillation. The Alfvén velocity is given by

$$V_A = \frac{B^2}{\sqrt{4\pi\rho}} \quad (2.39)$$

This means that super-Alfvénic winds ($v_r > V_A$) cannot transfer magnetic information downwind to the sub-Alfvén region ($v_r < V_A$). Of course this surface can be complex, as the wind velocity can vary substantially in all directions in 3D. Therefore, since magnetic information cannot propagate downwind above this point, the Alfvén surface is the maximum distance up to which the stellar winds can exert magnetic stresses that remove angular momentum from the star. This is frequently thought of as the torque "lever-arm" of the stellar wind. See Figure 5.2 for examples of simulated Alfvén surfaces, shown in orange. In these simulations we do not explicitly include energy deposited in the wind from Alfvén waves to drive the winds, for that we must use a slightly more complex model, discussed in Section 2.4.

2.4 3-DIMENSIONAL MAGNETOHYDRODYNAMICAL WAVE MODEL

For cooler stars, where the temperature at the base of the wind does not provide enough pressure to accelerate a wind, other methods must be considered. The implementation of wave-driven winds allows us to circumvent this issue by dissipating magnetic energy into the wind, causing heating and expansion. I use these wave-driven simulations in Chapter 6 to find solutions to the wind of λ Andromedae, a more evolved solar-like star.

In the previous section which describes the 3D polytropic MHD model, the driving force for the wind is the pressure forces defined through energy deposited from the polytropic index. An effective energy dissipated into the wind, described by the Γ value, which is converted into additional pressure which drives the wind. This can be replaced by some explicit source of energy, which here we assume to be Alfvén waves. Note that we do not solve the wave equations but rather the energy density of the waves as they travel and are dissipated and reflected throughout the wind plasma. These waves provide a source of energy to drive the wind as they are dissipated. Additionally, we also solve for two temperatures in the wind, the electron and ion temperature. The equations that differ from the 3D polytropic MHD model described in Section 2.3 are the momentum equation, which includes separated electron (P_e) and ion pressures (P_i), and the additional pressure from the Alfvén waves, given by P_A

$$\frac{\partial(\rho\mathbf{v})}{\partial t} + \nabla \cdot \left[\rho\mathbf{v}\mathbf{v} + \left(P_i + P_e + P_A + \frac{B^2}{8\pi} \right) I - \frac{\mathbf{B}\mathbf{B}}{4\pi} \right] = \rho\mathbf{g}. \quad (2.40)$$

and the energy equations for ions and electrons which become

$$\begin{aligned} \frac{\partial \varepsilon_i}{\partial t} + \nabla \cdot \left[\mathbf{v} \left(\varepsilon_i + P_i + \frac{B^2}{8\pi} \right) - \frac{(\mathbf{v} \cdot \mathbf{B})\mathbf{B}}{4\pi} \right] \\ = -(\mathbf{v} \cdot \nabla)(P_e + P_A) + \frac{n_i k_B}{\tau_{ei}} (T_e - T_i) + Q_i + \rho \mathbf{g} \cdot \mathbf{v} \end{aligned} \quad (2.41)$$

$$\frac{\partial}{\partial t} \left(\frac{P_e}{\gamma - 1} \right) + \nabla \cdot \left(\frac{P_e}{\gamma - 1} \mathbf{v} \right) + P_e \nabla \cdot \mathbf{v} = -\nabla \cdot \mathbf{q}_e + \frac{n_i k_B}{\tau_{ei}} (T_i - T_e) - Q_{\text{rad}} + Q_e \quad (2.42)$$

where ε_i represents the energy for the ions, according to Equation 2.31. $T_{e,i}$ and $n_{e,i}$ denote electron and ion temperatures and number densities respectively. We employ the equation of state $P_{e,i} = n_{e,i} k_B T_{e,i}$ and the polytropic index is $\Gamma = \gamma = 5/3$ (an adiabatic plasma which gains no additional energy from the polytropic index). \mathbf{q}_e represents the electron heat transport which transitions smoothly from collisional (Spitzer & Härm, 1953) to collisionless (Hollweg, 1978) heat flux so that the Spitzer-Härm collisional form dominates near the star, and the Hollweg collisionless form dominates further out in the wind. Q_e and Q_i are the heating functions for electrons and ions respectively and are partitioned forms of turbulent dissipation by Alfvén waves (Chandran et al., 2011). Q_{rad} is the radiative cooling function and is defined as

$$Q_{\text{rad}} = \Lambda n_e n_i, \quad (2.43)$$

where Λ is the radiative cooling rate from CHIANTI v9.0 (Dere et al., 2019). To determine the Alfvén wave pressure, P_A , the wave energy density equations must be solved. This wave pressure is defined as

$$P_A = \frac{\omega_+ + \omega_-}{2} \quad (2.44)$$

The Alfvén wave dissipation, reflection and propagation are governed by the wave energy density (w_{\pm}) equations

$$\frac{\partial w_{\pm}}{\partial t} + \nabla \cdot [(\mathbf{v} \pm \mathbf{V}_A) w_{\pm}] + \frac{w_{\pm}}{2} (\nabla \cdot \mathbf{v}) = \mp \Re \sqrt{w_- w_+} - \xi_{\pm} w_{\pm} \quad (2.45)$$

where w_{\pm} represents the wave energy densities for waves parallel (+) and anti-parallel (-) to the magnetic field. \Re is the wave reflection rate and ξ is the wave dissipation rate. The dissipation rate is

$$\xi_{\pm} = \frac{2}{L_{\perp}} \sqrt{\frac{w_{\mp}}{\rho}} \quad (2.46)$$

where L_{\perp} is the transverse correlation length of the Alfvén waves perpendicular to \mathbf{B} . As in [Hollweg \(1986\)](#), $L_{\perp} \propto \sqrt{B}$, with the proportionality constant (ℓ) set as an adjustable parameter of the model. The reflection rate \Re depends on the ratio of energy densities of parallel and anti-parallel waves, and the Alfvén velocity

$$\Re = \min [R_{\text{imb}}, \max (\xi_{\pm})] \quad (2.47)$$

where R_{imb} is the reflection coefficient when the ratio of energy densities for each direction wave are strongly imbalanced.

$$R_{\text{imb}} = \sqrt{[(\mathbf{V}_A \cdot \nabla) \log V_A]^2 + (\mathbf{b} \cdot [\nabla \times \mathbf{v}])^2} \quad (2.48)$$

where $\mathbf{b} = \mathbf{B}/B$ is the magnetic field unit vector. V_A is the Alfvén velocity, defined in [Equation 2.39](#). [Equation 2.47](#) also has an analytical correction factor not described here, accounting for strong differences in each wave energy density, or when they are very similar. A thorough description of this entire model can be found in [van der Holst et al. \(2014\)](#).

RADIO PROCESSES FROM IONISED PLASMA

In this work, we frequently discuss the thermal radio emission from ionised plasmas. An ionised plasma in thermal equilibrium will readily emit radio waves, which, if strong enough, we could detect here on Earth. There have been many detections of such radio emission from the winds of early-type stars, late-type stars, and massive stars ([Wright et al., 1975](#); [Panagia & Felli, 1975](#); [Abbott et al., 1986](#); [Scuderi et al., 1998](#); [Puls et al., 2008](#)). In these scenarios, the plasma is quite dense which boosts signal strength and allows detections. As we will show in this chapter, the radio emission is strongly dependent on wind density. In the case of low-mass stars, particularly those along the main sequence, the rarefied nature of their winds means their winds are undetectable in the radio regime with current radio telescopes. In this chapter we explain the physical mechanisms through which radio emission occurs in these plasmas. We investigate both analytical and numerical methods for estimating the radio flux density from stel-

lar winds, and its relationship to stellar mass-loss rates. In Chapter 5 I investigate our results in the context of current radio telescopes, and the detectability of these stellar winds.

3.1 MECHANICAL AND RADIATIVE PROCESSES IN THERMAL PLASMAS

If we consider a material of equal positive and negative charges (protons and electrons), we find that macroscopically, the material is neutral. If we displace the electrons by a distance δx , the material is out of equilibrium. This charge separation causes an electric field (E) to form, accelerating electrons in the opposite direction, the particles then oscillate around the original starting position. Note here we treat the protons as stationary due to the large mass difference between electrons and protons, giving protons a much larger inertia than electrons. Using Newton's law we find that

$$m_e a = m_e \frac{d^2 \delta x}{dt^2} = q_e E.$$

We can also define the electric field through electromagnetism

$$E = 4\pi\sigma = -4\pi n_e q_e \delta x,$$

where σ is the charge per unit area and ϵ_0 is the vacuum permittivity. From this point, we can define a plasma frequency ω_p ,

$$\frac{d^2 \delta x}{dt^2} = -\frac{4\pi n_e q_e^2 \delta x}{m_e} = -\omega_p^2 \delta x,$$

where

$$\omega_p = \sqrt{\frac{4\pi n_e q_e^2}{m_e}}.$$

Since many parameters in this equation are constants, the plasma frequency is usually written as

$$f_p = \omega_p/2\pi = 9000\sqrt{n_e} \text{ Hz}, \quad (3.1)$$

where n_e is the electron number density in cm^{-3} . For a material to be considered a plasma, the frequency of collisions must be less than the plasma frequency. In other words, the collision timescale must be much larger than the plasma period

$$\tau_c/\tau_p \gg 1,$$

otherwise the material will behave as a neutral gas. This criteria allows the plasma to oscillate freely before collisions of particles changes the directions of particles. Note that in plasmas, the thermal motions of particles is enough to drive this oscillation. Therefore we expect a plasma in thermal equilibrium to oscillate at the plasma frequency. This has implications for radio waves passing through the plasma at similar frequencies, as they resonate with the plasma and get reflected or absorbed. Another way to measure collisions is through the maximum travel distance of particles. This is known as the Debye length and is described as

$$\lambda_D = \sqrt{\frac{k_B T_e}{4\pi q_e^2 n_e}} \quad (3.2)$$

The material is considered a plasma only if the length scale (L) of the material is greater than the Debye length

$$L \gg \lambda_D.$$

Around the Earth, for example, the solar wind would exhibit a plasma frequency of about $\omega_p \simeq 2 \times 10^5 \text{ s}^{-1}$, and a Debye length of $\lambda_D \simeq 10 \text{ m}$.

In a plasma, free electrons are continually colliding with the ions (in this case, almost entirely protons), producing the phenomenon known as bremsstrahlung. Bremsstrahlung is German for *braking radiation*. It is a process driven by electromagnetic forces, through Coulomb collisions (although there are some quantum effects that are dealt with usu-

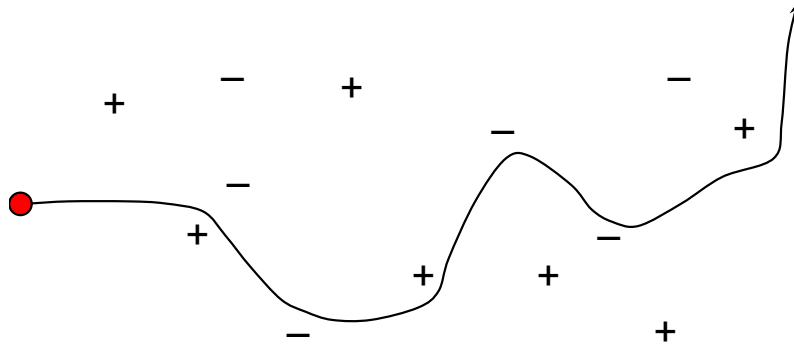


Figure 3.1: The path of an electron through a charged plasma. Path changes (exaggerated here of course) are caused by elastic Coulomb collisions, producing photons.

ally through the usage of a Gaunt factor, after the classical treatment). As a charged particle—i.e. an electron—passes through a charged plasma, it will experience elastic collisions with other charged particles (Figure 3.1). This change in direction and velocity causes an acceleration, which produces photons. This mechanism is also known as free-free emission.

An in depth examination of the physical mechanisms here is given in [Rybicki & Lightman \(1979\)](#). We will briefly discuss the theoretical formalisms for the emission and absorption of thermal bremsstrahlung, as they pertain to the subject matter of this work. We begin with the single-speed thermal emission formula from [Rybicki & Lightman \(1979\)](#) (Eq. 5.11 within), which describes the emission of radiation from a single electron during a Coulomb collision with a single proton.

$$\frac{dW}{d\omega dV dt} = \frac{16\pi q_e^6}{3\sqrt{3}c^3 m_e^2 v} n_e n_i Z^2 g_{\text{ff}} \quad (3.3)$$

where the left hand side represents the total energy emission per unit time per unit volume per unit frequency. Z is the ion charge, and g_{ff} is the Gaunt factor for free-free emission. This is what accounts for quantum effects additional to the classical treatment. As usual, it is more useful to treat plasmas as ensembles of particles instead of single particles, therefore we can average the above equation over a distribution of particles speeds. The probability that an electron has a velocity in the range $v + dv$ is

$$dP \propto e^{-E/k_B T_e} d^3 \mathbf{v} = \exp\left(-\frac{m_e v^2}{2k_B T_e}\right) d^3 \mathbf{v} = v^2 \exp\left(-\frac{m_e v^2}{2k_B T_e}\right) dv, \quad (3.4)$$

where the integral coordinate $d^3v = 4\pi v^2 dv$ for an isotropic distribution of velocities. We now integrate Equation 3.3 over this probability function.

$$\frac{dW(T_e, \omega)}{dV dt d\omega} = \frac{\int_{v_{\min}}^{\infty} \text{Equation 3.3} \times \text{Equation 3.4}}{\int_0^{\infty} \text{Equation 3.4}} \quad (3.5)$$

Carrying out this integration, we find

$$\frac{dW}{dV dt dv} = \frac{2^5 \pi q_e^6}{3m_e c^3} \left(\frac{2\pi}{3k_B m_e} \right)^{1/2} T_e^{-1/2} Z^2 n_e n_i e^{-hv/k_B T_e} g_{ff} \quad (3.6)$$

(note the transformation of $d\omega = 2\pi dv$ and the quantum effect of $v_{\min} = \sqrt{2hv/m_e}$, i.e. the kinetic energy must be large enough to form at least one photon of energy $h\nu$) where T_e is the electron temperature. Including all constants in c.g.s. units ($\text{erg s}^{-1} \text{cm}^{-3} \text{Hz}^{-1}$), we find the emissivity

$$\varepsilon_\nu \equiv \frac{dW}{dV dt dv} = 6.8 \times 10^{-38} Z^2 n_e n_i T_e^{-1/2} e^{-hv/k_B T_e} g_{ff} \quad (3.7)$$

In the case of moving charges, we can relate the thermal emission to the absorption by

$$j_\nu = \alpha_\nu B_\nu, \quad (3.8)$$

where B_ν is the Planck blackbody function, α_ν is the free-free absorption coefficient, and j_ν (known as the spontaneous emission coefficient) is related to the previous emission defined in Equation 3.7 as

$$j_\nu = \varepsilon_\nu / 4\pi \quad (3.9)$$

With the Planck function defined as

$$B_\nu = \frac{2h\nu^3}{c^2 [\exp(h\nu/kT) - 1]} \text{ erg s}^{-1} \text{ cm}^{-2} \text{ Hz}^{-1} \text{ ster}^{-1}, \quad (3.10)$$

we can rearrange the equations to find the absorption coefficient,

$$\alpha_\nu = 3.692 \times 10^8 [1 - \exp(-hv/k_B T_e)] Z^2 g_{ff} T_e^{-1/2} \nu^{-3} n_e n_i. \quad (3.11)$$

We can analytically describe the gaunt factor function here, as we are only going to examine radio regime (Cox & Pilachowski, 2002). In this regime the following function holds

$$g_{\text{ff}} = 10.6 + 1.90 \log_{10} T_e - 1.26 \log_{10} Z\nu \quad (3.12)$$

In the case of our radio studies, we only deal with those relating to thermal emissions. The equations laid out above detail the necessary theoretical functions with which we can describe the emitted radio waves in the context of stellar wind plasmas.

3.2 ANALYTICAL RADIO EMISSION

We have discussed the physical processes through which stellar winds can produce thermal radio waves. In this section we will describe how we analytically calculate their emitted radio flux densities. The equations here can be found in full in Panagia & Felli (1975); Wright et al. (1975); Rybicki & Lightman (1979). We can show that the density profile in a plasma will affect the spectrum produced in the radio regime. This occurs due to the optically thin/thick nature of the plasma. It is well known for example that a plasma that has uniform isotropic density will produce a flux density $S_\nu \propto \nu^2$ in the thick regime and $S_\nu \propto \nu^{-0.1}$ in the thin regime. However, this will change for plasmas that have differing density profiles, such as a stellar wind, which is $\propto r^{-2}$ at large distances from the stellar surface.

To begin, we will use the formal solution to the radiative transfer equation

$$I_\nu(\tau_\nu) = I_{\nu,0}e^{-\tau_\nu} + \int_0^{\tau_\nu} S_\nu(\tau'_\nu) e^{-(\tau_\nu - \tau'_\nu)} d\tau'_\nu \quad (3.13)$$

where I_ν and $I_{\nu,0}$ is the radiation intensity emitted towards the observer and any original starting intensity (i.e. from behind a source) respectively. τ_ν is the optical depth, where

$$d\tau_\nu = \alpha_\nu ds, \quad (3.14)$$

and s is the spatial coordinate. S_ν in this equation is the source function, defined as $S_\nu \equiv j_\nu/\alpha_\nu$. We assume that the source function is constant with optical depth to find

$$I_\nu(\tau_\nu) = I_{\nu,0}e^{-\tau_\nu} + S_\nu(1 - e^{-\tau_\nu}) \quad (3.15)$$

By Kirchoff's law of thermal radiation¹, we know that the source function is the same as the Planck function as the body behaves as a blackbody. Therefore,

$$I_\nu = I_{\nu,0} = B_\nu, \quad (3.16)$$

$$B_\nu = B_\nu e^{-\tau_\nu} + S_\nu(1 - e^{-\tau_\nu}) \quad (\text{from Equation 3.15}) \quad (3.17)$$

or

$$B_\nu(1 - e^{-\tau_\nu}) = S_\nu(1 - e^{-\tau_\nu}) \quad (3.18)$$

$$\therefore S_\nu = B_\nu \quad \text{and} \quad j_\nu = \alpha_\nu B_\nu \quad (3.19)$$

Assuming a stellar wind is in local thermodynamic equilibrium, and therefore $B_\nu = S_\nu$, we can write the emission from the wind of a star as (Wright et al., 1975)

$$I_\nu = \int_0^{\tau_{\max}} B_\nu e^{-\tau} d\tau \quad (3.20)$$

$$= B_\nu(1 - e^{-\tau}). \quad (3.21)$$

assuming the plasma is isothermal (otherwise B_ν would vary with optical depth), this is depicted in Figure 3.2. As there is no initial intensity source at $s=0$. We need a definition for τ , which we can describe as

$$\tau = \int_{-\infty}^{\infty} \alpha_\nu ds \quad (3.22)$$

¹ Kirchoff's law states that for a body absorbing and emitting radiation at thermodynamic equilibrium, the ratio of its emissive power to its absorption coefficient behaves as a universal function (the Planck function, Equation 3.10) for a perfectly emitting blackbody.

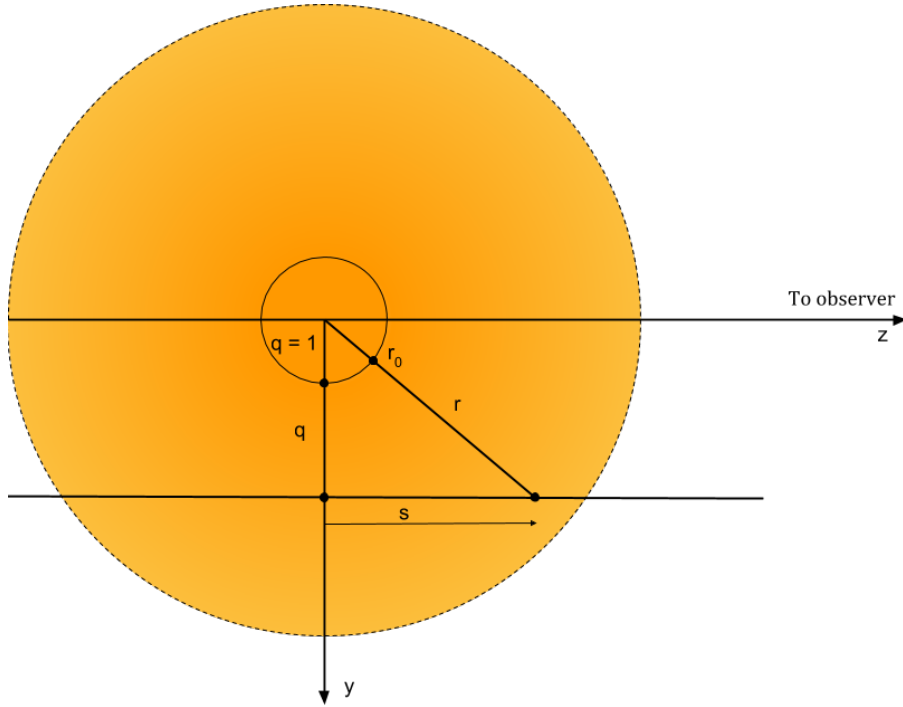


Figure 3.2: Schematic for analytical thermal bremsstrahlung coordinates

We separate out the density dependence on the absorption coefficient and call what is remaining κ_ν ($\alpha_\nu = \kappa_\nu n^2$)

$$\tau = 2\kappa_\nu \int_0^\infty n^2 ds \quad (3.23)$$

which can be rewritten as

$$\tau = 2\kappa_\nu \int_0^\infty \frac{n_0^2}{(s^2 + q^2)^2} ds \quad (3.24)$$

assuming that n_0 is the density at the lower boundary, and falls off with r^{-2} . Here s and q are normalised to r_0 . The variables s and q are described in Figure 3.2. In the case that $q > 1$, this integral becomes

$$\tau = 2\kappa_\nu n_0^2 \left[\frac{\pi}{4q^3} \right] \quad (3.25)$$

The total flux density can be defined by the integral of the specific intensity,

$$E_\nu = \oint I_\nu d\Omega \quad (3.26)$$

multiplied by 4π to account for isotropic emission, and converting the solid angle we find

$$E_\nu = 4\pi \int_0^\infty I_\nu \int_0^{2\pi} d\phi \int_0^{\pi/2} \sin(\theta) d\theta, \quad (3.27)$$

$$E_\nu = 4\pi \int_0^\infty I_\nu 2\pi r_0^2 q dq, \quad (3.28)$$

$$E_\nu = 4\pi \int_0^\infty B_\nu (1 - e^{-\tau_\nu}) 2\pi r_0^2 q dq \quad (3.29)$$

We can describe two parts to our solution

$$E_\nu = 4\pi^2 r_0^2 B_\nu \left[2 \int_0^{q_{\text{crit}}} q dq + 2 \int_{q_{\text{crit}}}^\infty (1 - e^{-\tau}) q dq \right] \quad (3.30)$$

The first term inside the brackets is easy to solve, and the second term can be approximated with a Taylor expansion

$$E_\nu = 4\pi^2 r_0^2 B_\nu q_{\text{crit}}^2 \left[1 + 2 \sum_{m=1}^\infty \frac{(-1)^{m+1}}{m!} \frac{\tau_{\text{crit}}}{(3m-2)} \right] \quad (3.31)$$

The first term of this equation relates to the opaque emission, and the second term relates to the optically thin extended envelope. The solution to this equation is not easily solved analytically, and one must make assumptions on the critical opacity to partially solve it (although nowadays, with increased computational power, this can be solved numerically). [Panagia & Felli \(1975\)](#) assume there is some critical value of q such that $q_{\text{crit}} \geq 1$ and $\tau_{\text{crit}} \geq 1$, and so

$$\tau_{\text{crit}} = \frac{\pi}{2q_{\text{crit}}^3} n_0^2 \kappa_\nu r_0 \quad (3.32)$$

$$q_{\text{crit}} = \left[\frac{\pi}{2\tau_{\text{crit}}} n_0^2 \kappa_\nu r_0 \right]^{2/3} \quad (3.33)$$

Given a large enough value of τ_{crit} ([Panagia & Felli 1975](#) assume $\tau_{\text{crit}} = 3$), the assumption can be made that the exponential term in Equation 3.29 can be neglected. Note the larger the critical optical depth, the more accurate the assumption. This leaves

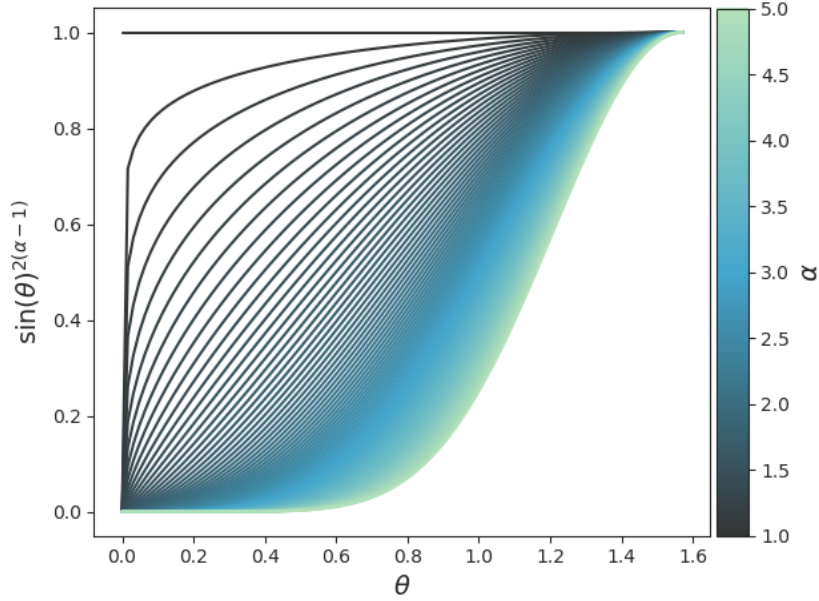


Figure 3.3: Trend of I_β for different α .

us with the radio flux density for that with a density envelope that decays $\propto r^{-2}$. However, we are more interested in the cases where the wind density has different decay rates. The wind density decay index, β , is defined as

$$n = n_0 \left[\frac{R_\star}{r} \right]^{-\beta}. \quad (3.34)$$

In this case the integral is not as easily solved and we must describe the optical depth in terms of the impact factor q

$$\tau = 2\kappa_\nu n_0^2 r_0 q^{-2(\beta-1)} I_\beta \quad (3.35)$$

[Panagia & Felli \(1975\)](#) generalise this for plasmas with differing decay rates with distance, which results in a radio flux density of

$$E_\nu = 10^{-29} A_\beta R_\star^2 \left[5.624 \times 10^{-28} I_\beta n_0^2 R_\star^2 \right]^{\frac{2}{2\beta-1}} \times \left[\frac{\nu}{10 \text{GHz}} \right]^\eta \times \left[\frac{T_0}{10^4 \text{K}} \right]^\lambda \times \left[\frac{d}{1 \text{kpc}} \right]^{-2} \text{ mJy}, \quad (3.36)$$

where the functions I_β and A_β are (trend of I_β shown in [Figure 3.3](#))

$$I_\beta = \int_0^{\pi/2} (\sin \theta)^{2(\beta-1)} d\theta, \quad (3.37)$$

$$A_\beta = 1 + 2 \sum_{j=1}^{\infty} (-1)^{j+1} \frac{\tau_c^j}{j! j(2\beta - 1) - 2}. \quad (3.38)$$

The indices η and λ in Equation 3.36 can be related to the density decay index β , and are defined as

$$\eta = \frac{-4.2}{2\beta - 1} + 2, \quad \lambda = \frac{-2.7}{2\beta - 1} + 1, \quad (3.39)$$

where $\tau_{\text{crit}} = 3$ and θ represents colatitude in radians. We can see from this result that the steeper the decay in the density in a stellar wind, the steeper the increase in the frequency spectrum of the optically thin regime of the stellar wind thermal free-free emission. This allows us to calculate radio flux density from our 1 dimensional wind simulations using the best fit α parameter, along with the base wind density. Results from our wind simulations using this derived method are presented in Chapter 4.

3.3 NUMERICAL RADIO EMISSION

While the analytical solutions outlined above give a good estimate of the radio flux density that one could expect from a stellar wind, they also have some limitations. We usually model the wind density decay within the first few R_\star . As we learned from previous sections, the stellar wind density should reach a state of $\rho \propto r^{-2}$ as it reaches terminal wind velocity, therefore there are usually at least two regimes in the density structure, which cannot be modelled sufficiently with the analytical solution. Additionally, the analytical solution is sufficient for the 1D wind models, as in those cases we are simply creating a 3D wind by assuming the wind along that one dimension is isotropic. When simulating 3D winds, this is not the case.

To address this issue, we take the formal radiative transfer equation (Equation 3.13), and write a Python script to solve this iteratively for our 3D volumes of stellar winds.

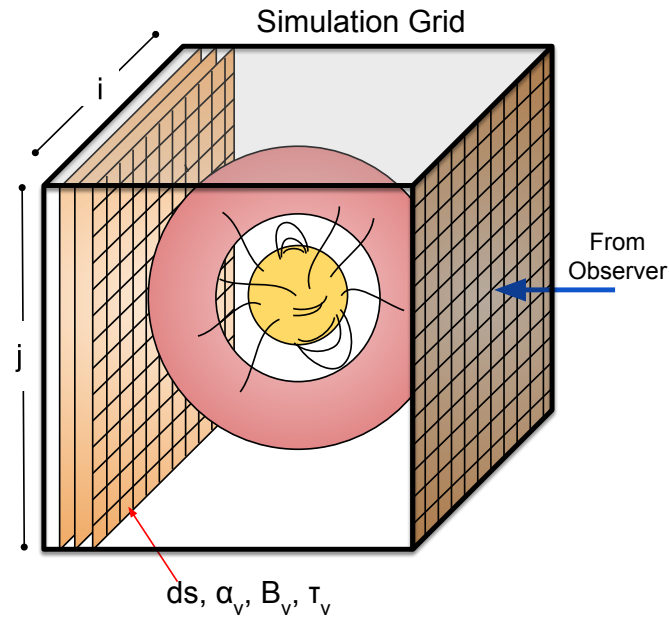


Figure 3.4: A schematic of a 3D wind and the method for calculating the radio flux density.

We outline the process through the schematic in Figure 3.4. The process through which the code works is as follows:

- The 3D wind solution from our BATS-R-US model (see Chapter 2) is linearly interpolated. The required values are the wind density and temperature at each location in space. This is done to reduce the amount of memory needed by Python, and to introduce a constant step size, which is faster for calculation.
- Any necessary rotation is included in the grid (usually stellar inclination)
- Density is artificially removed from inside and behind the star so it does not contribute to the radio flux
- Equation 3.13 is solved along the line of sight, which is represented by a row of cells in Figure 3.4. This is done with the `scipy` package, solving for absorption coefficient, blackbody flux, and optical depth.
- This results in the 2D image of specific intensity on the plane of the sky. Examples of this can be found in Figure 5.4.

- This specific intensity is then integrated to find the radio flux density (S_ν). From the intensity we can calculate the flux density (E_ν)¹ of the wind as,

$$E_\nu = \int I_\nu d\Omega = \frac{1}{d^2} \int I_\nu dA = \frac{1}{d^2} \sum^{i,j} I_\nu \Delta i \Delta j \quad (3.40)$$

where A is the area of integration, d is the distance to the object, and i and j denote the coordinates in our 2D image of I_ν values. Δi and Δj represent the spacing in our grid in the i and j directions. In this calculation we have assumed that the angle subtended by the stellar wind is small, therefore $d\Omega = dA/d^2$.

- Additionally, this code allowed us to solve for many observational frequencies, producing radio spectra for each wind source. This was essential for comparing to current radio telescopes, which possess a range of observations frequencies and sensitivities.

This process allows an insight into the distance of emission from the stellar surface (the radio photosphere, R_ν , discussed in Chapter 5), an important component when trying to disentangle observed radio flux from emission lower down in the stellar atmosphere. This method allows investigation of the distribution of radio flux and density structure in the wind. We see our radio emission is no longer isotropic. We were able to investigate the variability in stellar wind radio emission as the star rotated (given a fixed wind solution).

This code is openly available online at <https://github.com/ofionnad/radiowinds> (Ó Fionnagáin, 2018), with instructions on how to use it.

¹ Note in later chapters and publications, this is denoted as S_ν , but we leave as E_ν to avoid confusion with the source function.

II

THE SOLAR WIND IN TIME

This part outlines the research we conducted into the evolution of the solar wind by studying solar proxies. We focus on how the global parameters of the wind can affect the star itself. Initially, we present the evolution of solar proxies by studying their winds using a 1D polytropic model. From this we can derive global wind parameters that effect the evolution of these stars. We advance this work and simulate a smaller sample of stars in 3D, using an ideal magnetohydrodynamic formulation. This allows us to incorporate magnetic field constraints from ZDI observations, giving a better holistic view of the stellar winds. We can directly calculate the angular momentum-loss rate from these simulations. Finally, we focus in particular on the case of a post-MS solar-mass star, λ Andromedae, for which we conduct two cases of 3D MHD models, to find the best solution to its stellar wind. This provides an initial view at the post-MS life of a solar-mass stellar wind.

MAIN SEQUENCE SOLAR WIND EVOLUTION

4.1 INTRODUCTION

As discussed in Chapter 1, solar analogue stars lose angular momentum and mass through stellar winds. These magnetised winds determine how the rotation of a star will decay with time (Weber & Davis Jr., 1967; Vidotto et al., 2011), although the exact processes behind this occurrence is not fully understood. In this work, we assume the winds of these solar-type stars to be homologous to the solar wind at different ages. As these stars age, it is expected that various stellar properties also evolve over time, such as rotation and magnetic activity. (Skumanich, 1972; Dorren & Guinan, 1994; Ribas et al., 2005; Guinan & Engle, 2009; Vidotto et al., 2014b). Since the magnetic activity of a star is

one of the pre-eminent factors determining how active the stellar wind is (Wood et al., 2002), it suggests that the stellar wind will also trend in a similar fashion.

In recent years, there has been some work in observation-based research suggesting a break in solar analogue activity as stars cross a certain rotation or age threshold. Van Saders et al. (2016) modelled a set of 21 older stars that have been observed by Kepler and reported the abnormally rapid rotation in older main sequence (MS) stars, which does not agree with previous period-age relations. They suggested that magnetic braking seems to weaken significantly in evolved MS stars at Rossby number¹ $Ro \approx 2$, which they assumed corresponds to when the stars reach an age of $\approx 2-4$ Gyr. Since the rate of angular momentum loss is related to the mass-loss rate (Weber & Davis Jr., 1967; Vidotto et al., 2014b), this break in angular momentum loss is likely to be associated with a decline in mass-loss rate (\dot{M}). There has been additional evidence of some change in the stellar activity for solar-mass stars; Booth et al. (2017) showed that X-ray luminosity declines more rapidly for stars older than ≈ 1 Gyr. They suggest that this change in the relationship could be due to the increased stellar spin-down rate. This explanation disagrees with Van Saders et al. (2016) however. In this chapter, we present a way to explain both the observations of Van Saders et al. (2016) and Booth et al. (2017); our suggestion is that the observed decrease in X-ray luminosity is linked to a weaker stellar wind, which removes less angular momentum and thus, allows for higher rotation rates in older stars, as seen in Kepler observations (Chapter 1).

Additionally, other works have supported the idea of a sudden change in stellar activity around the same stellar age or Rossby number. Metcalfe et al. (2016) has shown that chromospheric activity from calcium lines display a break in activity levels, which they attribute to a possible change in the stellar dynamo around the solar age of 4.6 Gyr. Kitchatinov & Nepomnyashchikh (2017) demonstrated that if they turn off the global stellar dynamo after a critical lower rotational period, a similar decline in stellar spin down and magnetism can be achieved for older stars. Finally, Beck et al. (2017) found a sudden change in lithium abundances in solar analogues which drift beneath a surface

¹ Ro represents Rossby number, which is the ratio between stellar rotation and convective turnover time.
 $Ro = P_{\text{rot}}/\tau_{\text{conv}}$

rotation velocity of $\approx 2 - 3 \text{ kms}^{-1}$. All of this mentioned research indicates some significant transition between regimes in low-mass stars older than 1 Gyr. While the nature of this transition is not understood, it warrants further investigation.

Results from this chapter were published in "The solar wind in time: a change in the behaviour of older winds?", MNRAS, 476.2 (2018)

4.1.1 *Calibrating our simulations to the solar case*

In this section, we present a 1-dimensional, thermally-driven hydrodynamic wind model that is used to compute the steady state solutions of the winds of stars from the ‘Sun in Time’ sample (Table 4.1). We do not explicitly include magnetism in the wind equations, but we note that its presence is implicitly assumed as the cause of the $\approx 10^6 \text{ K}$ temperatures of the winds. Polytropic winds follow the momentum equation as described in Chapter 2. The first term in Equation 2.12 represents the acceleration of the wind, which is produced by the pressure gradient and gravity (second and third terms respectively). Since the wind in this case is polytropic, the temperature and pressure change with density as in Equation 2.22. Methods of defining base temperature and density are discussed in Section 4.3. Our 1D wind model assumes a spherically symmetric, steady wind, that behaves similarly to the Parker wind solution (Parker, 1958), except the energy deposition in the wind is altered to be less than that of an isothermal wind. This change in energy deposition slows the expansion of the wind as Γ is increased, giving rise to slower, denser winds. The theory behind these types of wind are discussed in detail in Chapter 2.

To benchmark our simulations of the ‘solar wind in time’, we constrain the parameters of our model so as to best reproduce the solar wind properties. The Sun is the only star for which we have direct wind measurements. In the solar wind, Van Doorselaere et al. (2011) derived an effective polytropic index of $\Gamma = 1.1$. Numerical models of solar-type stars usually adopt a range of 1.05 to 1.15 for Γ (Keppens & Goedbloed, 1999a; Matt et al., 2012; Johnstone et al., 2015a,b; Vidotto et al., 2015). In our model,

we adopt a value of 1.05. To further reproduce observations of the solar wind, we adopt a base wind density of $n_{\odot} = 2.2 \times 10^8 \text{ cm}^{-3}$, which is consistent with observations of coronal hole densities (Warren & Brooks, 2009). We use a wind base temperature of $T_{\odot} = 1.5 \text{ MK}$, which in conjunction with our $\Gamma = 1.05$, reproduces the solar wind velocities observed at the Earth, $v_{\oplus} = 443 \text{ kms}^{-1}$, which is consistent with observations (McComas et al. 2008; Usmanov et al. 2014). Our assumption predicts a number density of 10.5 cm^{-3} at the Earth’s orbit, which is also consistent with observations (Murdin, 2000; Bagenal, 2013; Usmanov et al., 2014). At the martian orbital distance, we find a wind density and velocity of 12 cm^{-3} and 450 km/s . These model values agree with observations made by the MAVEN spacecraft (Lee et al., 2017). The effects of the wind on planets such as Earth, Mars, and exoplanets are discussed in more detail in Part III. Finally, our model predicts a solar wind mass-loss rate of $3.5 \times 10^{-14} M_{\odot} \text{ yr}^{-1}$, which reproduces the observed values presented in Wang (1998).

4.2 SOLAR WIND IN TIME SAMPLE

The ‘Sun in Time’ project is used as the basis for selecting our sample for our study. The project was created to explore the life-long activity evolution of our own Sun, from when it reached the main sequence, by studying a group of solar-mass stars (e.g. Güdel 2007). Dorren & Guinan (1994) looked at the optical and UV Sun in Time, from which they could infer declining trends in activity with age. Güdel et al. (1997) examined how the high energy radiation (X-ray and ultraviolet) emitted from the Sun has evolved over time. They used X-ray observations of nine solar-like G type stars to probe their coronae and used this as a proxy for an evolving Sun. Since these high energy fluxes can be connected to coronal activity, they derived trends in coronal temperature and emission measure with rotation and age of these solar analogues (see also Telleschi et al. 2005). Ribas et al. (2005) built on this previous work and investigated how these high

Table 4.1: Sample of stars used in the present study: This sample is similar to that used in The Sun in Time sample (Güdel et al., 1997; Güdel, 2007), with the omission of β Hyi and 47 Cas B. Values are mostly taken from Güdel (2007); Vidotto et al. (2014b). The X-ray luminosity of the sun here is considered to be between maximum and minimum. Errors in age shown can be found in a) Stauffer et al. (1998), b) López-Santiago et al. (2006), c) King et al. (2003), d) Perryman et al. (1998), e) Mamajek & Hillenbrand (2008), f) Liu et al. (2002), g) Ramirez et al. (2014), h) Metcalfe et al. (2015).

Star	M (M_{\odot})	R (R_{\odot})	P_{rot} (d)	Age (Gyr)	$\log[L_X]$ (erg/s)	d (pc)
EK Dra	1.04	0.97	2.77	0.12 ± 0.008^a	29.93	34.5
HN Peg	1.10	1.04	4.55	0.26 ± 0.046^b	29.00	17.95
χ^1 Ori	1.03	1.05	4.83	0.5 ± 0.1^c	28.99	186.0
π^1 UMa	1.00	1.00	5	0.5 ± 0.1^c	28.97	14.36
BE Cet	1.09	1.00	12.4	0.6 ± 0.05^d	29.13	20.9
κ^1 Cet	1.03	0.95	9.3	$0.65 \pm 0.05^{e,d}$	28.79	9.14
β Com	1.10	1.10	12.4	$1.6^{+0.9}_{-0.1}^e$	28.21	9.13
15 Sge	1.01	1.10	13.5	$1.9^{+1.1}_{-0.9}^f$	28.06	17.69
18 Sco	0.98	1.02	22.7	$3.0^{+0.2}_{-0.6}^g$	26.8	13.9
Sun	1.00	1.00	27.2	4.6	≈ 27	1 AU
α Cen A	1.10	1.22	30	$5.5^{+0.0}_{-0.8}^e$	27.12	1.34
16 Cyg A	1.00	1.16	35	7.0 ± 0.3^h	26.89	21.1

irradiations would effect planetary atmospheres. The Sun in Time project inspired our investigation on how the solar wind has evolved during the main sequence.

Understanding how the wind of the Sun has evolved is an important step in understanding the long-term evolution of the planets in the solar system, including the Earth and the development of life (see e.g. Chassefière & Leblanc 2004). The sample for this study was selected by basing it off the original Sun in Time project (Güdel, 2007; Guinan & Engle, 2009). We omitted β Hyi as it has a radius of nearly twice that of the Sun, which gives it a much lower $\log(g)$ which implies that it is no longer on the MS. 47 Cas B was excluded from the study as it does not have very well constrained parameters such as mass, radius or rotation period (Güdel, 2007). It is also the secondary of a close binary system 47 Cas with an orbit of semi-major axis 1.32 AU (Güdel et al., 1998). The stars treated here are all G0-5 type stars in the MS phase. The Sun is also included in our dataset. Table 4.1 lists the most relevant quantities (mass, radius, rotation, age and X-ray luminosity) of these stars for this work. Studying these solar-analogues over a wide range of ages enables us to explore how the solar wind has evolved. Age ranges

are included in Table 4.1 and Figure 4.2. Since the stars have different methods of age determination, they have varying degrees of accuracy in their ages. We note, however, that this particular sample of stars is very well studied in the literature and their ages are relatively accurate. The preferred fit for our data is with rotation as it is more precise, but we also include the fit with age.

4.3 STELLAR WIND PARAMETERS AT THE WIND BASE

Unfortunately, observations cannot constrain the values for base wind temperature and density, which are fundamental input parameters for our model. There has been significant research into constraining base temperature and density, usually by assuming they evolve with age or rotation or other stellar attributes (e.g. [Holzwarth & Jardine 2007](#); [Cranmer & Saar 2011](#)). Here, we use the X-ray-rotation relation presented in Figure 4.1 of this paper to observationally constrain the base wind temperature. Although the X-ray emission and wind acceleration are believed to originate at different locations (closed and open magnetic field regions, respectively), both phenomena are magnetic in nature and, therefore, it is expected that changes in closed regions would also affect changes in open regions.

4.3.1 *Temperature-rotation relation*

We assume that the temperature of the corona of solar type stars is related to the temperature at the base of the wind. Thermally-driven winds are effected by the temperature at their base, with higher temperatures leading to faster winds. Currently, defining the temperature at the base of the wind of solar-type stars is not possible through observations and we must rely on empirical methods. [Johnstone & Güdel \(2015\)](#) took coronal

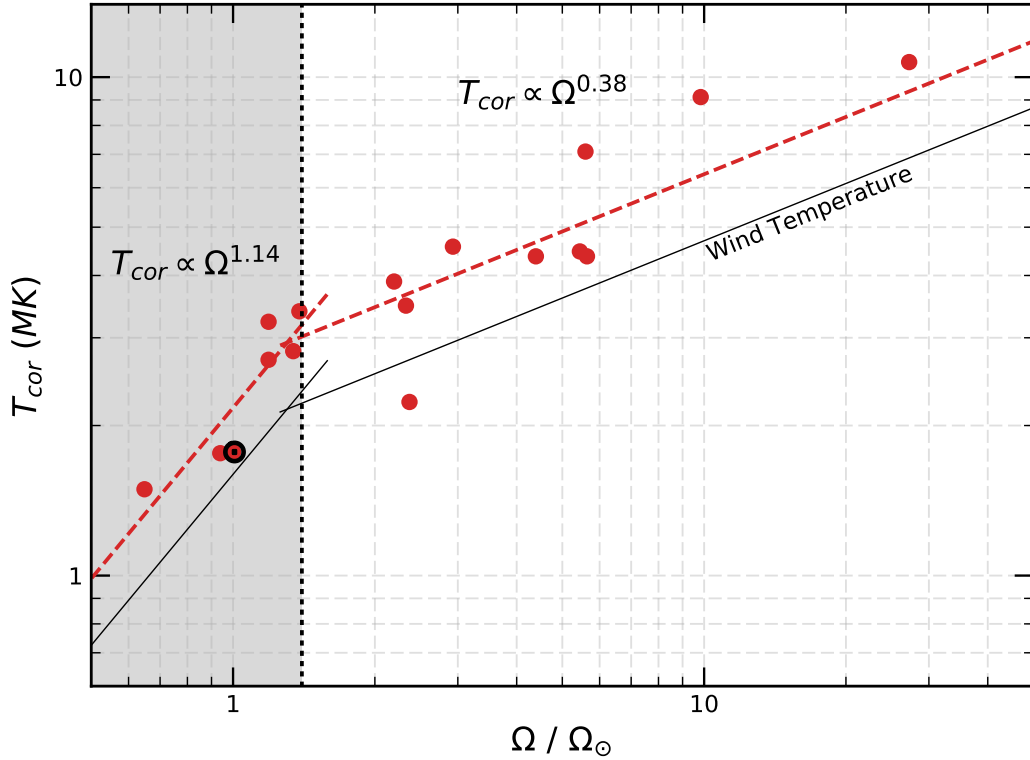


Figure 4.1: Average coronal temperature (T_{cor}) values derived from X-ray observations (Johnstone & Güdel, 2015) show a strong correlation with rotation (broken red line). This relation was scaled down to give a base wind temperature, which we use for our simulations. This break in temperatures occurs at $1.4 \Omega_{\odot}$, and while the physical mechanism for this break is not understood, it would imply some transition between regimes for solar-type stars. Interesting to note is that the Sun (\odot , representing solar average in the solar cycle) has just evolved past this transition. Both fits are shown in Equations 4.1 and 4.2. The statistical significance of these fits are discussed further in the text.

temperatures of low-mass main sequence stars and showed how they they are correlated to X-ray surface fluxes (Telleschi et al., 2005). Here, we find additional evidence that the coronal temperatures of solar-like stars show a steeper decay for older, slowly rotating stars (Figure 4.1). Coronal temperatures are from Johnstone & Güdel (2015), with rotation rates taken from Raassen et al. (2003); Telleschi et al. (2005); Wood & Linsky (2006, 2010); Güdel (2007); Vidotto et al. (2014b). We have excluded M dwarfs from their sample, so as to limit the trend found to solar-type stars. Figure 4.1 shows that there is an evident break in coronal temperature at $\approx 1.4 \Omega_{\odot}$. This break in behaviour at lower rotation rates results in power laws over two different regimes (Equations 4.1 and 4.2).

The $\Omega \approx 1.4 \Omega_{\odot}$ break occurs at ≈ 2 Gyr for the sample of stars used, which is around the same age as those found by Booth et al. (2017) (≈ 1 Gyr) and not dissimilar to ages found by Van Saders et al. (2016) ($\approx 2-4$ Gyr). Although these values are not identical they are a good match considering limitations in age constraints on these stars. From convective turnover times for solar mass stars (Kiraga & Stepien, 2007), we find this break occurring at $Ro = 1.14$. Note that the break in behaviour here is inherent to older solar-type stars above $\approx 1-2$ Gyr. This argument does not preclude the existence of a suggested sudden change in rotational braking at young ages, e.g. Johnstone et al. (2015a) and Gondoin (2017). The model we use is fitted to a piece-wise function around the value of $1.4 \Omega_{\odot}$. The relation we find for T_{cor} was scaled down to correspond to observed solar wind temperatures near the base. As a result, a factor of 1.36 difference between closed-field coronal temperatures and open-field base wind temperatures for all stars in our sample was found, shown in Table 4.2.

$$T_0 (\Omega < 1.4 \Omega_{\odot}) = 1.5 \pm 0.19 \left(\frac{\Omega_{\star}}{\Omega_{\odot}} \right)^{1.2 \pm 0.54} \text{ MK} \quad (4.1)$$

$$T_0 (\Omega > 1.4 \Omega_{\odot}) = 1.98 \pm 0.21 \left(\frac{\Omega_{\star}}{\Omega_{\odot}} \right)^{0.37 \pm 0.06} \text{ MK} \quad (4.2)$$

These relations are shown as solid lines in Figure 4.1. The errors in the exponents arise from fitting. Note that a single fit to the coronal temperature data is also possible, but provides a larger χ^2 . In light of the recent works presented in Section 4.1 (e.g. Van Saders et al. 2016; Booth et al. 2017; Beck et al. 2017), we proceed with the broken power law fit throughout this paper. Section 4.6.2 shows the results one would have obtained, in the case a single power law had been adopted.

4.3.2 Density-rotation relation

Currently, there is no available method to accurately define the density at the base of the wind, making it a difficult parameter to prescribe for simulations. Observations of

stellar mass-loss rates would provide meaningful upper limits to the base density, but these are available for only a small sample of stars (Wood et al., 2014). Ivanova & Taam (2003) find a relationship between rotation and coronal density (Equation 4.3, also used by Holzwarth & Jardine 2007; Réville et al. 2016), from X-ray luminosity observations. We adopt this relationship for the density at the base of the wind for our simulations (Table 4.2).

$$n_0 = n_{\odot} \left(\frac{\Omega_{\star}}{\Omega_{\odot}} \right)^{0.6}. \quad (4.3)$$

where n represents number density and is related to mass density by $n = \rho/(\mu m_p)$, where $\mu = 0.5$ is the mass fraction of a fully ionised hydrogen wind and m_p is the proton mass. $n_{\odot} = 2.2 \times 10^8 \text{ cm}^{-3}$ as described above.

4.4 EVOLUTION OF GLOBAL PROPERTIES OF THE SOLAR WIND

4.4.1 Mass-loss rate

Since the model parameters in Table 4.2 are dependent on stellar rotation, we find in Figure 4.2 that the mass-loss rate of stars is also dependent on rotation. The left panel of Figure 4.2 shows a mass-loss rate that increases with rotation, with a break occurring at $1.4 \Omega_{\odot}$. This dependence is as follows,

$$\dot{M} (\Omega < 1.4 \Omega_{\odot}) = 6.3 \times 10^{-14} \left(\frac{\Omega}{\Omega_{\odot}} \right)^{7.7 \pm 1.6} \text{ M}_{\odot} \text{ yr}^{-1} \quad (4.4)$$

$$\dot{M} (\Omega > 1.4 \Omega_{\odot}) = 6.3 \times 10^{-13} \left(\frac{\Omega}{\Omega_{\odot}} \right)^{1.4 \pm 0.15} \text{ M}_{\odot} \text{ yr}^{-1} \quad (4.5)$$

The mass-loss rate of solar-type stars is believed to decrease with time as the star ages. This is due to stellar spin down and a decrease in magnetic activity (e.g. Vidotto et al.

Table 4.2: Stellar wind properties for each of the simulated solar analogues in our sample. Values are displayed for base wind density, temperature and mass-loss rates (cf. Figure 4.2). The chosen values of n_0 and T_0 for the solar wind are such to reproduce observations (see text).

Star	n_0 (10^8cm^{-3})	T_0 (MK)	\dot{M} ($M_\odot \text{yr}^{-1}$)
EK Dra	8.8	4.7	1.4×10^{-11}
HN Peg	6.6	3.9	6.9×10^{-12}
χ^1 Ori	6.3	3.8	8.8×10^{-12}
π^1 UMa	6.2	3.7	7.3×10^{-12}
BE Cet	4.8	3.2	3.1×10^{-12}
κ^1 Cet	4.3	3.0	2.0×10^{-12}
β Com	3.6	2.7	1.9×10^{-12}
15 Sge	3.4	2.6	2.1×10^{-12}
18 Sco	2.5	1.9	2.8×10^{-13}
Sun	2.2	1.5	3.5×10^{-14}
α Cen A	2.1	1.4	4.5×10^{-14}
16 Cyg A	1.9	1.1	8.1×10^{-15}

2014b). Our results show a similar behaviour as the Sun evolves. However, our models predict a steep break in the mass-loss rate at an age of 2 Gyr (Figure 4.2), as a result of the break in T_{cor} with respect to rotation. The values of \dot{M} we find for each star in our sample is shown in Table 4.2 and Figure 4.2, and follow the relations

$$\dot{M} (t \lesssim 2 \text{ Gyr}) = 5.0 \times 10^{-10} t_{\text{Myr}}^{-0.74 \pm 0.19} M_\odot \text{yr}^{-1} \quad (4.6)$$

$$\dot{M} (t \gtrsim 2 \text{ Gyr}) = 9.0 t_{\text{Myr}}^{-3.9 \pm 0.81} M_\odot \text{yr}^{-1} \quad (4.7)$$

where t_{Myr} is the age given in Myr. This shows, for example, that a young Sun of 100 Myr would have a mass-loss rate of $1.5 \times 10^{-11} M_\odot \text{yr}^{-1}$, almost 2.5 orders of magnitude larger than the current rate.

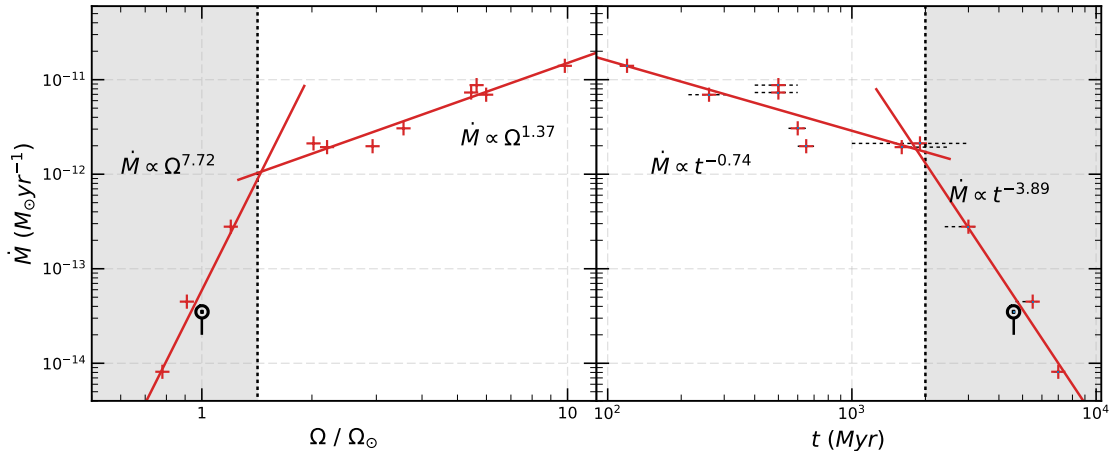


Figure 4.2: *Left:* Calculated mass-loss rates (red crosses) using our 1D polytropic model as the star spins down. *Right:* Plot showing how the mass-loss rate of the Sun would change as it ages. Included in our calculation is our estimation of the current solar mass-loss rate (\odot) and the range of values calculated directly from observations (black solid line) (Wang, 1998). Note the clear break into a rapidly declining mass-loss rate regime (grey shaded region) at $1.4\Omega_{\odot}$ and ≈ 2 Gyr respectively. Errors in ages are shown as dotted black lines, with sources described in Table 4.1.

4.5 RADIO EMISSIONS FROM STELLAR WINDS

One possible way of estimating wind densities (and mass-loss rates, \dot{M}) is by detecting these winds at radio wavelengths. The plasma that makes up stellar winds can emit in radio through the process of thermal bremsstrahlung from ionised plasma. This is discussed at length in Chapter 3. We can estimate the level of thermal radio emission from these winds using our model. According to previous studies by Panagia & Felli (1975); Wright et al. (1975); Güdel (2002); Vidotto & Bourrier (2017) the specific radio flux density produced by a wind is defined in Equation 3.36. This is an analytical approximation for the radio emission produced from a plasma. It has a strong dependence on the radio decay with distance. This power decay law is defined by the α index. Given enough distance from the star, the wind density will eventually become an inverse-square law, and $\alpha = 2$ as the wind reaches asymptotic terminal velocity. Since the radio emission originates near the base of the wind, the α parameter is likely to be greater than 2, denoting a fast density decay. For each star we found α by estimating the rate of density

decline in the 1-5 R_\star range. This range should account for the majority of “stronger” radio emission, as it is the densest region. It is important to note that the estimation of radio flux Equation 3.36 is based on an isothermal wind, whereas in our model the wind is a polytrope, allowing the temperature to vary as it expands. However the dependence on the plasma temperature is much weaker than the dependence on the plasma density. This approximation for radio flux should give a good indication of flux from these stars as emission is only estimated in the 1-5 R_\star range, and within this region the isothermal approximation is adequate.

The region where half of the emission occurs has a size

$$\frac{R_v}{R_\star} = \left[4.23 \times 10^{-27} I(\alpha) n_0^2 R_\star \right]^{\frac{1}{2\alpha-1}} \left[\frac{\nu}{10 \text{GHz}} \right]^{\frac{-2.1}{2\alpha-1}} \left[\frac{T_0}{10^4 \text{K}} \right]^{\frac{-1.35}{2\alpha-1}}, \quad (4.8)$$

which we refer to as the ‘radio photosphere’ of the star. This equation is derived from Equation 3.36. This parameter illustrates how close to the star the emission will emanate and whether the wind is optically thin, as described by Panagia & Felli (1975). Whether the stellar wind is optically thin or not at radio wavelengths will have significant consequences for attributing observed radio detections from these stars at these wavelengths. An optically thin wind will allow any more powerful thermal radio emissions that may occur, for example from the much denser chromosphere, to dominate the observed radio spectra.

4.5.1 *Radio emission from our simulations*

The densest parts of stellar winds might be able to produce free-free emission at radio wavelengths. Recently, Fichtinger et al. (2017) observed four stars, at 6 GHz and 14 GHz, using VLA and ALMA, namely: EK Dra, χ^1 Ori, π^1 UMa and κ^1 Cet. Only two of these stars showed radio emission (EK Dra and χ^1 Ori), however this emission did not emanate from their winds, but rather from the closed corona and flares. For π^1

Table 4.3: Radio properties of our wind models. Shown here are values for α , which describes the behaviour of the density as a function of distance. β and λ describe the radio emission dependence on frequency and wind temperature respectively, which themselves depend on α (Equation 3.39). Outlined are results for the critical frequency, ν_c , which describes the frequency below which the wind becomes optically thick. S_{ν_c} describes the radio flux at each respective critical frequency.

Star	α	β	λ	ν_c (GHz)	S_{ν_c} (μ Jy)
EK Dra	2.8	1.09	0.41	2.0	0.79
HN Peg	3.1	1.19	0.48	1.7	1.9
χ^1 Ori	3.1	1.19	0.48	1.7	0.017
π^1 UMa	3.0	1.16	0.46	1.6	2.5
BE Cet	3.3	1.25	0.52	1.4	0.70
κ^1 Cet	3.4	1.28	0.53	1.3	2.5
β Com	3.4	1.28	0.53	1.2	2.9
15 Sge	3.4	1.28	0.53	1.2	0.70
18 Sco	4.0	1.40	0.61	0.99	0.48
α Cen A	5.3	1.56	0.72	1.1	58
16 Cyg A	6.4	1.64	0.77	1.0	0.16

UMa and κ^1 Cet no detections were made, which allowed the authors to place upper limits on the mass-loss rates of these winds (see also [Vidotto & Bourrier 2017](#)).

Table 4.3 shows the density fit parameters (α, β, γ) we found for each star, with which we calculated radio emission over a range of frequencies (Equations 3.36 to 3.39). We also computed the ‘radio photosphere’ size (Equation 4.8) for all the stars in our sample and found that all have their radio photosphere inside the radius of the star at both 6 GHz and 14 GHz. This implies that their winds are optically thin and do not emit at these frequencies. This agrees with the non-detections reported by [Fichtinger et al. \(2017\)](#). To examine this further we computed the cut-off frequency, ν_c (Table 4.3), below which the radio photosphere surpasses the radius of the star and the wind becomes optically thick ([Wright et al., 1975](#)). From Equation 4.8, the critical frequency below which these winds emit is given by

$$\nu_c = [4.23 \times 10^{-27} I(\alpha) n_0^2 R_\star]^{0.48} \left[\frac{T_0}{10^4 K} \right]^{-0.64} 10 \text{ GHz}. \quad (4.9)$$

We calculate the expected flux density emitted from the wind at the same value of ν_c , given in Table 4.3 as S_c . These flux densities are quite low with the exception of α Cen A as it is relatively close compared to the other stars. Note that, the wind cannot emit at frequencies larger than ν_c . For stars in our sample, the cut-off frequency is around 1-2 GHz, implying that observations to detect these winds should be conducted at frequencies lower than 1 GHz. Also important to note is that if the radio photosphere is very close to the surface of the star, any thermal emission is likely dominated by other stellar emission (i.e. coronal emission or flares).

From Equation 4.9, we find that ν_c is weakly dependent on α and follows: $\nu_c \propto n_0^{0.96} T_0^{-0.64}$. Since our model assumes that both base wind temperature and density rely on rotation, we can relate this cut-off frequency to rotation as

$$\nu_c (\lesssim 1.4\Omega_\odot) \propto \Omega^{-0.20}. \quad (4.10)$$

$$\nu_c (\gtrsim 1.4\Omega_\odot) \propto \Omega^{0.33}, \quad (4.11)$$

This means that there is an inflection in the dependence of ν_c with rotation. Although it is a weak dependence, it suggests that the lowest critical frequencies occur for stars at $\sim 1.4 \Omega_\odot$.

4.6 DISCUSSION

4.6.1 Consequences for the ageing Sun

Since direct observations of mass-loss rate and radio emission from stellar winds are difficult to obtain, we can use models to help understand the physical processes behind these winds. These models can provide information on the strength and location of the wind emission, therefore aiding in observing these winds directly. Recently, there

has been research into the mass-loss rates of solar-analogue winds and how they would effect an orbiting planet, including a young Earth. While some work focuses directly on the Sun-Earth interaction (Sternberg et al., 2011), others focus more on the stellar evolution of these types of stars (Wood et al., 2002; Wood et al., 2005, 2014; Cranmer & Saar, 2011; Matt et al., 2012; Fichtinger et al., 2017) and their effects on exoplanets (Vidotto et al., 2012; Vidotto et al., 2013, 2015; See et al., 2014, 2017; Zuluaga et al., 2016).

The main basis of our models is the temperature-rotation relation we presented in Figure 4.1. This type of relation between wind temperatures and X-ray observations, which has a strong correlation, is unique in predicting the winds of these stars. Holzwarth & Jardine (2007) also derived a temperature-rotation relation which is based on activity-rotation relation. They attempted to constrain this dependence to a power law index, that lies somewhere between 0 and 0.5. They assumed a value of 0.1 for their model. This is a much weaker dependence than we find here for the slower rotators, but their ranges are within the values for the faster rotators.

The break we find in wind temperature filters through to the trend in stellar mass-loss rate (Figure 4.2). We see a clear decay in \dot{M} with stellar spin down and ageing, with a break in \dot{M} occurring at both $1.4 \Omega_{\odot}$ and 2 Gyr respectively. Since our stellar wind models depend on the base wind temperature, it follows that mass-loss rate displays a similar trend. Other models also predict a decay in mass-loss rate with stellar evolution. Cranmer & Saar (2011) developed an Alfvén-wave driven model for predicting winds from cool, late-type stars. They based their models on physically observed parameters from 47 stars of types G, K and M. Johnstone et al. (2015a,b) employed a different approach and used polytropic wind models to reproduce the rotational evolution of solar-mass stars in open clusters. Both of the models found a mass-loss rate for young suns (at an age of 100 Myr) that are 1-2 orders of magnitude smaller than our predictions. However, for older stars, our predictions become smaller than theirs, since our model shows a steep decay in \dot{M} for stars older than ≈ 2 Gyr. Note that Johnstone et al. (2015a) assumed that the wind saturates for very young stars (< 600 Myr) in the fast rotating

track. When plotted in the Ω -age diagram, the stars in our sample follow the 50th percentile track, as defined by [Gallet & Bouvier \(2013\)](#), which implies that they would not be part of the saturated regime explored by [Johnstone et al. \(2015a\)](#).

Regarding the mass-loss rate with age, in our models, for ages younger than 2 Gyr, we found that $\dot{M} \propto t^{-0.74}$. This is much flatter than the original dependence derived by [Wood et al. \(2014\)](#) ($t^{-2.33}$), which has been revised as $t^{-1.46}$ by [Johnstone et al. \(2015a\)](#). In their Alfvén wave-driven wind models, [Suzuki et al. \(2013\)](#) predicted $t^{-1.23}$, while [Cranmer & Saar \(2011\)](#) predicted $t^{-1.1}$. Given the uncertainties in age measurements, our derived age-dependence is consistent with these works. Note also that, if we were to fit one single power law to a temperature- Ω relation, this would imply that the wind mass-loss rate would not have the change in regimes that we suggest, and the corresponding age dependence would be $t^{-1.36}$, a unique power law for all ages. [See et al. \(2017\)](#) investigated the trends in mass-loss rate with stellar age by adopting a potential field source surface model. By doing so they could investigate the topology of the coronal magnetic field of stars, including the extent of open flux regions which in turn allows angular momentum and mass-loss rates to be determined. They found lower mass-loss rates than presented here for all overlapping stars in our sample, but with a similar trend with age.

These mass-loss rates are important for solar and terrestrial evolution, as it affects solar evolutionary models, which in turn directly effect the Earth through particle and radiation flux. A famous problem arose when these models predicted that the Sun would have been 25-30% fainter than it is today ([Newman & Rood, 1977](#); [Gough, 1981](#)), leading to a completely frozen Earth and Mars. Yet this prediction is inconsistent with the evidence suggesting that there was liquid water on the surface of both planets, implying planetary temperatures were not freezing ([Sagan & Mullen, 1972](#)). This is called the faint young Sun paradox ([Feulner, 2012](#)). It leads astronomers to the conclusion that there must be something awry with the standard solar model or the estimates surface temperatures of Earth and Mars. One solution to this issue is if the mass-loss rate of the Sun was higher in the past than expected. We integrated the mass-loss rate evolution

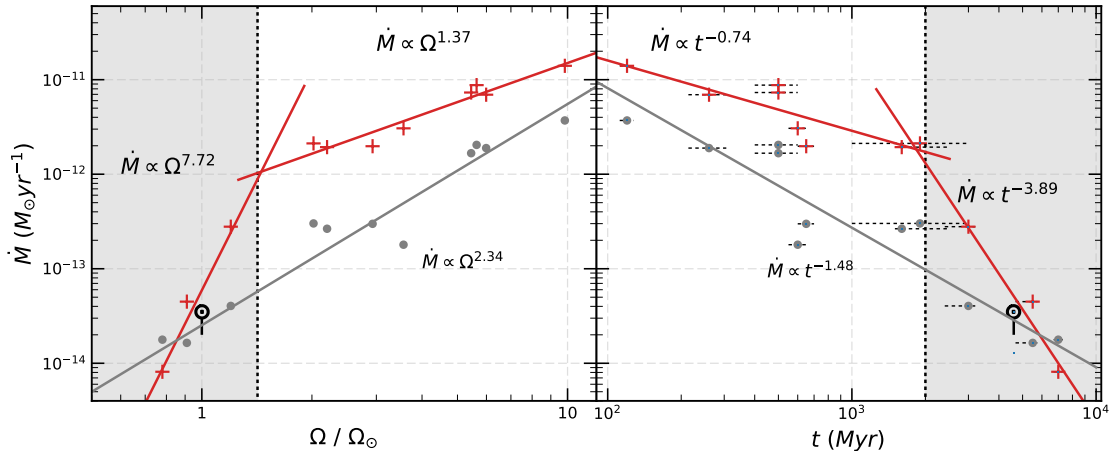


Figure 4.3: Plot similar to Figure 4.2 with the resulting mass-loss rate from a linear fit in $T_{\text{cor}}-\Omega$ (Figure 4.4) shown in grey. Other symbols represent the same as in Figure 4.2. We can see this produces lower mass-loss rates in most cases, with the exception of 16 Cyg A. The relation for each fit is shown beside the fitted line.

calculated here and find that the Sun has lost 0.8% M_{\odot} since an age of 100 Myr. Our model results in a higher mass-loss rate at younger ages than previous models, while also predicting lower mass-loss rates at older ages. Even with the increased mass-loss rate from this model in the past, it does not solve the faint young Sun paradox, where a mass loss of 3-7% M_{\odot} is required.

4.6.2 $T_{\text{cor}} - \Omega$: Goodness of fit

We present a fit between coronal temperature data and rotation rate for our sample, shown in Figure 4.4. We find that a broken power law best describes the trend in data, although we note that there are other possible fits to the data. Having carried out reduced χ^2 analysis on the goodness of fit, we find that both the low- Ω and high- Ω fits shown in Figure 4.1 have reduced χ^2 of 3.5 and 1.4 respectively, while a single power law fit would have a reduced χ^2 of 4.7. This would suggest that the broken power law fit produces a better result than a single power law. In addition, our choice of a broken power law is more in line with recent results (e.g. Van Saders et al. 2016; Metcalfe et al. 2016; Kitchatinov & Nepomnyashchikh 2017; Booth et al. 2017; Beck et al. 2017). We use this broken power law fit as an explanation as to why Van Saders et al. (2016)

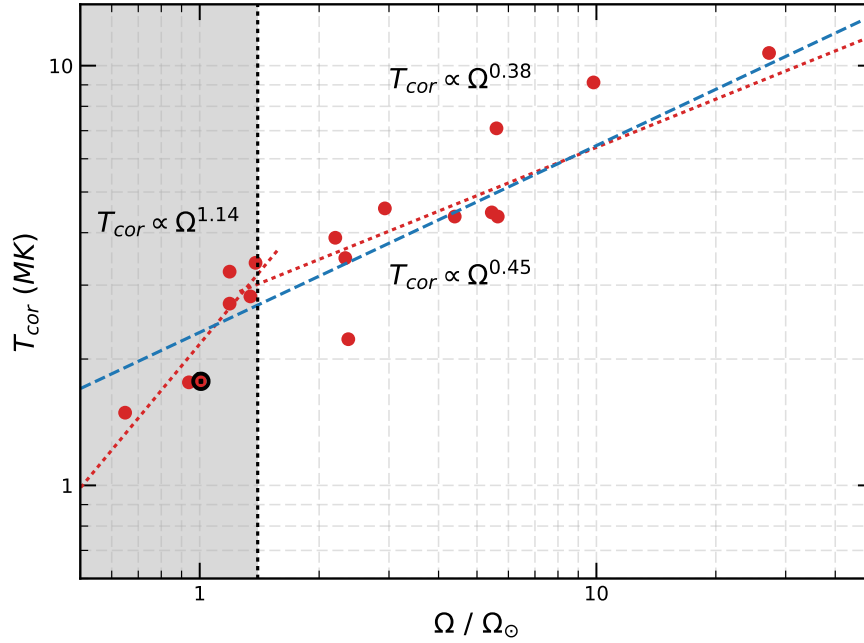


Figure 4.4: Comparison between a broken power law fit, which is used in this work, shown in red and a single power law fit, shown in blue.

find anomalously high rotation rates in older stars; we propose that these lower coronal temperatures will lead to cooler winds, causing lower mass loss rates and therefore reduced angular momentum loss. Simultaneously, it also agrees with the break in X-ray luminosities found by [Booth et al. \(2017\)](#) in older stars. Ideally, in this scenario, the parameter space for solar-mass stars with X-ray measurements would fill out, with a larger sample, this relationship could be more constrained. Perhaps these relationships are dependent on stellar mass, or another significant parameter, such as magnetic field, which could allow us to constrain the relationship even further. For completeness we calculate the mass-loss rates that would result from a single power law fit. Shown in blue in [Figure 4.4](#) is the fit produced by using a single power law to fit the coronal temperatures with stellar rotation. We find a relationship of $T_{\text{cor}} \propto \Omega^{0.45}$ for a single power law. This value lies between both values found for the broken power law (1.14 and 0.38). A single power law results in much higher temperatures as you move to slower rotators. We can see how this fit affects the mass-loss rates in [Figure 4.3](#). We find that $\dot{M} \propto \Omega^{2.34}$ and $\dot{M} \propto t^{-1.48}$. This fit produces lower mass-loss rates than our previous broken fit for any stars younger than the crossing point of both methods (≈ 5500 Myr or $8.5\Omega_{\odot}$).

It also results in higher mass loss rates for stars older than 5500 Myr, in our case only showing as an increased mass-loss rate for 16 Cyg A. If this new \dot{M} -Age relationship is integrated from 100 Myr to the present (4600 Myr), we find a total mass lost of 0.14% the current solar mass.

We conclude the efforts of this work in Chapter 9. This work provided good insight into the behaviour of ageing solar-mass stellar winds, as well as the parameters space that we shall be investigating. The next approach is to adopt 3D MHD simulations so as to further probe the winds of these stars, allowing us to numerically analyse the magnetic fields of these stars as they permeate their winds, and quantify the total angular momentum loss in a more robust manner.

THE SOLAR WIND IN TIME - 3D MHD SIMULATIONS

The mechanism by which stars spin down while traversing the main sequence is through angular momentum loss by their magnetised winds (e.g. [Weber & Davis Jr. 1967](#); [Vidotto et al. 2014b](#); [See et al. 2017](#)). Therefore, this indicates that the surface magnetic field of the star also evolves with time, as demonstrated with magnetic field observations analysed using the Zeeman-Doppler Imaging (ZDI) technique ([Vidotto et al., 2014a](#); [Folsom et al., 2016, 2018a](#)). ZDI is a method that allows for the reconstruction of the large-scale magnetic field of the stellar surface from a set of high-resolution spectropolarimetric data ([Semel, 1989](#); [Brown et al., 1991](#); [Donati et al., 1997](#)) and is described in Section 1.3 and shown here in Figure 5.1. Although it is insensitive to small-scale fields ([Lang et al., 2014](#); [Lehmann et al., 2018](#)), it gives an accurate representation of the large-scale surface magnetic field. [See et al. \(2017\)](#) determined, from 66 ZDI-observed stars, that the magnetic geometry as well as angular momentum and mass loss is correlated

to Rossby number. Other works have demonstrated that there is a link between all of stellar activity, magnetic strength and geometry, angular momentum loss, and stellar winds (Matt et al., 2012; Nicholson et al., 2016; Pantolmos & Matt, 2017; Finley et al., 2018).

Stellar angular momentum-loss depends upon how much mass is lost by their winds (Weber & Davis Jr., 1967). As discussed in Chapter 1, due to the tenuous nature of low-mass stellar winds, a direct measurement of their winds is difficult (e.g. Wood et al. 2005), but would prove extremely useful in the constraining of mass-loss rates and other global wind parameters. In this regard, the observations of radio emission from the winds of low-mass stars could provide meaningful constraints on wind density and mass-loss rate (Lim & White, 1996; Güdel, 2002; Villadsen et al., 2014; Fichtinger et al., 2017; Vidotto & Donati, 2017). The wind is expected to have continuum emission in radio through the mechanism of thermal free-free emission (Panagia & Felli, 1975; Wright et al., 1975). This emission is expected to be stronger for stars with denser winds and is also dependent on the density (n) gradient in the wind with radial distance, R : $n \propto R^{-a}$. We have discussed the analytical solution to this radio calculation in Chapters 3 and 4

With this idea in mind, Güdel et al. (1998) and Gaidos et al. (2000) observed various solar analogues. They could place upper limits on the radio fluxes from these objects, and so indirectly infer upper mass-loss rate constraints. All non-degenerate stars emit some form of radio emission from their atmospheres (Güdel, 2002). Although different radio emission mechanisms dominate at different layers in their atmosphere and wind (Güdel, 2002). For example, detecting coronal radio flares at a given frequency implies the surrounding wind is optically thin at those frequencies, allowing for placement of upper mass-loss limits. In addition, Güdel (2007) noted that thermal emission should dominate at radio frequencies as long as no flares occur while observing. The three dominant thermal emission mechanisms the author described are bremsstrahlung from the chromosphere, cyclotron emission above active regions, and coronal bremsstrahlung from hot coronal loops. These emission mechanisms must be addressed when attempting to detect the winds of solar-type stars at radio frequencies.

Observing these winds can become difficult as the fluxes expected from these sources is at the μJy level (see upper limits placed by [Gaidos et al. 2000](#); [Villadsen et al. 2014](#); [Fichtinger et al. 2017](#)), and can be drowned out by chromospheric and coronal emission as described in the previous paragraph. [Villadsen et al. \(2014\)](#) observed three low-mass stars, with positive detections for all three stars in the Ku band (centred at 34.5 GHz) of the VLA, and non-detections at lower frequencies. They suggested that the detected emissions originate in the chromosphere of these stars, with some contributions from other sources of radio emission. If emanating from the chromosphere, these detections do not aid in constraining the wind. More recently, [Fichtinger et al. \(2017\)](#) observed four solar-type stars with the VLA at radio frequencies, and provided upper limits to the mass-loss rates for each, ranging from $3 \times 10^{-12} - 7 \times 10^{-10} M_{\odot} \text{ yr}^{-1}$, depending on how collimated the winds are. [Bower et al. \(2016\)](#) observed radio emission from the young star V830 Tau, with which [Vidotto & Donati \(2017\)](#) were able to propose mass-loss rate constraints between 3×10^{-10} and $3 \times 10^{-12} M_{\odot} \text{ yr}^{-1}$. Transient CMEs should also be observable, which would cause more issues in detecting the ambient stellar wind, but these events are expected to be relatively short and could also help in constraining transient mass-loss from these stars ([Crosley et al., 2016](#)).

To aid in the radio detection and interpretation of the winds of solar-type stars, we here quantify the detectability of the winds of 6 solar-like stars of different ages within the radio regime from 100 MHz to 100 GHz. We aim to study the effects ageing stellar winds have on different solar analogues along the main sequence, allowing us to constrain global parameters and quantify the local wind environment. To do this, we conduct 3D magnetohydrodynamical simulations of winds of solar-type stars, investigating the main-sequence solar wind evolution in terms of angular-momentum loss rates (\dot{J}), mass-loss rates (\dot{M}) and wind structure. We then use the results of our simulations to quantify the detectability of the radio emission from the solar wind in time, which can help guiding and planning of future observations of solar-like winds.

Results from this chapter were published in "The solar wind in time II: 3D stellar wind structure and radio emission", MNRAS, 483, (2018)

Table 5.1: Stellar parameters of our sample are shown on the left (mass, radius, rotation period, age, and distance) and specifics of the simulations are shown on the right (base density, base temperature, mass-loss rate, angular momentum-loss rate, open magnetic flux, and flux ratio between surface and open magnetic fluxes). Stellar parameters were compiled in Vidotto et al. (2014b). Distances are found using the Gaia DR2 database^a (Prusti et al., 2016; Brown et al., 2018) values for parallax.

Star	Observables						Simulation					
	M_{\star} (M_{\odot})	R_{\star} (R_{\odot})	P_{rot} (d)	Ω (Ω_{\odot})	Age (Gyr)	d (pc)	n_0 (cm^{-3}) ($\times 10^8$)	T_0 (MK)	\dot{M} (M_{\odot}/yr) ($\times 10^{-13}$)	\dot{J} (ergs) ($\times 10^{30}$)	Φ_{open} (G cm) ($\times 10^{22}$)	f
χ^1 Ori	1.03	1.05	4.86	5.60	0.5	$8.84^{\pm 0.02}$	18.9	2.84	46.5	285	22.5	0.37
HD 190771	0.96	0.98	8.8	3.09	2.7	$19.02^{\pm 0.01}$	13.2	3.04	36.1	91.0	23.46	0.59
κ^1 Ceti	1.03	0.95	9.3	2.92	0.65	$9.15^{\pm 0.03}$	12.8	2.98	22.1	124	30.71	0.44
HD 76151	1.06	0.98	15.2	1.79	3.6	$16.85^{\pm 0.01}$	9.54	2.47	8.26	31.8	14.68	0.49
18 Sco	0.98	1.02	22.7	1.20	3.0	$14.13^{\pm 0.02}$	7.5	1.85	6.47	5.34	4.29	0.70
HD 9986	1.02	1.04	23	1.18	4.3	$25.46^{\pm 0.03}$	7.44	1.82	5.82	2.35	3.30	0.94
Sun Min	1.0	1.0	27.2	1	4.6	-	6.72	1.5	1.08	1.04	3.44	0.69
Sun Max	1.0	1.0	27.2	1	4.6	-	6.72	1.5	1.94	15.5	6.17	0.24

5.1 STELLAR SAMPLE

Our sample of solar-like stars was selected so as to closely resemble the Sun in both mass and radius. They cover a range of rotation rates (from 4.8-27 days or 1-5.6 Ω_{\odot}) with ZDI reconstructed by Petit et al. (2008); do Nascimento, Jr. et al. (2016) and Petit et al. (prep) as part of the BCool collaboration. Gallet & Bouvier (2013); Gallet & Bouvier (2015) depict different age-rotation evolutionary tracks for a 1 M_{\odot} star, which converge at 800 Myr to the Skumanich law (Skumanich, 1972). χ^1 Ori follows the fast rotator track, while the rest of our stars exist beyond the convergence point. We note that HD 190771 and HD 76151 exhibit faster rotation than the Skumanich law, which could be due to uncertainties in their ages. The stars in our sample are listed below, see also Table 5.1 for stellar parameters, and Figure 5.1 for observed ZDI maps.

χ^1 ORION This star is both the youngest star and the fastest rotator we have simulated, with a rotation period of 4.8 days and an age of 0.5 Gyr (Vidotto et al., 2014b). This fast rotation should indicate a more active star than the slower rotators, which we see confirmed in the high magnetic field strengths. The large-scale magnetic geometry reconstructed with ZDI for this star displays a complex structure (Figure 5.1), showing very un-dipolar like structure (Petit et al., in prep.).

Note that the ZDI observations here include 10 spherical harmonic degrees, which is the most of all simulations. This star is the closest star in our sample at 8.84 pc¹.

HD 190771 This star possesses an uncharacteristically short rotation period (8.8 days) for its commonly used age (2.7 Gyr, derived from isochrone fitting, [Valenti & Fischer 2005](#)). This fast rotation should indicate a more active star, which we see validated in the ZDI observations of the magnetic field at the stellar surface. We see one of the least dipolar fields in the sample, with large areas of strong magnetic field of both polarities in the northern hemisphere (Figure 5.1). Note that polarity reversal has been observed to occur in the magnetic field of this star ([Petit et al., 2009](#)).

κ^1 **CETI** is estimated to be the second youngest star in our selected sample, with an age of 0.65 Gyr ([Rosén et al., 2016](#)). The observed rotation period from photometry is 9.2 days ([Messina & Guinan 2003](#); [Rucinski et al. 2004](#), ground and space respectively). The higher levels of activity in this star are apparent when we examine the ZDI map, with non-dipolar geometry and relatively strong B field ($B_{r,max} \approx 35$ G, [do Nascimento, Jr. et al. 2016](#)). It is the second closest star in our sample (excluding the Sun), at a distance of 9.13 pc¹.

HD 76151 has a rotation period of 15.2 days ([Maldonado et al., 2010](#)). The age of HD 76151 is estimated to be 3.6 Gyr ([Petit et al., 2008](#)). ZDI observations of HD 76151 present a strong dipolar field, with $B_{r,max} \approx 10$ G, which is tilted to the axis of rotation by 30° ([Petit et al., 2008](#)). Considering the age of the star and the dipolar geometry of the magnetic field, we expect a slower wind than the faster, more magnetically active rotators.

18 SCORPII is 3 Gyr old and possesses a rotation period of 22.3 days. It displays very quiescent behaviour, with a weak, largely dipolar magnetic field ([Petit et al., 2008](#)). It is the most similar solar twin for which we have surface magnetic field measure-

¹ <https://gea.esac.esa.int/archive/>

ments, displaying very similar spectral lines to the Sun (Meléndez et al., 2014). Recently, many more solar twins have been identified (Lorenzo-Oliveira et al., 2018), however, these stars do not have magnetic field observations.

HD 9986 presents another off axis dipole, with a maximum field strength of 1.6 G and an age of 4.3 Gyr (Vidotto et al., 2014b). This is the weakest magnetic field of any star in the sample, Petit et al. (in prep.)

THE SUN has a well documented cyclical behaviour, of which we take one map at the maximum of the cycle, and another map at the minimum of the cycle. Maps for the minima and maxima are taken at Carrington rotations 1983 and 2078 respectively, which were observed with SOHO/MDI in the years 2001 and 2008. We have removed the higher degree harmonics ($\ell \geq 5$) for both maps, so as to replicate the Sun as if observed similarly to the other slowly rotating stars in the sample (Vidotto, 2016b; Vidotto et al., 2018; Lehmann et al., 2018). We note that the Sun at maximum possesses a much more complex magnetic geometry than the solar minimum, including a stronger magnetic field (e.g. DeRosa et al. 2010).

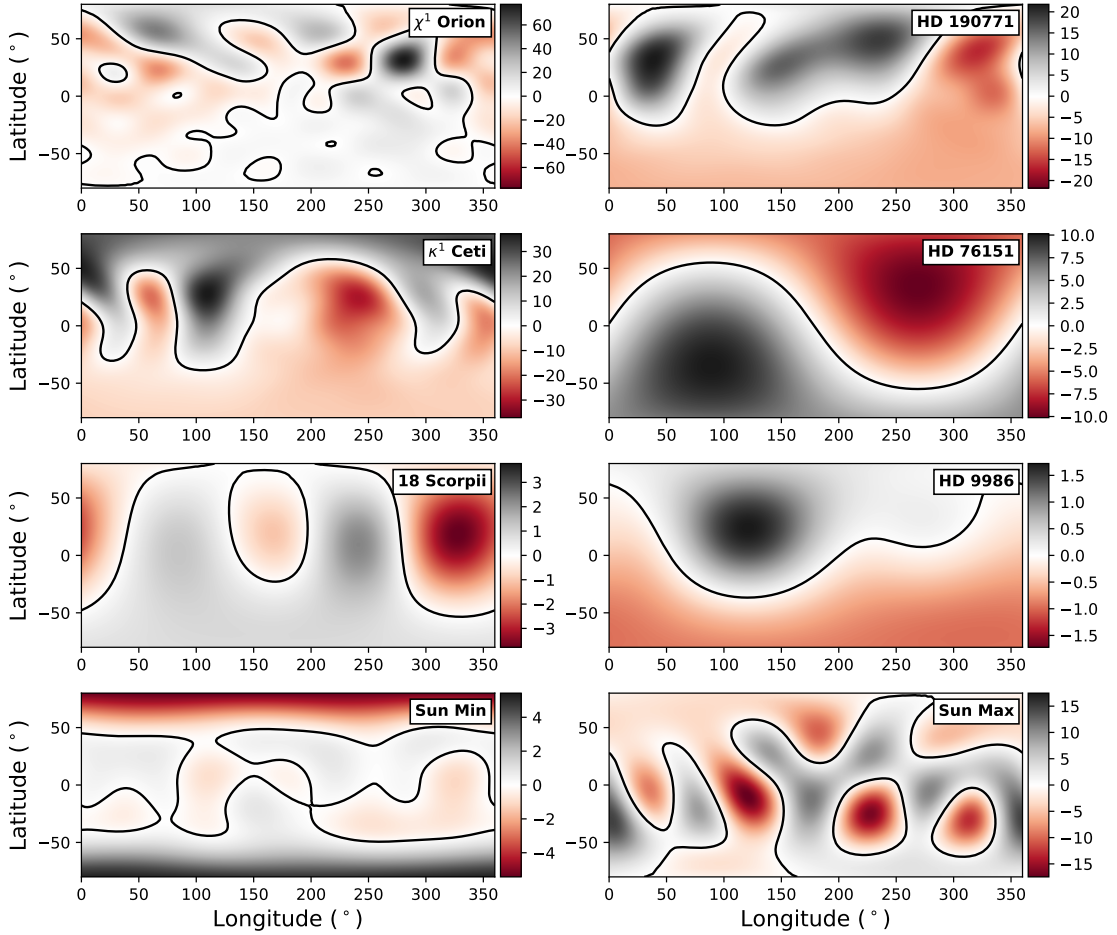


Figure 5.1: Radial surface magnetic fields of our stars. Each magnetic field is saturated at the maximum absolute value for each field respectively. Magnetic field contours are shown in Gauss. The maps are shown in latitude-longitude coordinates.

5.2 MASS-LOSS RATES, ANGULAR MOMENTUM-LOSS RATES & OPEN MAGNETIC FLUX

From our wind simulations we can calculate the mass-loss rate from each of the stars by integrating the mass flux through a spherical surface S around the star, as shown in Equation 2.37. In our simulations we see an overall decrease of \dot{M} with decreasing rotation rate, Table 5.1, which is consistent with the works of Cranmer & Saar (2011); Suzuki et al. (2013); Johnstone et al. (2015a,b); Ó Fionnagáin & Vidotto (2018). We

note that the mass-loss rate we find for the Sun is ≈ 5 times larger than the observed value of $\sim 2 \times 10^{-14} M_{\odot} \text{ yr}^{-1}$. This is as a result of our choice of base density, which is 3 times higher than in Ó Fionnagáin & Vidotto (2018). We opted for a 3 times higher base density as we were unable to find a stable solution for the winds of a few stars in our sample. Ó Fionnagáin & Vidotto (2018) suggested that the angular-momentum loss for

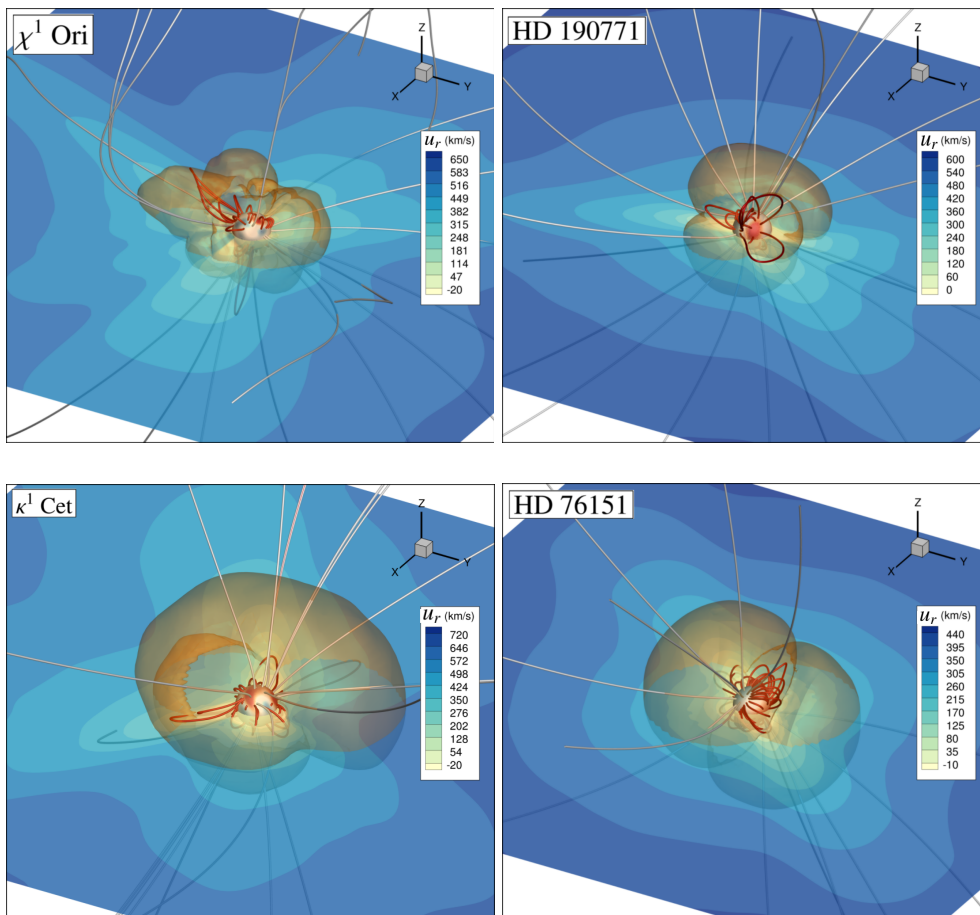


Figure 5.2: Steady state solutions for the simulated winds of the solar analogues. The translucent slice through the $z=0$ plane shows the wind radial velocity (u_r). Open and closed magnetic field lines are shown as grey and red streamlines respectively. Magnetic polarity is shown on the stellar surface as a red-blue diverging contour. The orange surface shows the Alfvén surface, where $u_r = u_A$, the Alfvén velocity. Note that the faster rotators have much less uniform, dipolar Alfvén surfaces, due to the less uniform magnetic fields topologically, at their surfaces.

solar-type stars would drop off substantially for slow rotators, causing older solar-type stars to rotate faster than expected. This would explain the findings of Van Saders et al. (2016), who observed a set of ageing solar-like stars and discovered that they rotated at much faster rates than expected by the traditional Skumanich age-rotation relationship.

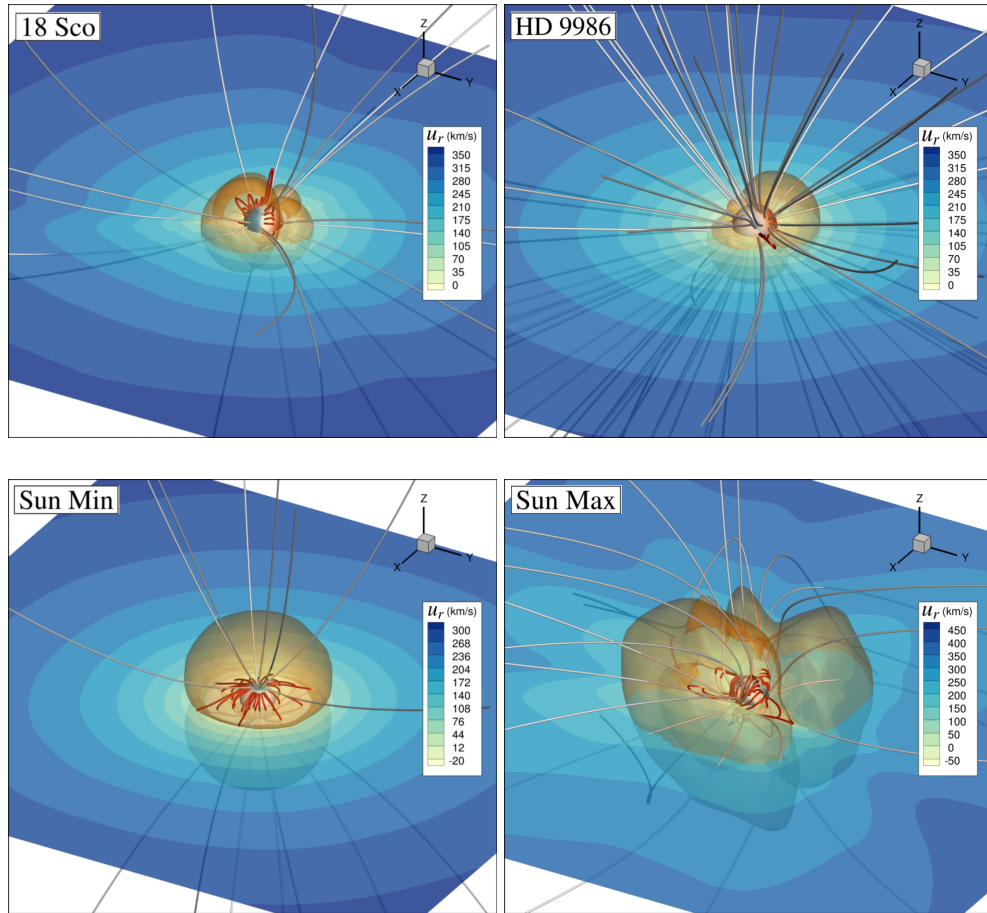


Figure 5.2: (cont.) Steady state solutions for the simulated winds of the solar analogues, showing the slower rotators in our sample.

In our previous work, [Ó Fionnagáin & Vidotto \(2018\)](#), we linked the anomalous fast rotation at older ages to the drop in mass-loss rates at older ages, and consequently, to a drop in the angular momentum-loss rate. Unfortunately, we could not verify this drop in angular momentum for slower rotators, as we do not have magnetic field maps for solar-mass stars that rotate much slower than the Sun. The lack in magnetic field maps in this regime can be explained observationally as detecting weak magnetic fields in slowly rotating stars is very challenging. Therefore, we compare mass-loss rates calculated here using the faster rotators. Figure 5.3 shows the mass-loss rate (red points) and the fit to these points (red line) which follows the relationship

$$\dot{M} = 4.7(\pm 0.1) \times 10^{-13} \left(\frac{\Omega_{\star}}{\Omega_{\odot}} \right)^{1.4 \pm 0.2} M_{\odot} \text{yr}^{-1}. \quad (5.1)$$

The fit to the faster rotators from Ó Fionnagáin & Vidotto (2018) (shown as a dotted black line), which possesses the power law index of 1.4, agrees within the error to the power law index fit here of 1.6 ± 0.2 . It is interesting that these mass-loss rates agree so well considering the base density of the 3D simulations is 3 times higher than in Ó Fionnagáin & Vidotto (2018). This suggests that the inclusion of a magnetic field in the 3D simulations would generate a much lower mass-loss rate than in the 1D simulations, given the same base densities. This is most likely due to closed magnetic regions, which act to hold in material, and reduce \dot{M} .

We also determine \dot{J} from our simulations as shown in Equation 2.38. The integral is performed over a spherical surface (S) in a region of open field lines. From Figure 5.3 we see a trend of decreasing \dot{J} towards slower rotating stars. We note that while the solar minimum simulation has a reasonable angular momentum loss rate, we find that the solar maximum simulation has a higher \dot{J} than expected (see e.g. Finley et al. 2018).

The magnetic field geometry and strength affect the wind in these simulations as it evolves, by establishing a pressure and tension against the ionised plasma. Here we calculate how much of the wind consists of open and closed field lines, by integrating the unsigned magnetic flux passing through a surface near the outer edge of our simulation domain, where all the field lines are open

$$\Phi_{\text{open}} = \oint_{S_{\text{sph}}} |B_r| dS. \quad (5.2)$$

The open flux of the wind, Φ_{open} , is relevant as regions of open flux are the origin of the fast solar/stellar wind (Verdini et al., 2010; Réville et al., 2016; Cranmer, 2017). It is also related to how efficient the wind is at transporting angular momentum from the star (Réville et al., 2015). In Figure 5.3 we see that across the rotation periods of our sample, open flux decreases as the stars spin down. There is also a hint of an open flux plateau in the faster rotators. In Table 5.1, we also present the ratio f of open to unsigned surface magnetic field flux (Φ_{surf}), following the convention: $\Phi_{\text{surf}} = f \Phi_{\text{open}}$.

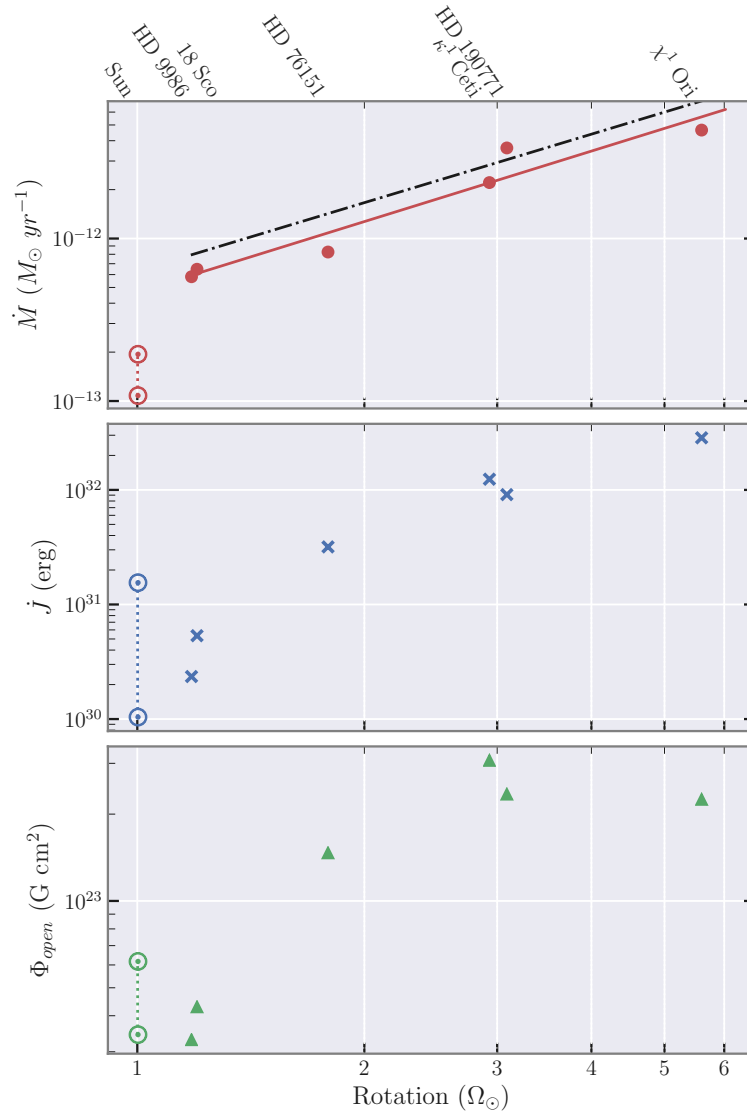


Figure 5.3: Top to bottom, the three panels above show the mass-loss rate, angular momentum-loss rate, and unsigned magnetic open flux from our sample of simulations. The stars are labelled at the top of the figure, with the solar simulations represented by the solar symbol (\odot), where activity maximum is always on top. In the top panel we include a fit to the data (red line, excluding the Sun) and compare this to the fast rotator fit as described in Ó Fionnagáin & Vidotto (2018) (black dashed line).

5.3 EVOLUTION OF THE RADIO EMISSION WITH AGE

Using Equations 3.10, 3.11, 3.14 and 3.15 we calculate 2D images for each frequency (cube of data) for the intensity and optical depth, across the plane of the sky, showing the intensity attributed to different regions of the wind, and the optical depth associated with it (see Chapter 3 and Figure 3.4). This is represented in Figure 5.4. Note that for comparison we calculate solar wind radio emission at a distance of 10 pc. We can see that the intensity of the emission increases as we increase the frequency, although it radiates from a much smaller region. This is due to the decrease in the optical depth with frequency and allows us to see further into the wind to much denser regions giving rise to more emission. The optical depth of the wind will have a major impact on the observations of these winds. Low optical depths allow emission from the low corona to escape and be detected, these regions are contaminated with other forms of radio emission, likely dominant, such as chromospheric emission and flaring. However, [Lim & White \(1996\)](#) suggest that we still can provide meaningful upper limits to the mass-loss rate of the star if a flare is detected as one must assume a maximum base density to the wind, therefore constraining mass-loss rates. From the intensity we can calculate the flux density (S_ν) of the wind as,

$$S_\nu = \frac{1}{d^2} \int I_\nu dA = \frac{1}{d^2} \sum^{i,j} I_\nu \Delta i \Delta j \quad (5.3)$$

where A is the area of integration, d is the distance to the object, and i and j denote the coordinates in our 2D image of I_ν values. Δi and Δj represent the spacing in our grid in the i and j directions. In this calculation we have assumed that the angle subtended by the stellar wind is small, therefore $d\Omega = dA/d^2$.

Table 5.2 shows the main results from our radio emission calculation, giving values for the expected flux density, from each star at 6 GHz. Figure 5.5 shows the spectrum of

Table 5.2: Predicted radio emission from our stellar wind models. Example fluxes at a frequency of 6 GHz are given ($S_{6\text{GHz}}$), in this case we find that all of the winds would be optically thin at this frequency. The power law fit to the spectra was conducted between 0.1 and 1 GHz, giving the coefficient (S_0) and power index (ϕ). However, the spectral slope between these two frequencies varies substantially, tending to shallower slopes at higher frequencies. Depending on the fitting range, slopes can range from 0.6 to 1.5. All slopes tend to -0.1 in the thin regime. The final column gives the frequency at which each wind becomes optically thin (ν_{thin}).

Star	$S_{6\text{GHz}}$ (μJy)	S_0	ϕ	ν_{thin} (GHz)
χ^1 Ori	8.28	2.78	1.26	2.80
HD 190771	0.73	0.39	1.32	1.85
κ^1 Ceti	2.83	1.67	1.35	2.13
HD 76151	0.55	0.37	1.41	1.61
18 Sco	0.60	0.40	1.40	1.63
HD 9986	0.19	0.13	1.42	1.63
Sun max (10 pc)	0.94	0.63	1.55	2.01
Sun min (10 pc)	0.93	0.62	1.47	2.00

each stellar wind for the range of frequencies 0.1-100 GHz. Our calculation uses actual density distribution in the simulated wind to find the optical depth and the flux density. We obtain a spectrum in the optically thick regime, leading to a power law fit which is related to the density gradient in the wind. Another result of using a numerical model is that the radio photosphere (R_ν), calculated at a distance where $\tau = 0.399$, is not spherical, but changes with the density variations in the wind, causing anisotropic emission, as evident from Figure 5.4 (dashed contours). Note that these radio winds are not resolvable with current radio telescopes but should indicate how the radio photosphere in the wind changes with frequency, and the anisotropy of the specific intensity, I_ν , in the wind. We also provide a power law fit to the optically thick regime of the radio emission (from 0.1-1 GHz) and note that it can vary quite significantly, depending on what range of frequencies is being fitted. In Table 5.2 we show the fit parameters we find according to

$$S_\nu = S_0 \nu^\phi. \quad (5.4)$$

Our radio calculations give an insight into the expected emissions from solar-type stars. We see that, at the appropriate sensitive frequencies for radio telescopes such as the VLA,

the winds all exhibit similar spectrum shapes. Figure 5.5 shows the spectrum for each star, using different colours as depicted in the legend. We show that the upper limits set by Fichtinger et al. (2017) (black arrows) are consistent with our estimations of the wind emission for κ^1 Ceti: our values are 3 times lower than these upper limits. χ^1 Ori is detected by Fichtinger et al. (2017), but they attribute this emission to the chromosphere and other sources as the star was observed to flare during the observation epoch (we discuss detection difficulties further in Section 5.5). Indeed, Figure 5.5 shows the detected emission occurs within the optically thin regime of the spectrum according to our models and at approximately 20 times higher flux density than we predict for the stellar wind emission. This supports the deduction that these detections are from other sources, and not the thermal wind. Fichtinger et al. (2017) estimated the thermal wind emission to possess a flux of $1.3 \mu\text{Jy}$ at 10 GHz, which agrees quite well with our calculation of $0.77 \mu\text{Jy}$. If the emission seen at $100 \mu\text{Jy}$ by Fichtinger et al. (2017) were coming from the stellar wind, our models would require a base density 5 times larger ($\approx 10^{10} \text{cm}^{-3}$). With this, we can actually infer that the mass-loss rate of χ^1 Ori is smaller than $1.4 \times 10^{-11} M_{\odot} \text{yr}^{-1}$, showing that even non-detections of stellar wind radio emission can still provide meaningful upper limits for the mass-loss rates. If we normalise the spectra shown in Figure 5.5 to remove the distance dependence, upon which the spectrum relies very heavily, we see that the younger more rapidly rotating stars display a higher flux density than the more evolved stars Figure 5.6. The Sun in this case would possess the weakest emission.

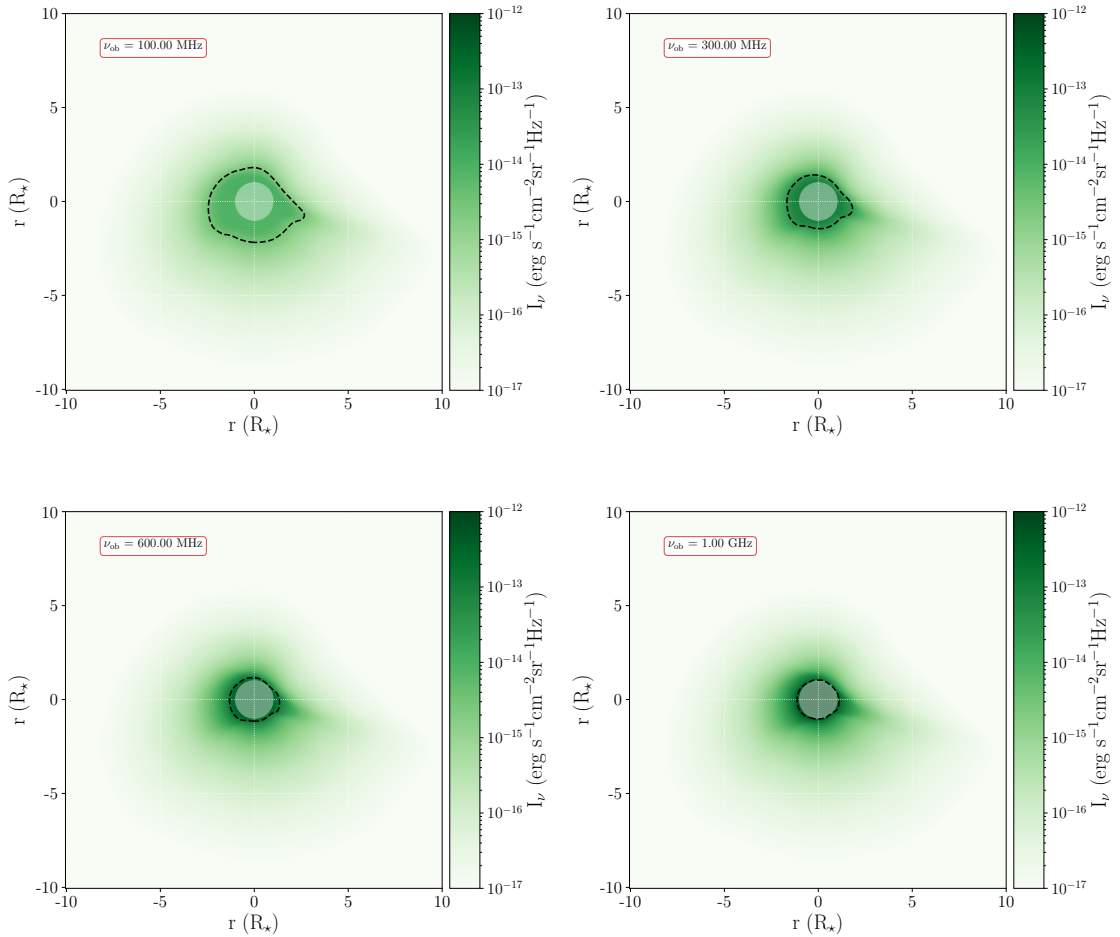


Figure 5.4: Example of intensity and optical depth for κ^1 Ceti at observing frequencies of 100 MHz (top left), 300 MHz (top right), 600 MHz (bottom left) and 1 GHz (bottom right). The green colour scale represents the intensity of emission from the wind, looking along the line-of-sight of our simulation grid. The dashed black contour represents the region where the wind becomes optically thick, according to [Panagia & Felli \(1975\)](#), $\tau = 0.39$. We can see that the emission is anisotropic due to the anisotropy of the wind density and temperature. The intensity reaches a maximum in the thin regime, as we can see emission from the entire wind. The white circle denotes $R = 1 R_\star$. Plasma in front of the star still emits in radio, but we have excluded any contribution from behind the star along the line-of-sight.

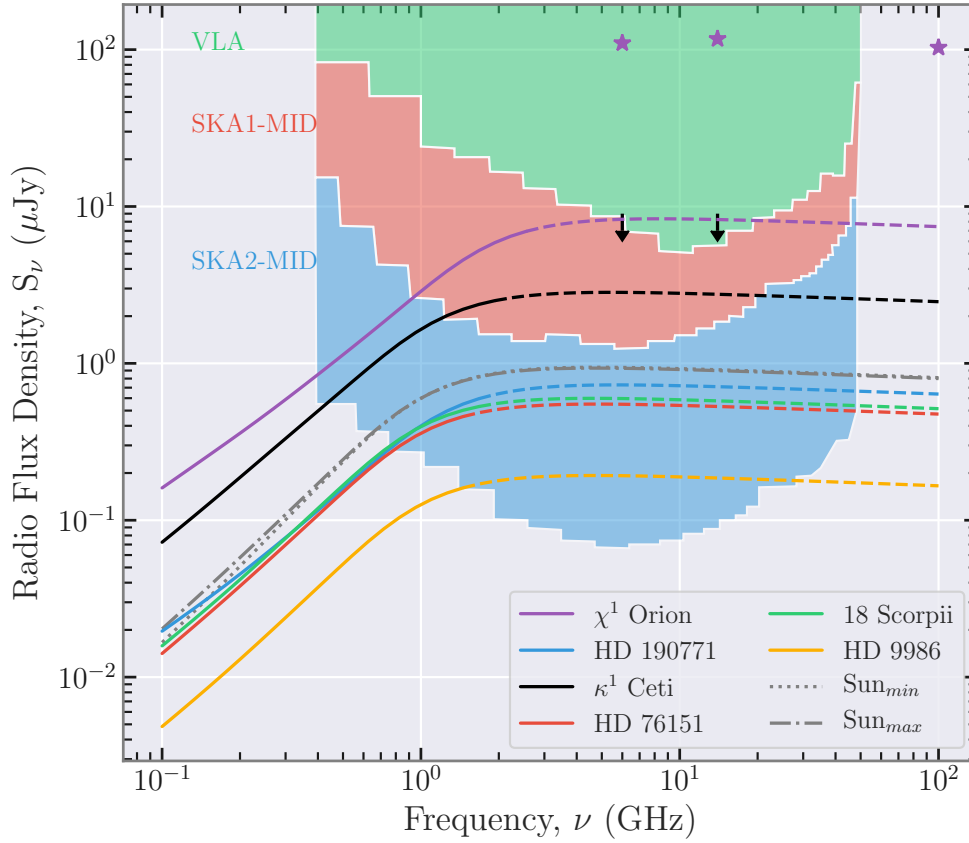


Figure 5.5: The calculated radio spectra for each wind are very similar in shape. Differences in flux density are strongly affected by distance to the object. The dashed lines represent the optically thin part of each spectrum, and there are differences in where the emission becomes optically thin from star to star at the frequency ν_{thin} . The black arrows indicate the observational upper limits of κ^1 Ceti found by [Fichtinger et al. \(2017\)](#). From the same work we mark the chromospheric detections of χ^1 Ori (purple stars), using both VLA and ALMA, which is concluded to originate from chromospheric emission. Our results show this conclusion to be valid as we predict the wind to emit at much lower fluxes. Sensitivities of the current VLA and future SKA1-MID and SKA2-MID are included shaded in green, red, and blue respectively (SKA sensitivities from [Pope et al. 2019](#) and adjusted for 2 hour integration time).

5.4 EVOLUTION WITH MAGNETIC CYCLE

In Figure 5.6 we calculate the expected radio emission from our solar maximum and solar minimum simulations assuming a distance of 10 pc (grey lines) to give an impression of the differences between the radio emission of the winds and the detectability of each star. We show that the thermal quiescent radio flux does not change substantially across a solar magnetic cycle. This is because the radio emission is heavily dependent on the density of the medium and both solar simulations have the same base density. Occurring mostly in the optically thick regime, the slight spectral differences are a consequence of the different magnetic fields causing different density gradients in the wind. For there to be substantial differences in thermal radio emission from a star displaying cyclic magnetic behaviour there would need to be a dramatic change in global density at the base of the wind. Note that the emission calculated here is quiescent wind emission and is the same in both the solar maximum and minimum cases. Non-thermal radio emission, such as 10.7 cm emission, is linked to solar activity and varies through the solar activity cycle (Solanki et al., 2010).

5.5 WIND DETECTABILITY IN RADIO

The density low in the stellar atmosphere (chromosphere, photosphere) is much higher than the stellar wind density. Radio emission from the lower atmosphere should dominate the emission in the optically thin regime of the stellar wind. This would most likely drown out any emission from the wind in the upper atmosphere and make detection of the wind impossible. However, as pointed out by Reynolds (1986), if the wind is entirely optically thin and emission is deduced to emanate from the lower stellar atmosphere, this can aid in placing limits on the stellar winds density and therefore the mass-loss rate of the star (cf. end of Section 5.3).

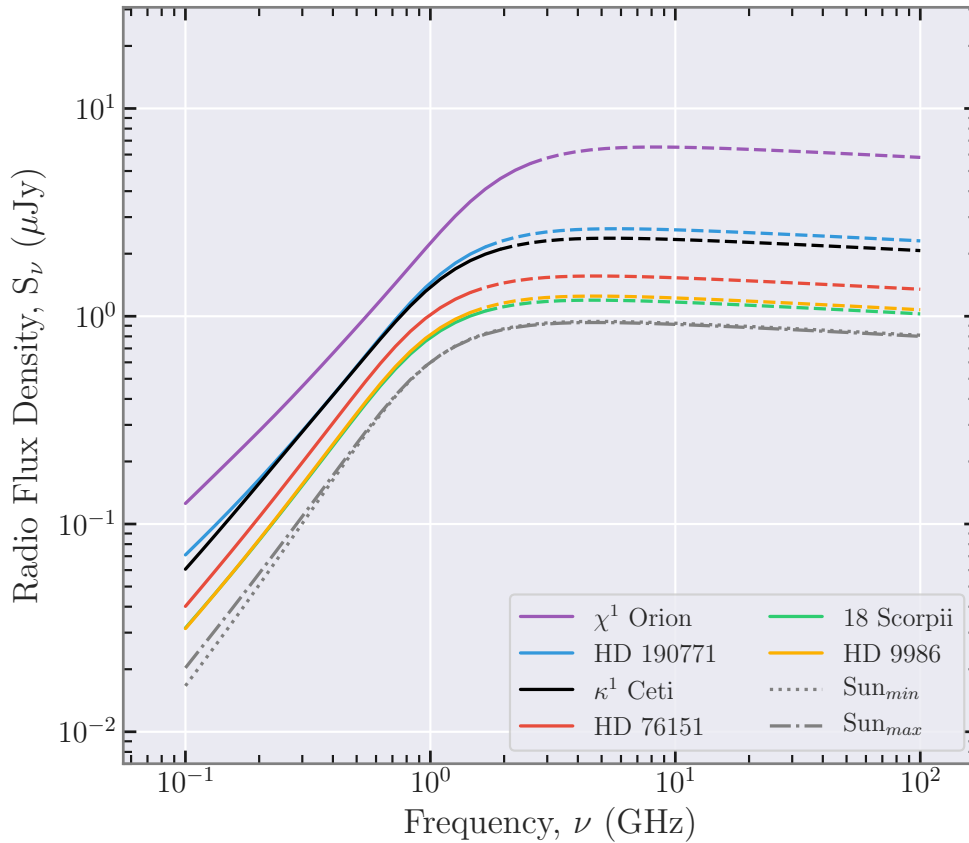


Figure 5.6: Here we normalised spectra in the top panel to a distance of 10 pc. This allows direct comparison of radio emission to an ageing solar wind. As the stars age and spin down the radio emission decreases by an order of magnitude between 500 Myr and 4.6 Gyr.

There have been many observations of solar-type low-mass stars in the radio regime (Güdel et al., 1998; Gaidos et al., 2000; Villadsen et al., 2014; Fichtinger et al., 2017), many of which have placed upper flux densities and mass-loss rates on the winds of these stars. Both Gaidos et al. (2000) and Fichtinger et al. (2017) used the VLA to observe a set of solar analogues, some of which overlap with the stars we have simulated here, placing tight constraints on the wind of κ^1 Ceti. Figure 5.5 displays the sensitivity of the VLA (purple shade) given some typical observational parameters (2 hour integration time, 128 MHz bandwidth) taken at central band frequencies. We show that the VLA is currently not sensitive enough to detect the winds simulated here. Villadsen et al. (2014) observed four nearby solar-like stars using the VLA (X, Ku and Ka bands, at 10 GHz, 15 GHz, and 34.5 GHz centre frequencies respectively). The authors find detections for all objects in the Ka band but can only provide upper limits to flux density for

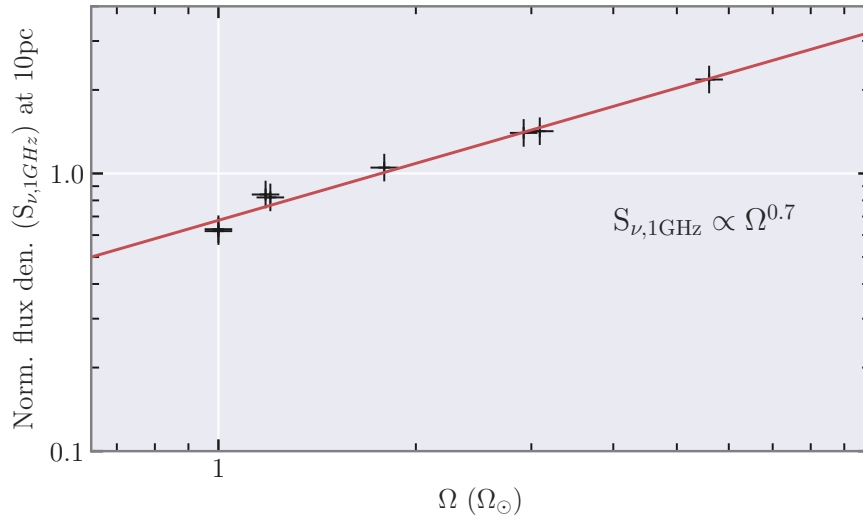


Figure 5.7: Normalised flux density at 1 GHz as a function of stellar rotation. We see a tight fit to this power-law (see Equation 5.5), with an almost linear dependence of stellar wind radio flux on stellar rotation at 1 GHz. Note that this relationship is strongly dependent on the observational frequency.

the other frequency bands. They conclude (similarly to Fichtinger et al. 2017) that all detections come from thermal chromospheric emission, and the upper limits set at lower frequencies infer rising spectra and therefore there is an optically thick regime at these frequencies.

In the future, upgrades to the existing VLA system (ngVLA, see Osten et al. 2018) could increase instrument sensitivity by a factor of 10. This increase in sensitivity means that stars simulated here, such as χ^1 Ori or κ^1 Ceti, would be detectable in their thin regime. The Square Kilometre Array (SKA) project is a future low-frequency radio telescope that will span a large frequency range. The expected sensitivity level of the future SKA1-MID and SKA2-MID telescopes (with a typical 2 hour integration time¹) are shown in Figure 5.5, shaded in red and blue (sensitivities for SKA taken from Pope et al. 2019, but adjusted to account for a 2 hour integration time). Given these sensitivities one could potentially directly detect the winds of χ^1 Ori and κ^1 Ceti using the SKA, below 1 GHz. This sensitivity level (sub- μ Jy) means other possible solar analogues not simulated here could also be detected, provided they are close enough. First light for SKA1-MID is expected after the mid 2020's.

¹ https://astronomers.skatelescope.org/wp-content/uploads/2016/05/SKA-TEL-SKO-0000002_03_SKA1SystemBaselineDesignV2.pdf

We show in Figure 5.6 that the faster rotators emit more flux. In Figure 5.7, we present the normalised flux density at 1 GHz and at a distance of 10 pc as a function of rotation rate. We found that

$$S_{\nu,1\text{GHz}} = 0.68 \left[\frac{\Omega}{\Omega_{\odot}} \right]^{0.7} \left[\frac{10\text{pc}}{d} \right]^2 \mu\text{Jy}. \quad (5.5)$$

Note that this exact relationship, and the rotation index, is heavily dependent on the observing frequency, but all exhibit the same increasing trend with rotation. This is due to different density structure in different winds, which depends on the stellar rotation and magnetic field strength, causing a different spectral slope in Figure 5.6. Important to note when considering these effects is the heavy dependence on stellar distance, which remains the dominating factor. Consequently, younger, rapidly rotating stars within a distance of 10 pc will be the most fruitful when observing thermal radio emission from stellar winds.

The work from this chapter is concluded in Chapter 9. I simulated the winds of a group of solar-type stars spanning ages across the MS, from 0.5–4.6 Gyr. This allowed insight into the trends for mass-loss, angular momentum-loss, open flux, and planetary environments as solar-type stars evolve throughout their MS lifetimes. The results I found are useful for those researching solar-mass stellar evolution, through stellar winds, magnetic fields, activity markers, rotation or age. Including the research conducted into planets orbiting solar-mass stars, their evolution through atmospheres and magnetospheres. I calculated the expected radio flux density for each of our wind sources, comparing them to current radio telescopes, showing that stars with higher rotation rates are expected to produce the most flux. In the future, large-scale projects such as SKA-2, should allow many solar-mass stellar winds to be detected, thereby constraining the stellar mass-loss rates. This research of solar-mass stellar winds across the MS lays the ground-work for research into solar-mass stellar winds that are *not* still on the main sequence. Leading to our next body of research in Chapter 6.

λ ANDROMEDAE: THE SOLAR WIND POST-MAIN SEQUENCE

Stellar atmospheres are highly dynamic environments that change on timescales varying from milliseconds (e.g. flares) to giga-years (e.g. spin-down). We expand upon our previous work and focus on the long timescale evolution of solar-type stars by simulating the wind of λ Andromedae, to infer the future evolution of our Sun. This G8 IV type star has a mass of $1.0 \pm 0.2M_{\odot}$, a radius of $7.0 \pm 0.7R_{\odot}$, a rotation rate of 54 days, and exists at a distance of 24.2 pc (Table 6.1). It is a well studied star with X-ray (Audard et al., 2003; Drake et al., 2011), EUV (Baliunas et al., 1984; Dupree et al., 1996; Sanz-Forcada et al., 2003), optical (Frasca et al., 2008), interferometric imaging (Parks et al., 2015), and radio observations (Bath & Wallerstein, 1976; Bowers & Kundu, 1981; Lang et al., 1985). This makes λ And a good candidate for an old solar proxy as we can draw physical constraints from past observations.

Results from this chapter have been submitted to MNRAS for publication under the title, “ λ Andromedae: The solar wind post main sequence”.

6.1 λ ANDROMEDAE IN CONTEXT

Cool stars that have evolved off the main sequence can be split into three distinct groups based on their coronae (formerly two groups, dividing line from [Linsky & Haisch 1979](#); [Drake & Linsky 1986](#)); sun-like stars with hot coronae, warm/weak coronal stars, and cold stars without coronae ([Linsky & Haisch, 1979](#); [Ayres et al., 2003](#); [Cranmer & Winebarger, 2019](#)). Simply by placing λ And on a HR-diagram we know that, while somewhat evolved with a radius of $7.0 R_{\odot}$, it has not yet lost its hot corona (Figure 6.1). Additionally, X-ray observations show that λ And fits into the hot corona category as its spectrum shows hot line formations ([Linsky & Haisch, 1979](#); [Drake et al., 2011](#)). [Ortolani et al. \(1997\)](#) showed that the coronal temperature should exist around 0.9 keV (≈ 10.4 MK), while [Sanz-Forcada et al. \(2003\)](#) found that during quiescence, the plasma temperature is closer to 7.9 MK. As a broad rule, stars in the ‘Hot Corona’ region tend to have mass-loss rates $10^{-10} M_{\odot} \text{ yr}^{-1}$ and terminal velocities of $\approx 100 \text{ km s}^{-1}$. Stars to the right of this divide, with ‘No Corona’, usually show mass-loss rates of $< 10^{-8} M_{\odot} \text{ yr}^{-1}$, and terminal velocities of $< 40 \text{ km s}^{-1}$ ([Drake & Linsky, 1986](#); [O’Gorman et al., 2018](#)). Figure 6.1 shows a roughly smooth transition between these two scenarios however, giving rise to an intermediate ‘Hybrid’ scenario, where the stars show signs of warm/weak coronae, perhaps giving rise to partially ionising winds, and having a combination of wind driving mechanisms.

[Müller et al. \(2001\)](#) and [Wood et al. \(2002\)](#) derived a mass-loss rate for λ And indirectly through Ly- α absorption of excess neutral hydrogen build-up between the stellar wind and the astrosphere. [Wood \(2018\)](#) found a mass-loss rate of $1 \times 10^{-13} M_{\odot} \text{ yr}^{-1}$, although the authors claim the detection is uncertain. More recent work suggested an even lower mass-loss rate of $2 \times 10^{-15} M_{\odot} \text{ yr}^{-1}$. This is unexpectedly low compared to

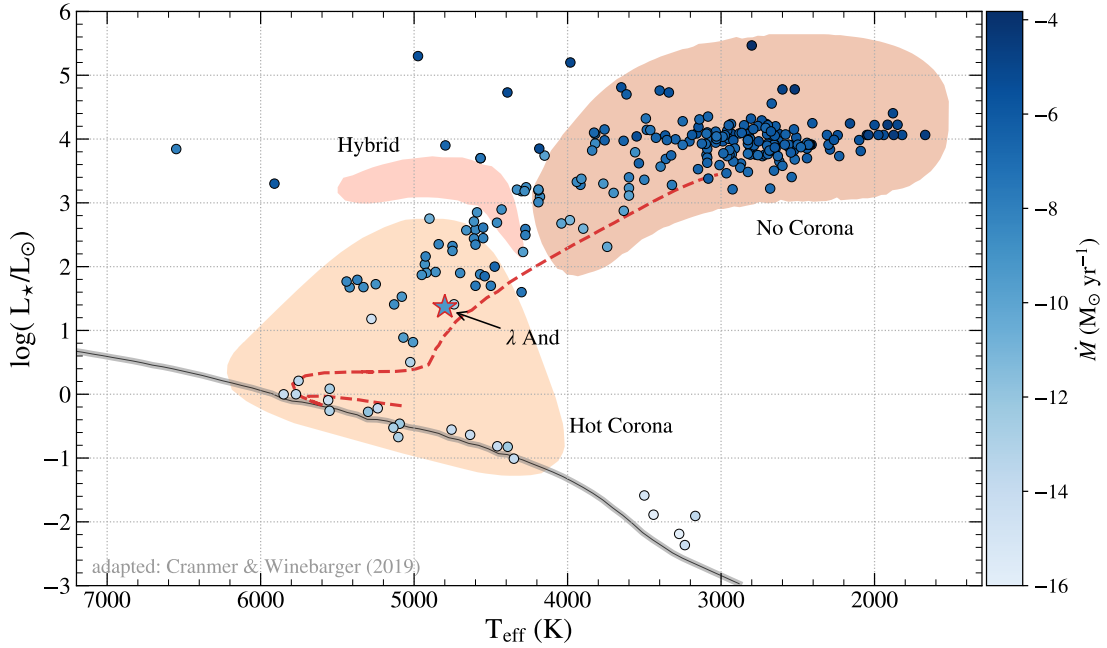


Figure 6.1: This is an adapted figure from [Cranmer & Winebarger \(2019\)](#). It shows the evolution of stellar mass-loss rates as low-mass stars evolve off the main sequence and become red giants. We contextualise the evolution of λ And, shown over-plotted (red outlined star symbol). We see that although λ And has begun to expand, it is still a sub-giant and retains its hot corona. Stellar mass-loss rate is shown as a blue scale. The grey line shows the zero-age main sequence, with filled regions shown for stars presenting hot corona, no corona, and a hybrid wind scenario ([Linsky & Haisch, 1979](#); [Hartmann & MacGregor, 1980](#); [Ayres et al., 2003](#)). The dashed red line shows the $1 M_\odot$ evolutionary track from [Drake et al. \(2011\)](#).

the previously mentioned mass-loss rates for post-main sequence stars, and is a much lower mass-loss rate per unit surface area than the Sun itself.

A particularly promising technique to constrain low-mass stellar winds is to use radio observations of the thermal bremsstrahlung from the ionised winds ([Panagia & Felli, 1975](#); [Wright et al., 1975](#); [Lim & White, 1996](#); [Villadsen et al., 2014](#); [Fichtinger et al., 2017](#); [Vidotto & Donati, 2017](#); [Ó'Fionnagáin et al., 2019](#)). While stars along the main sequence possess winds too tenuous to detect with current instrumentation, the increased mass-loss rates of the more evolved low-mass stars provide a more attainable target (eg. [O'Gorman et al. 2017](#)). There have been many radio observations of λ And, [Bath & Wallerstein \(1976\)](#); [Bowers & Kundu \(1981\)](#) and [Lang et al. \(1985\)](#) all presented detected radio flux densities ranging from 0.84 – 65 mJy across the frequency range 2 – 8 GHz. We use the [Bowers & Kundu \(1981\)](#) and [Lang et al. \(1985\)](#) value of ≈ 0.85

Table 6.1: Physical parameters of λ And from [Drake et al. \(2011\)](#)

$M (M_{\odot})$	$R (R_{\odot})$	$\log(L_{\star}/L_{\odot})$	$T_{\text{eff}} (\text{K})$	$P_{\text{rot}} (\text{d})$	$d (\text{pc})$
1.0 ± 0.2	7.0 ± 0.7	1.37	4800	54	24.2 ± 0.3

mJy at 4.5 – 5 GHz as a benchmark for our work presented here as they are at similar observation frequencies, and their observed flux densities agree with each other.

We present the first surface magnetic field observations of λ And and detect a strong magnetic field for such an evolved star. These observations, carried out on the Narval spectropolarimeter, allow us to constrain the surface magnetic field of λ And. These derived surface magnetic fields can constrain the lower boundary of the 3D magneto-hydrodynamic wind simulations that we run. Usually, we see a decay in magnetic field strength as solar-type stars evolve as their activity decreases along with their rotation ([Skumanich, 1972](#); [Vidotto et al., 2014b](#); [Booth et al., 2020](#)). However, this sub-giant star seems to have a relatively strong large-scale magnetic field compared to the Sun. The exact process through which this star would reach this stage in its evolution with such a magnetic field are yet unknown. Potential reasons are that it began with a much stronger dynamo in its past than anticipated, or perhaps the secondary companion had some effect on the primary star at a point in the past. λ And differs from the Sun as it is a RS Canum Venaticorum (RS CVn) variable, meaning it is a variable binary system and it is comparatively metal-poor ([Drake et al., 2011](#)). For the purposes of this work, we assume the binarity of this system will not effect our results, as the variability on this star is most likely due to stellar rotation or strong magnetic activity ([Drake et al., 2011](#)) and not caused by the orbit of the binary system, as is the typical case for classical RS CVn stars. We do not include the effects of different metal abundances on the stellar wind and stellar evolution, but the effects of which have been examined in other works ([Suzuki, 2018](#)).

In this work we employ two 3D MHD wind models, using BATS-R-US ([Powell et al., 1999](#); [Sokolov et al., 2013](#); [van der Holst et al., 2014](#)), including the stellar magnetic field, with which we aim to more accurately replicate the observed radio flux. We provide two cases for the stellar wind, a “hot” and “cold” case. As stars become

older they cool significantly, this cooling means they no longer have a hot corona to drive their stellar winds in the form of thermal acceleration. Despite this, the mass-loss rate of these stars dramatically increases by many orders of magnitude (see Figure 6.1). Therefore it is expected that in these cool evolved scenarios the wind is driven by waves, predominantly Alfvén waves. It is also possible that winds form some sort of hybrid wind, with characteristics from both a coronal driven hot wind, and cold wave-drive wind. In this work our hot and cold models include a polytropic thermally driven wind and an Alfvén wave driven wind respectively. We use these two different models to find which one better reproduces the radio observations of λ Andromedae.

In Section 6.2 we discuss the spectropolarimetric observations of the star and the results from Zeeman Doppler Imaging. We discuss the types of models that we use to describe the wind of λ And in Section 6.3, all of which are described in Chapter 2. In Sections 6.4 and 6.5 we discuss the results of our simulations, the global parameters of the wind, the calculated radio emissions and how they compare to the observations. We conclude and summarise the work conducted in this paper in Section 9.3.

6.2 OBSERVED SURFACE MAGNETIC FIELDS

λ And was observed with the NARVAL high resolution spectropolarimeter installed on the Bernard Lyot Telescope (TBL, Pic du Midi Observatory, France, [Aurière 2003](#)) in the frame of the BritePol program ([Neiner et al., 2017](#)). The circular polarization mode of NARVAL was used to acquire the data, providing a simultaneous measurement of Stokes V and Stokes I over a wavelength domain extending from 370 nm to 1 μ m at a spectral resolution of about 65,000.

Each Stokes V sequence consists of 4 sub-exposures of 56 seconds each, obtained with different azimuthal angles of the half wave Fresnel rhombs in the polarimetric module ([Semel et al., 1993](#)). A Null polarization spectrum was also computed for each observation by destructively combining the 4 sub-exposures. This allows us to check

for any spurious signal in Stokes V that may have been produced by variable weather conditions, instrumental issues or non-magnetic stellar variations such as pulsations.

The full set of BritePol observations consisted of 6 measurements obtained in December 2013, 1 in January 2014, and 19 from August to October 2016. Our magnetic model was restricted to the 2016 data, as the permanent evolution of surface features on cool active stars similar to λ And prevents us from combining data obtained over more than a few weeks (see e.g. [Petit et al. 2004a](#) for the active subgiant primary of the RS CVn system HR 1099). We also removed from this time series the observation obtained on Aug 10, as the LSD method (see paragraph below) led to an abnormal outcome for this specific spectrum. The subset selected here offers a good basis for tomographic mapping, with a dense set of observations spread over most of one stellar rotation (assuming a period of 54 d, [Drake et al. 2011](#)). All data used in this article are publicly available in the PolarBase data base ([Petit et al., 2014](#)). Our set of Stokes V spectra do not exhibit any line signatures, which is typical of the relatively small amplitude of Zeeman signatures recorded in most cool active stars. As usually done in this situation, we make use of the Least-Square Deconvolution method (LSD hereafter, [Donati et al. 1997](#)) to extract an average, pseudo line profile of enhanced signal-to-noise ratio. To do so, we adopt a list of lines produced by a photospheric model ([Kurucz, 1993](#)) with stellar parameters close to those of λ And ($T_{\text{eff}} = 4800 \pm 100$ K and $\log g = 2.75 \pm 0.25$, [Drake et al. 2011](#)). We impose for the LSD pseudo-line profiles an equivalent wavelength of 650 nm, and an equivalent Landé factor of 1.21. The outcome is a time-series of Stokes I and Stokes V pseudo line profiles, with the systematic detection of a polarised signature at the radial velocity of the line (Section 6.2).

The surface magnetic field geometry was calculated with the Zeeman-Doppler Imaging (ZDI) technique ([Semel, 1989](#)). Enabled by the spherical harmonics expansion proposed by [Donati et al. \(2006\)](#), and the latest Python implementation of [Folsom et al. \(2018a\)](#). In this framework, the stellar surface is paved with rectangular pixels linked to a local line model. Following [Folsom et al. \(2018b\)](#), the local Stokes I line profile takes the form of a Voigt profile weighted according to a projection factor and linear

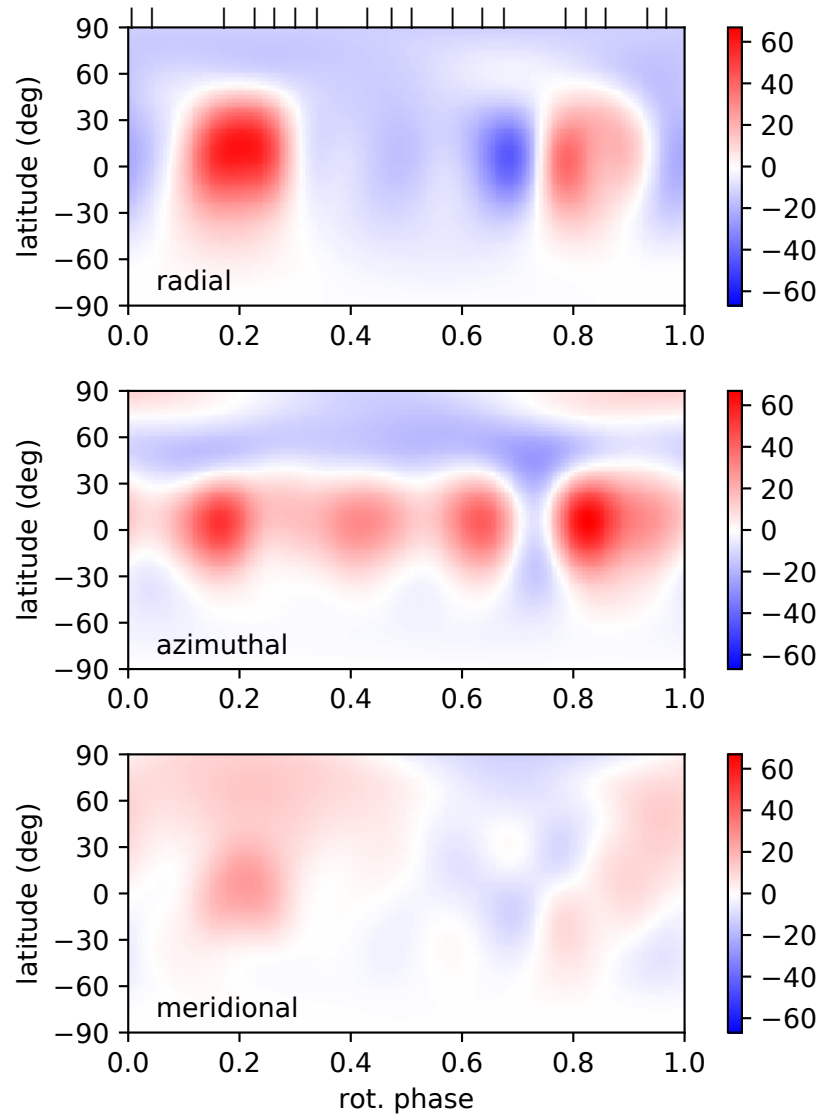


Figure 6.2: Large scale magnetic field geometry of λ And, as reconstructed with the ZDI method. From top to bottom, the three panels show the radial, azimuthal and meridional components of the photospheric magnetic field (in Gauss). The observed rotational phases are shown as vertical ticks above the radial field map.

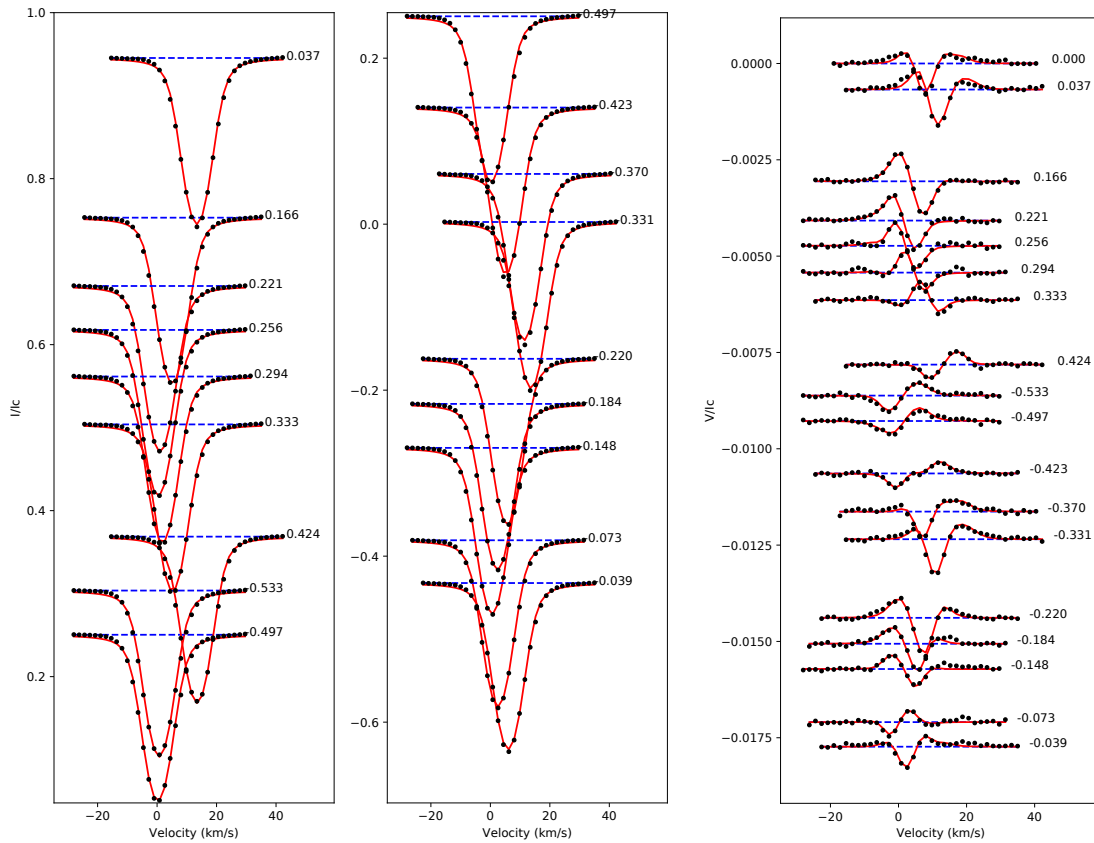


Figure 6.3: *Left & Middle:* Stokes I LSD pseudo-profiles of λ And (black points), overlaid with the set of synthetic Stokes I profiles produced by the ZDI model (red line). The profiles are vertically shifted for display clarity. The dashed blue lines show the continuum level, and the phases of observation are indicated on the right of every profile, assuming a 54 d rotation period, and taking our first observation as phase origin. *Right:* The same figure but for Stokes V profiles.

limb darkening coefficient (taken equal to 0.73, [Claret 2004](#)). Each local line profile is also Doppler shifted according to the local radial velocity produced by stellar rotation, assuming $v \cdot \sin i = 7.3 \text{ km.s}^{-1}$ ([Massarotti et al., 2008](#)). The local Stokes V line profile is computed from the local Stokes I profile and the local longitudinal field using the weak field approximation (where Stokes V is proportional to the first derivative of Stokes I). The global Stokes I and V profiles obtained after integrating over the visible stellar hemisphere are then Doppler shifted to follow the radial velocity variations produced by the orbital motion of the target. Our ZDI model includes spherical harmonics modes up to $\ell = 15$, as no noticeable improvement of the Stokes V fit is obtained when further increasing this number. The best ZDI model is obtained for an inclination angle equal to $71 \pm 2^\circ$, which is consistent (within uncertainties) with the estimate of [Donati et al. \(1995\)](#) (60^{+30}_{-10}). The sets of synthetic Stokes I and V profiles obtained with this ZDI procedure are illustrated in Section 6.2.

The resulting magnetic geometry is plotted in [Figure 6.2](#). Several magnetic spots are recovered and most of them are located near the equator (in both the radial and azimuthal field components). The maximum (local) field strength is equal to 83 G, while the average field strength is equal to 21 G. Most of the magnetic energy is reconstructed in the poloidal field component (64%), and most of the poloidal field is observed in low order spherical harmonics components, with about 78% of the poloidal magnetic energy in modes with $\ell \leq 3$. The low latitude azimuthal field forms a unipolar ring (of positive polarity), as already observed in several cool, evolved stars (e.g. [Donati et al. 2003](#); [Petit et al. 2004a,b](#)). We note that the rotation phases where the azimuthal field strength is large also have a strong radial field strength (around phase 0.2, and also between phases 0.6 and 0.9).

The reduced χ^2 obtained by the ZDI inversion is equal to 1.9, showing that our simple magnetic model cannot fully reproduce the shape of the observed Stokes V pseudo profiles. We assume here a solid rotation of the stellar surface, and this assumption is often the main limitation of ZDI models of cool stars, since the surface is expected to be differentially rotating. Following the procedure of [Petit et al. \(2002\)](#), we searched for

a progressive distortion of the magnetic geometry under the influence of a solar or anti-solar surface shear. This search was inconclusive, likely because our data set does not cover more than one rotation period. Another possible limiting factor is the continuous appearance and disappearance of magnetic spots, and the relatively large timespan of our data (slightly less than 2 months) is possibly responsible for some significant intrinsic evolution of the magnetic pattern.

To compare the surface magnetic field of λ And with the magnetic survey for evolved stars of [Aurière et al. \(2015\)](#), we have computed longitudinal field (B_l) values ([Rees & Semel, 1979](#)) for every observation included in the ZDI analysis. The maximal longitudinal field strength throughout the time series is $|B_l|_{\max} = 13.7 \pm 0.4$ G, in good agreement with $|B_l|_{\max}$ values reported by [Aurière et al. \(2015\)](#) at similar rotation periods. We therefore suggest that, although λ And is a member of a close binary system, the observed surface magnetic field strength is not noticeably influenced by the tidal interaction between the primary and its low-mass companion.

6.3 THE WIND OF λ ANDROMEDAE

We use two separate models to calculate the wind of λ And, and these are described in Chapter 2. We use both a polytropic model, similar to what we use in Chapter 5, and a wave driven model. The reasoning for this is discussed at length in this chapter. Ideally we would use a cold wave-driven model for a red giant star, but as we have previously discovered through the analysis of the H-R diagram, and observations of λ And, it is not yet a red giant, but more of a cooling sub-giant star. Therefore we use both the polytropic wind, which is a better representation for hot stellar winds, and the wave-driven model, which is a better representation of a cold giant wind, so that we can discuss which model fits the observations the best.

Table 6.2: Summary of our simulations. In the case of the cold model we have many iterations of the winds as we are varying the input Poynting flux (S_A) of the Alfvén waves and the proportionality constant for wave damping (ℓ) for different base wind densities. All cold simulations here possess a base temperature of 50,000 K, with a 1 MK base temperature for the hot wind scenario as the simulation begins embedded in the corona. Each lettered simulation denotes a different base density (n_{base}). The fiducial Poynting flux is $S_0 = 37 \text{ W m}^{-2} \text{ G}^{-1}$ and fiducial damping length $\ell_0 = 1.5 \times 10^5 \text{ m T}^{0.5}$.

Simulation Input					Simulation Output				
Sim	B field	$n_{\text{base}} \text{ cm}^{-3}$	$S_A [\text{W m}^{-2} \text{ T}^{-1}]$	$\ell [\text{m T}^{0.5}]$	$v_{\text{max}} [\text{km s}^{-1}]$	$T_{\text{max}} [\text{MK}]$	$\dot{M} [M_{\odot} \text{ yr}^{-1}]$	$f [\text{erg}]$	$\Phi_{\text{radio}} [\text{mJy}]$
A0	Dipole		S_0	ℓ_0	700	5.8	4.7×10^{-12}	3.1×10^{34}	0.005
A1	Dipole	1.5×10^{10}	$10 S_0$	ℓ_0	930	11	3.9×10^{-11}	1.1×10^{35}	0.011
A2	Dipole		S_0	$7 \ell_0$	817	6.6	4.1×10^{-12}	3.0×10^{34}	0.004
A3	Dipole		$S_0 / 10$	$7 \ell_0$	405	3.37	5.6×10^{-13}	1.6×10^{34}	0.004
B0	Dipole	1.5×10^{12}	S_0	$7 \ell_0$	765	5.7	3.7×10^{-12}	3.2×10^{34}	0.007
B1	Dipole		S_0	$253 \ell_0$	977	4.9	2.0×10^{-12}	2.5×10^{34}	0.008
C0	Dipole		S_0	$253 \ell_0$	497	4.4	1.9×10^{-11}	3.7×10^{34}	0.014
C1	ZDI	1.5×10^{13}	S_0	$253 \ell_0$	590	2.9	1.2×10^{-11}	9.8×10^{33}	0.014
C2	ZDI		$30 S_0$	$7 \ell_0$	619	4.3	1.7×10^{-10}	4.5×10^{34}	0.030
C3	ZDI		$S_0 / 10$	$253 \ell_0$	527	2.1	1.7×10^{-12}	3.0×10^{33}	0.007
D0	Dipole	1.5×10^{14}	S_0	$253 \ell_0$	765	5.6	4.0×10^{-12}	3.1×10^{34}	0.014
D1	Dipole		$S_0 / 10$	$253 \ell_0$	292	1.7	2.7×10^{-12}	1.8×10^{34}	0.013
Z0	ZDI	2.5×10^{10}	—	—	456	1.0	2.91×10^{-9}	2.2×10^{35}	0.890

*Base density calculated at the corona

6.3.1 *Hot wind model*

In this model, the inner boundary of the simulation begins in the corona of the star. We assume a polytropic index which drives the wind of the star by supplying energy to the wind. The polytropic index in the solar wind has been measured as $\Gamma = 1.1$ (Van Doorselaere et al., 2011), and many numerical solar wind simulations use $1 < \Gamma < 1.15$ (Keppens & Goedbloed, 1999b; Matt et al., 2012; Johnstone et al., 2015a,b), here we adopt a value of $\Gamma = 1.05$. BATS-R-US solves for 8 fluid quantities in this case: mass density (ρ), wind velocity ($\mathbf{u} = \{u_x, u_y, u_z\}$), magnetic field ($\mathbf{B} = \{B_x, B_y, B_z\}$), and gas pressure P . The equations that govern this model are shown in Section 2.3.

We take $\mu = 0.5$, which represents a fully ionised hydrogen wind. Polytropic index aside, the other free parameters are base coronal density, base coronal temperature, and base magnetic field. For this model we use $n_{\text{cor}} = 2.5 \times 10^{10} \text{ cm}^{-3}$ and $T_{\text{cor}} = 1 \text{ MK}$. The base magnetic field is constrained using ZDI observations, of which we only include the radial field component, B_r , in our simulations, which are thoroughly described in Section 6.2. Note that all parameters here equate to coronal values, as this is where the bottom of this simulation begins. We use a Cartesian grid, with the minimum resolution of $0.01 R_\star$ and a maximum resolution of $0.3 R_\star$, totalling 622672 blocks, or 3.98×10^7 cells. (Figure 2.4).

6.3.2 *Cold wind model*

The mathematical description of this model is described in Chapter 2. The inner boundary condition for this model is the stellar chromosphere (whether it exists for the star or not, its defining feature here is that it is much cooler and closer to the star than the corona). The cold wind model requires values to be set for free parameters, which range from the chromospheric density (n_{chr}), chromospheric temperature (T_{chr}), Alfvén wave Poynting flux (S_A), and the damping proportionality constant (ℓ). These physical pa-

parameters do not have direct constraints from observations although we can limit some of these parameters *a posteriori*. For example, selecting a base density that is too large could cause an unrealistically high mass-loss rate and the estimated radio emission could exceed observed levels (see Section 4.5). For our cold wind scenario we ran a number of simulations varying these base parameters, shown in Table 6.2. We began these simulations with a maximum dipolar magnetic field of 60 G, which is similar to the maximum field strength in the radial component of the ZDI map (Figure 6.2). This is a similar magnetic field strength to the average and maximum magnetic fields found in the ZDI map of λ And (Figure 6.2). Additionally, we ran a set of simulations using the ZDI map for the cold wind scenario, three of which are shown in Table 6.2: C1, C2, and C3.

Contrary to the hot wind simulation, the cold wind simulations reach a quasi-steady state. This occurs as the heating depends on the dissipation of Alfvén waves, which in turn depends on the magnetic field geometry and strength, the simulations tend to reach a point where they oscillate. In these cases, an average of the states is taken for the simulation parameters.

The SC module in the Alfvén wave-driven model uses a 3D spherical grid, with radial stretching from 1-30 R_\star . It also employs adaptive mesh refinement (AMR), adding extra refinement to the volume surrounding the current sheet. Radial stretching and AMR are quite efficient, increasing the resolution near the star and in required locations, without significantly increasing the number of cells in the simulation. The AMR is turned on for a single timestep after 100 timesteps to add refinement to the current sheet, which is the region where the magnetic field changes polarity and is susceptible to magnetic reconnection and high currents, which could cause issues in simulations without AMR. Our simulation mesh has $r_{\min, \max} = 0.0003, 1.25R_\star$ and $\phi/\theta_{\min, \max} = 0.025, 1.5R_\star$, resulting in an average of 45k blocks, and 4.3×10^6 cells (Figure 2.4).

6.4 POST-MS WINDS FROM MHD SIMULATIONS

As presented in Section 6.1, we have observational constraints on the wind of λ And that we use here to constrain the free parameters of our model. For example, the location λ And on the H-R diagram provides loose constraints on mass-loss rates based on studies of other evolved low-mass stars: 10^{-11} – 10^{-9} M_{\odot} yr^{-1} (see Figure 6.1, Linsky & Haisch 1979; Cranmer & Winebarger 2019). It is possible that λ And is transitioning from a hot corona to no corona implying it could have a “hybrid” wind, with mixed characteristics of the hot coronal winds and the cool wave-driven winds. However, the X-ray observations point more strongly towards λ And still showing signs of a hot corona (Ortolani et al., 1997; Sanz-Forcada et al., 2004; Drake et al., 2011), with maximum coronal temperatures of 7–10 MK. While giants more evolved than λ And usually possess winds with low terminal velocities (< 40 km/s Drake & Linsky 1986; O’Gorman et al. 2018), the presence of a hot corona is likely to lead to moderate terminal wind velocities ($\approx 300 - 400$ km s^{-1}), and mass-loss rates of 10^{-11} – 10^{-9} M_{\odot} yr^{-1} (Linsky & Haisch, 1979; Drake & Linsky, 1986). The aforementioned mass-loss rate derived from comparison to neighbour stars in the HR diagram, however, is at odds with the mass-loss rate derived in astrospheric observations, which can be as low as 2×10^{-15} M_{\odot} yr^{-1} and as high as 1×10^{-13} M_{\odot} yr^{-1} (Wood, 2018; Müller et al., 2001).

The several orders of magnitude differences in the mass-loss rates of λ And derived so far in the literature has led to us to use a different approach to constrain the wind of λ And, using radio observations. Radio emission from stellar winds provide us a direct detection of the wind (Bath & Wallerstein, 1976; Bowers & Kundu, 1981; Lang et al., 1985; Panagia & Felli, 1975; Wright et al., 1975), which limits the density adopted in our simulations and, consequently, the mass-loss rate (Vidotto, 2017; Ó Fionnagáin & Vidotto, 2018; Ó Fionnagáin et al., 2019). In the particular case of λ And there are detections of 0.86 mJy at 4.5 GHz (Bowers & Kundu, 1981) and 0.84 mJy at 5 GHz

(Lang et al., 1985), with older observations finding even higher radio flux from this source of 65 mJy at 5 GHz and 20 mJy at 8.1 GHz (Bath & Wallerstein, 1976). In this paper, we will use the more recent observations for comparison. Here, we aim to find a wind solution that matches as many of these constraints as possible, using our two numerical models. We take two separate approaches in this work to simulate the wind of λ And (Section 6.3). Our first approach, the hot wind model, begins at the base of the corona, with the thermal pressure and polytropic index determining wind acceleration and energy deposition. Our second approach, the cold wind model, begins at the chromosphere, with wind acceleration and heating determined by Alfvén wave dissipation. Our input parameters for our simulations are shown in Table 6.2, detailing the base wind density, base magnetic field (either the ZDI map or a dipolar field), the Poynting flux and damping length coefficient. The latter two parameters do not apply to the hot wind scenario. We derive some indicative output parameters of the simulations in Table 6.2, the most important of which are the mass-loss rate and radio flux density.

As can be seen in the last row of Table 6.2, we find quite an agreeable solution for the wind of λ And for our hot wind scenario using the BATS-R-US polytropic model. Our derived radio flux density of 0.89 mJy at a frequency of 4.5 GHz is very similar to the observed values of 0.86 mJy at 4.5 GHz and 0.84 mJy at 5 GHz (Lang et al., 1985; Bowers & Kundu, 1981). We will present more details of our radio emission calculation in Section 4.5. The simulation temperature and wind velocity are shown in Figure 6.4. This polytropic simulation displays a mass-loss rate of $2.9 \times 10^{-9} \dot{M}_{\odot} \text{ yr}^{-1}$ or 1.3×10^5 times the solar mass-loss rate. This value is much greater than astrospheric estimates ($2 \times 10^{-15} - 10^{-13} \text{ M}_{\odot} \text{ yr}^{-1}$, Müller et al. 2001; Wood 2018, even though our terminal wind velocities ($\approx 400 \text{ km s}^{-1}$) agree with the one adopted by these authors. Our mass-loss rate is more in line with the mass-loss rates of neighbour stars in the HR diagram (Figure 6.1). We also computed the angular-momentum loss from λ And, which amounts to $2.2 \times 10^{35} \text{ erg}$. While we have no good age estimates for λ And, other than it is more evolved than the Sun, it has a much stronger spin-down rate than the Sun $\approx 2 \times 10^5 \dot{J}_{\odot}$ (where $\dot{J}_{\odot} = 10^{29} - 10^{30} \text{ erg}$, Finley et al. 2018). It was previously

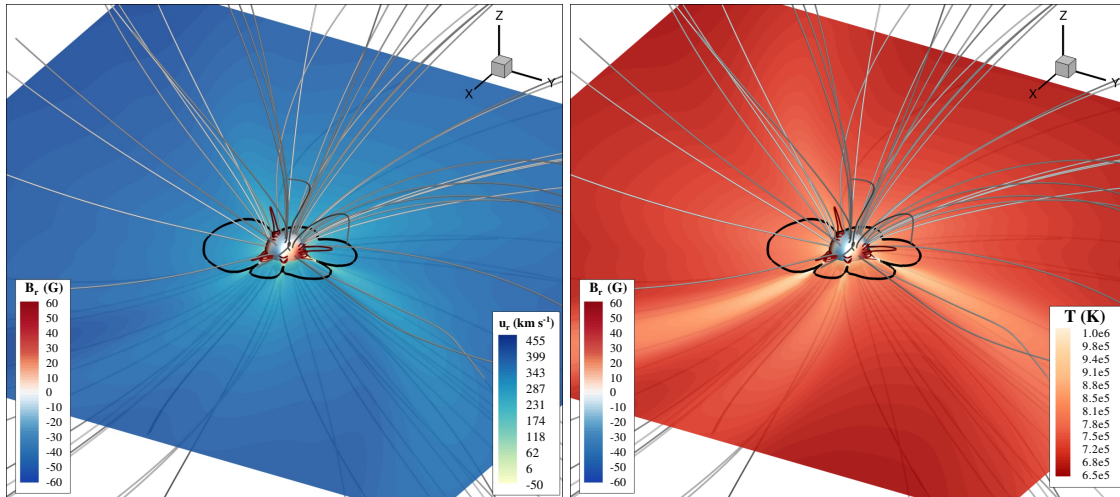


Figure 6.4: Result of our “hot” wind, a thermally driven, polytropic, 3D MHD simulation. *Left:* Wind velocities displayed along the equatorial plane (yellow-blue) *Right:* Wind temperatures displayed along the equatorial plane (orange-red). In both plots, surface magnetic fields are displayed in blue-red. Closed magnetic field lines are red, open magnetic field lines are grey. The Alfvén surface intersection with the x-y plane is shown as a black line.

believed that stellar rotation followed a simple power law with age (Skumanich, 1972), and this seems to hold true for main-sequence stars, but more recently it has been found that evolved stars do not follow this relationship (Van Saders et al., 2016; Booth et al., 2017; Ó Fionnagáin et al., 2019; Metcalfe et al., 2019; Metcalfe & Egeland, 2019). More research into the complex relationship of stellar rotation, age and their activity is needed for evolved stars before we can accurately say what is happening here.

Note that our polytropic wind model is unable to reproduce the high temperatures seen in X-ray observations. Similarly to the Sun, it is believed that X-ray emission originates in small-scale magnetic field, likely due to reconnection events (Priest, 2003; Aschwanden, 2004; Shibata & Magara, 2011; Lehmann et al., 2018). The X-ray emission is larger inside regions of closed field lines, with X-ray dark regions along open magnetic field lines, along which the solar wind propagates. Given that our simulations only account for the large scale magnetic field, it is not surprising that our simulations do not reach the largest temperatures observed in the closed corona.

Our second model, using the AWSOM code, results in relatively similar wind velocities, as can be seen in Table 6.2, and a much cooler wind structure outside of magnetic loop regions. An example of a cold wind model with a ZDI map at the lower bound-

Table 6.3: Compiled list of radio observations for λ And. We show each flux density (mJy) for observing frequencies (GHz).

ν [GHz]	Φ_{radio} [mJy]	Ref.
2.72	< 15	Bath & Wallerstein (1976)
5	65	Bath & Wallerstein (1976)
8.1	20	Bath & Wallerstein (1976)
5	0.84	Lang et al. (1985)
4.5	0.86	Bowers & Kundu (1981)

ary is shown in Figure 6.5, and another one with a dipolar field as the lower boundary condition is shown in Figure 6.6. Since the AWSOM code usually can not find a truly steady-state solution, we average the global variables over 1000 timesteps at the end of the simulation. Table 6.2 shows a compilation of the AWSOM models we ran. For our simulations we varied the Poynting flux (S_A), the damping length (ℓ), and the base wind density (n_{chr}). S_A alters the amount of energy the Alfvén waves begin with at the base of the simulation, which can then be dissipated into the wind. ℓ changes the damping length of the waves. Increasing the value of ℓ will cause the dissipation of energy to be much more extended, while a small ℓ value will cause much of the energy to be deposited lower in the wind near the chromosphere. The base density plays a large role in the final wind structure as many physical processes depend heavily on the density structure. The wave dissipation (Equation 2.46), and particularly the radiative cooling (Equation 2.43) have strong dependencies on density, and subsequently have strong consequences for the density structure in the wind. Suzuki et al. (2013) (Figure 5 within) have shown how increasing input Poynting flux at the stellar surface can change the transition region height, and also cause a significant reduction in density with height in the wind. We see a similar effect in our simulations, which is consequential for our predicted radio flux densities. Our cold wind models all have substantially smaller radio fluxes than what is observed, as can be seen in Table 6.2. We will detail these results in Section 4.5. We also note that while the hot wind solution discussed above does not present the high temperatures seen in X-ray observations of hot coronal lines, the cold wind solutions produce much hotter, albeit confined, regions within closed magnetic

loops. Therefore, the cold wind scenarios produce hotter maximum temperatures as can be seen in Table 6.2. This is in better agreement with X-ray-derived temperatures from observations than that of the hot wind model. However, we have not directly computed the X-ray luminosities from our simulations—through radiative transfer methods like our work in Section 4.5 for radio emissions—therefore we can only say that our maximum temperatures from our simulations are similar to derived temperatures from observations, and not conclude anything about X-ray luminosity itself.

Our cold-wind models produce much lower mass-loss rates than our hot wind models. The largest mass-loss rate from our cold wind models is $1.9 \times 10^{-10} M_{\odot} \text{ yr}^{-1}$, which is still one order of magnitude less than our hot wind model. The lowest mass-loss rates calculated come from the A4 model, with $5.6 \times 10^{-13} M_{\odot} \text{ yr}^{-1}$. This is one order of magnitude larger than the currently accepted solar mass-loss rate. We find it difficult to constrain this value for these simulations as these winds do not produce similar radio flux density to the observed values (see Section 4.5). The cold wind model produces slightly lower angular momentum-loss rates than the hot wind model. It is worth noting here that the use of either the ZDI magnetic field, or a dipole, does not dominate the global wind parameters such as mass-loss rate and angular momentum-loss rate. These seem to be mostly dominated by the Poynting flux and damping length parameters.

Figures 6.4 to 6.6 show the Alfvén surfaces (the surface where the wind velocity equals the Alfvén velocity) as black contours. While the Alfvén surfaces in the hot wind (Z0) and cold wind (C1) models are relatively small, we see that the Alfvén surface is quite extended in the dipolar model D1 ($\approx 30 R_{\star}$). The surface is so large ($\sim 30 R_{\star}$) that it extends beyond the orbit of the secondary star. In this case, interesting effects can take place in the system. Perturbations caused by an orbiting companion could travel downwind through plasma waves, allowing this information to reach the base of the wind and modifying the wind structure globally. This is similar to the physical processes seen in the cases of exoplanets orbiting in sub-Alfvénic regions (Strugarek et al., 2019; Folsom et al., 2020). We ignore the companion star in this work and assume that the companion is not actively affecting the stellar wind, which might not be true, in the

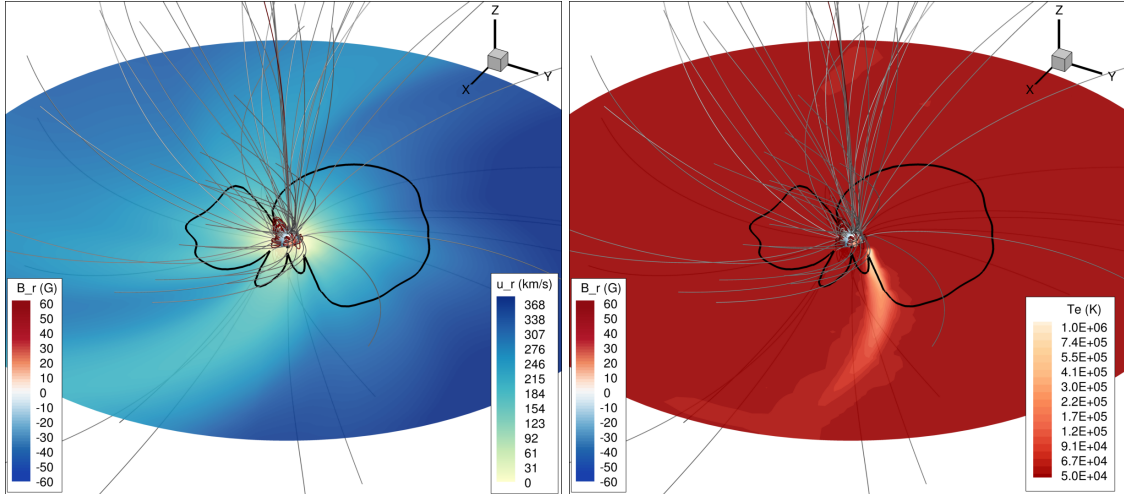


Figure 6.5: Model C1, one of the “cold” wind, Alfvén wave-driven, 3D MHD simulations, with the ZDI map set as the inner boundary for the magnetic field. *Left:* Wind velocities displayed along the equatorial plane (yellow-blue) *Right:* Wind temperatures displayed along the equatorial plane (orange-red). In both plots, surface magnetic fields are displayed in blue-red. Closed magnetic field lines are red, open magnetic field lines are grey. The Alfvén surface intersection with the x-y plane is shown as a black line.

simulation case D1, for example. Of course in our other simulations the Alfvén surface is much less extended, in which case we expect the companion not to affect the stellar wind.

6.5 RADIO EMISSION FROM THE WIND OF λ AND

In Chapter 3 we discussed that stellar winds can be constrained or detected through radio observations. This thermal radio emission scales with the wind plasma density squared ($\propto n^2$), which means the tenuous winds of low-mass main sequence stars remain mostly undetectable for current radio telescopes. However, in the case of solar-mass red giants their winds are much denser due to an increase in mass-loss rate, allowing these winds to be readily detected at radio wavelengths. Observations show a radio flux density of $\sim 0.8\text{mJy}$ at 4.5–5 GHz (Bowers & Kundu, 1981; Lang et al., 1985).

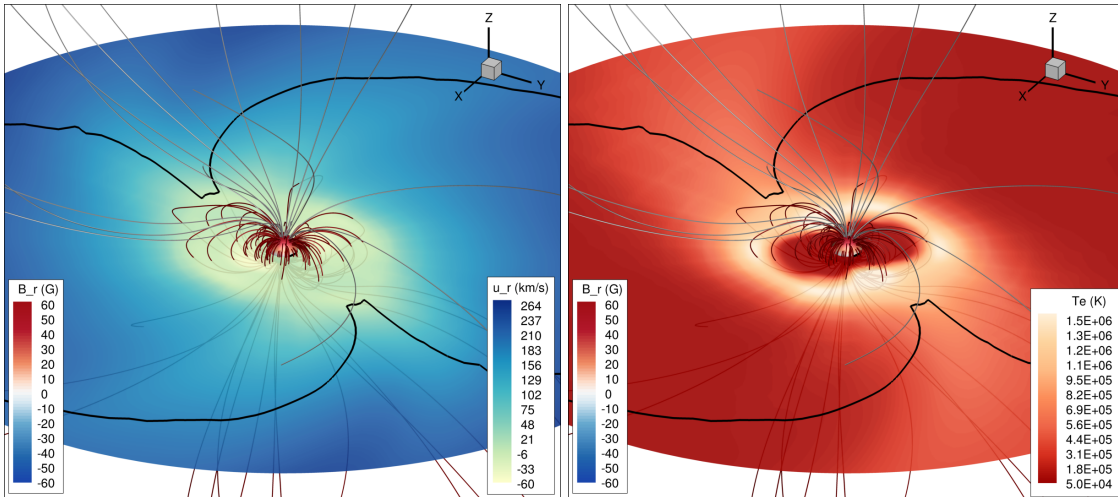


Figure 6.6: Model D1, one of the “cold” wind, Alfvén wave-driven, 3D MHD simulations, with a dipolar field of $B_{\text{dip,max}} = 60\text{G}$. *Left:* Wind velocities displayed along the equatorial plane (yellow-blue) *Right:* Wind temperatures displayed along the equatorial plane (orange-red). In both plots, surface magnetic fields are displayed in blue-red. Closed magnetic field lines are red, open magnetic field lines are grey. The Alfvén surface intersection with the x-y plane is shown as a black line.

We describe the equations for calculating our simulations predicted radio flux density in Chapter 2. In the case of our hot wind scenario we find an agreeable radio flux of 0.89 mJy at a frequency of 4.5 GHz . This is close to the observed value for [Bowers & Kundu \(1981\)](#) and [Lang et al. \(1985\)](#). The radio intensity of this wind model is shown in [Figure 6.7 \(Top\)](#). We can see that there seems to be quite an extended region of specific radio intensity, outside of the optically thick region, shown by the dashed contour. It is from outside the optically thick barrier that the emitted radio flux can escape. The geometry of the optically thick region, including its size, is determined almost exclusively by the density structure of the wind. We find that in the case of the cold wind simulations, the density structure results in radio flux densities that are very low and do not agree with observations.

In the case of the Alfvén driven wind, none of our simulations reached the required level of radio flux to reproduce the observations (see [Table 6.2](#)). The largest radio flux of any of the cold wind simulations was the C2 case, which possesses a very dense chromospheric boundary condition of $1.5 \times 10^{13}\text{ cm}^{-3}$. The wave-driven wind, due to the cold inner regions that are almost isothermal, causes a strong exponential density decay with distance. We found that increasing the base density further does not necessarily

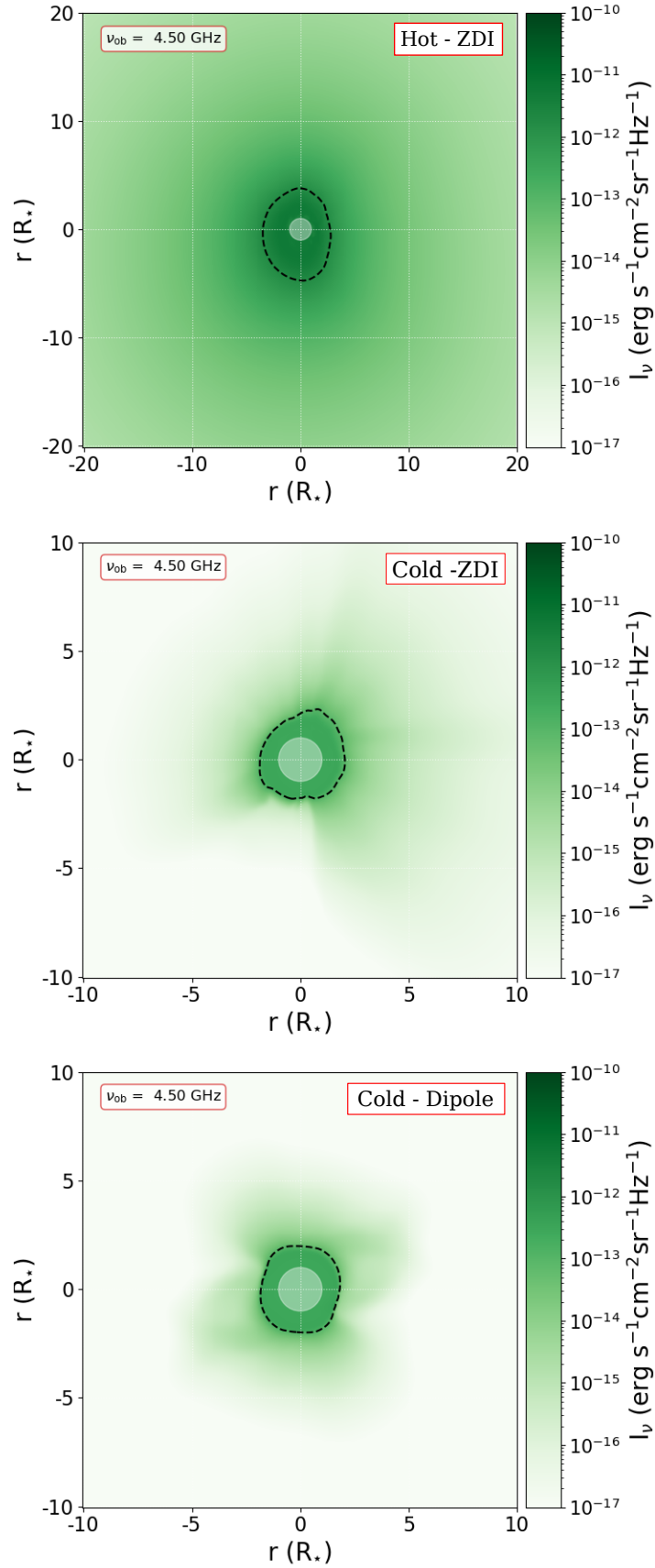


Figure 6.7: Radio intensities of the hot wind, cold wind with a ZDI map, and cold wind with a dipole, respectively, shown in Figures 6.4 to 6.6. Plots from the cold wind models is zoomed in to $R \in [-10, +10]$ to display more detail. It is very evident from these plots that the density decay in the Alfvén wave driven winds has a significant effect on the radio flux density emitted from the wind.

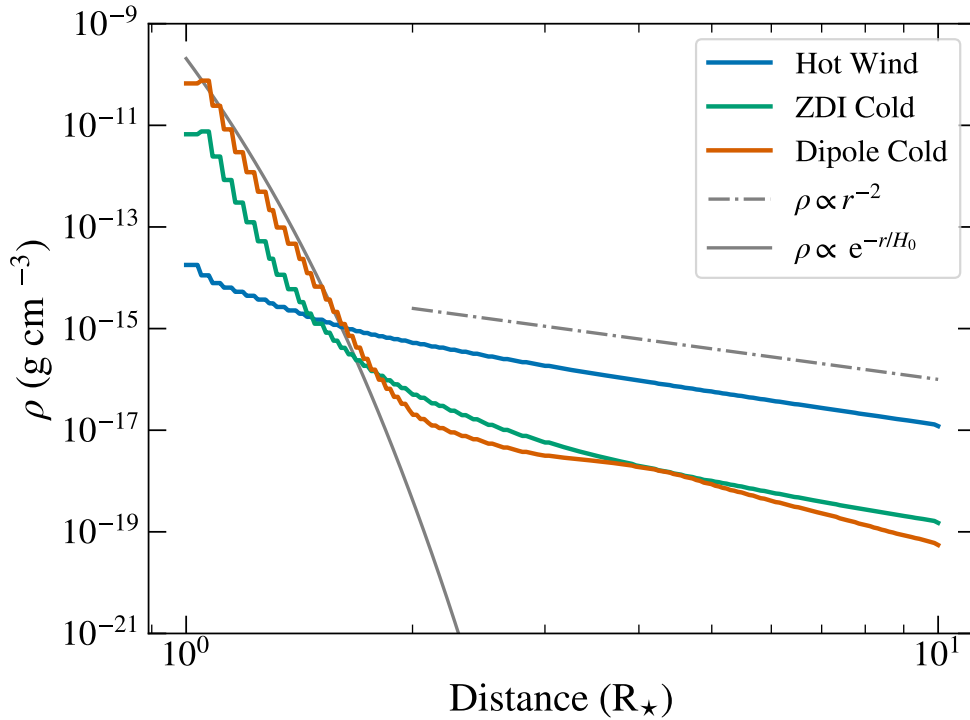


Figure 6.8: In this plot we show the averaged density around the equator of 3 simulations shown in blue (Figure 6.4), green (Figure 6.5), and orange (Figure 6.6) respectively. The wave-driven cold wind scenarios display hydrostatic behaviour close to the stellar surface and we see an exponential decay with a scale height of $0.05 R_{\star}$. Gray lines show examples of r^{-2} (dot-dash) and exponential decay (solid).

increase the radio flux, as the density drops off in a more rapid fashion than the lower base density cases. This happens as the high density near the star causes this region to become hydrostatic-like, leading to an exponential decay in wind density. The higher base density, being so confined near the star, does not contribute much to the emitted radio flux density at 4.5 GHz as the wind is optically thick out to $\approx 2 R_{\star}$. As a result of the exponential decay, outside this optically thick region, the wave-driven winds display much lower density than the thermally driven polytropic wind, resulting in lower radio flux densities.

This is more easily illustrated in Figure 6.8, which shows the averaged equatorial density profile for the three plotted simulations in Figures 6.4 to 6.6. The hot wind model (shown in blue) begins with a lower base density, but with a mostly r^{-2} dependency on distance. The cold wind models however, produce an exponential decay in density up to $\approx 2 R_{\star}$, at which point, they have a much lower density than the hot wind

scenario. This results in much lower radio intensity in the optically thin region shown in Figure 6.7.

6.5.1 *Other sources of radio emission*

Stars have many sources of radio emission, including thermal and non-thermal processes. While in this work, I examined the case of radio emission from λ And as thermal radio emission from the wind, this might not include the full picture of radio processes at play. In particular, gyrosynchrotron processes in the stellar coronae could contribute to the observed radio emission. This type of radio emission is known to correlate extremely well with the X-ray luminosity of the star (as they both originate from similar regions) and this is known as the Gudel-Benz relationship (Guedel & Benz, 1993). If observed radio emissions from the star lie on the trend of the Gudel-Benz relationship, it is most likely this is not thermal radio bremsstrahlung (the X-ray emission is usually thermal in this case, Guedel & Benz 1993), but is instead due to magnetic processes in the corona.

In Figure 6.9 below, I show the Gudel-Benz relationship from Williams et al. (2014), with the radio luminosity (Bowers & Kundu, 1981) and X-ray luminosity (Dempsey et al. 1993 with corrected distance from Drake et al. 2011) of λ And over-plotted. If the radio emission instead was dominated by the thermal emission, we would expect this point to lie off the trend between radio and X-ray luminosity. This would be due to the fact that the thermally emitting regions in the wind would not produce the hot X-ray emission processes leading to the trend in Figure 6.9. However there are no concurrent radio and X-ray observations of the star, therefore it is difficult to irrefutably state the source of the radio emission.

Further evidence for the radio emission being non-thermal in nature is the spectral shapes of some recently realised archival data (VLA, Hallinan, private communication). The star has been observed in an additional 3 epochs, 12th Dec 1998, 17th Dec 1998, and 13th Feb 1999. These archival data show spectral indices that are not pursuant to thermal processes, which leads us to believe that the radio emission from λ Andromedae is

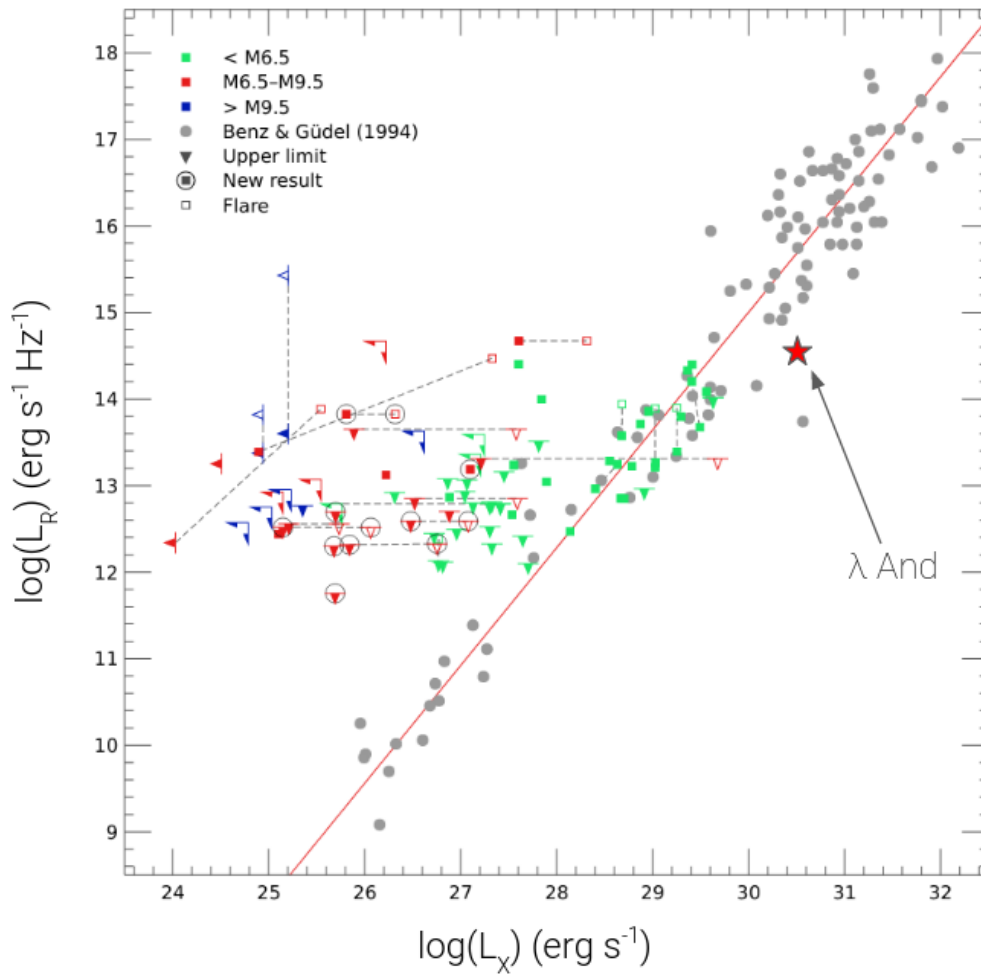


Figure 6.9: This plot shows the Güdel-Benz relationship from [Williams et al. \(2014\)](#). The position of λ And in this plot is shown as a red star, with values from [Bowers & Kundu \(1981\)](#) and [Drake et al. \(2011\)](#). Note that the star is quite variable and can exhibit strong variations in the radio flux detected.

dominated by non-thermal gyrosynchrotron processes in the stellar corona. This means that important parameters derived from the wind simulations in this chapter (such as mass-loss rate) are most likely to be upper-limits to the true wind values. To provide better constraints for λ And it would be ideal to obtain simultaneous observations in X-ray, radio and ZDI maps. This is something that should be feasible given the brightness of λ And.

III

EFFECTS OF WIND EVOLUTION ON PLANETS

Stars and their winds can have severe effects on the planets that orbit them. This is true for exoplanets as well as the Earth. Transient events such as coronal mass ejections on the Sun, show us the possible powerful energies that the Sun can subject the solar system to. This process, and ones similar to it, can be even more frequent, or even consistent in other stellar systems. In this part of the thesis, we quantify the effects of the ageing solar wind on planets, focusing on the Earth, but also some other systems. We discuss how stars at different ages can lead to exceptionally different scenarios on an orbiting planet. We look at more extreme systems, and investigate how more direct interactions, can effect the host star itself. All of these mechanisms fall into the category of star-planet interactions.

PLANETARY ENVIRONMENTS EMBEDDED IN STELLAR WINDS

As we have previously shown, stellar winds can have vastly different densities and speeds depending on the host star. This range of scenarios must be considered when studying exo- (or solar-system) planets. These winds permeate the entire space between the stellar surface up to the astropause, where the wind meets the ISM. Stars are incredibly dynamic, especially on small-length scales, however, this is also true for the wind on longer, global length-scales. The solar wind exhibits a fast (800 km/s) and slow (400 km/s) winds ([McComas et al., 2008](#)), from the poles (mainly coronal holes, which dominate the polar regions) and equatorial regions respectively. Temporally short CMEs can produce even faster particles, over 1000 km/s ([Chen, 2011](#)). For a planet, this translates into a higher ram pressure from the wind, causing a compacting of the planetary magnetosphere (if one exists), or possibly altering any induced magnetospheres. In the solar system, the Earth has the largest magnetosphere of the terrestrial planets. This

magnetosphere shields the Earth from the harmful solar wind and also dynamically changes with the evolving solar wind (Cravens, 1997; Bagenal, 2013).. If the wind of the Sun changes on evolutionary timescales, then it is expected that the Earth's magnetosphere will evolve on similar timescales. Of course, this is also dependant on the internal changes of the planet itself, which produce the planetary dynamo (Zuluaga et al., 2013). If a planet has no magnetosphere, an increase in the stellar wind could cause vast amounts of atmospheric loss. This will have significant effects along the evolution of the Earth regarding retention of its atmosphere. Any erosion of atmosphere would also have significant implications for the development of any life on a planet (Chassefière & Leblanc, 2004). The opposite is also true, given a weaker stellar wind, the removal of little atmosphere could lead to a hydrogen rich atmosphere, making the planet uninhabitable. Through the impingement of intense stellar winds, planets without internally produced magnetospheres can form *induced magnetospheres*, through the movement of high energy particles ionising the atmosphere and creating a magnetic field. Mars possesses an induced magnetosphere, which does not originate from the interior of the planet, but rather the build up of ions near the ionosphere where the solar wind impacts the upper atmosphere producing currents and their own magnetic field (Bertucci et al., 2011). Depending on these exact physical conditions, the quantity of atmospheric loss can be greatly altered.

The goal of this chapter is to construct an overall picture of solar wind evolution by using the models we produced of solar-analogues in Part II. Our models provide us with densities, velocities, mass-loss rates, which can be used to predict how the local environment around the Earth and exoplanets evolves with time.

7.1 EVOLUTION OF THE LOCAL PROPERTIES OF THE WIND ON SOLAR SYSTEM PLANETS

In Chapter 4 I presented 1D polytropic wind models that simulate the evolution of the solar wind. These models provided a way to efficiently describe the winds of many solar-analogues, which are listed in Table 4.1. Using the output of our models, such as local velocity and density, we can estimate how the solar wind properties surrounding the Earth evolve as the system ages. The ram pressure that impinges upon a planet would be

$$P_{\text{ram,p}} = \rho_p v_p^2. \quad (7.1)$$

In the equation above, P_{ram} is the ram pressure, ρ_p and v_p are the wind density and velocity at the distance of the planet. This equation can be used at any point in the wind, here we easily adopt it for the case of the Earth and Mars, by changing velocities and densities to the relevant wind values at the proper distances. In Figure 7.1 we show the local wind velocity, v_{\oplus} , the local proton number density, $n_{p\oplus}$, and the ram pressure, P_{ram} at the orbital distance of the Earth as the stars evolve (in blue; the grey line represents the martian values). Evidently, the break in stellar wind temperature, shown in Figure 4.1, filters down to the local environment, which also displays a break in behaviour as these systems age. This happens at the age of 2 Gyr, denoted by a shaded region. This suggests that the young solar wind exhibited typical wind velocities of 10^3 km/s at the orbital distance of the Earth.

Once we know the ram pressure incident on the magnetosphere of the Earth, the magnetospheric standoff radius, R_M , at the sub-solar point can be calculated (see the schematic in Figure 7.2). As a first order approximation, this is done by balancing the ram pressure of the wind to the magnetic pressure of the planet's magnetosphere (Cravens, 1997).

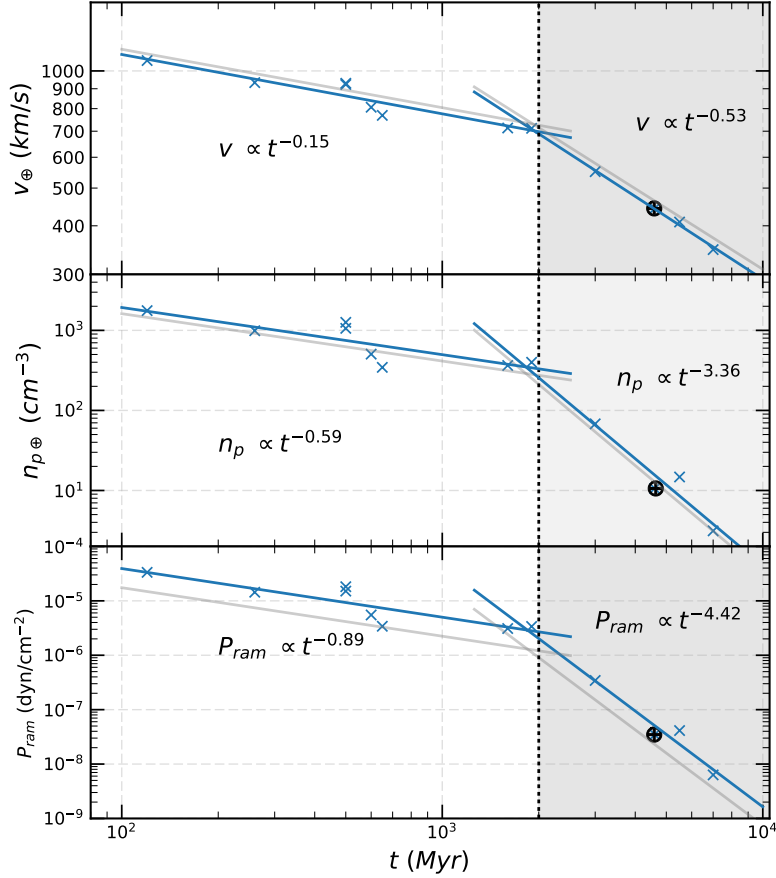


Figure 7.1: Local parameters for the solar wind in the vicinity of the Earth. We show local wind velocity (*top*) and proton density (*middle*) as stars evolve. This results in a present-day solar wind value (\oplus) at the Earth of 443 km/s and 10.5 cm^{-3} , respectively. From these values we calculate the expected ram pressure (*bottom*) impinging on the Earth as it evolves. Shown are best fits to simulated values in separate regimes. Shown in grey are the expected values for a martian proxy planet orbiting each star.

$$\frac{R_M}{R_\oplus} = 1.4 \left[\frac{B_p^2}{8\pi P_{ram}} \right]^{\frac{1}{6}}. \quad (7.2)$$

R_M is given here in planetary radii normalised to Earth radii, B_p is the surface planetary magnetic field at the equator, which we assume to be the dipolar field only. The factor of 1.4 accounts for currents that develop near the magnetopause boundary and produce their own magnetic fields (Cravens, 1997; Bagenal, 2013). Equation 7.2 shows a dependence on stellar wind strength, which could have important ramifications for the development of life, as the solar wind is expected to have varied in the past on long timescales, as we have shown in Section 4.4. A smaller magnetosphere can lead to esca-

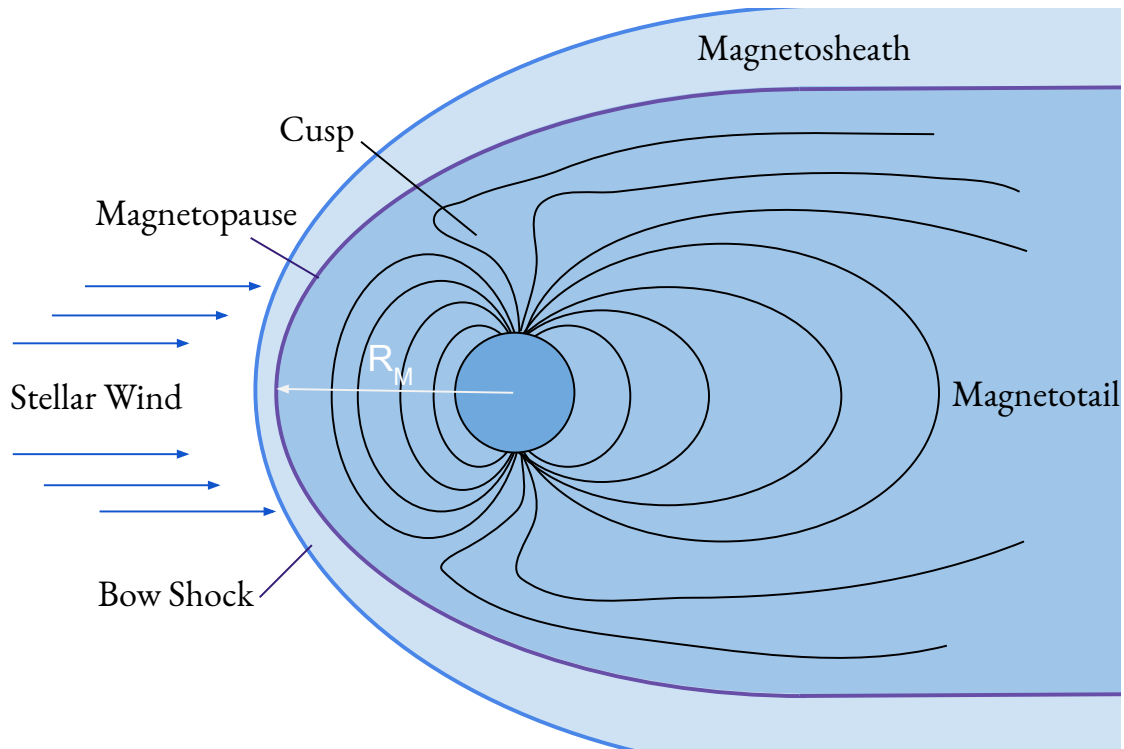


Figure 7.2: Schematic of a typical magnetosphere. Labelled are the important components of the magnetosphere structure. Here the planetary magnetic field (black lines) has no inclination, but in the case of the Earth this is tilted around $\sim 10^\circ$.

lated atmospheric loss and reduced protection from the ionised wind (discussed further in Section 7.2).

Figure 7.3 shows the trend in magnetospheric size for the Earth, both with solar rotation and age. We calculate the magnetospheric size considering the Earth’s magnetic field to be constant with time (blue solid line) and varying with time according to the model by Zuluaga et al. (2013) (purple dotted line). This model is constrained by magnetic field measurements showing a 50% field strength for a 1 Gyr system estimated by Tarduno et al. (2010). We can see that both models differ only slightly, with the most significant differences occurring around 1-2 Gyr, showing a spread of just under $1 R_E$. In particular, we find at early ages, both models predict magnetospheric sizes of $\approx 3 R_E$. This is understandable, considering the weak dependence on the planetary magnetic field of $1/6$, shown in Equation 7.2. We find a small magnetospheric standoff distance of $3.0 R_E$ for a young Earth 100 Myr old, with the same planetary magnetic field as today ($B_p = 0.3 \text{ G}$). These standoff distances would be similar to extreme modern day events, such as the 2003 Halloween storm (Rosenqvist et al., 2005), caused by CMEs.

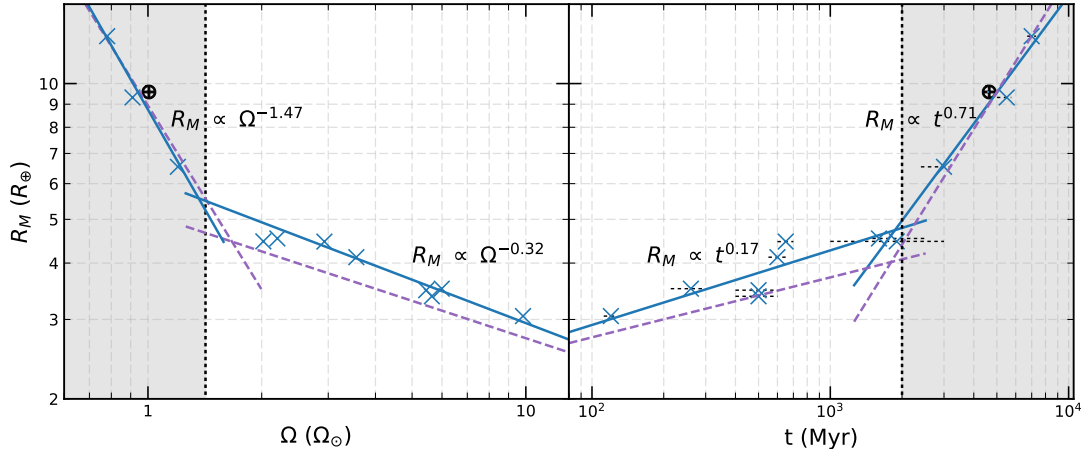


Figure 7.3: We observe trends in magnetospheric size with respect to rotation (*left*) and age (*right*). *Blue x's*: Calculated standoff distances with a constant planetary magnetic field of 0.3G. The solar-Earth scenario as it is currently, given as \oplus . *Purple dashed line*: This depicts the standoff distances of the magnetosphere if the planetary magnetic field varied according to models described in Zuluaga et al. (2013).

However, these transient CME events last only on the scale of hours, but at 100 Myr, these magnetosphere sizes would have been typical. Increased solar activity at younger ages (e.g. CMEs) would further compress the young magnetosphere, resulting in even smaller standoff distances. Younger stars are expected to be more active and would be more likely to produce large and more frequent transient events such as CMEs.

7.2 PLANETARY MAGNETOSPHERE EFFECTS

We have shown in Figure 7.3 that a young Earth orbiting a young Sun would possess a significantly smaller magnetosphere. In our results for magnetospheric standoff distance, we assumed that the magnetic dipole moment of the Earth has remained the same up to this day. However it is believed that this is not the case, although there is no consensus on how it has changed or by what amount. Tarduno et al. (2010) showed from ancient silicate crystals that the paleo-magnetic field of the Earth was much weaker than today, and estimated it to be 50-70% of the current strength. We took a model which is constrained by these parameters and describes how the magnetic moment of the Earth has evolved over time from Zuluaga et al. (2013). Using these values for B_p , we calculated

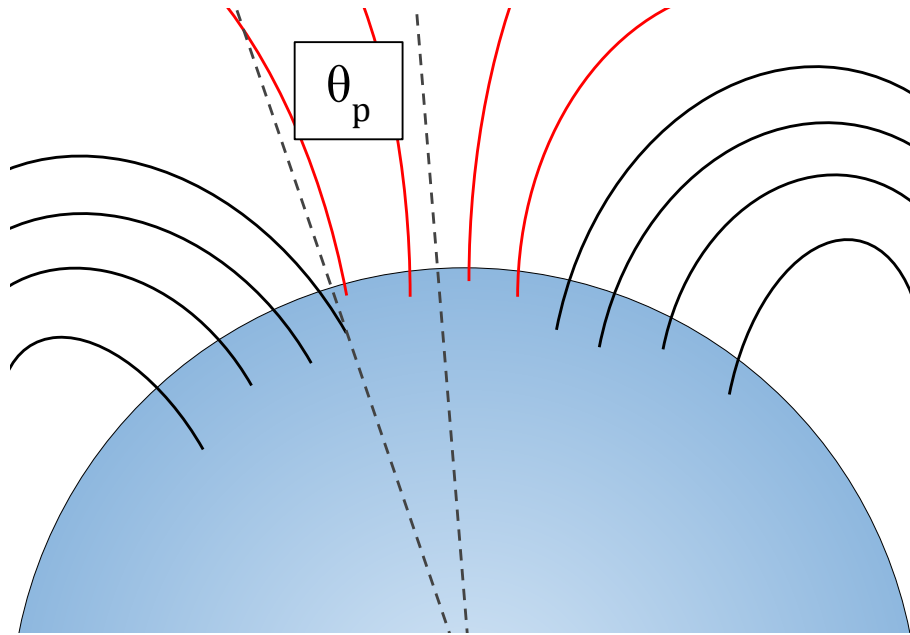


Figure 7.4: The polar opening angle. Closed field lines in black, open field lines in red.

R_M , shown as the purple dashed line in Figure 7.3. This plot shows how significant the changes in the Earth's magnetic field can be over time, when calculating R_M . At 100 Myr we can see that the magnetosphere is approximately $2.8 R_\oplus$ using a varying magnetic field, which is almost the same size derived with a constant magnetic field ($3 R_\oplus$). See et al. (2014) conducted a study into the effects that winds from solar type stars have on magnetosphere sizes of planets. They investigated how varying host star mass influenced the magnetospheric size and how this could effect habitability on any Earth-like exoplanets. This work complements the results of See et al. (2014) as it shows how magnetosphere size will vary across different ages of solar analogues. Both Vidotto et al. (2013) (M dwarfs only) and do Nascimento, Jr. et al. (2016) (κ^1 Ceti) considered how stellar winds effected the interplanetary medium and how this could have impacted habitability on Earth-like exoplanets orbiting these stars. Also of interest is Airapetian & Usmanov (2016), who used 3D MHD Alfvén wave driven models and found a paleo-solar wind that is twice as fast and 50 times as dense at 1AU at an age of 0.7 Gyr. We found very similar results for the wind of 1.9 times the velocity and 58 times as dense at 1AU for similar epochs.

For a stronger solar wind, the ‘polar opening’ angle (θ_p)

$$\theta_p = \sin^{-1} \left(\sqrt{\frac{R_E}{R_M}} \right) \quad (7.3)$$

of the young Earth’s magnetosphere, defined by the region which is covered by open magnetic field lines that extend into the magnetotail (in contrast to the closed dipolar magnetic regions in lower latitudes), can extend significantly further down in latitude than it does presently (71.9° , [Tarduno et al. 2010](#)). Note Equation 7.3 is in colatitude, although it can also be defined using \cos^{-1} , in which case the angle given in latitude. This latitude is usually the extent to which the aurora are visible, with visibilities at lower latitudes usually due to increased solar wind activity. We estimate that at an age of 100 Myr the polar opening region would extend as far as $55\text{-}60^\circ$ from the equator. It is thought that this larger polar opening region would have many implications for life developing on Earth, namely reduced protection from the harmful solar wind, and increased rates of atmospheric loss, through the expansion of the atmosphere and loss of volatiles. To intensify this effect, a younger Sun would be expected to be more active, with increased flaring rates and energy, potentially leading to additional atmospheric loss.

Figure 7.1 also shows the local parameters of the wind around Mars. This allows us to calculate the height of the ionosphere, which acts to produce an induced magnetosphere above the martian surface. This is done by equating the stellar wind ram pressure with the thermal pressure of the martian atmosphere, taking today’s values for the latter ($7800 \text{ dyne/cm}^{-2}$, [Harri et al. 2014](#)). We find a present day ionospheric height value of 292 km (given by Equation 7.4), which is consistent with observations ([Hanson et al., 1977](#); [Withers, 2009](#)).

$$z = -H_0 \ln \left(\frac{P}{P_0} \right) \quad (7.4)$$

where $H_0 = k_B T / mg$, is the scale height of the atmosphere, P is the wind pressure at Mars, which balances with the atmospheric pressure, and P_0 is the pressure at the martian surface. Assuming the current state of the martian magnetosphere, which is

very weak given the lack of a global magnetic field, our models find the ionosphere height increases as the Sun-Mars system evolved, in a similar fashion to the Earth's magnetosphere size. It also predicts that for the immediate future, the ionosphere height will continue to grow. The change found in martian ionosphere height seems small compared to changes in Earth's magnetosphere over the same time period. We find a 42% increase in ionosphere height for Mars from 100 Myr (218 km) to 7 Gyr (310 km). This is much smaller than the 324% increase found in the Earth's magnetosphere from 100 Myr ($3 R_{\oplus}$) to 7 Gyr ($12.7 R_{\oplus}$). This arises due to the martian ionosphere size depending on the inverted natural logarithm of the wind ram pressure, giving a weaker dependence on the solar wind.

Our wind models provided us with the local properties of the solar wind from very close to the Sun, all the way to the orbit of Mars. However, the 1D models neglect azimuthal and meridional variations of the stellar winds. In particular, close to the star, the wind is much less homogeneous (Vidotto et al., 2015). Therefore, to investigate the local wind parameters of close-in planets, we use the results of our 3D models.

7.3 LOCAL WIND PARAMETERS FOR PLANETS AROUND SOLAR-TYPE STARS - 3D

After expanding our stellar wind simulations to full 3D MHD models, it allowed us to examine the local environment of hypothetical hot Jupiters around the stars we simulated. These exoplanets are objects of interest due to their observational abundance and extreme environments close to their host stars. The advantage of moving to a more advanced 3D MHD code is that we can then quantify the effects of the wind, and how they change on orbital timescales as a hypothetical planet orbits the host star. The addition of stellar magnetic fields allows us to examine the effects of stellar magnetic pressure on planets. At close separation of star and planet, such as the case for hot Jupiters, the total pressure impinging on the planet can be a combination of different factors, from ram

pressure, to thermal, or magnetic pressure. This gives a much more holistic approach to the environment these exoplanets are embedded in.

7.3.1 *Wind derived properties at typical hot-Jupiter distances*

Through our wind simulations, we can study the local parameters that each star would impose on a hypothetical hot Jupiter. Hot Jupiters are classified as exoplanets who are similar to Jupiter in mass and radius, but orbit their host stars at extremely close separation. This is typically on the order of a few stellar radii from the stellar surface. Due to their heated environment, the atmospheres of these hot Jupiters can be extended, forming a large hydrogen envelope. This is due to the irradiation from the host star causing the atmosphere to heat. High energy stellar radiation in particular can cause significant atmospheric expansion. Therefore hot Jupiters around active stars, which have high flaring rates, producing a lot of XUV and X-ray emission, are expected to have the largest atmospheres.

The most effective way to quantify the effect of a stellar wind on an exoplanet is through pressures. The main components of the wind affecting exoplanets are magnetic pressure (for close in exoplanets) and ram pressure (for distantly orbiting exoplanets). There also exists a thermal pressure constituent to the wind, but this is usually much smaller than both of the previous pressures. Ram pressure is defined above in Equation 7.1, it is a convenient way to express both the density and velocity of the wind impinging on the planet. The magnetic pressure is given by the stellar magnetic field at the distance of the planetary orbit as

$$P_{\text{mag}} = B^2/8\pi \quad (7.5)$$

In our case, we investigate the local parameters at a distance of 0.1 au. At this distance the ram pressure dominates as this is well above the Alfvén surface for each star, although we include all pressure components in our analysis. Here we assume the planetary orbit to

be in the equatorial plane aligned with the rotation axis, but we note that this might not always be the case for hot Jupiters (Huber et al., 2013; Anderson et al., 2016). Figure 7.5 shows the local conditions of the stellar wind at 0.1 au where the left panels show the slower stellar rotators and the right panels the faster stellar rotators. We show density (top), velocity (middle) and ram pressure (bottom). We see that there can be large variations in the ram pressure impinging upon an orbiting exoplanet at 0.1 au, both within a single orbit around a particular host star, and between each host star. From these, we infer the evolution of the planetary environment around a solar-like star as it evolves. We see that the Sun at minimum possesses the lowest ram pressure of any of the stars in our sample.

We can compare the distribution of velocities for all of the stars by histogramming the velocities across a sphere of 0.1 au, shown in Figure 7.6. This method can give insight into the structure of the wind, discerning uni-modal and multi-modal wind structures. We observe that more complex and stronger fields lead to less uniform wind structures. We can see that the winds of 18 Sco, HD 9986 and the Sun at minimum display unimodality, while other stars such as χ^1 Ori and HD 190771 have a very skewed velocity distributions. The magnetic field strength and geometry seems to directly affect the wind structure even at these distances. This is discussed in Réville et al. (2016), who noted that the expansion of magnetic flux tubes can cause an acceleration in the wind. We see this effect even in the Solar maximum case, where both Solar maps only possess the lowest order spherical harmonics, so as to adequately compare them to the other stars. This suggests that this effect is not only an aspect of limited magnetic field resolution from ZDI observations.

Similarly to Jupiter, these planets are expected to have strong magnetic fields (Christensen et al., 2009; Yadav & Thorngren, 2017). There have been some detections of this so far. Cauley et al. (2019) calculated the magnetic fields of HD 179949 b (3.2 G), HD 189733 b (27.0 G), τ Boo b (2.6 G), and ν And b (2.5 G). This was done using an indirect method whereby anomalous emission of Ca II K (3,933.66Å) is observed caused by the magnetically induced star-planet interactions. Making assumptions on the transfer of

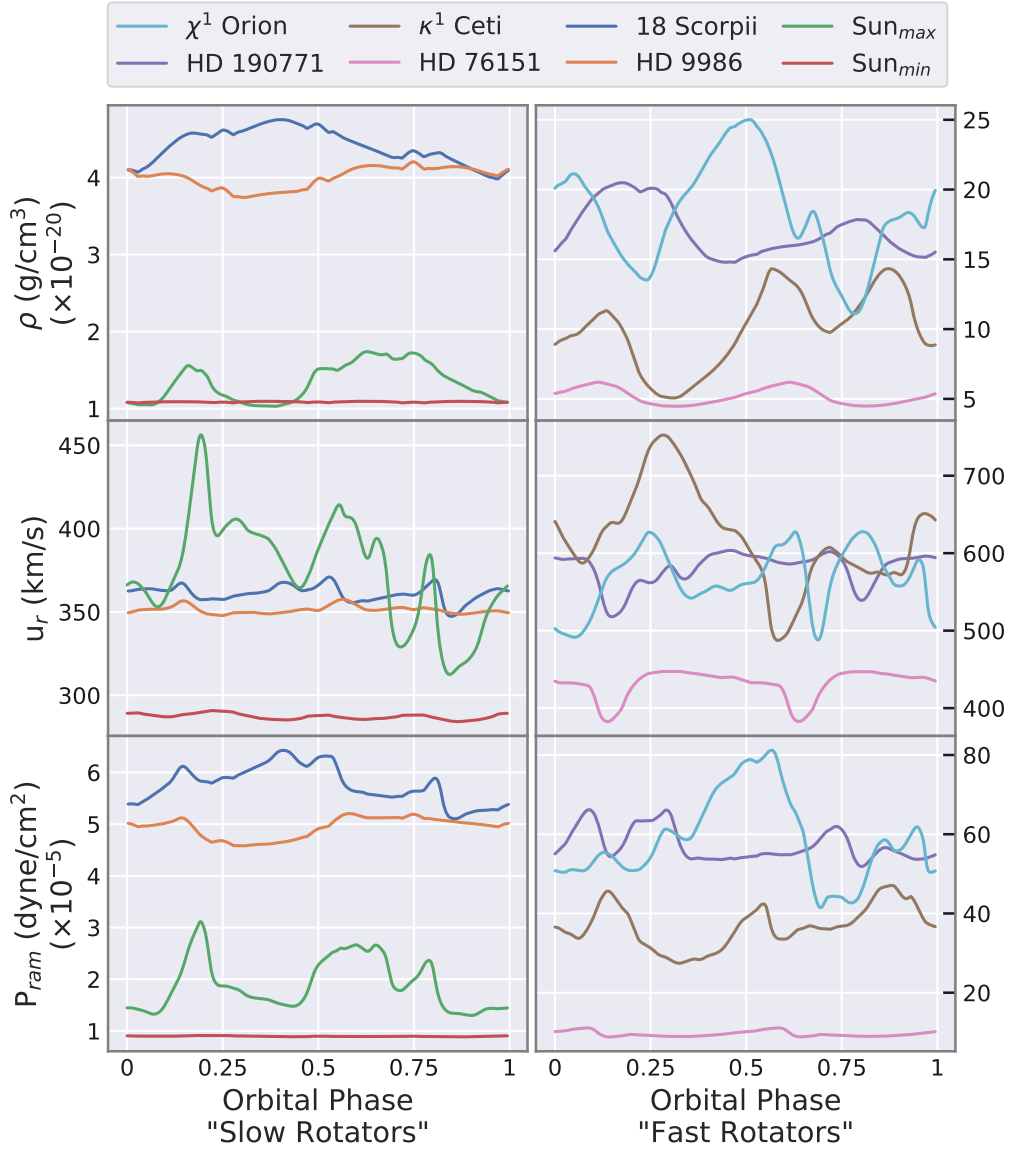


Figure 7.5: *Top:* Figure showing the density variations of the wind at the equator ($z=0$ plane) for each star in our sample, at a distance of 0.1 au. *Middle:* The velocity variations of the wind at the equator at 0.1 au. *Bottom:* Calculated ram pressures of the wind at 0.1 au at the equator, using Equation 7.1. The figures are split into slow (left) and fast (right) rotators so to conserve the visibility of variation across all winds. Note that the y-axes on the left and right have different scales. This figure is optimally viewed in colour.

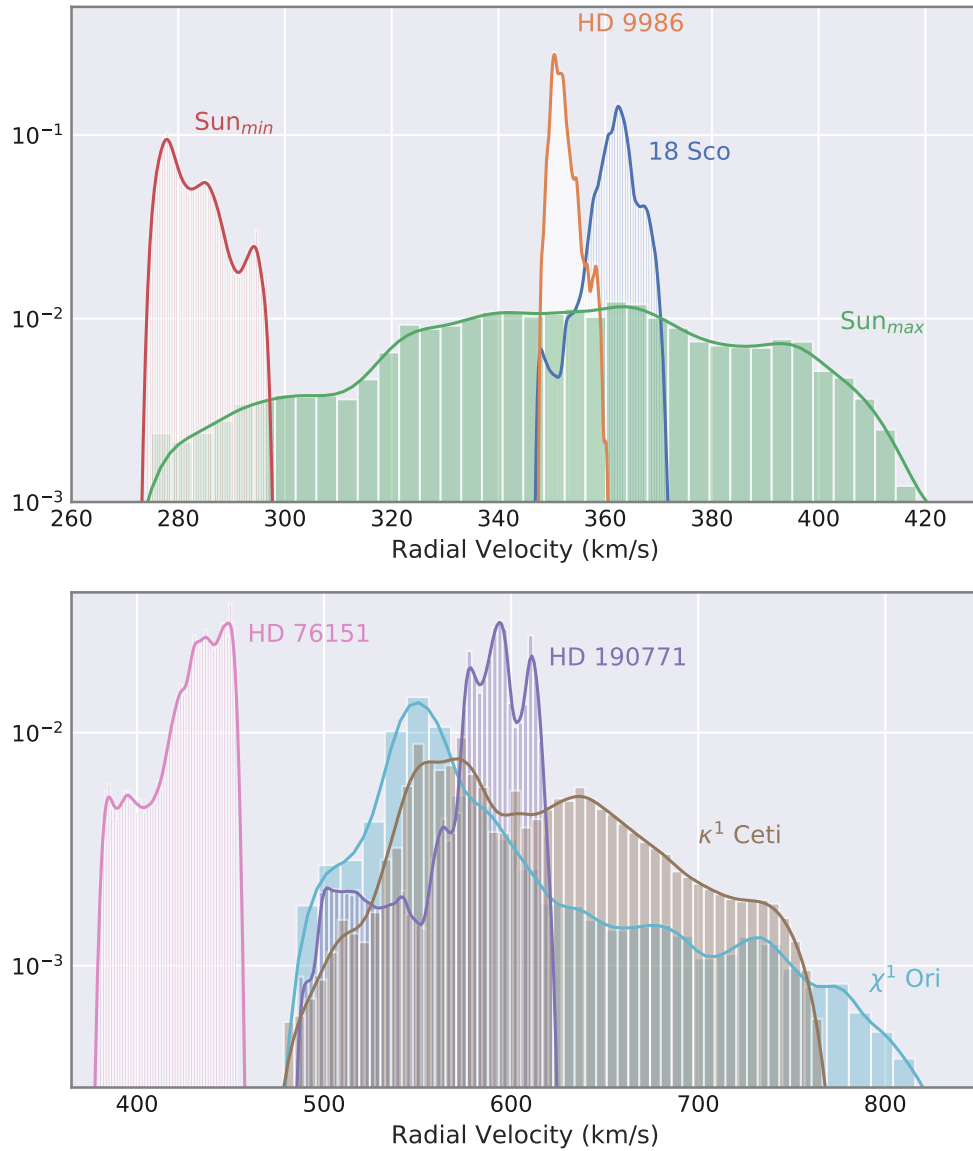


Figure 7.6: Velocity histogram for our stellar sample, allowing insight into the wind structure (e.g. Réville et al. 2016). Velocities are taken at a distance of 0.1 au, and split into slower rotators (top) and faster rotators (bottom). Note the different velocity scales on each panel. This histogram shows the normalised frequency of each velocity present in the wind at this distance. We can see that the winds of 18 Sco and HD 9986 are extremely unimodal, while other stars such as HD 190771 have a very skewed distribution of velocities. The magnetic field strength and geometry seems to directly affect the wind structure even at these distances. Bin size is selected using the Freedman-Diaconis rule.

energy and the limits of the observations, a magnetic field can be derived. Not long ago, [Callingham et al. \(2020\)](#); [Vedantham et al. \(2020\)](#) both made low frequency radio observations of close in exoplanets, with detections suggesting the presence of a magnetic field. [Vedantham et al. \(2020\)](#) found indirect evidence of a planet producing coherent low frequency radio emission through star-planet interactions. These magnetic fields would provide a certain amount of protection from the stellar wind, however we expect that a similar phenomenon would occur as described above. Planets without magnetic fields will find their atmospheres stripped by the stellar wind impacting on the planetary atmosphere. Planets possessing magnetic fields, will find a compressed magnetosphere due to the stellar wind, and the effects on the atmospheric loss are not yet fully certain (whether this increases or decreases atmospheric mass-loss is still being debated in the literature). These aspects of planetary atmospherics are important for evolutionary modelling of exoplanets. Therefore we provide an examination of the stellar wind facet of this environment. We focus on hot Jupiters, as they are the most ubiquitous of the close in exoplanets, but in reality this analysis applies to any exoplanet close to their host star. It is clear that these indirect detections of exoplanetary magnetic fields are highly dependent on the environment they are embedded in. The most promising mechanism for consistent star-planet interactions (as transient interactions are more difficult to detect) are sub-Alfvénic Alfvén wings. The star-planet interactions will be discussed more in detail in Chapter 8.

THE CIRCUMSTELLAR ENVIRONMENT OF 55 CANCRI

It has been suggested that closely orbiting exoplanets could enhance stellar activity due to strong star-planet interactions (SPI), which would be able to generate induced-chromospheric hotspots in the host star (Cuntz et al., 2000; Cuntz & Shkolnik, 2002). Potential signatures of SPI in the form of anomalous chromospheric emission modulated by a planet has been observed for a few systems, such as in the case of HD179949 (Shkolnik et al., 2008; Fares et al., 2012) and HD189733 (Cauley et al., 2018). However, not all close-in planets can generate induced emission in their host stars (Miller et al., 2012). One possible suggestion is that if the planet orbits beyond the Alfvén surface, information from a potential star-planet magnetic reconnection event would be prevented from propagating towards the star. Given the sub-Alfvénic orbit of 55 Cnc e, we investigate here the potential sites of generation of chromospheric hotspots, caused by SPI.

The 55 Cnc system is one of the most relevant systems for understanding planets with masses/radii in between those of Earth and Neptune. This mass-radius regime, which is characterised by a large variety of bulk densities, does not exist in the solar system, yet constitutes a large portion of discovered exoplanets. As shown in this chapter, 55 Cnc is also a prime target for the exhibition of SPI, given the planetary and stellar wind conditions. In this work, we aim to understand possible SPIs in this system, which requires a thorough understanding of the stellar magnetic field and stellar wind. I use ZDI derived maps of the large-scale magnetic field to simulate the wind of 55 Cnc, and analyse the environment surrounding the adjacent planet e.

The observational aspect of this work (spectropolarimetric observations and ZDI) was conducted by Folsom, C. and Petit, P., while I led the contributions of wind modelling to the work. *Results from this chapter were published in "The circumstellar environment of 55 Cnc: the super-Earth 55 Cnc e as a primary target for star-planet interactions", A & A, 633, A48, 2020*

8.1 THE SYSTEM OF 55 CANCRI

55 Cnc (late G) hosts five known exoplanets, most notably the close-in super-Earth 55 Cnc e ($M_p = 8.37 \pm 0.38 M_\oplus$, $R_p = 1.92 \pm 0.08 R_\oplus$, $P_{\text{orb}} = 18$ hrs), which offers a great opportunity for detailed characterisation of a super-Earth due to two properties: at $V \approx 6$, the host star is the third brightest star known to host a transiting planet and, because of the high planetary temperature, the planet has a high planet-star flux contrast, making the planetary emission well detectable at optical and infrared (IR) wavelengths.

Observations suggest that 55 Cnc and planet e may be an larger analogue of the Jupiter-Io system (Demory et al., 2016b). This would imply the presence of a significant exosphere surrounding the planet and plasma flowing from the planet towards the star, following the stellar magnetic field lines. Spitzer observations conducted at $4.5\text{-}\mu\text{m}$ indicate the planet's dayside thermal emission varies by 300%, with temperatures rang-

ing between 1300–3000 K (Demory et al., 2016a). This can be explained assuming that the planetary lithosphere is partially molten, particularly on the dayside. Recent inferences of disintegrating exo-mercuries in close-in orbits have used volcanic out-gassing as a way to inject dust into the planetary atmosphere, to be carried away by thermal winds (Rappaport et al., 2012).

Planet e’s phase-curve has recently been detected in the infrared (Demory et al., 2016a) with Spitzer. The phase-curve exhibits asymmetric dayside emission and a strong day-night temperature difference, indicating an inefficient heat redistribution from the dayside to the nightside, with differences of ~ 1300 K, thus dismissing the presence of a thick atmosphere.

MOST satellite observations (Winn et al., 2011; Dragomir et al., 2014) show variability in the visible that could be linked to the IR variability. The facts that the 2012 MOST phase-curve shows a smaller amplitude than that recorded in 2011, and that the former is comparable to the IR phase curve, suggests that there is opaque material in both the IR and the visible, such as grains of dust coupled to hot plasma, in a similar manner as Io (Krüger et al., 2003).

Ridden-Harper et al. (2016) detected absorption at the position of the Ca II H&K resonance lines, that is likely connected with planet e, as the absorption’s Doppler shift corresponds to the expected velocity of the planet. The observations suggest variability in the optical depth of the material surrounding the planet, as previously observed for Mercury, frequently in emission (Killen et al., 2007), and less so in absorption (Potter et al., 2013).

It was unexpected that a preliminary analysis of HST/WFC3 emission spectra of planet e resulted in a signal being detected in just 2 out of 4 visits (Dragomir et al., 2017). These observations corroborate the changes observed with Spitzer, MOST, and HARPS.

Reconciling these properties would require the presence of an azimuthally inhomogeneous circumstellar torus and/or of a large exosphere made of ions and charged dust particles similar to Io (Krüger et al., 2003) that could contribute to a variable grey opac-

ity along the line of sight through diffusion of stellar light. The grey behaviour of dust could provide the same opacity both in the visible and IR. Io's cold torus, which fills its orbit and girdles Jupiter, rotates at the same rate as Jupiter (Belcher, 1987). Assuming the same scenario holds for 55 Cnc e, the torus rotates with the same period as the host star (about 40 d), causing a modulation of the transit and occultation depths over similar time-scales.

Detecting the presence of a significant magnetic field of the host star would support the idea that this system is a scaled-up version of the Jupiter-Io system. Examining the stellar magnetic and wind properties would also be revealing of how likely is the occurrence of magnetic star-planet interactions. We present here the detection and characterisation of the stellar surface magnetic field and the further inference of the stellar wind properties.

8.1.1 *The surface magnetic field of 55 Cancri*

To detect and characterise the magnetic field of 55 Cnc, my colleagues and co-authors used the Narval spectropolarimeter, at the Pic du Midi Observatory in France. Narval is an instrument that includes a polarimeter connected by fibre to high resolution échelle spectrograph ($R \sim 65,000$; 3700–10500 Å). I will describe the observations of 55 Cnc using Narval as conducted by my co-authors. Observations utilised the Stokes V mode, providing both the total intensity (Stokes I) and the circularly polarised intensity (Stokes V). The data was reduced using the LIBREESPRIT pipeline (Donati et al., 1997).

20 observations of 55 Cnc were conducted over ten nights between March 1 and April 21, 2017. Co-adding of observations from each night was not required as the magnetic detections were obtained in single observations reliably. A total exposure of 3600 s was used (four 900 s sub-exposures).

As standard, the Zeeman splitting in Stokes V was detected using least squares deconvolution (LSD; Donati et al., 1997; Kochukhov et al., 2010), a cross-correlation technique that produces pseudo-average line profiles with greatly reduced noise. The

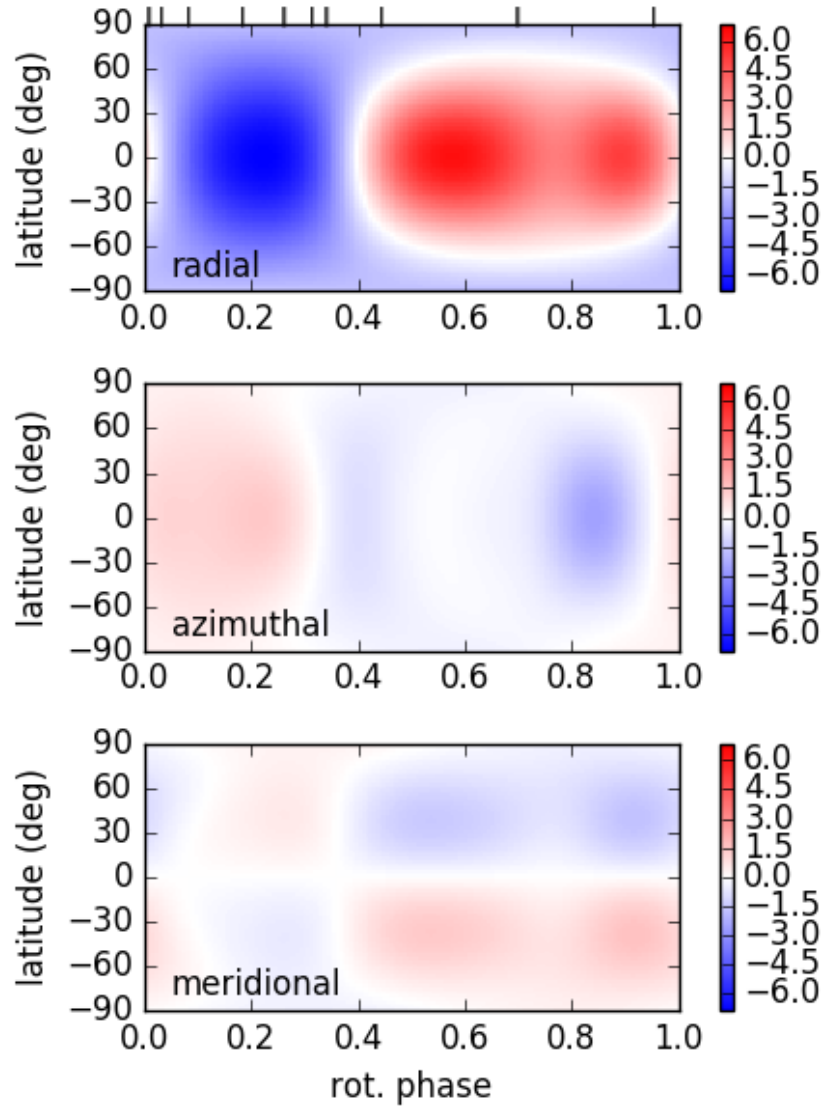


Figure 8.1: Magnetic map of 55 Cnc from ZDI. The radial, azimuthal, and meridional components of the magnetic field are presented, in units of G. Ticks along the top indicate phases where observations were obtained.

details of this technique are not within the scope of this thesis. Magnetic detections were found in V LSD line profiles for all nights except April 10.

The ZDI technique was used to characterise the magnetic field strength and geometry of 55 Cnc (Donati et al., 2006). This technique is briefly discussed in Part I, to give the reader an understanding of the process, however a deep examination of this technique is beyond the scope of this thesis. For a full background on this technique, please refer to works such as Donati et al. (1995, 1997); Folsom et al. (2016). The ZDI technique models the rotationally modulated Stokes V LSD profiles and finds the simplest magnetic geometry needed to reproduce the profiles. The code used for this task

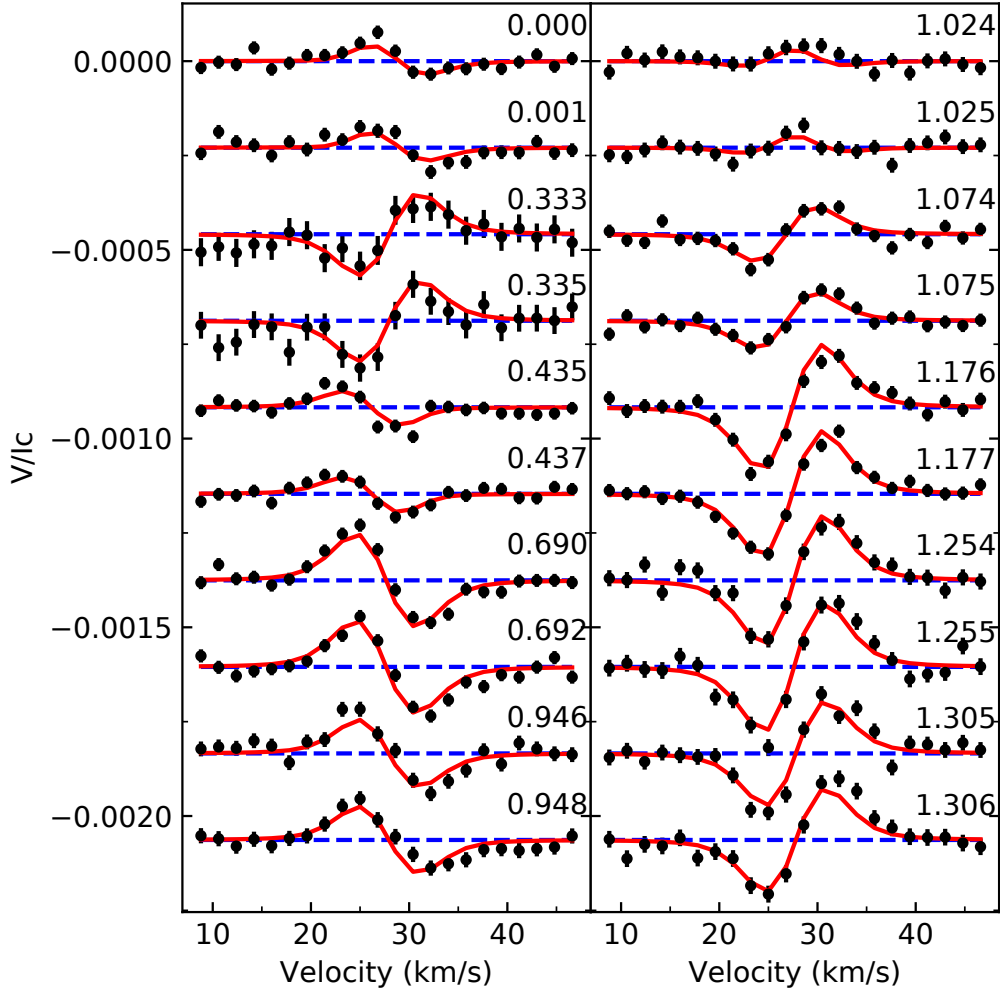


Figure 8.2: LSD Stokes V profiles of 55 Cnc (black points), labelled by rotation cycle for a 39-day period, and shifted vertically for clarity. Dashed lines indicate zero and solid lines are the best fit ZDI model profiles.

is described in [Folsom et al. \(2018a\)](#) which is a modified version of codes described in [Donati et al. \(2006\)](#); [Folsom et al. \(2016\)](#). The $v \sin i$ of 55 Cnc is poorly constrained since it is below the resolution of Narval. Therefore, a equatorial velocity of 1.24 km s^{-1} is inferred from the interferometric radius of $0.943 \pm 0.010 R_{\odot}$ ([von Braun et al. 2011](#); [Ligi et al. 2016](#)), and the rotation period of $38.8 \pm 0.05 \text{ d}$ ([Bourrier et al., 2018](#)). To constrain the line profile shape, we fit the line in Stokes I with a Voigt profile, broadened by this upper limit for $v \sin i$, and found a Gaussian width of 2.32 km s^{-1} and a Lorentzian width of $0.81 (2.84 \text{ km s}^{-1})$ (cf. [Folsom et al. 2018a](#)).

Using these values for equatorial velocity and intrinsic line widths, the inclination of the stellar rotation axis can be constrained via ZDI. This is done by simply using ZDI to fit a wide range of inclinations and see which produces the best fit. We find that the

rotation axis of 55 Cnc is $i > 80^\circ$ with 1σ confidence, and $i > 65^\circ$ with 3σ confidence, with the most likely value occurring near 90° . [Bourrier et al. \(2018\)](#) find that 55 Cnc e orbits with a $83.59_{-0.44}^{+0.47}^\circ$ orbital inclination, thus our rotational inclination is consistent with the stellar rotation axis and planetary orbital axis being aligned.

Our final magnetic map is presented in [Figure 8.1](#) and the corresponding line profiles are given in [Figure 8.2](#).

8.2 THE STELLAR WIND AROUND THE PLANETS ORBITING 55 CNC

We use BATS-R-US ([Powell et al., 1999](#)) (Chapter 2) to simulate the stellar wind of 55 Cnc. This code has been extensively described in Chapters 2 and 5. We use a Cartesian grid whose resolution is varying uniformly from the stellar corona to the edge of the domain. The domain extends to $30 R_\star$ in each direction. Our simulation has a range of resolutions from $0.019 - 0.625 R_\star$. In this stellar wind scenario we tried two different boundary conditions. Initially we set a base density of $\rho_0 = 3 \times 10^{-17} \text{ g cm}^{-3}$, this gave satisfactory results and is discussed below, however we also ran a simulation with a base density of $\rho_{0,\text{high}} = 10^{-16} \text{ g cm}^{-3}$ and another with $\rho_{0,\text{low}} = 1 \times 10^{-17} \text{ g cm}^{-3}$. Our main aim here was to determine with how much certainty we can conclude that planet e orbits within the Alfvén surface. This would provide the planet with a magnetic link back to the surface of the star, as magnetic plasma waves could travel downstream as long as the wind plasma is sub-Alfvénic. In the initial simulation there was quite a large Alfvén surface (where the Alfvén speed and wind speed are equal). The Alfvén velocity is heavily dependent on the density, therefore a wind with a higher density would lead to lower Alfvén velocities and therefore a smaller Alfvén radius. This was a method for testing if the inner planet, planet e, still orbited within the Alfvén surface, which is an important factor for SPI, even given more extreme base densities. For our base temperature we used $T_0 = 1 \text{ MK}$ for both simulations. We find that 55 Cnc is losing

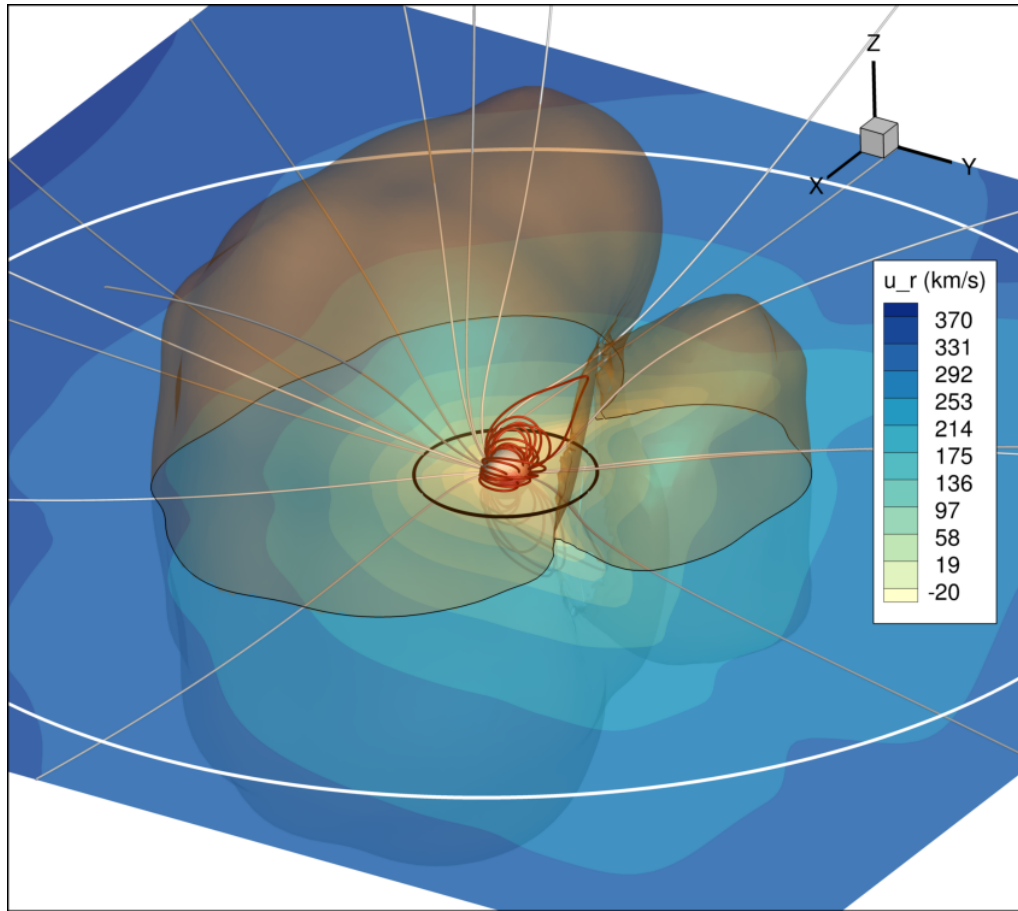


Figure 8.3: 3D MHD simulation of 55 Cnc. Wind velocity is shown as a slice at the $z = 0$ plane and extends to $30 R_{\star}$. The Alfvén surface is shown in orange, with its intersection with the orbital plane of the planets highlighted with a thin black line. Open magnetic field lines are shown in grey and closed magnetic field lines are shown in red. The orbits of 55 Cnc e and b are displayed in black and white respectively.

mass at a rate of $2.23 \times 10^{-14} M_{\odot} \text{ yr}^{-1}$, similar to the solar mass-loss rate of $2 \times 10^{-14} M_{\odot} \text{ yr}^{-1}$, and angular momentum at a rate of $8.16 \times 10^{29} \text{ erg}$.

Figure 8.3 shows the output of our simulation, where the black and white circles represent the orbits of planets e and b, at 3.5 and $26.2 R_{\star}$, respectively. Extracting values from the wind at these orbits allows us to investigate the environment surrounding these planets. Table 8.1 shows the values of the stellar wind properties averaged over one planetary orbit for each of the known planets. As some of the planets are outside the domain of our simulation, we perform an extrapolation of the wind values at planets c, f, and d. While planet e is impacted by a much slower wind, the wind still imparts a higher ram pressure upon planet e than upon planet b, due to the much higher wind density closer to the star (Figure 8.4). Figure 8.3 shows that planet e exists entirely within

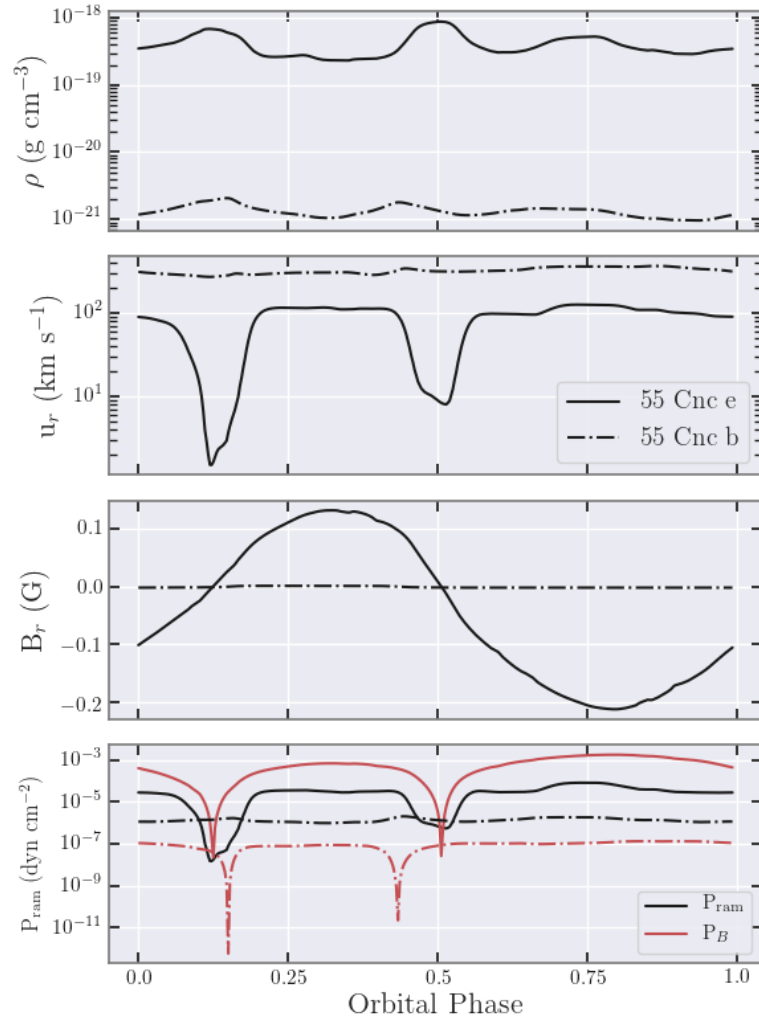


Figure 8.4: The wind parameter surrounding planets e and b, which are within our simulation domain. We show wind density (*top*), velocity (*middle top*), wind magnetic field (*middle bottom*), and wind magnetic and ram pressure (*bottom*).

the Alfvén surface of the wind of 55 Cnc. This means that the wind is magnetically dominated around this planet. Being in a sub-Alfvénic regime means that planet e has a direct connection to the star, i.e., information can travel back to the star. This scenario has ramifications for SPI, as we will discuss in the next section. An important factor to keep in mind that the size of the Alfvén surface depends on the stellar magnetic field and wind base density. We performed two additional sets of simulations, assuming a base density that is three times higher and three times lower than our original simulation. In all these scenarios, the orbit of planet e remains entirely within the Alfvén surface.

Table 8.1: Stellar wind local properties around the known 55 Cnc planets averaged over one planetary orbit.

Orbital Wind Properties	‘e’	‘b’	‘c’	‘f’	‘d’	Reference
orbital period (days)	0.74	14.7	44.4	262	4825	Baluev (2015)
semi-major axis (au)	0.0154	0.1134	0.2373	0.7708	5.957	Bourrier et al. (2018)
semi-major axis (R_{\star})	3.52	25.85	54.10	175.74	1358.17	Bourrier et al. (2018)
stellar wind density (g cm^{-3})	4.5×10^{-19}	7.7×10^{-22}	1.4×10^{-22}	1.2×10^{-23}	1.7×10^{-25}	this work
velocity (km s^{-1})	87.5	343.0	384.5	384.5	384.5	this work
velocity incl. orbital motion (km s^{-1})	244.1	349.4	388.9	385.9	384.6	this work
ram pressure ($10^{-7} \text{ dyn cm}^{-2}$)	313.1	8.69	2.06	0.27	0.008	this work
temperature (10^6 K)	1.08	0.837	0.761	0.666	0.528	this work
magnetic field (nT)	5021	39.02	7.04	0.56	0.007	this work

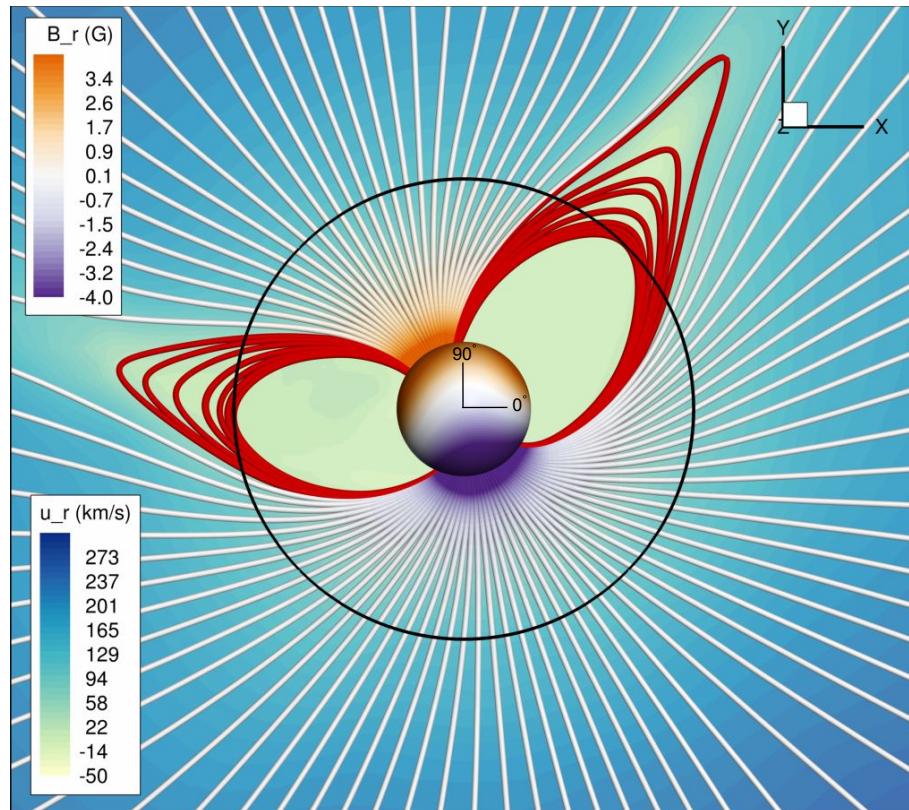


Figure 8.5: Stellar magnetic field lines that intercept planet e as it orbits around the star (black circle). Stellar rotation axis is perpendicular to this orbital plane. The red field lines correspond to closed field regions. The top colourbar shows magnetic field strength (purple-orange) and bottom one shows the stellar wind velocity (yellow-blue).

8.3 STAR-PLANET INTERACTIONS?

Figure 8.5 shows a set of 100 magnetic field lines that intercept planet e as it orbits around the star. If chromospheric hotspots can be formed due to “magnetic SPI” (i.e., through magnetic reconnection or Alfvén wings; Neubauer 1980), the footpoints of the connecting lines would tell us where such hotspots would appear. Figure 8.5 shows that the magnetic field lines linking the planet to the star are a combination of open lines and closed loops. These closed magnetic loops will cause the SPI-related chromospheric spots on the star to move differently from the planetary orbit, with large jumps occurring where the planet moves from one branch of the closed loop to another. This phase lag and jumping effect is evident from Figure 8.6 (see also prediction by McIvor et al. 2006). Recently, Strugarek et al. (2019) showed a similar effect in the case of Kepler-78,

where the magnetic topology of the host star can greatly affect the transient nature of SPI. Although these simulations do not explain the amplitude of enhanced activity observed by [Moutou et al. \(2016\)](#), in stars with stronger magnetic fields (e.g., HD179949, [Fares et al., 2012](#)), the effect may be detectable. As the observed magnetic field of 55 Cnc is largely described by a dipole tilted by 90° to the rotation axis, all of the magnetic field lines that intersect with the planetary orbit lie within the equatorial plane. This is specific for the case of 55 Cnc and specific to the epoch of ZDI observation. For other planetary systems and/or different observing epochs, the magnetic field footpoints may lie above/below the equator, and this is dependent on the large-scale stellar magnetic field geometry. The magnetic field is essential for identifying the theoretical period of modulation for magnetic SPI. An aligned dipole will generate a modulation at the synodic period, while a dipole tilted at 90° will generate a modulation of half the synodic period. In the case of 55 Cnc, because the field is not purely dipolar, the distribution of footpoints in the stellar surface is not symmetric about the rotation axis – the branch of footpoints of positive polarity (Figure 8.5) occupies a smaller range of stellar longitudes than that of negative polarities. This results in a skewed periodic modulation. SPI would be modulated with a cycle shorter than half the synodic period, followed by a cycle longer than half the synodic period, or vice versa. This can also be seen in the top panel of Figure 8.6, where we see that the branch of footpoints above 180° lasts longer than the footpoints below 180° of stellar longitude.

An additional phase lag between the planet and induced stellar activity may be present due to the travel time of Alfvén waves ([Strugarek et al., 2019](#)). We show in Figure 8.7 the Alfvén wave velocities in the vicinity of planet e and the stellar surface. We can see there is a quite a large range of values here, depending heavily on the wind density and magnetic field. Performing a line integral along the magnetic field lines which connect the planetary orbit to the stellar surface will result in the propagation time for Alfvén waves. Through this way, we can determine if any detectable signal that would theoretically be present would lag even further behind than anticipated simply

from magnetic field geometry. For 55 Cnc, this travel time lag is consistently less than 10% of the orbital period, shown in Figure 8.8.

Due to the inclination of the rotation axis of 55 Cnc being near 90° , we cannot strongly constrain the axisymmetric dipolar component of the magnetic field. Unfortunately, this limitation is intrinsic to any Stokes V observations, and additional observations will not simply resolve it. Depending on how strong an unseen $m = 0$ dipole is, this could change the position of hotspots in the surface of the star, mostly in latitude, as the connectivity between the stellar magnetic field and planet could change. In terms of wind modelling, an added component to the magnetic field would imply an Alfvén surface that is larger than the one we computed. In this case, an unseen axisymmetric dipolar component would only reinforce our results that 55 Cnc e orbits inside the Alfvén surface, strengthening possible SPI.

8.3.1 *Energy budget for SPI*

The amount of energy emitted from the magnetic interaction of the planet and the star could be estimated by calculating the Poynting flux at the orbit of the planet. In this case, some assumptions would be necessary, but order of magnitude estimations for the magnetic power available to any anomalous emission could be made, similarly to [Strugarek et al. \(2019\)](#). Note that the values here are most likely upper limits to the energy available to the emission mechanisms from the star, as there will be inefficiencies in energy transfer from the wind/magnetic field to the stellar surface and into radiated emission. The Poynting flux is defined as $\mathbf{S} = \frac{c}{4\pi} \mathbf{E} \times \mathbf{B}$. In the MHD approximation for the electric field we can show that $\mathbf{S} = \frac{1}{4\pi} \mathbf{B} \times (\mathbf{v} \times \mathbf{B})$, which results in the Poynting flux for MHD

$$\mathbf{S} = \frac{1}{4\pi} \mathbf{v}_\perp B^2 \quad (8.1)$$

where \mathbf{v}_\perp is the velocity vector component perpendicular to the magnetic field. Note that \mathbf{S} is calculated at the orbit of the planet, therefore the vector for the velocity includes the

Keplerian velocity: $\mathbf{v} = \mathbf{v}_{\text{wind}} - \mathbf{v}_{\text{kep}}$. To find the velocity perpendicular to the magnetic field, I conduct a vector rejection from \mathbf{v} onto \mathbf{B} :

$$\begin{aligned}\mathbf{v}_{\perp} &= \mathbf{v} - v_{\parallel} \\ \mathbf{v}_{\parallel} &= \frac{\mathbf{v} \cdot \mathbf{B}}{\|\mathbf{B}\|^2} \mathbf{B}\end{aligned}$$

Assuming that 55 Cancri e is non-magnetised, the total available energy for SPI at the orbit of the planet is shown in Figure 8.9 below. The maximum energy available from Poynting flux is $S_{\text{max}} = 1.43 \times 10^6 \text{ erg s}^{-1} \text{ cm}^{-2}$, while the mean flux is $S_{\text{mean}} = 4.0 \times 10^5 \text{ erg s}^{-1} \text{ cm}^{-2}$. The energy available is quite small (even at maximum) compared to the Kepler-78 system (Strugarek et al., 2019). This is likely due to the sensitivity to magnetic field strength and 55 Cancri has a much weaker observed B field than Kepler-78. To estimate the amount of power at the stellar surface, the flux tube from the planet to the stellar surface must be analysed. In this case, as the flux tube approaches the star it will decrease in cross-sectional area (A_{fp}). For simplicity, we assume this shrinking is constant throughout the orbit, however, in reality this will depend on the Alfvén characteristics, and the size of the obstacle (Strugarek et al. 2019, the planet and magnetosphere, if there is one). $A_{fp} = 0.005$ was calculated by obtaining the average of the change in size of magnetic flux tube from the planet 55 Cnc e to the stellar surface. This results in a surface Poynting energy density shown in the bottom panel of Figure 8.9. It is important to note here that the strength of the planetary magnetic field and the size of its magnetosphere will affect the translation of energy from the planet to the stellar surface, and here we assume the planet is unmagnetised (c.f. Cauley et al. 2019 where they estimate planetary magnetic field strengths by inverting the process shown here from observed lines in stellar chromospheres). Nonetheless, this estimation of the power of any anomalous emissions related to SPI is convenient when conducting observations attempting to detect such emission, as it allows it to be gauged against possible power outputs from simulations.

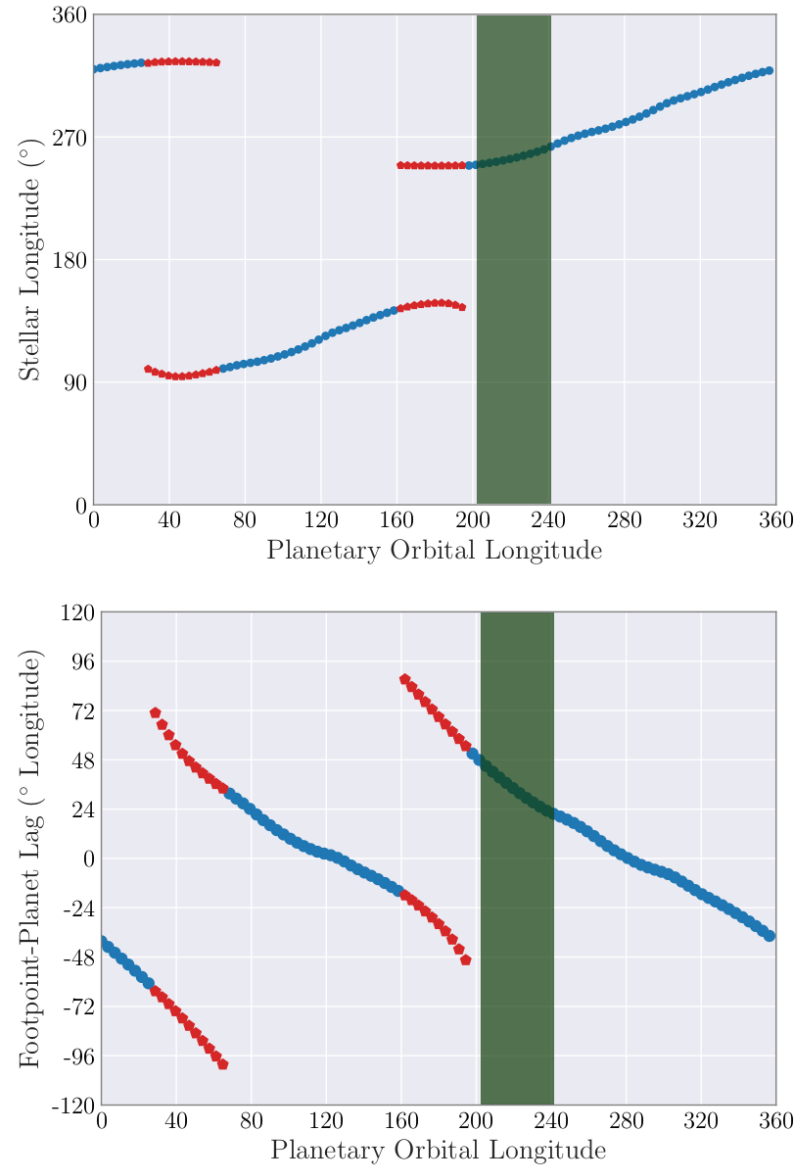


Figure 8.6: *Top:* The longitude of the footpoint on the stellar surface vs. the longitude of the planetary orbit, as defined in Figure 8.5. Footpoints of open (closed) magnetic field lines are shown in blue (red). *Bottom:* Phase lag (difference in longitudes between footpoint and sub-planetary point) versus the orbital longitude of the planet. The footpoints move from lagging behind the planet orbit to ahead of the planet orbit. For the closed loops, it is expected that the SPI will occur at both footpoints of the loop, unless that loop exceeds the Alfvén surface as it extends outwards. The green region displays the planetary transit.

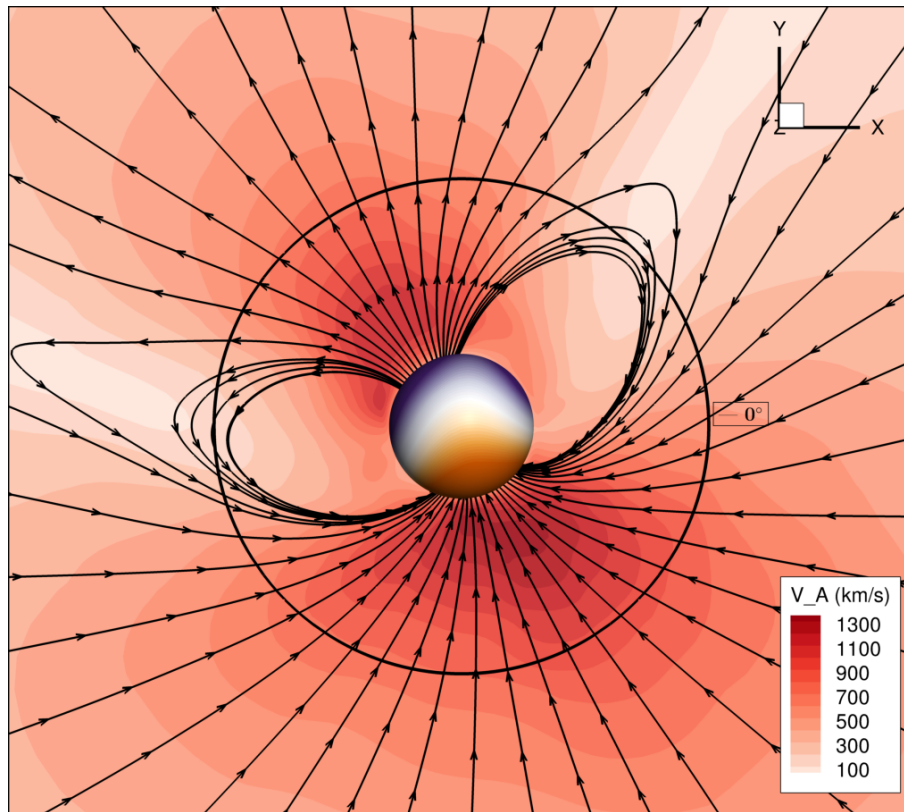


Figure 8.7: This figure shows the propagation speeds of the Alfvén waves from the planet *e* to the surface of the star. Doing a line integral of this data along magnetic field lines connecting the planetary orbit to the star will result in the travel time for the Alfvén wave.

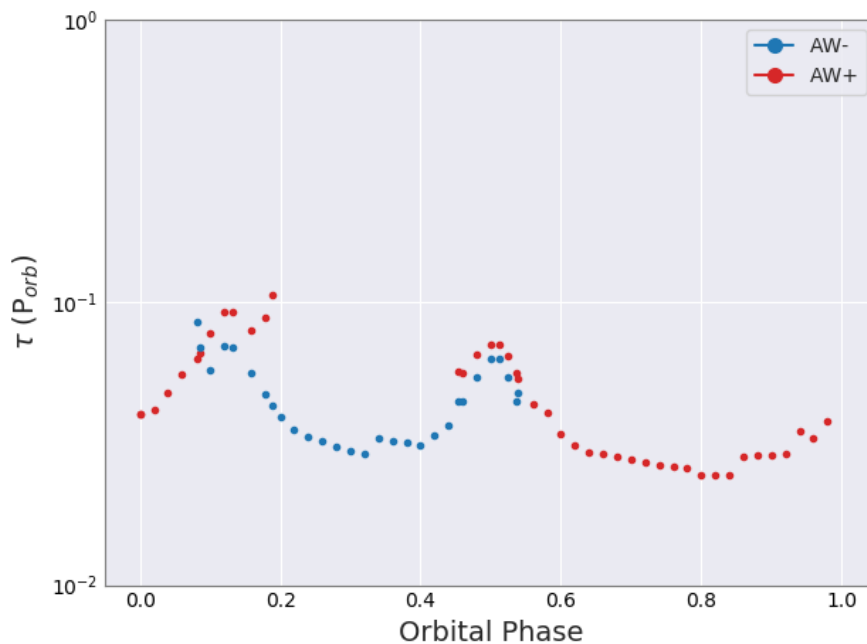


Figure 8.8: This plot shows the travel time of the Alfvén waves, in units of orbital planetary orbital period. We see that at most, the lag due to Alfvén wave propagation is $\sim 10\%$. Red shows one direction of waves, blue shows the opposite direction waves. Peaks occur where the Alfvén velocity is slow, which causes the perturbations by the planet to slow down as they propagate towards the star.

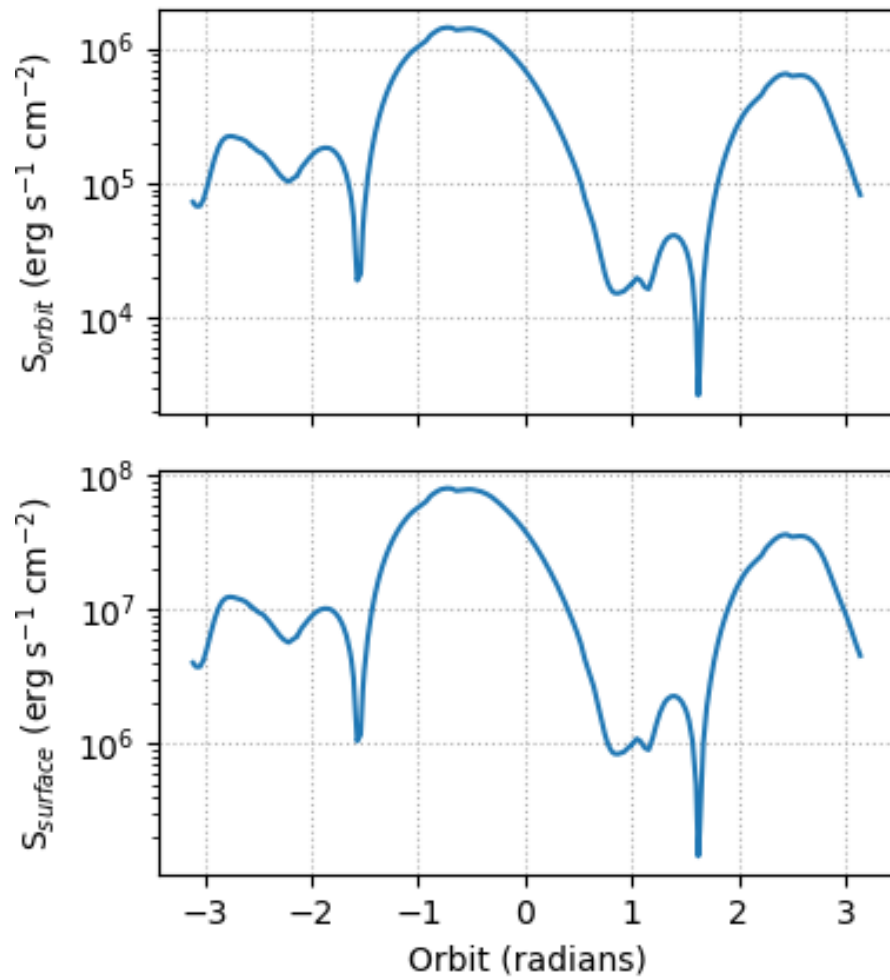


Figure 8.9: The top panel shows the Poynting flux energy density available to the system at the orbit of 55 Cnc e. The lower panel shows the Poynting flux energy density available at the stellar surface due to Alfvén wings channelling energy to the star from the planet.

CONCLUSIONS & FUTURE WORK

This chapter summarises the results presented in the preceding chapters, while also providing indications of future work that would be of importance to the astronomical community. My work has shown novel research into the links between stellar winds and the evolution of their host stars. I have provided evidence for the complex interlinked nature of the physical processes at play in the star-wind-planet systems, first introduced in Part I. I examined the evolution of the solar wind throughout its main sequence, from the youngest age examined here of 100 Myr, to the oldest of ≈ 14 Gyr. I have shown the effects these evolving winds will have on planets such as the Earth, Mars, and commonly observed exoplanets such as Hot Jupiters. The emission of radio waves from these stellar winds have been elusive in the past, due to their rarefied nature. In this work, I have identified candidates could be within the regime of observations through current and future radio instrumentation. Direct radio detections of these stellar winds would provide us with valuable constraints on plasma densities. This thesis also examines the links between stellar winds and the possibilities for observing SPI. I have shown that in

simulations of the 55 Cnc system, SPI can be expected to occur readily. I present the main conclusions from each of the published works below, from which the chapters in this thesis were derived. For a list of the published works that were produced from this research please refer to the PUBLICATIONS at the beginning of this thesis.

9.1 THE SOLAR WIND IN TIME: A CHANGE IN THE BEHAVIOUR OF OLDER WINDS?

Ó Fionnagáin & Vidotto (2018)

In Chapter 4, I simulated winds of a sample of solar analogue stars using 1D polytropic models. I selected the sample based on the ‘Sun in Time’ program, which aimed to investigate possible trends in the evolution of solar activity (Ribas et al., 2005; Güdel, 2007). I presented a new rotation-temperature relation, that I used as an input for the simulations based off X-ray observations from Johnstone & Güdel (2015). I found a break in base wind temperatures at a rotation rate of $1.4 \Omega_{\odot}$. This leads to a sharp decline in wind temperatures as stars spin down past this point. I found stars rotating slower than this follow $T_{\text{wind}} \propto \Omega^{1.20}$, and stars rotating faster follow $T_{\text{wind}} \propto \Omega^{0.37}$.

This dependence between the wind temperature and rotation is rooted in the coronal temperature-rotation dependence. Although the wind and the corona originate from different magnetic geometries (open and closed field lines, respectively), they are both caused by magnetic fields and therefore it is natural to assume that they will follow similar trends. The base temperature of the stellar wind is an important parameter for the simulations. It defines the rate of acceleration of the wind as it is launched from the surface of the star. We use semi-empirical relations to define the base temperature in our simulations since there are currently few observations to constrain this quantity.

I found that the rate of mass loss from these stars appears to decline rapidly after 2 Gyr, with $\dot{M} = 8 \times 10^{-15} M_{\odot} \text{yr}^{-1}$ for a solar-like star of 7 Gyr. This steep decay in \dot{M}

could explain why older stars are inefficient at losing angular momentum, as shown by the atypically high rotation rates found in some older stars (Van Saders et al., 2016).

The simulations provided us with the necessary parameters to estimate the amount of thermal bremsstrahlung emission from the winds of the stars in our sample. I found that their winds only become optically thick below their critical frequencies, $\nu_c \approx 1 - 2$ GHz, which has a shallow dependence on stellar rotation as follows: $\nu_c(> 1.4 \Omega_\odot) \propto \Omega^{0.33}$ and $\nu_c(< 1.4 \Omega_\odot) \propto \Omega^{-0.20}$. I presented estimates for their fluxes at this critical frequency, $S_{\nu,c}$ (Table 4.3). These values are pivotal in guiding efforts to observe these stellar winds, and may explain some previous non-detections (Fichtinger et al., 2017). Equations 4.10 and 4.11 show that there is an inflection in the rotation dependence of ν_c , although the dependence is relatively shallow. Stars rotating faster than $1.4 \Omega_\odot$ have higher cut-off frequencies.

I demonstrated the effects the ageing solar wind has had on the evolving Earth, showing a steep increase in the growth of the magnetosphere since an age of 2 Gyr. I estimated the size of the magnetosphere at young ages to be $\sim 3 R_\oplus$ at 100 Myr. This could have had implications for development of life due to the increased loss of atmosphere and a decrease in shielding ability from the solar wind. I found similar trends in the ionospheric height above the martian surface, yet the effect is not as extreme.

Although the young Sun's mass-loss rate had a shallow decline up to 2 Gyr, the total mass lost is still quite small. From our model I estimate a total mass loss of $0.8\% M_\odot$, which is not enough to solve the faint young Sun paradox. This paradox has been studied at length, and a total mass loss of 3-7% is required to solve it.

The model provides a semi-empirical method for determining base wind temperatures from X-ray observations of stars, which, in turn, allows an in depth analysis of the wind conditions surrounding these stars. The model used in this work did not allow an evaluation of angular momentum losses. This was developed further in Chapter 5 by incorporating realistic distributions of stellar surface magnetism.

9.2 THE SOLAR WIND IN TIME II: 3D

STELLAR WIND STRUCTURE AND RADIO

EMISSION

Ó Fionnagáin et al., (2019)

In Chapter 5, I presented wind simulations of 8 solar-analogues (including 2 of the Sun itself, from Carrington rotations 1983 and 2078) with a range of rotation rates and ages, using a fully 3D MHD code (Figure 5.2). I selected a sample of solar-type stars and constrained the sample to those for which I had observations of their surface magnetic fields (Figure 5.1). Other input parameters for our model include base temperatures and densities retrieved from semi-empirical laws scaled with rotation, Equations 4.1 to 4.3 (Ó Fionnagáin & Vidotto, 2018).

I demonstrated that the angular-momentum loss rate decreases steadily along with mass-loss rate over evolutionary timescales (Figure 5.3). Younger stars ($\approx 500\text{Myr}$) rotating more rapidly ($P_{\text{rot}} \approx 5$ days) display \dot{J} values up to $\approx 10^{32}$ erg. The Sun (4.6 Gyr, $P_{\text{rot}} = 27.2$ days) alternatively exhibits a much lower \dot{J} at minimum $\approx 10^{30}$ erg, with significant variance of one order of magnitude over the solar magnetic cycle. The difference in solar \dot{J} from minimum to maximum is explained by the greater amount of Φ_{open} in the solar maximum case. Given that our solar maximum and minimum simulations differ, this incentivises the monitoring of stars across entire magnetic cycles to deepen our understanding of stellar activity cycles (Jeffers et al., 2017, 2018). I found a similar declining rotation trend with \dot{M} , with slower rotators losing less mass than their faster rotating counterparts. Our solar analogues display a \dot{M} ranging from $1 \times 10^{-13} - 5 \times 10^{-12} M_{\odot} \text{ yr}^{-1}$.

I showed in Figure 7.5 how the density, velocity and ram pressures would vary for a hot Jupiter orbiting any of these solar-like stars at a distance of 0.1 au. It is clear that the sun at minimum provides the lowest ram pressures of the sample ($< 10^5 \text{ dyn cm}^{-2}$) while HD 190771 and χ^1 Ori display the highest ram pressures with a maximum $>$

$80 \times 10^{-5} \text{ dyn cm}^{-2}$. This is useful for any further studies on planetary environment within the winds of G-type stars, with the age and rotation of the host star indirectly playing a role in the final ram pressure impacting the planets and therefore upon atmospheric evaporation. I examined how the velocities of these stellar winds are distributed globally, by taking a histogram of velocities at a distance of 0.1 au, shown in Figure 7.6. I showed that more magnetically active stars display less uniform density distributions and overall have a more complicated structure.

I developed a numerical tool for calculating the thermal radio emission from stellar winds given a simulation grid, removing the need for analytical formulations that have been used in the past (Panagia & Felli, 1975; Fichtinger et al., 2017; Vidotto & Donati, 2017). This tool solves the radiative transfer equation for our wind models, which allowed us to derive radio flux densities, intensities and spectra. I found emission at the μJy level with the winds staying optically thick up to 2 GHz. I compared our calculated flux densities with recent observations and found our predictions agree with the observational upper-limits of κ^1 Ceti and χ^1 Ori (Fichtinger et al. 2017 & Gaidos et al. 2000). Previous radio detections have been interpreted as originating in the chromospheres of solar-like stars and not their winds (Fichtinger et al. 2017 & Villadsen et al. 2014), which is supported by these simulations. The code used here is available on GitHub¹ and has been used in Kavanagh et al. (2018).

The normalised radio flux density emitted from these stellar winds is found to relate to stellar rotation as $S_{\nu,1\text{GHz}} \propto \Omega^{0.7}$. This indicates that promising observational targets would be stars with fast rotation rates within a distance of 10 pc. I showed in Figure 5.5 that the stellar winds of more active close by stars like χ^1 Ori and κ^1 Ceti should be readily detectable with the next generation of radio telescopes such as SKA and ngVLA.

¹ <https://github.com/ofionnad/radiowinds>

9.3 λ ANDROMEDAE: A SOLAR WIND PROXY

POST-MAIN SEQUENCE

Ó Fionnagáin, Vidotto, Petit, Folsom, Neiner, Manchester IV & Folsom (subm)

In Chapter 6, observations of the surface magnetic field of λ Andromedae were presented, a solar mass G8 IV star, along with simulations of its stellar wind. In my simulations, I use two wind models and compared those to radio and X-ray observations of λ And.

BritePol spectropolarimetric observations from August to October 2016 of λ And were obtained and used to derive a surface magnetic field through ZDI. We found a magnetic field that exhibits mostly low order spherical harmonics (78% are $\ell \leq 3$), with most of the magnetic energy in the poloidal component. The geometry of the field is tilted at 90° with respect to the rotation axis of the star. We found a maximum local magnetic field of $B_{r,\max} = 83$ G, with an average of $B_{r,\text{avg}} = 21$ G (Figure 6.2). This is a relatively strong magnetic field compared to the solar magnetic field, considering the evolved state of λ And.

Using the ZDI magnetic map, I carried out simulations using two different models: a hot wind model and a cold wind model. I included a single hot polytropic wind case, for which I found results that agree with previous radio observations. In the cold wave-driven model, I ran a set of simulations varying the input parameters of Poynting flux (S_A) and damping length (ℓ). I found that increasing the Poynting flux consistently results in hotter, faster stellar winds, while the damping length has a more complicated relationship to wind velocity and temperature, with shorter damping lengths depositing more energy near the star.

My hot wind model agrees very well with previous radio observations of λ Andromedae (Bath & Wallerstein, 1976; Bowers & Kundu, 1981; Lang et al., 1985). I found a radio flux density of 0.89 mJy at 4.5 GHz. I have shown the cold wind implementation struggled to reach the same level of radio emission, which I attribute to exponential density decay in the lower atmosphere of our simulations, suggesting a hydrostatic-like

region near the star. This steep density declivity causes the highest density regions to be obscured from the observer by the opaque wind. This agreement with radio observations allows placement of confident constraints on the stellar mass-loss rate.

The mass-loss rate of the hot wind model is $2.91 \times 10^{-9} M_{\odot} \text{ yr}^{-1}$. This result is in line with general trends in evolved low-mass stellar mass-loss rates (see Figure 6.1). The cold wind model produces lower mass-loss rates overall, with a high of $1.7 \times 10^{-10} M_{\odot} \text{ yr}^{-1}$ and a low of $5.6 \times 10^{-13} M_{\odot} \text{ yr}^{-1}$, still much larger than the current accepted solar mass-loss rate. The hot wind simulation displays a strong spin-down rate of $\dot{J} = 2.2 \times 10^{35} \text{ erg}$. The cold wind model maximum spin-down rate is similar at $\dot{J} = 1.1 \times 10^{35} \text{ erg}$ for a dipolar magnetic field, and $\dot{J} = 4.5 \times 10^{34} \text{ erg}$ for the observed surface magnetic field. As there is no consensus on low-mass stellar spin-down rates for stars older than our Sun, it is difficult to place these spin-down rates in a solar evolutionary context, but these angular momentum-loss rates are much larger than current accepted values for \dot{J}_{\odot} (Finley et al., 2018).

The maximum temperatures I found exist in the cold wind simulations ($T_{\text{max}} = 11 \text{ MK}$; model A1), but are notably confined to small regions in the wind. There is a maximum temperature of 1 MK in the hot wind model, which is markedly below the derived temperatures from X-ray observations. This is due to the lack of small-scale magnetic field in these simulations. It is generally accepted that the small-scale field, which can produce strong local magnetic fields, produces the hottest plasma, which emits hot X-ray lines. The ZDI technique is not sensitive to these small-scale fields, and so they are excluded from our simulation. Furthermore, the stellar winds emanate from open field regions, whereas it is the closed field regions that produce this hot plasma.

Overall, we expect the wind of λ Andromedae to be most similar to our hot wind scenario. Assuming the hottest coronal regions arise from the small-scale magnetic field, it is not surprising we do not see this in our hot wind model. Importantly, the hot wind model provides very good agreement with observed radio flux densities, strengthening the support for our derived mass-loss rate. Simulating the winds of sub-giant solar-type stars seems to be adequately described by using polytropic models to produce global

wind parameters. However, we expect that this is not the case for stars further along the red giant branch which possess no corona at all. Our hot wind model constrains the mass-loss rate of λ Andromedae to $1.3 \times 10^{-10} M_{\odot} \text{ yr}^{-1}$, within the expected range of mass-loss rates for a stars of a similar ilk.

9.4 THE CIRCUMSTELLAR ENVIRONMENT OF 55 CNC: THE SUPER-EARTH 55 CNC E AS A PRIMARY TARGET FOR STAR-PLANET INTERACTIONS

[Folsom, Fionnagáin, Fossati, Vidotto, Moutou, Petit, Dragomir & Donati \(2020\)](#)

In Chapter 8, spectropolarimetric observations of 55 Cnc were made to detect the stellar magnetic field. These were used to map the large-scale magnetic field using ZDI, in which a largely tilted dipolar field was found. This magnetic map was used as input for a 3D MHD simulation of the stellar wind, and the wind properties at the positions of the known planets, were estimated. I found that 55 Cnc e orbits entirely within the Alfvén surface of the stellar wind, which implies magnetic field lines connect planet e to the star, allowing for magnetic star-planet interactions. Using these simulations, I estimated the possible position of chromospheric hotspots due to this interaction, and found they would be offset in phase from the planet’s orbital position, and that apparent activity due to SPI may be modulated at close to double the orbital or synodic period. Recently, [Sulis et al. \(2019\)](#) detected a stellar flux modulation in phase with the orbital period of planet e and the activity of the star. This modulation may be caused by magnetic interaction occurring as a consequence of the planet lying entirely within the Alfvén surface of the star. Unfortunately, the magnetic field observations and the observations of [Sulis et al. \(2019\)](#) have been done more than two years apart. Given that SPI depends on the topology of stellar magnetic fields, studies of planet-star interactions in general

should be conducted contemporaneously to spectropolarimetric monitoring whenever possible (e.g. [Fares et al., 2017](#)). Thanks to its high photometric precision, the CHEOPS mission is going to be in the position to confirm or dispute this connection.

9.5 FUTURE WORK

The research in this thesis has provided insight into evolution of solar type stars along their main sequence, through simulations of their stellar winds. I calculated and predicted thermal radio flux densities for a range of solar-mass stellar winds across the MS. Following this work, I extended the study to include a more evolved solar-mass stellar wind, and while λ And is not a solar twin, it sets the stage for further 3D MHD simulations and magnetic field observations of evolved solar-mass stars to constrain this regime in low-mass stellar research. While the work in this thesis has been fruitful in quantifying the trends of solar-mass stellar evolution, there is much that can follow. A main theme in this work was the detection of thermal radio bremsstrahlung from the winds of low-mass stars. While this is more easily done for the most evolved stars as their winds become more dense, the MS solar-mass stellar winds are much more elusive. In this thesis I have shown that new radio telescopes on the horizon will be able to detect these winds directly. Specifically SKA-2 will possess the necessary sensitivity to detect $\sim 1 \mu\text{Jy}$ radio flux densities at the emission frequencies of $\sim 1 \text{ GHz}$. These direct detections would provide constraints on the wind density at various heights in the astrosphere, which in turn would provide constraints on stellar mass-loss rates and angular-momentum loss. This would be a pivotal discovery in the study of low-mass stars. It would also allow a more accurate estimation of stellar wind radio emission to be made while searching for exoplanetary sources. While they are expected to emit at different frequencies, eliminating possible emission sources for radio flux will help with the certainty of observations of exoplanets.

9.5.1 *Winds of solar-mass stars off the main sequence*

This thesis provided the surface magnetic field and 3D MHD wind simulations for a sub-giant solar-mass star. I determined the wind parameters that are most agreeable with radio observations of the wind, allowing constraints of certain wind parameters such as mass-loss rate. As this sub-giant still retains its hot corona, it is not yet a fully evolved red giant, as evident from Figure 6.1. There is research into the driving mechanisms of winds of evolved late-type low-mass stars, mostly carried out in 1D (Yasuda et al., 2019). A significant portion of this research is into Alfvén wave driven winds. Expanding this research to include observed surface magnetic fields of red giants and implementing those in full 3D MHD Alfvén wave-driven wind simulations would be very interesting. This is a challenging task as solar-mass red giants are expected to have weak surface magnetic fields (due to magnetic flux conservation), and rotate very slowly, so very sensitive and long-exposure observations would be required to get a full surface magnetic field map. However, as shown by Konstantinova-Antova et al. (2013), these evolved, late-type stars are magnetically active. Examining how these fields drive the stellar winds is integral to our understanding of the evolution of stellar winds and the mechanisms of cold winds.

In the particular case of λ And, which is discussed extensively in this thesis, it would be extremely useful to obtain concurrent observations of the star in X-ray, radio, and spectropolarimetric observations to study the stellar magnetic field. This would allow strong constraints to be placed on the sources of emission in the star and the stellar corona. The ZDI map could be used to project coronal shapes using potential field models as well used to create 3D wind models for the star. Combined with radio and X-ray an in depth coronal structure and wind driving mechanism could be derived.

On the other end of stellar evolution, there are pre-MS stars. Young solar-type stars are expected to have a large range of rotation rates (Gallet & Bouvier, 2015) and saturated X-ray activity (Wright et al., 2011). This suggests hot coronal temperatures, and high magnetic field strengths. Combining this together with full 3D MHD simulations

would be interesting to see the evolution of angular momentum in the early stages of the stellar life. As shown in [Gallet & Bouvier \(2015\)](#) young low-mass stars have a wide range of rotation rates, studying this further to try and quantify this effect would be interesting in itself. Not only would this provide essential insight into the early life of stars, but also into the conditions surrounding planet formation. As most planets are carved out from debris disks, it would be interesting to investigate how early stage stellar winds interact with these disks in 3D MHD simulations.

9.5.2 *Investigating wind effects on exoplanets*

Throughout Part III I have shown the range of effects that a stellar wind (from the same mass star over its lifetime) can have on a planet. Both small terrestrial planets such as Earth, and larger expanded hot Jupiters are affected by being embedded in the extreme environment of the stellar wind. This promising area of research will allow an entire 3D view of the effects of stellar winds on exoplanets. Determining how the atmospheric, surface, and chemical conditions on these planets develop and change over time is an essential component for exoplanetary evolution studies.

I have shown in this work that SPI could occur on 55 Cancri, between the star and planet e. [Strugarek et al. \(2019\)](#) has shown that this effect could also occur in the Kepler-78 system. Observational work of star-planet interactions are promising and it is an area that is still yet to be fully exploited. With the combination of observations and simulations, great progress could be made here. In the future, this technique could be applied to many star-planet systems, and in particular, full 3D MHD simulations of the planetary environment and variations on imposed planetary magnetic field strengths and topologies could give a concise idea as to which systems are most promising to observe with regards to SPI.

9.5.3 *Transient events in low-mass stellar systems*

In recent years there has been a lot of excitement around the first detection of a CME on another star (Argiroffi et al., 2019). This was done through X-ray observations of spectral lines suggesting the outward motion of plasma material, linked to a recent flaring event. CMEs are rapid expulsions of material from the surface of a star from highly active regions on the stellar surface. In the sun, CMEs are observed to emit plasma emission through Langmuir waves, but given the high density and temperature material they contain, some thermal emission could also be generated. Using the radio code written in Python, discussed earlier in this thesis, it could be insightful to apply this to active stars and their winds to determine if these CMEs are visible at various frequencies or if the wind could be a determining factor in radiative absorption. Could that be why no stellar CMEs have been directly detected in radio? Using the relationship between active flaring regions and CME sizes on the Sun has been used to determine the hypothetical CME mass on other active stars (Aarnio et al., 2011; Drake et al., 2013; Osten & Wolk, 2015). These works estimate that the CMEs would be rather large given the extreme flaring seen in other stars.

First order approximations of the thermal emission from these CMEs could be made quite easily using the code described in this thesis. An example of this is shown in Figure 9.1, where I introduce a CME of mass 7.5×10^{16} g to a stellar wind scenario. This mass is on the larger scale for solar CMEs but still not as large as the ones predicted on more active stars (Moschou et al., 2019). We can see that while the CME changes the radio flux density, it is not a significant amount, and in fact actually reduces the flux density due to absorption in the very highest density regions. The case without the CME exhibits a radio flux density of $S_\nu = 1.74 \mu\text{Jy}$, and the case with the CME exhibits a radio flux density of $S_\nu = 1.36 \mu\text{Jy}$. As the CMEs have a large density, radiative absorption begins to play a significant role and suppress the specific radio intensity. The other radio emission from the shock front however would be expected to be much stronger. This emits at the plasma frequency due to Langmuir waves in the shock. Without know-

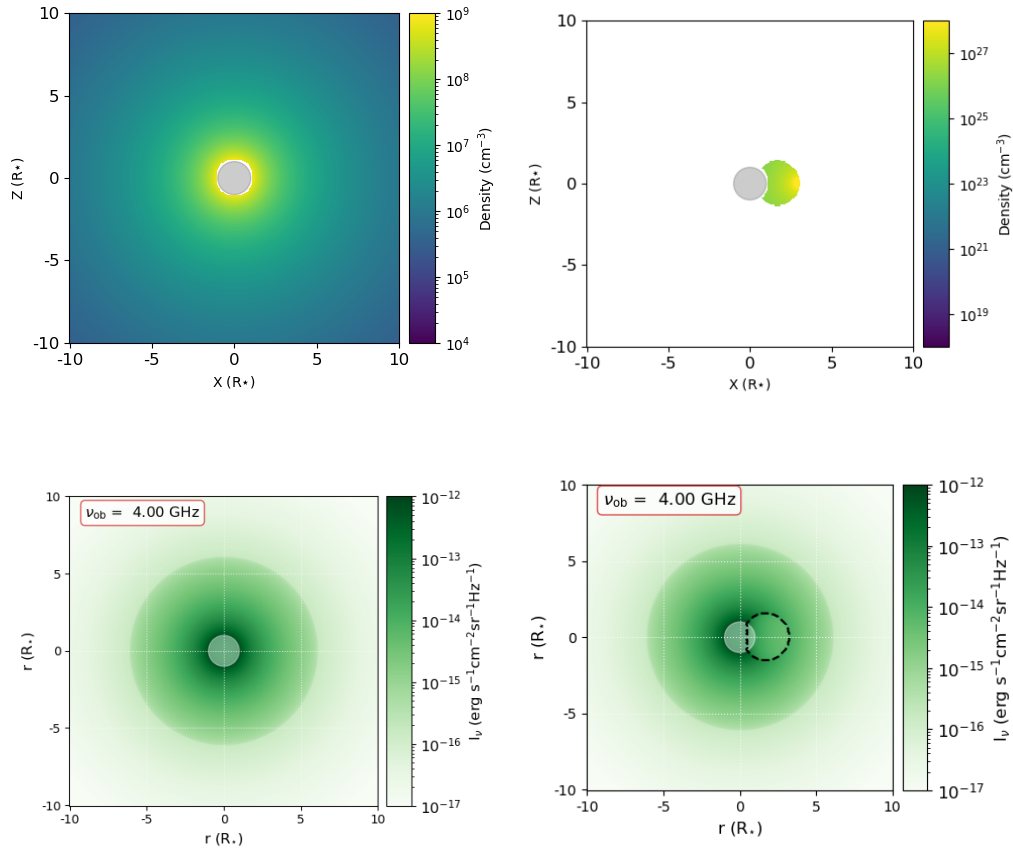


Figure 9.1: The top panels show density, while the bottom panels show the specific radio intensities at 4 GHz. The panels on the right include a CME of mass 7.5×10^{16} g and a $2 R_{\star}$ extension. While the CME produces an optically thick region (it is much denser than the surrounding wind), the flux density is not changed as the emission from the densest regions are absorbed.

ing the wind density and including the increase in density at the shock front make it difficult to determine the radio frequency that these CMEs would appear with. Stellar wind simulations could aid in that regard, with the wind density allowing a calculation for the expected density at typical distances of CMEs from the star, giving an estimate for their emission frequencies. Expanding from the first order approximation for emission, one could run full 3D MHD simulations for flux emergence and CME propagation through the stellar wind for a number of stars, similarly to work by [Liu et al. \(2008\)](#) and [Alvarado-Gómez et al. \(2019\)](#). The research in [Alvarado-Gómez et al. \(2020\)](#) is quite unique and interesting and warrants much further work in this area. Amendments to the code in this thesis could be made to include the plasma emission due to Langmuir waves at the shock front, giving reasonable estimates for the radio emission for type-II

radio bursts on other stars. The flare X-ray emission – CME-mass relationship for solar CMEs could be used to constrain CME masses for other stars by extending to more active stars which exhibit very strong X-ray flares (Moschou et al., 2019).

Detection of such events is still extremely difficult and formation/emission could be suppressed for multiple reasons including CME magnetic confinement, Alfvénic suppression, the stellar wind conditions, density, etc., the ionospheric cut-off frequency on the Earth and importantly the transient nature of these objects. Such objects and our ambitions to detect them are excellent motivation to place a radio telescope in space.

9.5.4 *Cosmic rays & solar wind evolution*

The heliosphere is constantly being bombarded by galactic cosmic rays. The spectrum of these cosmic rays has been measured at Earth many times (McDonald, 1998; Shikaze et al., 2007; Adriani et al., 2013). We also know the interstellar galactic cosmic ray spectrum as measured by Voyager 1 (Cummings et al., 2016). The differences in these spectra is due to the *solar wind*, as the cosmic rays are subjected to diffusion, advection, and momentum advection. Therefore, the effect of the solar wind as it changes throughout time can be quantified by using the evolutionary parameters found in this work (see eg. Rodgers-Lee et. al, *submitted*). Cosmic rays themselves can have significant effects on the atmospheres of planets by ionising different layers, with the highest energies reaching planetary surfaces Rimmer & Helling (2013). They may, in fact, have been instrumental in the beginning of life on Earth (Mojzsis et al., 1996). Whether this is through ionisation of planetary surfaces allowing complex chemistry to occur, or the lack thereof allowing biological life to form, it is clear cosmic rays play a critical role in the development of life on a planet. Quantifying the effects of stellar winds on these cosmic ray spectra is therefore quite important, for which the work in this thesis on the evolutionary properties of the solar wind is essential. Looking forward, the cosmic ray spectra on exoplanetary surfaces could be quantified using models of stellar winds, cosmic ray spectra modification and propagation through exoplanet atmospheres

to determine the cosmic ray environment on exoplanet surfaces. Given the cosmic ray spectrum of the local ISM, one could assume this is ubiquitous for the solar neighbourhood. There are plenty of stars with exoplanets in this region. Once you include the stellar cosmic rays for the star, which could be scaled based on the solar values, you could estimate the cosmic rays impinging on the exoplanetary surface.

9.5.5 *Understanding the solar wind driving mechanisms*

In recent years there have been many advances in solar space missions. The Parker Solar Probe was launched in 2018, and will be the first spacecraft to encounter the solar corona. By the end of its lifetime, its closest approach will be $< 10 R_{\odot}$, making large elliptical passes close to the Sun. The probe possesses the instruments to measure the plasma parameters, which will be the first *in situ* measurements of the solar wind so close to the solar surface. With much modelling of the environment the Parker Solar Probe will encounter (van der Holst et al., 2019), the first observations are currently being published (McComas et al., 2019; Kasper et al., 2019; Howard et al., 2019; Bale et al., 2019), which can be contrasted with the previous models. These will greatly influence our understanding of the solar coronal environment.

The ESA mission, Solar Orbiter was launched recently in 2020. This spacecraft orbits the Sun at a distance of $\sim 60 R_{\odot}$, well within the orbit of Mercury. Designed to observe and probe the inner heliosphere and the nascent solar wind, it carries on board both *in situ* and remote measurement instruments, which will be pivotal in understanding the wind driving mechanisms that occur in the lower solar wind. Combined with theoretical models and simulations, this new era of solar wind measurements will provide invaluable information to advance our understanding of the formation and processes in low-mass stellar winds. Very recently, the first images from the instruments on board have been published (Figure 9.2). A ubiquitous feature of the solar surface, revealed for the first time by these images, have been called ‘campfires’. They are om-

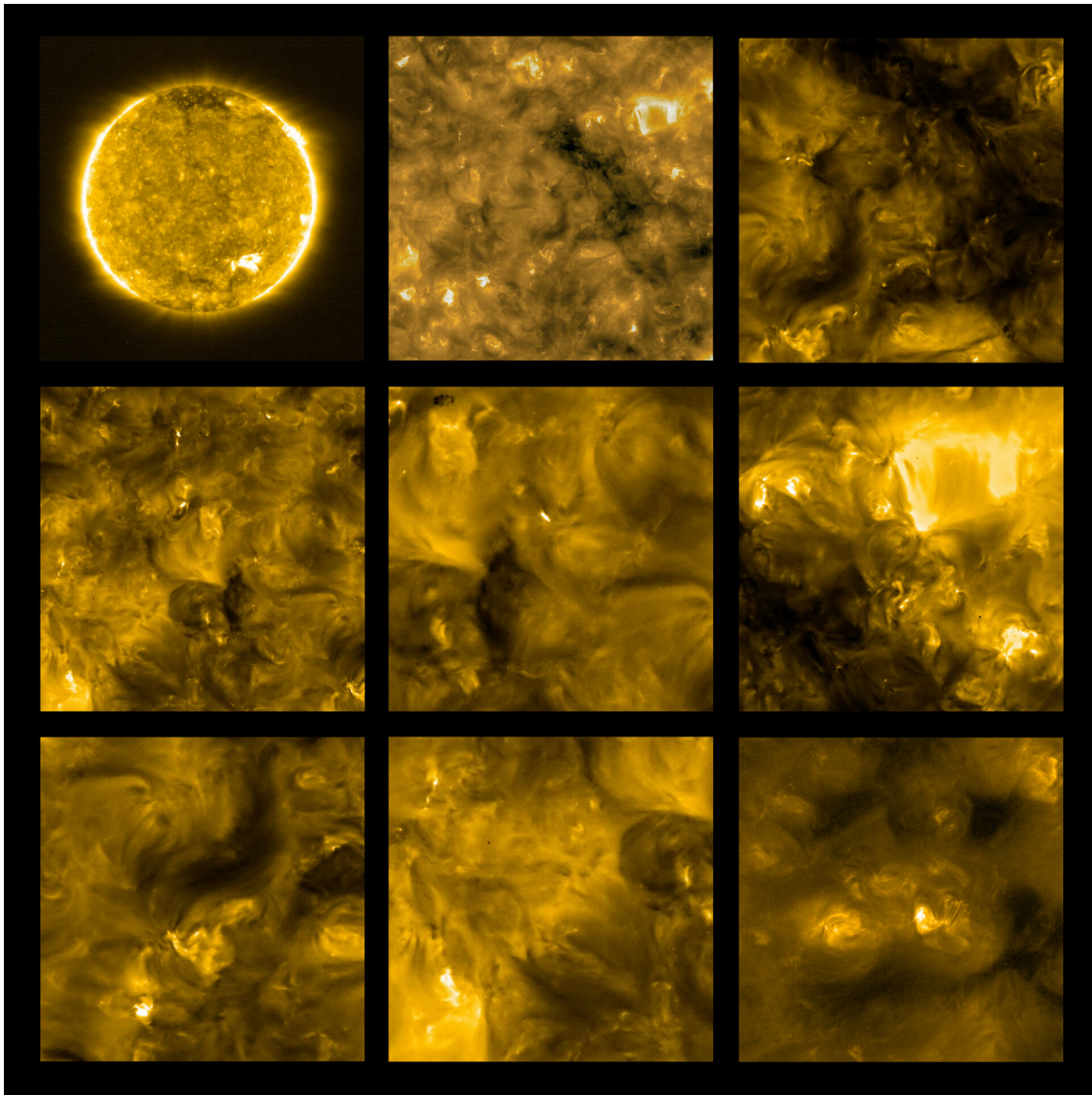


Figure 9.2: This image shows the first release of observations from the EUI instrument on Solar Orbiter. There is unprecedented detail in these images, showing miniature eruptions all over the solar surface, newly coined as ‘campfires’, due to their appearance. Credit: Solar Orbiter/ESA/NASA.

nipresent miniature eruptions that could be contributing to the high temperatures of the solar corona and the origin of the solar wind.

The research presented in this thesis provided a novel insight into the evolution of the solar wind in time, through the use of many different stellar wind modelling tools. I adopted numerical methods from 1 to 3 dimensions, including hydrodynamic flows and magnetic fields to simulate the winds of solar analogues. I provided quantitative links from stellar evolution to the stellar winds. I calculated radio fluxes from solar-mass stars, showing that in the near future, state-of-the-art radio telescopes such as SKA will be able to detect these stellar winds. This thesis also conducted an examination of SPI, looking at a case study of 55 Cancri for wind simulations. Future research that attempts to further our understanding of the link between stellar winds, their hosts, and orbiting planets, will be essential in providing a holistic view of the star-planet system. This research will further the understanding of our own Sun, and other stars similar to the Sun, and the physical mechanisms at play.

BIBLIOGRAPHY

- Aarnio A. N., Stassun K. G., Hughes W. J., McGregor S. L., 2011, *Sol. Phys.*, 268, 195
- Abbott D. C., Biegging J. H., Churchwell E., Cassinelli J. P., 1980, *Astrophys. J.*, 238, 196
- Abbott D. C., Beiging J. H., Churchwell E., Torres A. V., 1986, *Astrophys. J.*, 303, 239
- Adriani O., et al., 2013, *Astrophys. J.*, 765, 91
- Airapetian V. S., Usmanov A. V., 2016, *Astrophys. J. Lett.*, 817, L24
- Alazraki G., Couturier P., 1971, *Astron. & Astrophys.*, 13, 380
- Alfvén H., 1942, *Nature*, 150, 405
- Alfvén H., 1957, *Tellus Series A*, 9, 92
- Altschuler M. D., Newkirk G., 1969, *Sol. Phys.*, 9, 131
- Alvarado-Gómez J. D., Drake J. J., Cohen O., Moschou S. P., Garraffo C., 2018, *Astrophys. J.*, 862, 93
- Alvarado-Gómez J. D., Drake J. J., Garraffo C., Moschou S. P., Cohen O., Yadav R. K., Frascetti F., 2019, arXiv e-prints, p. [arXiv:1912.12314](https://arxiv.org/abs/1912.12314)

- Alvarado-Gómez J. D., et al., 2020, *Astrophys. J.*, 895, 47
- Anderson K. R., Storch N. I., Lai D., 2016, *Mon. Not. R. Astron. Soc.*, 456, 3671
- Argiroffi C., et al., 2019, *Nature Astronomy*, 3, 742
- Aschwanden M. J., 2004, *Physics of the Solar Corona. An Introduction*
- Audard M., Güdel M., Sres A., Raassen A., Mewe R., 2003, *Astron. Astrophys.*, 398, 1137
- Aurière M., 2003, in Arnaud J., Meunier N., eds, *EAS Publications Series Vol. 9, EAS Publ. Ser.* p. 105
- Aurière M., et al., 2015, *Astron. Astrophys.*, 574, A90
- Ayres T. R., Brown A., Harper G. M., 2003, *Astrophys. J.*, 598, 610
- Bagenal F., 2013, in Oswald T., French L., Kalas P., eds, *Planets, Stars Stellar Syst. 3 Sol. Stellar Planet. Syst.* Springer Netherlands, Dordrecht, pp 251–307, http://link.springer.com/10.1007/978-94-007-5606-9_{_}6
- Bale S. D., et al., 2019, *Nature*, 576, 237
- Baliunas S., Guinan E., Dupree A., 1984, *Astrophys. J.*, 282, 733
- Baluev R. V., 2015, *Mon. Not. Royal Ast. Soc.*, 446, 1493
- Bath G. T., Wallerstein G., 1976, *Publ. Astron. Soc. Pacific*, 88, 759
- Beck P. G., et al., 2017, *Astron. & Astrophys.*, 602, A63
- Belcher J., 1987, *Science (80-)*, 238, 170
- Bertucci C., Duru F., Edberg N., Fraenz M., Martinecz C., Szego K., Vaisberg O., 2011, *Space Sci. Rev.*, 162, 113
- Biermann L., 1951, *ZAp*, 29, 274
- Booth R. S., Poppenhaeger K., Watson C. A., Aguirre V. S., Silva Aguirre V., Aguirre V. S., Wolk S. J., 2017, *Mon. Not. R. Astron. Soc.*, 471, 1012

- Booth R., Poppenhaeger K., Watson C., Silva Aguirre V., Stello D., Bruntt H., 2020, *Mon. Not. Royal Ast. Soc.*, 491, 455
- Boro Saikia S., Jeffers S. V., Petit P., Marsden S., Morin J., Folsom C. P., 2015, *Astron. & Astrophys.*, 573, A17
- Boro Saikia S., Jin M., Johnstone C. P., Lüftinger T., Güdel M., Airapetian V. S., Kislyakova K. G., Folsom C. P., 2020, *Astron. & Astrophys.*, 635, A178
- Bourrier V., Lecavelier des Etangs A., Ehrenreich D., Tanaka Y. A., Vidotto A. A., 2016, *Astron. & Astrophys.*, 591, A121
- Bourrier V., et al., 2018, *Astron. & Astrophys.*, 619, A1
- Bower G. C., Loinard L., Dzib S., Galli P. A. B., Ortiz-León G. N., Moutou C., Donati J.-F., 2016, *Astrophys. J.*, 830, 107
- Bowers P., Kundu M., 1981, *Astron. J.*, 86, 569
- Brown S. F., Donati J.-F., Rees D. E., Semel M., 1991, *Astron. Astrophys.*, 250, 463
- Brown A. G. A., Vallenari A., Prusti T., de Bruijne J. H. J., Babusiaux C., Zurbach C., Zwitter T., 2018, *Astron. Astrophys.*, 616, A1
- Brun A. S., Browning M. K., 2017, *Living Rev. Sol. Phys.*, 14, 4
- Callingham J., Vedantham H., Shimwell T., Pope B. J., LoTSS Team 2020, in American Astronomical Society Meeting Abstracts. American Astronomical Society Meeting Abstracts. p. 342.02
- Castor J. I., Abbott D. C., Klein R. I., 1975, *Astrophys. J.*, 195, 157
- Cauley P. W., Shkolnik E. L., Llama J., Bourrier V., Moutou C., 2018, *AJ*, 156, 262
- Cauley P. W., Shkolnik E. L., Llama J., Lanza A. F., 2019, *Nature Astronomy*, 3, 1128
- Chabrier G., 2003, *PASP*, 115, 763
- Chandran B. D. G., Dennis T. J., Quataert E., Bale S. D., 2011,] 10.1088/0004-637X/743/2/197
- Chapman S., Zirin H., 1957, *Smithsonian Contributions to Astrophysics*, 2, 1

- Chassefière E., Leblanc F., 2004, *Planet. Space Sci.*, 52, 1039
- Chen P. F., 2011, *Living Reviews in Solar Physics*, 8, 1
- Christensen U. R., Holzwarth V., Reiners A., 2009, *Nature*, 457, 167
- Claret A., 2004, *Astron. & Astrophys.*, 428, 1001
- Coleman Paul J. J., 1967, *Planet. Space Sci.*, 15, 953
- Cox A. N., Pilachowski C. A., 2002, *Allen's Astrophysical Quantities*. Vol. 53, Springer New York, doi:10.1007/978-1-4612-1186-0
- Cranmer S. R., 2017, *Astrophys. J.*, 840, 114
- Cranmer S. R., Saar S. H., 2007, arXiv e-prints, pp astro-ph/0702530
- Cranmer S. R., Saar S. H., 2011, *Astrophys. J.*, 741, 54
- Cranmer S. R., Winebarger A. R., 2019, *ARA&A*, 57, 157
- Cranmer S. R., van Ballegooijen A. A., Edgar R. J., 2007, *Astrophys. J. Suppl. Ser.*, 171, 520
- Cravens T. E., 1997, in Cravens T., ed., Vol. 1, Cambridge Atmos. Sp. Sci. Ser., doi:10.1017/CBO9780511529467, <http://adsabs.harvard.edu/abs/2004pssp.book...C>
- Crosley M. K., et al., 2016, *Astrophys. J.*, 830, 24
- Cummings A. C., et al., 2016, *Astrophys. J.*, 831, 18
- Cuntz M., Shkolnik E., 2002, *Astron. Nachrichten*, 323, 387
- Cuntz M., Saar S. H., Musielak Z. E., 2000, *Astrophys. J.*, 533, L151
- Daley-Yates S., Stevens I. R., 2019, *Mon. Not. Royal Ast. Soc.*, 483, 2600
- Davenport J. R. A., 2015, PhD thesis, University of Washington
- Davenport J. R. A., Covey K. R., Clarke R. W., Boeck A. C., Cornet J., Hawley S. L., 2019, *Astrophys. J.*, 871, 241

- DeRosa M. L., Brun A. S., Hoeksema J. T., 2010, *Proc. Int. Astron. Union*, 6, 94
- Demory B.-O., Gillon M., Madhusudhan N., Queloz D., 2016a, *Mon. Not. Royal Ast. Soc.*, 455, 2018
- Demory B.-O., et al., 2016b, *Nature*, 532, 207
- Dempsey R. C., Linsky J. L., Fleming T. A., Schmitt J. H. M. M., 1993, *ApJS*, 86, 599
- Dere K., Del Zanna G., Young P., Landi E., Sutherland R., 2019, *Astrophys. J.s*, 241, 22
- Donati J. F., Brown S. F., 1997, *Astron. & Astrophys.*, 326, 1135
- Donati J. F., Landstreet J. D., 2009, *ARA&A*, 47, 333
- Donati J.-F., Henry G., Hall D., 1995, *Astron. Astrophys.*, 293, 107
- Donati J.-F., Semel M., Carter B. D., Rees D. E., Cameron A. C., 1997, *Mon. Not. R. Astron. Soc.*, 291, 658
- Donati J. F., et al., 2003, *Mon. Not. Royal Ast. Soc.*, 345, 1145
- Donati J.-F., et al., 2006, *MNRAS*, 370, 629
- Dorren J. D., Guinan E. F., 1994, *Astrophys. J.*, 428, 805
- Dragomir D., Matthews J. M., Winn J. N., Rowe J. F., 2014, in Haghhighipour N., ed., *IAU Symposium Vol. 293, Form. Detect. Charact. Extrasolar Habitable Planets*. pp 52–57 ([arXiv:1302.3321](https://arxiv.org/abs/1302.3321))
- Dragomir D., Bean J., Kreidberg L., Stevenson K. B., Line M. R., 2017, in *Am. Astron. Soc. Meet. Abstr. # 229*. p. 301.05
- Drake S. A., Linsky J. L., 1986, *Astron. J.*, 91, 602
- Drake J. J., Ball B., Eldridge J. J., Ness J.-U. U., Stancliffe R. J., 2011, *Astron. J.*, 142, 144
- Drake J. J., Cohen O., Yashiro S., Gopalswamy N., 2013, *Astrophys. J.*, 764, 170
- Dupree A. K., Brickhouse N. S., Hanson G. J., 1996, in , *Astrophys. Extrem. Ultrav.* Springer, pp 141–145

- Ehrenreich D., et al., 2015, *Nature*, 522, 459
- Fares R., et al., 2012, *Mon. Not. Royal Ast. Soc.*, 423, 1006
- Fares R., et al., 2017, *Mon. Not. R. Astron. Soc.*, 471, 1246
- Feulner G., 2012, *Rev. Geophys.*, 50, RG2006
- Fichtinger B., Güdel M., Mutel R. L., Hallinan G., Gaidos E., Skinner S. L., Lynch C., Gayley K. G., 2017, *Astron. Astrophys.*, 599, A127
- Finley A. J., Matt S. P., See V., 2018, preprint ([arXiv:1808.00063](https://arxiv.org/abs/1808.00063))
- Folsom C. P., Petit P., Bouvier J., Morin J., Lèbre A., Donati J.-F., 2016, *Mon. Not. R. Astron. Soc.*, 10, 113
- Folsom C. P., et al., 2018a, *Mon. Not. R. Astron. Soc.*, 474, 4956
- Folsom C., et al., 2018b, *Mon. Not. Royal Ast. Soc.*, 481, 5286
- Folsom C. P., Fionnagáin D. Ó., Fossati L., Vidotto A. A., Moutou C., Petit P., Dragomir D., Donati J. F., 2020, *Astron. & Astrophys.*, 633, A48
- Frasca A., Biazzo K., Tassan-Gomponi G., Evren S., Lanzafame A., 2008, *Astron. Astrophys.*, 479, 557
- Gaia Collaboration et al., 2018, *Astron. & Astrophys.*, 616, A10
- Gaidos E. J., Güdel M., Blake G. A., 2000, *Geophys. Res. Lett.*, 27, 501
- Gaidos E., et al., 2020, *Mon. Not. Royal Ast. Soc.*,
- Gallet F., Bouvier J., 2013, *Astron. & Astrophys.*, 556, A36
- Gallet F., Bouvier J., 2015, *Astron. & Astrophys.*, 577, A98
- Gary D. E., Linsky J. L., 1981, *Astrophys. J.*, 250, 284
- Gombosi T. I., van der Holst B., Manchester W. B., Sokolov I. V., 2018, *Living Rev. Sol. Phys.*, 15, 4
- Gondoin P., 2017, *Astron. & Astrophys.*, 599, A122

- Gough D. O., 1981, *Sol. Phys.*, 74, 21
- Güdel M., 2002, *ARA&A*, 40, 217
- Güdel M., 2007, *Living Reviews in Solar Physics*, 4, 3
- Güdel M., Guinan E. F., Skinner S. L., 1997, *Astrophys. J.*, 483, 947
- Güdel M., Guinan E. F., Skinner S., 1998, *ASP Conf. Ser.*, 154, 1041
- Guedel M., Benz A. O., 1993, *Astrophys. J. Lett.*, 405, L63
- Guinan E., Engle S., 2009, in Mamajek E., Soderblom D., Wyse R., eds, *IAU Symposium Vol. 258, Ages Stars*. pp 395–408 ([arXiv:0903.4148](https://arxiv.org/abs/0903.4148)), [doi:10.1017/S1743921309032050](https://doi.org/10.1017/S1743921309032050)
- Hale G. E., 1908, *Astrophys. J.*, 28, 315
- Hanson W. B., Sanatani S., Zuccaro D. R., 1977, *J. Geophys. Res.*, 82, 4351
- Harri A. M., et al., 2014, *J. Geophys. Res. E Planets*, 119, 82
- Hartmann L., MacGregor K., 1980, *Astrophys. J.*, 242, 260
- Hayashi K., 2005, *Astrophys. J.s*, 161, 480
- Hollweg J. V., 1973, *Astrophys. J.*, 181, 547
- Hollweg J. V., 1976, 81, 1649
- Hollweg J., 1978, *Rev. Geophys. Sp. Phys.*, 16, 689
- Hollweg J. V., 1986, *J. Geophys. Res.*, 91, 4111
- Holzwarth V., Jardine M., 2007, *Astron. & Astrophys.*, 463, 11
- Howard A. W., et al., 2012, *Astrophys. J.s*, 201, 15
- Howard R. A., et al., 2019, *Nature*, 576, 232
- Huber D., et al., 2013, *Science (80-.)*, 342, 331
- Ip W.-H., Kopp A., Hu J.-H., 2004, *Astrophys. J. Lett.*, 602, L53

- Ivanova N., Taam R. E., 2003, *Astrophys. J.*, 599, 516
- Jeffers S. V., Saikia S. B., Barnes J. R., Petit P., Marsden S. C., Jardine M. M., Vidotto A. A., 2017, *Mon. Not. R. Astron. Soc. Lett.*
- Jeffers S. V., et al., 2018, *Mon. Not. R. Astron. Soc.*, 479, 5266
- Johnstone C. P., Güdel M., 2015, *Astron. Astrophys.*, 578, A129
- Johnstone C. P., Güdel M., Lüftinger T., Toth G., Brott I., 2015a, *Astron. & Astrophys.*, 577, A27
- Johnstone C. P., Güdel M., Brott I., Lüftinger T., 2015b, *Astron. & Astrophys.*, 577, A28
- Kasper J. C., et al., 2019, *Nature*, 576, 228
- Kavanagh R. D., Vidotto A. A., Ó Fionnagáin D., 2018, 10, 1
- Kawaler S. D., 1988, *Astrophys. J.*, 333, 236
- Keppens R., Goedbloed J. P., 1999a, *Astron. & Astrophys.*, 343, 251
- Keppens R., Goedbloed J. P., 1999b, *Astrophys. J.*, 530, 1036
- Killen R., et al., 2007, *Space Sci. Rev.*, 132, 433
- King J. R., Villarreal A. R., Soderblom D. R., Gulliver A. F., Adelman S. J., 2003, *Astron. J.*, 125, 1980
- Kiraga M., Stepien K., 2007, *Acta Astronomica*, 57, 149
- Kitchatinov L., Nepomnyashchikh A., 2017, *Mon. Not. R. Astron. Soc.*, 470, 3124
- Kochukhov O., Makaganiuk V., Piskunov N., 2010, *Astron. & Astrophys.*, 524, A5
- Konstantinova-Antova R., et al., 2013, *Bulgarian Astronomical Journal*, 19, 14
- Kraft R. P., 1967, *Astrophys. J.*, 150, 551
- Krüger H., et al., 2003, *Geophys. Res. Lett.*, 30, 2101
- Kulow J. R., France K., Linsky J., Loyd R. O. P., 2014, *Astrophys. J.*, 786, 132

- Kurucz R. L., 1993, SYNTHE spectrum synthesis programs and line data
- Lamers H. J. G. L. M., Cassinelli J. P., 1999, Introduction to Stellar Winds
- Lammer H., Selsis F., Ribas I., Guinan E. F., Bauer S. J., Weiss W. W., 2003, *Astrophys. J. Lett.*, 598, L121
- Landi Degl'Innocenti E., Landolfi M., 2004, Polarization in Spectral Lines. Vol. 307, doi:10.1007/978-1-4020-2415-3,
- Lang K., Willson R., Pallavicini R., 1985, VLA Observations of Late-Type Stars. p. 267, doi:10.1007/978-94-009-5420-5_38
- Lang P., Jardine M., Morin J., Donati J.-F., Jeffers S., Vidotto A. A., Fares R., 2014, *Mon. Not. R. Astron. Soc.*, 439, 2122
- Lee C. O., et al., 2017, *J. Geophys. Res. Sp. Phys.*, 122, 2768
- Lehmann L. T., et al., 2017, *Mon. Not. R. Astron. Soc. Lett.*, 466, L24
- Lehmann L. T., Jardine M. M., Mackay D. H., Vidotto A. A., 2018, *Mon. Not. R. Astron. Soc.*, 478, 4390
- Ligi R., et al., 2016, *Astron. & Astrophys.*, 586, A94
- Lim J., White S. M., 1996, *Astrophys. J.*, 462, L91
- Linsky J. L., Haisch B. M., 1979, *Astrophys. J.*, 229, L27
- Liu M. C., Fischer D. a., Graham J. R., Lloyd J. P., Marcy G. W., Butler R. P., 2002, *Astrophys. J.*, 571, 519
- Liu Y. C. M., Opher M., Cohen O., Liewer P. C., Gombosi T. I., 2008, *Astrophys. J.*, 680, 757
- López-Santiago J., Montes D., Crespo-Chacón I., Fernández-Figueroa M., 2006, *Astrophys. J.*, 643, 1160
- Lorenzo-Oliveira D., et al., 2018, preprint ([arXiv:1806.08014](https://arxiv.org/abs/1806.08014))
- Maldonado J., Martínez-Arnáiz R. M., Eiroa C., Montes D., Montesinos B., 2010, *Astron. Astrophys.*, 521, A12

- Mamajek E. E., Hillenbrand L. A., 2008, *Astrophys. J.*, 687, 1264
- Manchester IV W. B., et al., 2008, *Astrophys. J.*, 684, 1448
- Marsh T. R., Horne K., 1988, *Mon. Not. Royal Ast. Soc.*, 235, 269
- Massarotti A., Latham D. W., Stefanik R. P., Fogel J., 2008, *AJ*, 135, 209
- Matt S. P., MacGregor K. B., Pinsonneault M. H., Greene T. P., 2012, *Astrophys. J.*, 754, L26
- McComas D. J., Ebert R. W., Elliott H. A., Goldstein B. E., Gosling J. T., Schwadron N. A., Skoug R. M., 2008, *Geophys. Res. Lett.*, 35, L18103
- McComas D. J., et al., 2019, *Nature*, 576, 223
- McDonald F. B., 1998, *Space Sci. Rev.*, 83, 33
- McIvor T., Jardine M., Holzwarth V., 2006, *Mon. Not. R. Astron. Soc. Lett.*, 367, L1
- Meléndez J., et al., 2014, *Astrophys. J.*, 791, 14
- Messina S., Guinan E. F., 2003, *Astron. Astrophys.*, 409, 1017
- Mestel L., 1999, *Stellar magnetism*. Oxford University Press
- Metcalf T. S., Egeland R., 2019, *Astrophys. J.*, 871, 39
- Metcalf T. S., Creevey O. L., Davies G. R., 2015, *Astrophys. J. Lett.*, 811, L37
- Metcalf T. S., Egeland R., van Saders J., 2016, *Astrophys. J. Lett.*, 826, L2
- Metcalf T. S., Kochukhov O., Ilyin I. V., Strassmeier K. G., Godoy-Rivera D., Pinsonneault M. H., 2019, *Astrophys. J.*, 887, L38
- Miller B. P., Gallo E., Wright J. T., Dupree A. K., 2012, *Astrophys. J.*, 754, 137
- Mojzsis S. J., Arrhenius G., McKeegan K. D., Harrison T. M., Nutman A. P., Friend C. R. L., 1996, *Nature*, 384, 55
- Morin J., et al., 2008, *Mon. Not. Royal Ast. Soc.*, 390, 567

- Morin J., Donati J. F., Petit P., Delfosse X., Forveille T., Jardine M. M., 2010, *Mon. Not. Royal Ast. Soc.*, 407, 2269
- Moschou S.-P., Drake J., Cohen O., Alvarado-Gomez J. D., Garraffo C., Frascchetti F., 2019
- Moutou C., Donati J. F., Lin D., Laine R., Hatzes A., 2016, *Mon. Not. Royal Ast. Soc.*, 459, 1993
- Müller H.-R., Zank G. P., Wood B. E., 2001, *Astrophys. J.*, 551, 495
- Murdin P., 2000, *Encyclopedia of Astronomy and Astrophysics*
- Neiner C., Wade G., Marsden S., Blazère A., 2017, in *Second BRITTE-Constellation Sci. Conf. Small Satell. - Big Sci.* pp 86–93 ([arXiv:1611.03285](https://arxiv.org/abs/1611.03285))
- Neubauer F., 1980, *J. Geophys. Res.*, 85, 1171
- Neugebauer M., Snyder C. W., 1962, *Science*, 138, 1095
- Newman M. J., Rood R. T., 1977, *Science (80-)*, 198, 1035
- Nicholson B. A., et al., 2016, *Mon. Not. R. Astron. Soc.*, 459, 1907
- Nielsen M. B., Gizon L., Cameron R. H., Miesch M., 2019, *Astron. & Astrophys.*, 622, A85
- Noble L. M., Scarf F. L., 1963, *Astrophys. J.*, 138, 1169
- Noyes R. W., Hartmann L. W., Baliunas S. L., Duncan D. K., Vaughan A. H., 1984, *Astrophys. J.*, 279, 763
- Ó Fionnagáin D., 2018, ofionnad/radiowinds: Calculating Thermal Bremsstrahlung Emission from Stellar Winds, [doi:10.5281/zenodo.3607434](https://doi.org/10.5281/zenodo.3607434), <https://doi.org/10.5281/zenodo.3607434>
- Ó Fionnagáin D., Vidotto A. A., 2018, *Mon. Not. Royal Ast. Soc.*, 476, 2465
- Ó Fionnagáin D., Vidotto A., Petit P., Folsom C., Neiner C., Manchester IV W., Folsom C., subm., *Mon. Not. Royal Ast. Soc.*
- Ó Fionnagáin D., et al., 2019, *Mon. Not. R. Astron. Soc.*, 483, 873

- O’Gorman E., Harper G. M., Vlemmings W., 2017, *Astron. Astrophys.*, 599, A47
- O’Gorman E., Coughlan C. P., Vlemmings W., Varenus E., Sirothia S., Ray T. P., Olofsson H., 2018, *Astron. & Astrophys.*, 612, A52
- Ortolani A., Maggio A., Pallavicini R., Sciortino S., Drake J., Drake S., 1997, *Astron. Astrophys.*, 325, 664
- Osten R. A., Wolk S. J., 2015, *Astrophys. J.*, 809, 79
- Osten R. A., Crosley M. K., Gudel M., Kowalski A. F., Lazio J., Linsky J., Murphy E., White S., 2018
- Pallavicini R., Golub L., Rosner R., Vaiana G. S., Ayres T., Linsky J. L., 1981, *Astrophys. J.*, 248, 279
- Panagia N., Felli M., 1975, *Astron. Astrophys.*, 39, 1
- Pantolmos G., Matt S. P., 2017, *Astrophys. J.*, 849, 83
- Parker E. N., 1958, *Astrophys. J.*, 128, 664
- Parker E. N., 1960, *Astrophys. J.*, 132, 821
- Parker E. N., 1965, *Space Sci. Rev.*, 4, 666
- Parks J. R., et al., 2015, arXiv Prepr. arXiv1508.04755
- Perryman M., et al., 1998, *Astron. Astrophys.*, 331, 81
- Petit P., Donati J.-F., Collier Cameron A., 2002, *Mon. Not. Royal Ast. Soc.*, 334, 374
- Petit P., et al., 2004a, *Mon. Not. Royal Ast. Soc.*, 348, 1175
- Petit P., et al., 2004b, *Mon. Not. Royal Ast. Soc.*, 351, 826
- Petit P., et al., 2008, *Mon. Not. R. Astron. Soc.*, 388, 80
- Petit P., Dintrans B., Morgenthaler A., Van Grootel V., Morin J., Lanoux J., Aurière M., Konstantinova-Antova R., 2009, *Astron. Astrophys.*, 508, L9

- Petit P., Louge T., Théado S., Paletou F., Manset N., Morin J., Marsden S., Jeffers S., 2014, *PASP*, 126, 469
- Petit P., et al., in prep.
- Pinsonneault M. H., Kawaler S. D., Demarque P., 1990, *ApJS*, 74, 501
- Piskunov N., Kochukhov O., 2002, *Astron. & Astrophys.*, 381, 736
- Pizzo V., 1978, *J. Geophys. Res.*, 83, 5563
- Pizzo V. J., 1980, *J. Geophys. Res.*, 85, 727
- Pneuman G. W., Kopp R. A., 1971, *Sol. Phys.*, 18, 258
- Pope B. J. S., Withers P., Callingham J. R., Vogt M. F., 2019, *Mon. Not. Royal Ast. Soc.*, 484, 648
- Potter A. E., Killen R. M., Reardon K. P., Bida T. A., 2013, *Icarus*, 226, 172
- Powell K. G., Roe P. L., Linde T. J., Gombosi T. I., De Zeeuw D. L., 1999, *J. Comput. Phys.*, 154, 284
- Preston T., 1899, *Nature*, 59, 224
- Priest E., 2003, *Adv. Sp. Res.*, 32, 1021
- Prusti T., et al., 2016, *Astron. Astrophys.*, 595, A1
- Puls J., Vink J. S., Najarro F., 2008, *Astron. & Astrophys.r*, 16, 209
- Raassen A. J. J., Ness J.-U., Mewe R., van der Meer R. L. J., Burwitz V., Kaastra J. S., 2003, *Astron. Astrophys.*, 400, 671
- Ramirez I., et al., 2014, *Astron. Astrophys.*, 572, A48
- Rappaport S., et al., 2012, *Astrophys. J.*, 752, 1
- Rees D., Semel M., 1979, *Astron. & Astrophys.*, 74, 1
- Reiners A., 2012, *Living Reviews in Solar Physics*, 9, 1

- Réville V., Brun A. S., Strugarek A., Matt S. P., Bouvier J., Folsom C. P., Petit P., 2015, *Astrophys. J.*, 814, 99
- Réville V., Folsom C. P., Strugarek A., Brun A. S., 2016, *Astrophys. J.*, 832, 145
- Reynolds S. P., 1986, *Astrophys. J.*, 304, 713
- Ribas I., Guinan E. F., Güdel M., Audard M., 2005, *Astrophys. J.*, 622, 680
- Ridden-Harper A., et al., 2016, *Astron. & Astrophys.*, 593, A129
- Rimmer P. B., Helling C., 2013, *Astrophys. J.*, 774, 108
- Roe P. L., 1981, *Journal of Computational Physics*, 43, 357
- Rosén L., Kochukhov O., Hackman T., Lehtinen J., 2016, *Astron. & Astrophys.*, 593, A35
- Rosenqvist L., Opgenoorth H., Buchert S., McCrea I., Amm O., Lathuillere C., 2005, *J. Geophys. Res. Sp. Phys.*, 110, A09S23
- Rucinski S. M., et al., 2004, *PASP*, 116, 1093
- Rybicki G. B., Lightman A. P., 1979, *Radiative processes in astrophysics*
- Sagan C., Mullen G., 1972, *Science*, 177, 52
- Saikia S. B., et al., 2018
- Sanz-Forcada J., Brickhouse N., Dupree A., 2003, *Astrophys. J.*, 145, 147
- Sanz-Forcada J., Favata F., Micela G., 2004, *Astron. Astrophys.*, 416, 281
- Scarf F. L., Noble L. M., 1965, *Astrophys. J.*, 141, 1479
- Schatzman E., 1962, *Annales d'Astrophysique*, 25, 18
- Schmitt J. H. M. M., Collura A., Sciortino S., Vaiana G. S., Harnden F. R. J., Rosner R., 1990, *Astrophys. J.*, 365, 704
- Schrijver C. J., Mewe R., Walter F. M., 1984, *Astron. & Astrophys.*, 138, 258

- Scuderi S., Panagia N., Stanghellini C., Trigilio C., Umana G., 1998, *Astron. & Astrophys.*, **332**, 251
- See V., Jardine M., Vidotto A. A., Petit P., Marsden S. C., Jeffers S. V., do Nascimento J. D., 2014, *Astron. Astrophys.*, 570, A99
- See V., et al., 2017, *Mon. Not. R. Astron. Soc.*
- See V., et al., 2019a, *Astrophys. J.*, **876**, 118
- See V., et al., 2019b, *Astrophys. J.*, **886**, 120
- Semel M., 1989, *Astron. & Astrophys.*, **225**, 456
- Semel M., Donati J. F., Rees D., 1993, *Astron. & Astrophys.*, 278, 231
- Shibata K., Magara T., 2011, *Living Rev. Sol. Phys.*, 8, 6
- Shikaze Y., et al., 2007, *Astroparticle Physics*, **28**, 154
- Shkolnik E., Walker G. A. H., Bohlender D. A., 2002, in American Astronomical Society Meeting Abstracts. p. 46.16
- Shkolnik E., Walker G. A. H., Bohlender D. A., Gu P., Kurster M., 2005, *Astrophys. J.*, 622, 1075
- Shkolnik E., Bohlender D. A., Walker G. A. H., Collier Cameron A., 2008, *Astrophys. J.*, 676, 628
- Shoda M., Yokoyama T., Suzuki T. K., 2018a, *Astrophys. J.*, **853**, 190
- Shoda M., Yokoyama T., Suzuki T. K., 2018b, *Astrophys. J.*, **860**, 17
- Skumanich A., 1972, *Astrophys. J.*, **171**, 565
- Sokolov I. V., et al., 2013, *Astrophys. J.*, 764, 23
- Solanki S. K., et al., 2010, *Astrophys. J.*, **723**, L127
- Spitzer L., Härm R., 1953, *Phys. Rev.*, 89, 977
- Stauffer J., Schultz G., Kirkpatrick J. D., 1998, *Astrophys. J. Let.*, 499, 12

- Steinolfson R. S., Dryer M., Nakagawa Y., 1975, *J. Geophys. Res.*, **80**, 1223
- Steinolfson R. S., Suess S. T., Wu S. T., 1982, *Astrophys. J.*, **255**, 730
- Sterenborg M. G., Cohen O., Drake J. J., Gombosi T. I., 2011, *J. Geophys. Res. Sp. Phys.*, **116**, A01217
- Stokes G. G., 1852, *Philosophical Transactions of the Royal Society of London Series I*, **142**, 463
- Strugarek A., Brun A. S., Matt S. P., Réville V., 2015, *Astrophys. J.*, **815**, 111
- Strugarek A., Brun A., Donati J. F., Moutou C., Réville V., 2019, *arXiv e-prints*, 881, 136
- Sturrock P. A., Hartle R. E., 1966, *Phys. Rev. Lett.*, **16**, 628
- Süli E., Mayers D. F., 2003, *An introduction to numerical analysis*. Cambridge university press
- Sulis S., et al., 2019, *Astron. & Astrophys.*, **631**, A129
- Suzuki T. K., 2002, *Astrophys. J.*, **578**, 598
- Suzuki T. K., 2018, *Publ. Astron. Soc. Japan*, **70**, 1
- Suzuki T. K., Imada S., Kataoka R., Kato Y., Matsumoto T., Miyahara H., Tsuneta S., 2013, *Publ. Astron. Soc. Japan*, **65**, 98
- Tarduno J. A., et al., 2010, *Science*, **327**, 1238
- Telleschi A., Güdel M., Briggs K., Audard M., Ness J.-U., Skinner S. L., 2005, *Astrophys. J.*, **622**, 653
- Toro E. F., 2013, *Riemann solvers and numerical methods for fluid dynamics: a practical introduction*. Springer Science & Business Media
- Tóth G., et al., 2005, *Journal of Geophysical Research (Space Physics)*, **110**, A12226
- Usmanov A. V., Goldstein M. L., Besser B. P., Fritzer J. M., 2000, *J. Geophys. Res.*, **105**, 12675
- Usmanov A. V., Goldstein M. L., Matthaeus W. H., 2014, *Astrophys. J.*, **788**, 43
- Valenti J. A., Fischer D. A., 2005, *Astrophys. J. Suppl. Ser.*, **159**, 141

- Van Doorselaere T., Wardle N., Del Zanna G., Jansari K., Verwichte E., Nakariakov V. M., 2011, *Astrophys. J.*, **727**, L32
- Van Saders J. L., Ceillier T., Metcalfe T. S., Aguirre V. S., Pinsonneault M. H., García R. A., Mathur S., Davies G. R., 2016, *Nature*, **529**, 181
- Vedantham H. K., et al., 2020, *Nature Astronomy*,
- Verdini A., Velli M., Mattheaus W. H., Oughton S., Dmitruk P., 2010, *Astrophys. J.*, **708**, L116
- Vidal-Madjar A., Lecavelier des Etangs A., Désert J. M., Ballester G. E., Ferlet R., Hébrard G., Mayor M., 2003, *Nature*, **422**, 143
- Vidotto A. A., 2016a, in 19th Cambridge Workshop on Cool Stars, Stellar Systems, and the Sun (CS19). Cambridge Workshop on Cool Stars, Stellar Systems, and the Sun. p. 147 ([arXiv:1608.03833](https://arxiv.org/abs/1608.03833)), [doi:10.5281/zenodo.60058](https://doi.org/10.5281/zenodo.60058)
- Vidotto A. A., 2016b, *Mon. Not. R. Astron. Soc.*, **459**, 1533
- Vidotto A., 2017, *EPJ Web Conf.*, **160**, 05011
- Vidotto A. A., 2019, arXiv e-prints, p. [arXiv:1911.10915](https://arxiv.org/abs/1911.10915)
- Vidotto A. A., Bourrier V., 2017, *Mon. Not. Royal Ast. Soc.*, **470**, 4026
- Vidotto A. A., Donati J.-F., 2017, *Astron. Astrophys.*, **602**, A39
- Vidotto A. A., Jardine M., Opher M., Donati J.-F., Gombosi T. I., 2011, in Johns-Krull C., Browning M., West A., eds, Astronomical Society of the Pacific Conference Series Vol. 2, *Ast. Soc. Pac. Conf. Ser.*. pp 1–8 ([arXiv:1101.1233v1](https://arxiv.org/abs/1101.1233v1))
- Vidotto A. A., Fares R., Jardine M., Donati J. F., Opher M., Moutou C., Catala C., Gombosi T. I., 2012, *Mon. Not. R. Astron. Soc.*, **423**, 3285
- Vidotto A. A., Jardine M., Morin J., Donati J. F., Lang P., Russell A. J. B., 2013, *Astron. & Astrophys.*, **557**, A67
- Vidotto A. A., Jardine M., Morin J., Donati J. F., Opher M., Gombosi T. I., 2014a, *Mon. Not. Royal Ast. Soc.*, **438**, 1162

- Vidotto A. A., et al., 2014b, *Mon. Not. R. Astron. Soc.*, 441, 2361
- Vidotto A. A., Fares R., Jardine M., Moutou C., Donati J. F., 2015, *Mon. Not. Royal Ast. Soc.*, 449, 4117
- Vidotto A. A., Lehmann L., Jardine M., Pevtsov A., 2018, 12, 1
- Vidotto A. A., Feeney N., Groh J. H., 2019, *Mon. Not. Royal Ast. Soc.*, 488, 633
- Villadsen J., Hallinan G., Bourke S., Güdel M., Rupen M., 2014, *Astrophys. J.*, 788, 112
- Wang Y.-M., 1998, in Donahue R., Bookbinder J., eds, *Astronomical Society of the Pacific Conference Series Vol. 154*, *Ast. Soc. Pac. Conf. Ser.* p. 131, <http://adsabs.harvard.edu/abs/1998ASPC..154..131W>
- Warren H. P., Brooks D. H., 2009, *Astrophys. J.*, 700, 762
- Weaire D., O'Connor S., 1987, *Annals of Science*, 44, 617
- Weber J. E., Davis Jr. L., 1967, *Astrophys. J.*, 148, 217
- Williams P. K. G., Cook B. A., Berger E., 2014, *Astrophys. J.*, 785, 9
- Winn J. N., et al., 2011, *Astrophys. J.*, 737, L18
- Withers P., 2009, *Adv. Sp. Res.*, 44, 277
- Wood B. E., 2018, in *J. Phys. Conf. Ser.* p. 12028 ([arXiv:1809.01109](https://arxiv.org/abs/1809.01109)), [doi:10.1088/1742-6596/1100/1/012028](https://doi.org/10.1088/1742-6596/1100/1/012028)
- Wood B. E., Linsky J. L., 2006, *Astrophys. J.*, 643, 444
- Wood B. E., Linsky J. L., 2010, *Astrophys. J.*, 717, 1279
- Wood B. E., Muller H., Zank G. P., Linsky J. L., 2002, *Astrophys. J.*, 574, 412
- Wood B. E., Müller H. R., Zank G. P., Linsky J. L., Redfield S., 2005, *Astrophys. J.*, 628, L143
- Wood B. E., Müller H.-R., Redfield S., Edelman E., 2014, *Astrophys. J.*, 781, L33
- Wright A. E., Barlow M. J., Michael J., 1975, *Mon. Not. R. Astron. Soc.*, 170, 41

- Wright N. J., Drake J. J., Mamajek E. E., Henry G. W., 2011, *Astrophys. J.*, 743, 48
- Xia C., Teunissen J., El Mellah I., Chané E., Keppens R., 2018, *ApJS*, 234, 30
- Yadav R. K., Thorngren D. P., 2017, *Astrophys. J. Lett.*, 849, L12
- Yasuda Y., Suzuki T. K., Kozasa T., 2019,] 10.3847/1538-4357/ab23f7
- Zeeman P., 1897, *Nature*, 55, 347
- Zuluaga J. I., Bustamante S., Cuartas P. A., Hoyos J. H., 2013, *Astrophys. J.*, 770, 23
- Zuluaga J. I., Mason P. A., Cuartas-Restrepo P. A., 2016, *Astrophys. J.*, 818, 160
- do Nascimento, Jr. J.-D., et al., 2016, *Astrophys. J.*, 820, L15
- ud-Doula A., Owocki S. P., 2002, *Astrophys. J.*, 576, 413
- van der Holst B., Sokolov I. V., Meng X., Jin M., Manchester W. B. I., Tóth G., Gombosi T. I., 2014, *Astrophys. J.*, 782, 81
- van der Holst B., Manchester W. B. I., Klein K. G., Kasper J. C., 2019, *Astrophys. J. Lett.*, 872, L18
- von Braun K., et al., 2011, *Astrophys. J.*, 740, 49

Published & submitted works

The solar wind in time: a change in the behaviour of older winds?

D. Ó Fionnagáin[★] and A. A. Vidotto[★]

School of Physics, Trinity College Dublin, College Green, Dublin 2, Ireland

Accepted 2018 February 13. Received 2018 January 11; in original form 2017 September 21

ABSTRACT

In this paper, we model the wind of solar analogues at different ages to investigate the evolution of the solar wind. Recently, it has been suggested that winds of solar type stars might undergo a change in properties at old ages, whereby stars older than the Sun would be less efficient in carrying away angular momentum than what was traditionally believed. Adding to this, recent observations suggest that old solar-type stars show a break in coronal properties, with a steeper decay in X-ray luminosities and temperatures at older ages. We use these X-ray observations to constrain the thermal acceleration of winds of solar analogues. Our sample is based on the stars from the ‘Sun in Time’ project with ages between 120 and 7000 Myr. The break in X-ray properties leads to a break in wind mass-loss rates (\dot{M}) at roughly 2 Gyr, with $\dot{M} (t < 2 \text{ Gyr}) \propto t^{-0.74}$ and $\dot{M} (t > 2 \text{ Gyr}) \propto t^{-3.9}$. This steep decay in \dot{M} at older ages could be the reason why older stars are less efficient at carrying away angular momentum, which would explain the anomalously rapid rotation observed in older stars. We also show that none of the stars in our sample would have winds dense enough to produce thermal emission above 1–2 GHz, explaining why their radio emissions have not yet been detected. Combining our models with dynamo evolution models for the magnetic field of the Earth, we find that, at early ages (≈ 100 Myr), our Earth had a magnetosphere that was three or more times smaller than its current size.

Key words: stars: mass-loss – stars: solar-type – stars: winds, outflows.

1 INTRODUCTION

Solar analogue stars lose angular momentum and mass through stellar winds. These magnetized winds determine how the rotation of a star will decay with time (Weber & Davis 1967; Vidotto et al. 2011), although the exact processes behind this occurrence are not fully understood. These winds are assumed to be homologous to the solar wind at different ages, which is composed of a fully ionized plasma that streams outwards from the Sun (Parker 1958). As these stars are similar to our own Sun age, various properties seem to evolve over time, such as rotation and magnetic activity (Skumanich 1972; Dorren & Guinan 1994; Ribas et al. 2005; Guinan & Engle 2009; Vidotto et al. 2014). Since the magnetic activity of a star is one of the preeminent factors determining how active the stellar wind is (Wood et al. 2002), it suggests that the stellar wind will also trend in a similar fashion.

1.1 Evolution of stellar activity

Stellar magnetic activity is observed to decline with age and rotation (Skumanich 1972; Ribas et al. 2005; Vidotto et al. 2014). There are many proxies for the activity of a star such as rotation, magnetism,

chromospheric emission, and X-ray luminosity. In recent years, there has been a surge in observation-based research, suggesting a break in solar analogue activity as stars cross a certain rotation or age threshold. van Saders et al. (2016) modelled a set of 21 older stars that have been observed by *Kepler* and reported the abnormally rapid rotation in older main-sequence (MS) stars, which does not agree with previous period–age relations. They suggested that magnetic braking seems to weaken significantly in evolved MS stars at Rossby number¹ $Ro \approx 2$, which they assumed corresponds to when the stars reach an age of ≈ 2 –4 Gyr. Since the rate of angular momentum loss is related to the mass-loss rate (Weber & Davis 1967; Vidotto et al. 2014), this break in angular momentum loss is likely to be associated with a decline in mass-loss rate (\dot{M}). We investigate this further in this work. Recently, Booth et al. (2017) have shown that X-ray luminosity declines more rapidly for stars older than ≈ 1 Gyr. They found a steep decrease in the age–activity relationship and suggested this could be due to increased stellar spin-down. Their explanation, however, contradicts the findings of van Saders et al. (2016), which found unusually high rotation rates in older stars. Here, we present a way to simultaneously explain the observations from Booth et al. 2017 and van Saders et al. 2016; our suggestion

¹ Ro represents Rossby number, which is the ratio between stellar rotation and convective turnover time. $Ro = P_{\text{rot}}/\tau_{\text{conv}}$.

[★] E-mail: ofionnad@tcd.ie (DOF); aline.vidotto@tcd.ie (AAV)

is that the observed decrease in X-ray luminosity is linked to a weaker stellar wind, which removes less angular momentum and, thus, allows for higher rotation rates in older stars, as seen in *Kepler* observations. Metcalfe, Egeland & van Saders (2016) examined chromospheric activity observations from calcium lines of solar analogues. They suggested that the break in activity is caused by a change in the dynamo properties at approximately the solar age, which is related to the break observed by van Saders et al. (2016). Kitchatinov & Nepomnyashchikh (2017) recently demonstrated that by switching off the global dynamo once a critical rotation period is reached, a similar decline in stellar spin-down and magnetism can be achieved for older stars. Vidotto et al. (2014, , fig. 2 within) showed that there is a trend in surface averaged magnetic field with age for solar-type stars, a power-law dependence was found but there is an apparent drop in magnetic activity for stars older than ≈ 2 – 2.5 Gyr. Another break in behaviour in solar-type stars is presented by Beck et al. (2017, fig. 5 within). They have shown that there is a break in lithium abundances in solar analogue stars, which drift beneath a surface rotation velocity of ≈ 2 – 3 km s $^{-1}$. Each of these works suggests that there exists a transition between regimes for aged low-mass stars past 1 Gyr. Although the nature of this transition has not yet been entirely defined, there is enough evidence for further investigation.

Thermally driven winds are effected by the temperature at their base, with higher temperatures leading to faster winds. Currently, defining the temperature at the base of the wind of solar-type stars is not possible through observations and we must rely on empirical methods. Johnstone & Güdel (2015) took coronal temperatures of low-mass MS stars and showed how they are correlated to X-ray surface fluxes (Telleschi et al. 2005). Here, we find additional evidence that the coronal temperatures of solar-like stars show a steeper decay for older, slowly rotating stars (Fig. 1). Coronal temperatures are from Johnstone & Güdel (2015), with rotation rates taken from Raassen et al. (2003), Telleschi et al. (2005), Wood & Linsky (2006), Wood & Linsky (2010), Güdel (2007), and Vidotto

et al. (2014). We have excluded M dwarfs from their sample, so as to limit the trend found to solar-type stars. Fig. 1 shows that there is an evident break in coronal temperature at $\approx 1.4 \Omega_{\odot}$. This break in behaviour at lower rotation rates results in power laws over two different regimes

$$T_{\text{cor}} (\Omega < 1.4 \Omega_{\odot}) \propto \Omega^{1.20}, \quad (1)$$

$$T_{\text{cor}} (\Omega > 1.4 \Omega_{\odot}) \propto \Omega^{0.37}. \quad (2)$$

The $\Omega \approx 1.4 \Omega_{\odot}$ break occurs at ≈ 2 Gyr for the sample of stars used, which is around the same age as those found by Booth et al. (2017) (≈ 1 Gyr) and not dissimilar to ages found by van Saders et al. (2016; ≈ 2 – 4 Gyr). Although these values are not identical, they are a good match considering limitations in age constraints on these stars. From convective turnover times for solar mass stars (Kiraga & Stepien 2007), we find this break occurring at $Ro = 1.14$. Note that, the break in behaviour here is inherent to older solar-type stars above ≈ 1 – 2 Gyr. This argument does not preclude the existence of a suggested sudden change in rotational braking at young ages, e.g. Johnstone et al. (2015a) and Gondoin (2017).

1.2 The Sun in Time project

The ‘Sun in Time’ project is used as the basis for selecting our sample for our study, discussed further in Section 2.1. The project was created to explore the life-long activity evolution of our own Sun, from when it reached the MS, by studying a group of solar-mass stars (e.g. Güdel 2007). Dorren & Guinan (1994) looked at the optical and ultraviolet (UV) Sun in Time, from which they could infer declining trends in activity with age. Güdel, Guinan & Skinner (1997) examined how the high energy radiation (X-ray and ultraviolet) emitted from the Sun has evolved over time. They used X-ray observations of nine solar-like G type stars to probe their coronae and used this as a proxy for an evolving Sun. Since these high energy fluxes can be connected to coronal activity, they derived trends in coronal temperature and emission measure with rotation and age of these solar analogues (see also Telleschi et al. 2005). Ribas et al. (2005) built on this previous work and investigated how these high irradiances would effect planetary atmospheres. The Sun in Time project inspired our investigation on how the solar wind has evolved during the MS. Understanding how the wind of the Sun has evolved is an important step in understanding the long-term evolution of the planets in the Solar system, including the Earth and the development of life (see e.g. Chassefière & Leblanc 2004).

1.3 Planetary environments

Stellar winds originate at the stellar surface and interact with all bodies in their path as they expand into the interplanetary medium, up to the astropause. Therefore, similarly to planets in our Solar system, exoplanets are expected to react to changes in the wind. In the Solar system, the Earth has the largest magnetosphere of the terrestrial planets. This magnetosphere shields the Earth from the harmful solar wind and also dynamically changes with the evolving solar wind (Cravens 1997; Bagenal 2013) and planetary dynamo. If the wind of the Sun changes on evolutionary time-scales, then it is expected that the Earth’s magnetosphere will evolve on similar time-scales. In practicality, this will also be effected on time-scales related to the changing internal planetary dynamo (Zuluaga et al. 2013). This will have significant effects along the evolution of the Earth regarding retention of its atmosphere. Any erosion of atmosphere would also have significant implications for the development of any

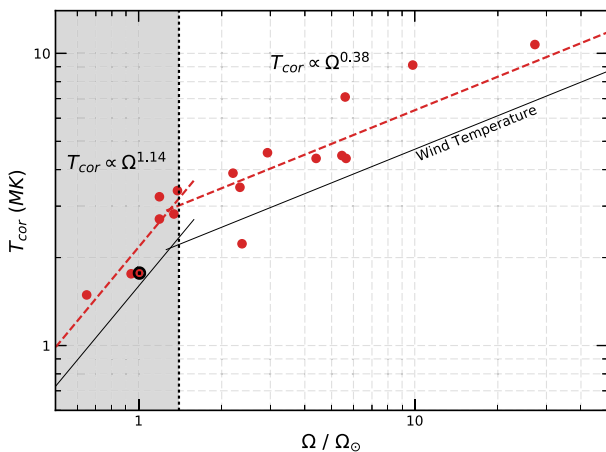


Figure 1. Average coronal temperature (T_{cor}) values derived from X-ray observations (Johnstone & Güdel 2015) show a strong correlation with rotation (broken red line). This relation was scaled down to give a base wind temperature, which we use for our simulations. This break in temperatures occurs at $1.4 \Omega_{\odot}$, and while the physical mechanism for this break is not understood, it would imply some transition between regimes for solar-type stars. Interesting to note is that the Sun (\odot , representing solar minimum and maximum) has just evolved past this transition. Both fits are shown in equations (1), (2), (6), and (7). The statistical significance of these fits is discussed further in Appendix A.

life on a planet (Chassefière & Leblanc 2004). Mars possesses an induced magnetosphere, which does not originate from the interior of the planet, but rather the build up of ions near the ionosphere where the wind impacts the upper atmosphere producing currents and their own magnetic field (Bertucci et al. 2011).

The goal of this paper is to construct an overall picture of solar wind evolution by modelling winds of solar-analogues. Our models predict stellar mass-loss rates, wind radio emission and can be used to predict how the local environment around the Earth evolves with time. In Section 2, we define the model used for these winds and the input parameters required. We describe the sample of stars used, and how we calculate radio emission from each of their winds. Section 3 describes the results we find for global wind properties. This includes mass-loss rates and radio emission from the winds and local wind properties, which focuses on the local conditions around a fictitious Earth orbiting each of the stars in our sample. In Section 4, we include a discussion on the results and their significance compared to other works. We finalize by drawing conclusions from this work and summarizing in Section 5.

2 STELLAR WIND MODELLING

The first work to propose that stars undergo mass-loss was Parker (1958). He suggested that the solar wind is in hydrodynamical expansion. However, the isothermal nature of Parker winds leads to excessive acceleration of the wind as it expands radially, leading to exaggerated wind velocities and temperatures at distances far from the solar surface. Polytropic models alleviate this issue as they do not constrain the wind to being isothermal, which allows a more reasonable representation of the wind at further distances (Keppens & Goedbloed 1999). Here, we present one-dimensional (1D) thermally driven hydrodynamic wind model that is used to compute the steady-state solutions of the winds of stars from the ‘Sun in Time’ sample (Table 1). We do not explicitly include magnetism in the wind equations, but we note that its presence is implicitly assumed as the cause of the MK temperatures of the winds. Polytropic winds

Table 1. Sample of stars used in this study: this sample is similar to that used in The Sun in Time sample (Güdel et al. 1997; Güdel 2007), with the omission of β Hyi and 47 Cas B. Values are mostly taken from Güdel (2007) and Vidotto et al. (2014). The X-ray luminosity of the sun here is considered to be between maximum and minimum.

Star	M (M_{\odot})	R (R_{\odot})	P_{rot} (d)	Age (Gyr)	$\log(L_X)$ (erg s^{-1})	d (pc)
EK Dra	1.04	0.97	2.77	0.12 ± 0.008^a	29.93	34.5
HN Peg	1.10	1.04	4.55	0.26 ± 0.046^b	29.00	17.95
χ^1 Ori	1.03	1.05	4.83	0.5 ± 0.1^c	28.99	186.0
π^1 UMa	1.00	1.00	5	0.5 ± 0.1^c	28.97	14.36
BE Cet	1.09	1.00	12.4	0.6 ± 0.05^d	29.13	20.9
κ^1 Cet	1.03	0.95	9.3	$0.65 \pm 0.05^{e,d}$	28.79	9.14
β Com	1.10	1.10	12.4	$1.6^{+0.9}_{-0.1}^e$	28.21	9.13
15 Sge	1.01	1.10	13.5	$1.9^{+1.1}_{-0.9}^f$	28.06	17.69
18 Sco	0.98	1.02	22.7	$3.0^{+0.2}_{-0.6}^g$	26.8	13.9
Sun	1.00	1.00	27.2	4.6	≈ 27	1 au
α Cen A	1.10	1.22	30	$5.5^{+0.0}_{-0.8}^e$	27.12	1.34
16 Cyg A	1.00	1.16	35	7.0 ± 0.3^h	26.89	21.1

Errors in age shown can be found in (a) Stauffer, Schultz & Kirkpatrick (1998), (b) López-Santiago et al. (2006), (c) King et al. (2003), (d) Perryman et al. (1998), (e) Mamajek & Hillenbrand (2008), (f) Liu et al. (2002), (g) Ramírez et al. (2014), and (h) Metcalfe, Creevey & Davies (2015).

follow the momentum equation

$$v \frac{dv}{dr} + \frac{1}{\rho} \frac{dp}{dr} + \frac{GM_*}{r^2} = 0, \quad (3)$$

where v is the velocity of the wind, ρ is the mass density of the wind, p represents the pressure of the wind, M_* is the stellar mass, G is the gravitational constant, and r represents distance from the stellar centre. The first term in equation (3) represents the acceleration of the wind, which is produced by the pressure gradient and gravity (second and third terms, respectively). Since the wind in this case is polytropic, the temperature and pressure change with density

$$T = T_0 \left(\frac{\rho}{\rho_0} \right)^{\Gamma-1}, \quad p = p_0 \left(\frac{\rho}{\rho_0} \right)^{\Gamma}, \quad (4)$$

where Γ is the polytropic index, and represents the energy deposition in the wind (when $\Gamma = 1$ the wind is isothermal). T_0 , p_0 , and ρ_0 represent the base temperature, pressure, and density of the wind, respectively. Methods of defining base temperature and density are discussed in Sections 2.2 and 2.3. Our 1D wind model assumes a spherically symmetric, steady wind, which behaves similarly to the Parker wind solution (Parker 1958), except the energy deposition in the wind is altered to be less than that of an isothermal wind. This change in energy deposition slows the expansion of the wind as Γ is increased, giving rise to slower, denser winds. It begins with a subsonic flow, which transitions to a supersonic flow once it passes through the critical radius (known as the sonic point):

$$r_c = \frac{GM_*}{2\Gamma[a(r_c)]^2}, \quad (5)$$

where $a(r_c)$ is the sound speed at the sonic point. To benchmark our simulations of the ‘solar wind in time’, we constrain the parameters of our model so as to best reproduce the solar wind properties. The Sun is the only star for which we have direct wind measurements. In the solar wind, Van Doorselaere et al. (2011) derived an effective polytropic index of $\Gamma = 1.1$. Numerical models of solar-type stars usually adopt a range of 1.05–1.15 for Γ (Matt et al. 2012; Johnstone et al. 2015a,b; Vidotto et al. 2015; Keppens & Goedbloed 1999). In our model, we adopt a value of 1.05. To further reproduce observations of the solar wind, we adopt a base wind density of $2.2 \times 10^8 \text{ cm}^{-3}$, which is consistent with observations of coronal hole densities (Warren & Brooks 2009). We use a wind base temperature of 1.5 MK, which, in conjunction with our $\Gamma = 1.05$, reproduces the solar wind velocities observed at the Earth, $v_{\oplus} = 443 \text{ km s}^{-1}$, which is consistent with observations (McComas et al. 2008; Usmanov, Goldstein & Matthaeus 2014). Our model predicts a number density of 10.5 cm^{-3} at the Earth’s orbit, which is also consistent with observations (Schwenn & Murrin 2000; Bagenal 2013; Usmanov et al. 2014). At the martian orbital distance, we find a wind density and velocity of 12 cm^{-3} and 450 km s^{-1} , respectively. These model values agree with observations made by the MAVEN spacecraft (Lee et al. 2017). Finally, our model predicts a solar wind mass-loss rate of $3.5 \times 10^{-14} M_{\odot} \text{ yr}^{-1}$, which reproduces the observed values presented in Wang (1998).

2.1 Solar wind in time sample

The sample for this study was selected by basing it off the original Sun in Time project (Güdel 2007; Guinan & Engle 2009). We omitted β Hyi as it has a radius of nearly twice that of the Sun, this gives it a much lower $\log(g)$, which implies that it is no longer on the MS. 47 Cas B was excluded from the study as it does not have very well-constrained parameters such as mass, radius, or rotation period

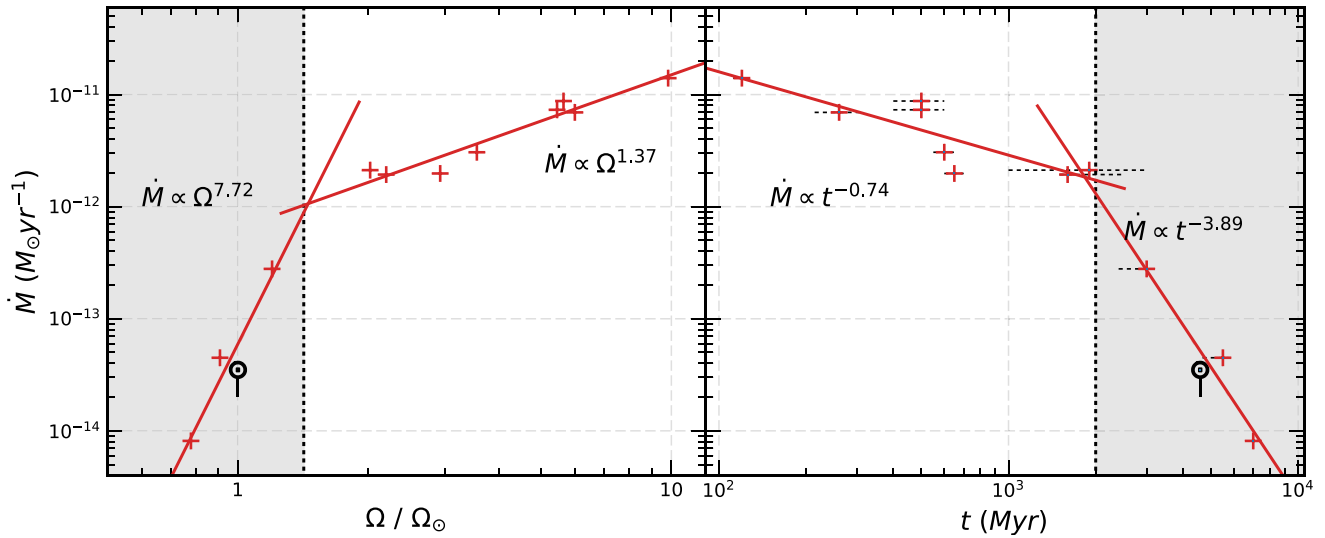


Figure 2. Left-hand panel: calculated mass-loss rates (red crosses) using our 1D polytropic model as the star spins down. Right-hand panel: plot showing how the mass-loss rate of the Sun would change as it ages. Included in our calculation is our estimation of the current solar mass-loss rate (\odot) and the range of values calculated directly from observations (black solid line) (Wang 1998). Note the clear break in to a rapidly declining mass-loss rate regime (grey shaded region) at $1.4\Omega_{\odot}$ and ≈ 2 Gyr, respectively. Errors in ages are shown as dotted black lines, with sources described in Table 1.

(Güdel 2007). It is also the secondary of a close binary system 47 Cas with an orbit of semi-major axis 1.32 au (Güdel et al. 1998). The stars treated here are all G0-5 type stars in the MS phase. The Sun is also included in our data set. Table 1 lists the most relevant quantities (mass, radius, rotation, age, and X-ray luminosity) of these stars for this work. Studying these solar-analogues over a wide range of ages enables us to explore how the solar wind has evolved. Age ranges are included in Table 1 and Fig. 2. Since the stars have different methods of age determination, they have varying degrees of accuracy in their ages. We note, however, that this particular sample of stars is very well studied in the literature and their ages are relatively accurate. The preferred fit for our data is with rotation as it is more precise, but we also include the fit with age.

2.2 Temperature–rotation relation

Unfortunately, observations cannot constrain the values for base wind temperature and density, which are fundamental input parameters for our model. There has been significant research into constraining base temperature and density, usually by assuming that they evolve with age or rotation or other stellar attributes (e.g. Holzwarth & Jardine 2007; Cranmer & Saar 2011). Here, we use the X-ray–rotation relation presented in Fig. 1 to observationally constrain the base wind temperature. Although the X-ray emission and wind acceleration are believed to originate at different locations (closed and open magnetic field regions, respectively), both phenomena are magnetic in nature and, therefore, it is expected that changes in closed regions would also affect changes in open regions. We assume that the temperature of the corona of solar type stars is related to the temperature at the base of the wind. The model we use is fitted to a piece-wise function around the value of $1.4\Omega_{\odot}$. The relation we find for T_{cor} was scaled down to correspond to observed solar wind temperatures near the base. As a result, a factor of 1.36 difference between coronal temperatures and base wind temperatures for all stars in our sample was found, shown in Table 2.

Table 2. Stellar wind properties for each of the simulated solar analogues in our sample. Values are displayed for base wind density, temperature, and mass-loss rates (cf. Fig. 2). The chosen values of n_0 and T_0 for the solar wind are such to reproduce observations (see text).

Star	n_0 (10^8 cm^{-3})	T_0 (MK)	\dot{M} ($M_{\odot} \text{ yr}^{-1}$)
EK Dra	8.8	4.7	1.4×10^{-11}
HN Peg	6.6	3.9	6.9×10^{-12}
χ^1 Ori	6.3	3.8	8.8×10^{-12}
π^1 UMa	6.2	3.7	7.3×10^{-12}
BE Cet	4.8	3.2	3.1×10^{-12}
κ^1 Cet	4.3	3.0	2.0×10^{-12}
β Com	3.6	2.7	1.9×10^{-12}
15 Sge	3.4	2.6	2.1×10^{-12}
18 Sco	2.5	1.9	2.8×10^{-13}
Sun	2.2	1.5	3.5×10^{-14}
α Cen A	2.1	1.4	4.5×10^{-14}
16 Cyg A	1.9	1.1	8.1×10^{-15}

$$T_0 (\Omega < 1.4 \Omega_{\odot}) = 1.5 \pm 0.19 \left(\frac{\Omega_{\star}}{\Omega_{\odot}} \right)^{1.2 \pm 0.54} \text{ MK}, \quad (6)$$

$$T_0 (\Omega > 1.4 \Omega_{\odot}) = 1.98 \pm 0.21 \left(\frac{\Omega_{\star}}{\Omega_{\odot}} \right)^{0.37 \pm 0.06} \text{ MK}. \quad (7)$$

These relations are shown as solid lines in Fig. 1. The errors in the exponents arise from fitting. Note that a single fit to the coronal temperature data is also possible, but provides a larger χ^2 . In light of the recent works presented in Section 1.1 (e.g. van Saders et al. 2016; Booth et al. 2017; Beck et al. 2017), we proceed with the broken power-law fit throughout this paper. Appendix A shows the results one would have obtained in the case a single power law had been adopted.

2.3 Density–rotation relation

Currently, there is no available method to accurately define the density at the base of the wind, making it a difficult parameter to

prescribe for simulations. Observations of stellar mass-loss rates would provide meaningful upper limits to the base density, but these are available for only a small sample of stars (Wood et al. 2014). Ivanova & Taam (2003) find a relationship between rotation and coronal density (equation 8, also used by Holzwarth & Jardine 2007; Réville et al. 2016), from X-ray luminosity observations. We adopt this relationship for the density at the base of the wind for our simulations (Table 2).

$$n_0 = n_{\odot} \left(\frac{\Omega_{\star}}{\Omega_{\odot}} \right)^{0.6}, \quad (8)$$

where n represents number density and is related to mass density by $n = \rho/\mu m_p$, where $\mu = 0.5$ is the mass fraction of a fully ionized hydrogen wind and m_p is the proton mass.

2.4 Radio emissions from stellar winds

One possible way of estimating wind densities (and mass-loss rates, \dot{M}) is by detecting these winds at radio wavelengths. The plasma that makes up stellar winds can emit in radio through the process of thermal bremsstrahlung from ionized plasma. This originates from the inner regions of the wind, where the density is highest (Panagia & Felli 1975; Wright & Barlow 1975; Lim & White 1996; Güdel 2002). We can estimate the level of thermal radio emission from these winds using our model. According to previous studies by Panagia & Felli (1975), Wright & Barlow (1975), Güdel (2002), and Vidotto & Donati (2017), the radio flux produced by a wind is

$$S_{\nu} = 10^{-29} A(\alpha) R_{\star}^2 \left[5.624 \times 10^{-28} I(\alpha) n_0^2 R_{\star}^2 \right]^{\frac{2}{2\alpha-1}} \times \left[\frac{\nu}{10 \text{ GHz}} \right]^{\beta} \times \left[\frac{T_0}{10^4 \text{ K}} \right]^{\lambda} \times \left[\frac{d}{1 \text{ kpc}} \right]^{-2} \text{ mJy}, \quad (9)$$

where the functions $I(\alpha)$ and $A(\alpha)$ are

$$I(\alpha) = \int_0^{\pi/2} (\sin \theta)^{2(\alpha-1)} d\theta, \quad (10)$$

$$A(\alpha) = 1 + 2 \sum_{j=1}^{\infty} (-1)^{j+1} \frac{\tau_c^j}{j! j(2\alpha-1) - 2}. \quad (11)$$

The indices β and λ in equation (9) are defined as

$$\beta = \frac{-4.2}{2\alpha-1} + 2, \quad \lambda = \frac{-2.7}{2\alpha-1} + 1, \quad (12)$$

with $\tau_c = 3$ and θ representing colatitude in radians. The wind density decay index, α is defined as

$$n = n_0 \left[\frac{R_{\star}}{r} \right]^{-\alpha}. \quad (13)$$

The density decay index will eventually become $\alpha = 2$ as the wind reaches asymptotic terminal velocity. Since the radio emission originates near the base of the wind, the α parameter is likely to be greater than 2. For each star, we found α by estimating the rate of density decline in the $1-5R_{\star}$ range. This range should account for the majority of ‘stronger’ radio emission, as it is the densest region. It is important to note that the estimation of radio flux equation (9) is based on an isothermal wind, whereas in our model the wind is a polytrope, allowing the temperature to vary as it expands. This approximation for radio flux should give a good indication of flux from these stars as emission is only estimated in the $1-5R_{\star}$ range, within which the isothermal approximation is adequate.

The region where half of the emission occurs has a size

$$\frac{R_{\nu}}{R_{\star}} = \left[4.23 \times 10^{-27} I(\alpha) n_0^2 R_{\star}^2 \right]^{\frac{1}{2\alpha-1}} \left[\frac{\nu}{10 \text{ GHz}} \right]^{\frac{-2.1}{2\alpha-1}} \left[\frac{T_0}{10^4 \text{ K}} \right]^{\frac{-1.35}{2\alpha-1}}, \quad (14)$$

which we refer to as the ‘radio photosphere’ of the star. This is an important parameter as it illustrates how close to the star the emission will emanate and whether the wind is optically thin, as described by Panagia & Felli (1975).

3 EVOLUTION OF GLOBAL PROPERTIES OF THE SOLAR WIND

3.1 Mass-loss rate

Since the model parameters in Table 2 are dependent on stellar rotation, we find in Fig. 2 that the mass-loss rate of stars is also dependent on rotation. The left-hand panel of Fig. 2 shows a mass-loss rate that increases with rotation, with a break occurring at $1.4 \Omega_{\odot}$. This dependence is as follows:

$$\dot{M} (\Omega < 1.4 \Omega_{\odot}) = 6.3 \times 10^{-14} \left(\frac{\Omega}{\Omega_{\odot}} \right)^{7.7 \pm 1.6} \text{ M}_{\odot} \text{ yr}^{-1}, \quad (15)$$

$$\dot{M} (\Omega > 1.4 \Omega_{\odot}) = 6.3 \times 10^{-13} \left(\frac{\Omega}{\Omega_{\odot}} \right)^{1.4 \pm 0.15} \text{ M}_{\odot} \text{ yr}^{-1}. \quad (16)$$

The mass-loss rate of solar-type stars is believed to decrease with time as the star ages. This is due to stellar spin-down and a decrease in magnetic activity (e.g. Vidotto et al. 2014). Our results show a similar behaviour as the Sun evolves. However, our models predict a steep break in the mass-loss rate at an age of 2 Gyr (Fig. 2), as a result of the break in T_{cor} with respect to rotation. The values of \dot{M} we find for each star in our sample is shown in Table 2 and Fig. 2, and follow the relations

$$\dot{M} (t \lesssim 2 \text{ Gyr}) = 5.0 \times 10^{-10} t_{\text{Myr}}^{-0.74 \pm 0.19} \text{ M}_{\odot} \text{ yr}^{-1}, \quad (17)$$

$$\dot{M} (t \gtrsim 2 \text{ Gyr}) = 9.0 t_{\text{Myr}}^{-3.9 \pm 0.81} \text{ M}_{\odot} \text{ yr}^{-1}, \quad (18)$$

where t_{Myr} is the age given in Myr. This shows, for example, that a young Sun of 100 Myr would have a mass-loss rate of $1.5 \times 10^{-11} \text{ M}_{\odot} \text{ yr}^{-1}$, almost 2.5 orders of magnitude larger than the current rate.

3.2 Radio emission from stellar winds

The densest parts of stellar winds might be able to produce free-free emission at radio wavelengths. Recently, Fichtinger et al. (2017) observed four stars, at 6 and 14 GHz, using VLA and ALMA, namely: EK Dra, χ^1 Ori, π^1 UMa, and κ^1 Cet. Only two of these stars showed radio emission (EK Dra and χ^1 Ori); however, this emission did not emanate from their winds, but rather from the closed corona and flares. For π^1 UMa and κ^1 Cet, no detections were made, which allowed the authors to place upper limits on the mass-loss rates of these winds (see also Vidotto & Donati 2017).

Table 3 shows the density fit parameters (α , β , γ) we found for each star, with which we calculated radio emission over a range of frequencies (equations 9–12). We also computed the ‘radio photosphere’ size (equation 14) for all the stars in our sample and found that all have their radio photosphere inside the radius of the star at both 6 and 14 GHz. This implies that their winds are optically thin and do not emit at these frequencies. This agrees with the

Table 3. Radio properties of our wind models. Shown here are values for α , which describes the behaviour of the density as a function of distance. β and λ describe the radio emission dependence on frequency and wind temperature, respectively, which themselves depend on α (equation 12). Outlined are results for the critical frequency, ν_c , which describes the frequency below which the wind becomes optically thick. S_{ν_c} describes the radio flux at each respective critical frequency.

Star	α	β	λ	ν_c (GHz)	S_{ν_c} (μ Jy)
EK Dra	2.8	1.09	0.41	2.0	0.79
HN Peg	3.1	1.19	0.48	1.7	1.9
χ^1 Ori	3.1	1.19	0.48	1.7	0.017
π^1 UMa	3.0	1.16	0.46	1.6	2.5
BE Cet	3.3	1.25	0.52	1.4	0.70
κ^1 Cet	3.4	1.28	0.53	1.3	2.5
β Com	3.4	1.28	0.53	1.2	2.9
15 Sge	3.4	1.28	0.53	1.2	0.70
18 Sco	4.0	1.40	0.61	0.99	0.48
α Cen A	5.3	1.56	0.72	1.1	58
16 Cyg A	6.4	1.64	0.77	1.0	0.16

non-detections reported by Fichtinger et al. (2017). To examine this further, we computed the cut-off frequency, ν_c (Table 3), below which the radio photosphere surpasses the radius of the star and the wind becomes optically thick (Wright & Barlow 1975). From equation (14), the critical frequency below which these winds emit is given by

$$\nu_c = [4.23 \times 10^{-27} I(\alpha) n_0^2 R_*]^{0.48} \left[\frac{T_0}{10^4 \text{ K}} \right]^{-0.64} 10 \text{ GHz}. \quad (19)$$

We calculate the expected flux density emitted from the wind at the same value of ν_c , given in Table 3 as S_{ν_c} . These flux densities are quite low with the exception of α Cen A as it is relatively close compared to the other stars. Note that, the wind cannot emit at frequencies larger than ν_c . For stars in our sample, the cut-off frequency is around 1–2 GHz, implying that observations to detect these winds should be conducted at frequencies lower than 1 GHz. Also important to note is that, if the radio photosphere is very close to the surface of the star, any thermal emission is likely dominated by other stellar emission (i.e. coronal emission or flares).

From equation (19), we find that ν_c is weakly dependent on α and follows: $\nu_c \propto n_0^{0.96} T_0^{-0.64}$. Since our model assumes that both base wind temperature and density rely on rotation, we can relate this cut-off frequency to rotation as

$$\nu_c (\lesssim 1.4 \Omega_\odot) \propto \Omega^{-0.20}, \quad (20)$$

$$\nu_c (\gtrsim 1.4 \Omega_\odot) \propto \Omega^{0.33}. \quad (21)$$

This means that there is an inflection in the dependence of ν_c with rotation. Although it is a weak dependence, it suggests that the lowest critical frequencies occur for stars at $\sim 1.4 \Omega_\odot$.

4 EVOLUTION OF THE LOCAL PROPERTIES OF THE WIND

A direct output of our wind simulations is the local velocity and density for the wind at the position of the Earth. Therefore, we can use these values to estimate the local velocity and density of the wind surrounding an evolving Earth as the system ages. The ram pressure that impinges upon an evolving Earth is

$$P_{\text{ram}} = \rho_\oplus v_\oplus^2. \quad (22)$$

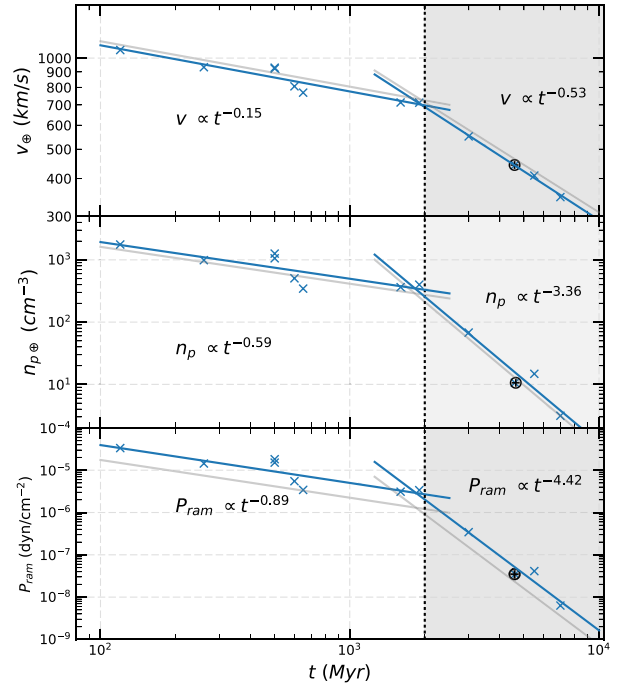


Figure 3. Local parameters for the solar wind in the vicinity of the Earth. We show local wind velocity (top panel) and proton density (middle panel) as stars evolve. This results in a present-day solar wind value (\oplus) at the Earth of 443 km s^{-1} and 10.5 cm^{-3} , respectively. From these values, we calculate the expected ram pressure (bottom panel) impinging on the Earth as it evolves. Shown are best fits to simulated values in separate regimes. Shown in grey are the expected values for a martian proxy planet orbiting each star.

This equation can be easily adopted to the martian case, by changing velocities and densities to those in the martian vicinity. In Fig. 3, we show the local wind velocity, v_\oplus , the local proton number density, $n_{p\oplus}$, and the ram pressure, P_{ram} , at the orbital distance of the Earth as the stars evolve (in blue; the grey line represents the martian values). Evidently, the break in stellar wind temperature, shown in Fig. 1, filters down to the local environment, which also displays a break in behaviour as these systems age. This happens at the age of 2 Gyr, denoted by a shaded region. This suggests that the young solar wind exhibited typical wind velocities of 10^3 km s^{-1} at the orbital distance of the Earth.

Once we know the ram pressure incident on the magnetosphere of the Earth, the magnetospheric standoff radius, R_M , at the sub-solar point can be calculated. This is done by balancing the ram pressure of the wind to the magnetic pressure of the planet’s magnetosphere (Cravens 1997).

$$\frac{R_M}{R_\oplus} = 1.4 \left[\frac{B_p^2}{8\pi P_{\text{ram}}} \right]^{1/6}. \quad (23)$$

R_M is given here in planetary radii, B_p is the surface planetary magnetic field at the equator, which we assume to be the dipolar field only. The factor of 1.4 accounts for currents that develop near the magnetopause boundary and produce their own magnetic fields (Cravens 1997; Bagenal 2013). Equation (23) shows a dependence on stellar wind strength, which could have important ramifications for the development of life, as the solar wind is expected to have varied in the past on long time-scales, as we have shown in Section 3. A smaller magnetosphere can lead to escalated atmospheric loss

and reduced protection from the ionized wind (discussed further in Section 5).

Fig. 4 shows the trend in magnetospheric size for the Earth, both with solar rotation and age. We calculate the magnetospheric size considering the Earth’s magnetic field to be constant with time (blue solid line) and varying with time according to the model by Zuluaga et al. (2013; purple dotted line). This model is constrained by magnetic field measurements showing a 50 per cent field strength for a 1 Gyr system estimated by Tarduno et al. (2010). We can see that both models differ only slightly, with the most significant differences occurring around 1–2 Gyr, showing a spread of just under 1 R_M . In particular, we find at early ages, both models predict magnetospheric sizes of $\approx 3R_E$. This is understandable, considering the weak dependence on the planetary magnetic field of 1/6, shown in equation (23). We find a small magnetospheric standoff distance of $3.0R_E$ for a young Earth 100 Myr old, with the same planetary magnetic field as today ($B_p = 0.3$ G). These standoff distances would be similar to extreme modern day events, such as the 2003 Halloween storm (Rosenqvist et al. 2005), caused by coronal mass ejections (CMEs). However, these transient CME events last only on the scale of hours, but at 100 Myr these magnetosphere sizes would have been typical. Increased solar activity at younger ages (e.g. CMEs) would further compress the young magnetosphere, resulting in even smaller standoff distances. Younger stars are expected to be more active and would be more likely to produce large and more frequent transient events such as CMEs.

5 DISCUSSION

5.1 Global properties

Since direct observations of mass-loss rate and radio emission from stellar winds are difficult to obtain, we can use models to help understand the physical processes behind these winds. These models can provide information on the strength and location of the wind emission, therefore aiding in observing these winds directly. Recently, there has been research into the mass-loss rates of solar-analogue winds and how they would effect an orbiting planet, including a young Earth. Although some work focuses directly on the Sun–Earth interaction (Sternborg et al. 2011), others focus more on the stellar evolution of these types of stars (Wood et al. 2002, 2005, 2014; Cranmer & Saar 2011; Matt et al. 2012; Fichtinger et al. 2017) and their effects on exoplanets (Vidotto et al. 2012, 2013, 2015; See et al. 2014; Zuluaga, Mason & Cuartas-Restrepo 2016; See et al. 2017).

The main basis of our models is the temperature–rotation relation we presented in Fig. 1.² This type of relation between wind temperatures and X-ray observations, which has a strong correlation, is unique in predicting the winds of these stars. The break we find in wind temperature filters through the trend in stellar mass-loss rate (Fig. 2). We see a clear decay in \dot{M} with stellar spin-down and aging, with a break in \dot{M} occurring at both $1.4 \Omega_\odot$ and 2 Gyr, respectively. Since our stellar wind models depend on the base wind temperature, it follows that mass-loss rate displays a similar trend.

² Holzwarth & Jardine (2007) also derived a temperature–rotation relation which is based on activity–rotation relation. They attempted to constrain this dependence to a power law index, that lies somewhere between 0 and 0.5. They assumed a value of 0.1 for their model. This is a much weaker dependence than we find here for the slower rotators, but their ranges are within the values for the faster rotators.

Other models also predict a decay in mass-loss rate with stellar evolution. Cranmer & Saar (2011) developed an Alfvén-wave driven model for predicting winds from cool, late-type stars. They based their models on physically observed parameters from 47 stars of types G, K, and M. Johnstone et al. (2015a,b) employed a different approach and used polytropic wind models to reproduce the rotational evolution of solar-mass stars in open clusters. Both of the models found a mass-loss rate for young suns (at an age of 100 Myr) that are 1–2 orders of magnitude smaller than our predictions. However, for older stars, our predictions become smaller than theirs, since our model shows a steep decay in \dot{M} for stars older than ≈ 2 Gyr. Note that, Johnstone et al. (2015b) assumed that the wind saturates for very young stars (<600 Myr) in the fast rotating track. When plotted in the Ω –age diagram, the stars in our sample follow the 50th percentile track, as defined by Gallet & Bouvier (2013), which implies that they would not be part of the saturated regime explored by Johnstone et al. (2015b).

Regarding the mass-loss rate with age, in our models, for ages younger than 2 Gyr, we found that $\dot{M} \propto t^{-0.74}$. This is much flatter than the original dependence derived by Wood et al. (2014) ($t^{-2.33}$), which has been revised as $t^{-1.46}$ by Johnstone et al. (2015b). In their Alfvén wave-driven wind models, Suzuki et al. (2013) predicted $t^{-1.23}$, whereas Cranmer & Saar (2011) predicted $t^{-1.1}$. Given the uncertainties in age measurements, our derived age-dependence is consistent with these works. Note also that, if we were to fit one single power law to a temperature– Ω relation, this would imply that the wind mass-loss rate would not have the change in regimes that we suggest, and the corresponding age dependence would be $t^{-1.36}$, a unique power law for all ages. See et al. (2017) investigated the trends in mass-loss rate with stellar age by adopting a potential field source surface model. By doing so, they could investigate the topology of the coronal magnetic field of stars, including the extent of open flux regions, which, in turn, allows angular momentum and mass-loss rates to be determined. They found lower mass-loss rates than presented here for all overlapping stars in our sample, but with a similar trend with age.

These mass-loss rates are important for solar and terrestrial evolution, as it affects solar evolutionary models, which, in turn, directly effect the Earth through particle and radiation flux. A famous problem arose when these models predicted that the Sun would have been 25–30 per cent fainter than it is today (Newman & Rood 1977; Gough 1981), leading to a completely frozen Earth and Mars. Yet, this prediction is inconsistent with the evidence suggesting that there was liquid water on the surface of both planets, implying planetary temperatures were not freezing (Sagan & Mullen 1972). This is called the faint young Sun paradox (Feulner 2012). It leads us to the conclusion that there must be something awry with the standard solar model or the estimates surface temperatures of Earth and Mars. One solution to this issue is if the mass-loss rate of the Sun was higher in the past than expected. We integrated the mass-loss rate evolution calculated here and find that the Sun has lost 0.8 per cent M_\odot since an age of 100 Myr. Our model results in a higher mass-loss rate at younger ages than previous models, while also predicting lower mass-loss rates at older ages. Even with the increased mass-loss rate from this model in the past, it does not solve the faint young Sun paradox, where a mass-loss of 3–7 per cent M_\odot is required.

5.2 Local properties

We have shown in Fig. 4 that a young Earth orbiting a young Sun would possess a significantly smaller magnetosphere. In our

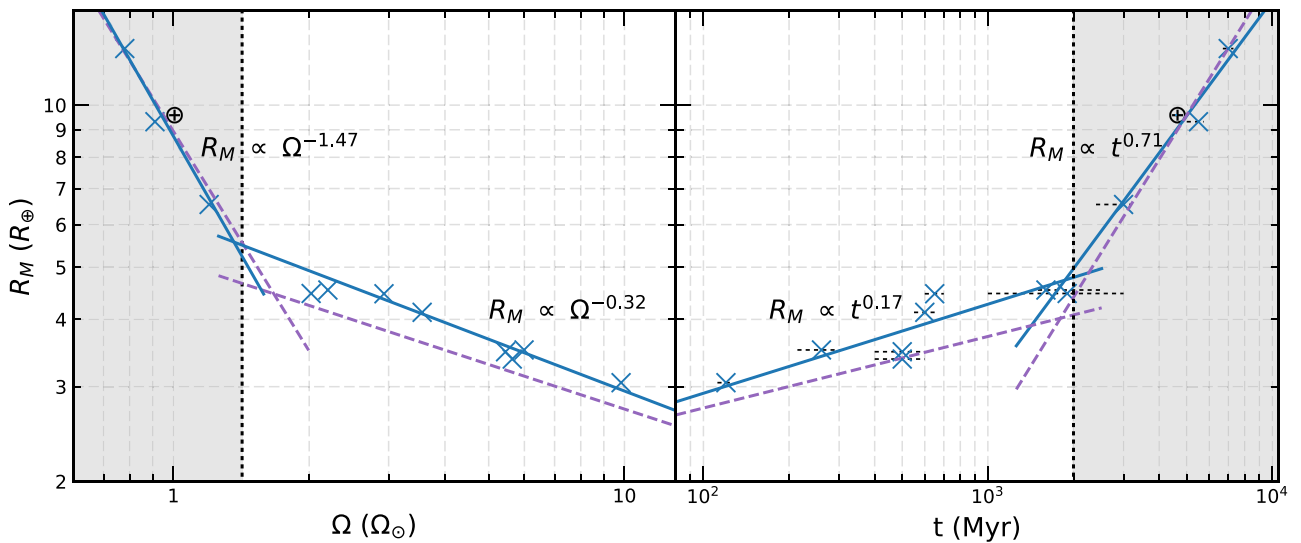


Figure 4. We observe trends in magnetospheric size with respect to rotation (left-hand panel) and age (right-hand panel). Blue x 's: calculated standoff distances with a constant planetary magnetic field of 0.3G. The solar-Earth scenario as it is currently, given as \oplus . Purple dashed line: This depicts the standoff distances of the magnetosphere if the planetary magnetic field varied according to models described in Zuluaga et al. (2013).

results for magnetospheric standoff distance, we assumed that the magnetic dipole moment of the Earth has remained the same up to this day. However, it is believed that this is not the case, although there is no consensus on how it has changed or by what amount. Tarduno et al. (2010) showed from ancient silicate crystals that the paleo-magnetic field of the Earth was much weaker than today, and estimated it to be 50–70 per cent of the current strength. We took a model that is constrained by these parameters and describes how the magnetic moment of the Earth has evolved over time from Zuluaga et al. (2013). Using these values for B_p , we calculated R_M , shown as the purple dashed line in Fig. 4. This plot shows how significant the changes in the Earth's magnetic field can be over time, when calculating R_M . At 100 Myr, we can see that the magnetosphere is approximately $2.8R_\oplus$ using a varying magnetic field, which is almost the same size derived with a constant magnetic field ($3R_\oplus$). See et al. (2014) conducted a study into the effects that winds from solar type stars have on magnetosphere sizes of planets. They investigated how varying host star mass influenced the magnetospheric size and how this could effect habitability on any Earth-like exoplanets. This work complements the results of See et al. (2014) as it shows how magnetosphere size will vary across different ages of solar analogues. Both Vidotto et al. (2013) (M dwarfs only) and do Nascimento et al. (2016) (κ^1 Ceti) considered how stellar winds effected the interplanetary medium and how this could have impacted habitability on Earth-like exoplanets orbiting these stars. Also of interest is Airapetian & Usmanov (2016), who used 3D MHD Alfvén wave driven models and found a paleo-solar wind that is twice as fast and 50 times as dense at 1 au at an age of 0.7 Gyr. We found very similar results for the wind of 1.9 times the velocity and 58 times as dense at 1 au for similar epochs.

For a stronger solar wind, the ‘polar opening’ region of the young Earth's magnetosphere, defined by the region that is covered by open magnetic field lines that extend into the magnetotail (in contrast to the closed dipolar magnetic regions in lower latitudes), can extend significantly further down in latitude than it does presently (71° :9, Tarduno et al. 2010). We estimate that at an age of 100 Myr, the polar opening region would extend as far as 55° – 60° from the equator. This larger polar opening region would have many implications

for life developing on Earth, namely reduced protection from the harmful solar wind, and increased rates of atmospheric loss, through the expansion of the atmosphere and loss of volatiles. To intensify this effect, a younger Sun would be expected to be more active, with increased flaring rates and energy, potentially leading to additional atmospheric loss.

Fig. 3 also shows the local parameters of the wind around Mars. This allows us to calculate the height of the ionosphere, which acts to produce an induced magnetosphere above the martian surface. This is done by equating the stellar wind ram pressure with the thermal pressure of the martian atmosphere, taking today's values for the latter ($7800 \text{ dyne cm}^{-2}$, Harri et al. 2014). We find a present day value of 292 km, which is consistent with observations (Hanson, Sanatani & Zuccaro 1977; Withers 2009). Assuming the current state of the martian magnetosphere, which is very weak, given the lack of a global magnetic field, our models find that the ionosphere height increases as the Sun–Mars system evolves, in a similar fashion to the Earth's magnetosphere size. It also predicts that for the immediate future, the ionosphere height will continue to grow. The change found in martian ionosphere height seems small compared to changes in Earth's magnetosphere over the same time period. We find a 42 per cent increase in ionosphere height for Mars from 100 Myr (218 km) to 7 Gyr (310 km). This is much smaller than the 324 per cent increase found in the Earth's magnetosphere from 100 Myr ($3R_\oplus$) to 7 Gyr ($12.7R_\oplus$). This arises due to the martian ionosphere size depending on the inverted natural logarithm of the wind ram pressure, giving a weaker dependence on the solar wind.

6 CONCLUSIONS

We simulated winds of a sample of solar analogue stars using 1D polytropic models. We selected our sample based of the ‘Sun in Time’ program, which aimed to find a comprehensive trend in the evolution of solar activity (Ribas et al. 2005; Güdel 2007). We presented a new rotation–temperature relation, which we used as an input for our simulations based off X-ray observations from Johnstone & Güdel (2015). We found a break in base wind temperatures at $1.4 \Omega_\odot$. This leads to a sharp decline in wind temperatures as

stars spin down past this point. We found stars rotating slower than this follow $T_{\text{wind}} \propto \Omega^{1.20}$, and stars rotating faster follow $T_{\text{wind}} \propto \Omega^{0.37}$.

This dependence between the wind temperature and rotation is rooted in the coronal temperature–rotation dependence. Although both the wind and the corona originate from different magnetic geometries (open and closed field lines, respectively), they are both caused by magnetism, and therefore it is natural to assume that they will follow similar trends. The base temperature of the stellar wind is an important parameter for our simulations. It defines the rate of acceleration of the wind as it is launched from the surface of the star. Yet, it is very difficult to constrain without direct observations from the stellar winds, which leaves only semi-empirical methods, which we employ here, to define the temperatures of these winds.

We found that the rate of mass-loss from these stars seems to decline rapidly after 2 Gyr, with $\dot{M} = 8 \times 10^{-15} M_{\odot} \text{ yr}^{-1}$ for a Sun of 7 Gyr. This steep decay in \dot{M} could explain why older stars are inefficient at losing angular momentum, as shown by the atypically high rotation rates found in some older stars (van Saders et al. 2016).

Our simulations provided us with the necessary parameters to make estimations on the thermal bremsstrahlung emissions from the winds of stars in our sample. We found that their winds only become optically thick below their critical frequencies, $\nu_c \approx 1\text{--}2$ GHz, which has a shallow dependence on stellar rotation as follows: $\nu_c(>1.4 \Omega_{\odot}) \propto \Omega^{0.33}$ and $\nu_c(<1.4 \Omega_{\odot}) \propto \Omega^{-0.20}$. We presented estimates for their fluxes at this critical frequency, S_{ν_c} (Table 3). These values are pivotal to observing these stellar winds, and could explain some non-detections by previous attempts (Fichtinger et al. 2017). Equations (20) and (21) show that there is an inflection in the rotation dependence of ν_c , although the dependence is relatively shallow. Stars rotating faster than $1.4 \Omega_{\odot}$ have higher cut-off frequencies.

We demonstrated the effects the aging solar wind has had on the evolving Earth, showing a steep increase in the growth of our magnetosphere since an age of 2 Gyr. We estimated the size of the magnetosphere at young ages to be $\sim 3R_{\oplus}$ at 100 Myr. This could have had implications for development of life due to the increased loss of atmosphere and a decrease in shielding ability from the solar wind. We found similar trends in the ionospheric height above the martian surface, yet the effect is not as extreme.

Although the young Sun's mass-loss rate had a shallow decline up to 2 Gyr, the total mass lost is still quite small. From our model, we estimate a total mass-loss of 0.8 per cent M_{\odot} , which is not enough to solve the faint young Sun paradox. This paradox has been studied at length, and a total mass-loss of 3–7 per cent is required to solve it.

Our model provides a semi-empirical method for determining base wind temperatures from X-ray observations of stars, which, in turn, allows an in depth analysis of the wind conditions surrounding these stars. Our current model did not allow us to evaluate angular momentum losses. This will be developed further by incorporating realistic distributions of stellar surface magnetism. The work here will be the initial foundation of a forthcoming 3D study into the winds of solar analogues.

ACKNOWLEDGEMENTS

DOF acknowledges funding from a Trinity College Postgraduate Award through the School of Physics. We also thank the Jorge Zuluaga for his constructive comments on the paper.

REFERENCES

- Airapetian V. S., Usmanov A. V., 2016, *ApJ*, 817, L24
 Bagenal F., 2013, Planetary Magnetospheres. Springer Science+Business Media, Dordrecht, p. 251
 Beck P. G. et al., 2017, *A&A*, 602, A63
 Bertucci C., Duru F., Edberg N., Fraenz M., Martinecz C., Szego K., Vaisberg O., 2011, *Space Sci. Rev.*, 162, 113
 Booth R. S., Poppenhaeger K., Watson C. A., Silva Aguirre V., Wolk S. J., 2017, *MNRAS*, 471, 1012
 Chassefière E., Leblanc F., 2004, *Planet. Space Sci.*, 52, 1039
 Cranmer S. R., Saar S. H., 2011, *ApJ*, 741, 54
 Cravens T. E. ed., 1997, Physics of Solar System Plasmas. Cambridge Univ. Press, Cambridge
 do Nascimento Jr J.-D. et al., 2016, *ApJ*, 820, L15
 Dorren J. D., Guinan E. F., 1994, *ApJ*, 428, 805
 Feulner G., 2012, *Rev. Geophys.*, 50, RG2006
 Fichtinger B., Güdel M., Mutel R. L., Hallinan G., Gaidos E., Skinner S. L., Lynch C., Gayley K. G., 2017, *A&A*, 599, A127
 Gallet F., Bouvier J., 2013, *A&A*, 556, A36
 Gondoin P., 2017, *A&A*, 599, A122
 Gough D. O., 1981, *Sol. Phys.*, 74, 21
 Güdel M., 2002, *ARA&A*, 40, 217
 Güdel M., 2007, *Living Rev. Sol. Phys.*, 4, 3
 Güdel M., Guinan E. F., Skinner S. L., 1997, *ApJ*, 483, 947
 Güdel M., Guinan E. F., Etzel P. B., Mewe R., Kaastra J. S., Skinner S. L., 1998, in Donahue R. A., Bookbinder J. A., eds, ASP Conf. Ser. Vol. 154, Cool Stars, Stellar Systems, and the Sun. Astron. Soc. Pac., San Francisco, p. 1247
 Guinan E. F., Engle S. G., 2009, in Mamajek E. E., Soderblom D. R., Wyse R. F. G., eds, Proc. IAU Symp. Vol. 258, The Ages of Stars. Kluwer, Dordrecht, p. 395 (arXiv:0903.4148), doi:10.1017/S1743921309032050
 Hanson W. B., Sanatani S., Zuccaro D. R., 1977, *J. Geophys. Res.*, 82, 4351
 Harri A.-M. et al., 2014, *J. Geophys. Res.*, 119, 82
 Holzwarth V., Jardine M., 2007, *A&A*, 463, 11
 Ivanova N., Taam R. E., 2003, *ApJ*, 599, 516
 Johnstone C. P., Güdel M., 2015, *A&A*, 578, A129
 Johnstone C. P., Güdel M., Lüftinger T., Toth G., Brott I., 2015a, *A&A*, 577, A27
 Johnstone C. P., Güdel M., Brott I., Lüftinger T., 2015b, *A&A*, 577, A28
 Keppens R., Goedbloed J. P., 1999, *A&A*, 343, 251
 King J. R., Villarreal A. R., Soderblom D. R., Gulliver A. F., Adelman S. J., 2003, *AJ*, 125, 1980
 Kiraga M., Stepien K., 2007, *Acta Astron.*, 57, 149
 Kitchatinov L., Nepomnyashchikh A., 2017, *MNRAS*, 470, 3124
 Lee C. O. et al., 2017, *J. Geophys. Res.*, 122, 2768
 Lim J., White S. M., 1996, *ApJ*, 462, L91
 Liu M. C., Fischer D. A., Graham J. R., Lloyd J. P., Marcy G. W., Butler R. P., 2002, *ApJ*, 571, 519
 López-Santiago J., Montes D., Crespo-Chacón I., Fernández-Figueroa M. J., 2006, *ApJ*, 643, 1160
 Mamajek E. E., Hillenbrand L. A., 2008, *ApJ*, 687, 1264
 Matt S. P., MacGregor K. B., Pinsonneault M. H., Greene T. P., 2012, *ApJ*, 754, L26
 McComas D. J., Ebert R. W., Elliott H. A., Goldstein B. E., Gosling J. T., Schwadron N. A., Skoug R. M., 2008, *Geophys. Res. Lett.*, 35, L18103
 Metcalfe T. S., Creevey O. L., Davies G. R., 2015, *ApJ*, 811, L37
 Metcalfe T. S., Egeland R., van Saders J., 2016, *ApJ*, 826, L2
 Newman M. J., Rood R. T., 1977, *Science*, 198, 1035
 Panagia N., Felli M., 1975, *A&A*, 39, 1
 Parker E. N., 1958, *ApJ*, 128, 664
 Perryman M. A. C. et al., 1998, *A&A*, 331, 81
 Raassen A. J. J., Ness J.-U., Mewe R., van der Meer R. L. J., Burwitz V., Kaastra J. S., 2003, *A&A*, 400, 671
 Ramírez I. et al., 2014, *A&A*, 572, A48
 Réville V., Folsom C. P., Strugarek A., Brun A. S., 2016, *ApJ*, 832, 145
 Ribas I., Guinan E. F., Güdel M., Audard M., 2005, *ApJ*, 622, 680

- Rosenqvist L., Opgenoorth H., Buchert S., McCrea I., Amm O., Lathuillere C., 2005, *J. Geophys. Res.*, 110, A09S23
- Sagan C., Mullen G., 1972, *Science*, 177, 52
- Schwenn R., Murdin P., 2000, *Encyclopedia of Astronomy and Astrophysics*, 2301
- See V., Jardine M., Vidotto A. A., Petit P., Marsden S. C., Jeffers S. V., do Nascimento J. D., 2014, *A&A*, 570, A99
- See V. et al., 2017, *MNRAS*, 466, 1542
- Skumanich A., 1972, *ApJ*, 171, 565
- Stauffer J. R., Schultz G., Kirkpatrick J. D., 1998, *ApJ*, 499, L199
- Sterenberg M. G., Cohen O., Drake J. J., Gombosi T. I., 2011, *J. Geophys. Res.*, 116, A01217
- Suzuki T. K., Imada S., Kataoka R., Kato Y., Matsumoto T., Miyahara H., Tsuneta S., 2013, *PASJ*, 65, 98
- Tarduno J. A. et al., 2010, *Science*, 327, 1238
- Telleschi A., Güdel M., Briggs K., Audard M., Ness J.-U., Skinner S. L., 2005, *ApJ*, 622, 653
- Usmanov A. V., Goldstein M. L., Matthaeus W. H., 2014, *ApJ*, 788, 43
- Van Doorselaere T., Wardle N., Del Zanna G., Jansari K., Verwichte E., Nakariakov V. M., 2011, *ApJ*, 727, L32
- van Saders J. L., Ceillier T., Metcalfe T. S., Silva Aguirre V., Pinsonneault M. H., García R. A., Mathur S., Davies G. R., 2016, *Nature*, 529, 181
- Vidotto A. A., Donati J.-F., 2017, *A&A*, 602, A39
- Vidotto A. A., Jardine M., Opher M., Donati J. F., Gombosi T. I., 2011, in Johns-Krull C., Browning M. K., West A. A., eds, *ASP Conf. Ser. Vol. 448, 16th Cambridge Workshop on Cool Stars, Stellar Systems, and the Sun*. Astron. Soc. Pac., San Francisco, p. 1293 ([arXiv:1101.1233](https://arxiv.org/abs/1101.1233))
- Vidotto A. A., Fares R., Jardine M., Donati J.-F., Opher M., Moutou C., Catala C., Gombosi T. I., 2012, *MNRAS*, 423, 3285
- Vidotto A. A., Jardine M., Morin J., Donati J.-F., Lang P., Russell A. J. B., 2013, *A&A*, 557, A67
- Vidotto A. A. et al., 2014, *MNRAS*, 441, 2361
- Vidotto A. A., Fares R., Jardine M., Moutou C., Donati J.-F., 2015, *MNRAS*, 449, 4117
- Wang Y.-M., 1998, in Donahue R. A., Bookbinder J. A., eds, *ASP Conf. Ser. Vol. 154, Cool Stars, Stellar Systems, and the Sun*. Astron. Soc. Pac., San Francisco, p. 131
- Warren H. P., Brooks D. H., 2009, *ApJ*, 700, 762
- Weber E. J., Davis L., Jr, 1967, *ApJ*, 148, 217
- Withers P., 2009, *Adv. Space Res.*, 44, 277
- Wood B. E., Linsky J. L., 2006, *ApJ*, 643, 444
- Wood B. E., Linsky J. L., 2010, *ApJ*, 717, 1279
- Wood B. E., Müller H.-R., Zank G. P., Linsky J. L., 2002, *ApJ*, 574, 412
- Wood B. E., Müller H.-R., Zank G. P., Linsky J. L., Redfield S., 2005, *ApJ*, 628, L143
- Wood B. E., Müller H.-R., Redfield S., Edelman E., 2014, *ApJ*, 781, L33
- Wright A. E., Barlow M. J., 1975, *MNRAS*, 170, 41
- Zuluaga J. I., Bustamante S., Cuartas P. A., Hoyos J. H., 2013, *ApJ*, 770, 23
- Zuluaga J. I., Mason P. A., Cuartas-Restrepo P. A., 2016, *ApJ*, 818, 160

APPENDIX A: T_{COR} VERSUS OMEGA: GOODNESS OF FIT

In this work, we present a fit between coronal temperature data and rotation rate for our sample. We find that a broken power law best describes the trend in data, although we note that there are other

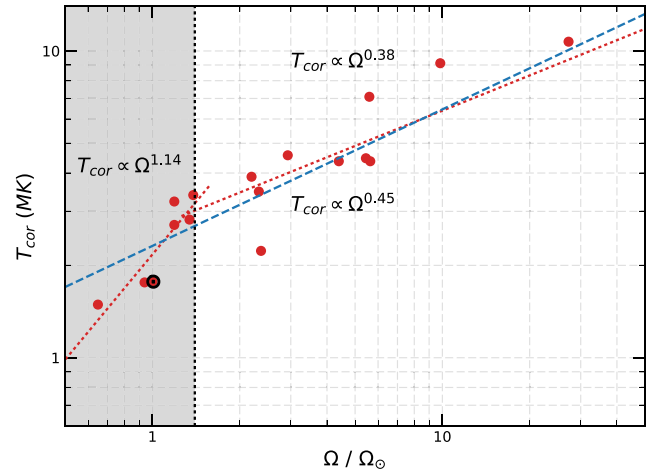


Figure A1. Comparison between a broken power-law fit, which is used in this work, shown in red and a single power-law fit, shown in blue.

possible fits to the data. Having carried out reduced χ^2 analysis on the goodness of fit, we find that both the low- and high- Ω fits shown in Fig. 1 have reduced χ^2 of 3.5 and 1.4, respectively, whereas a single power-law fit would have a reduced χ^2 of 4.7. This would suggest that the broken power-law fit produces a better result than a single power law. In addition, our choice of a broken power law is more in line with recent results (e.g. Metcalfe et al. 2016; van Saders et al. 2016; Beck et al. 2017; Booth et al. 2017; Kitchatinov & Nepomnyashchikh 2017). We use this broken power-law fit as an explanation as to why van Saders et al. (2016) find anomalously high rotation rates in older stars; we propose that these lower coronal temperatures will lead to cooler winds, causing lower mass-loss rates and therefore reduced angular momentum loss. Simultaneously, it also agrees with the break in X-ray luminosities found by Booth et al. (2017) in older stars.

For completeness, we calculate the mass-loss rates that would result from a single power-law fit. Shown in blue in Fig. A1 is the fit produced by using a single power law to fit the coronal temperatures with stellar rotation. We find a relationship of $T_{\text{cor}} \propto \Omega^{0.45}$ for a single power law. This value lies between both values found for the broken power law (1.14 and 0.38). A single power law results in much higher temperatures as you move to slower rotators. We can see how this fit affects the mass-loss rates in Fig. A2. We find that $\dot{M} \propto \Omega^{2.34}$ and $\dot{M} \propto t^{-1.48}$. This fit produces lower mass-loss rates than our previous broken fit for any stars younger than the crossing point of both methods (≈ 5500 Myr or $8.5\Omega_{\odot}$). It also results in higher mass-loss rates for stars older than 5500 Myr, in our case only showing as an increased mass-loss rate for 16 Cyg A. If this new \dot{M} -Age relationship is integrated from 100 Myr to the present (4600 Myr), we find a total mass loss of 0.14 percent the current solar mass.

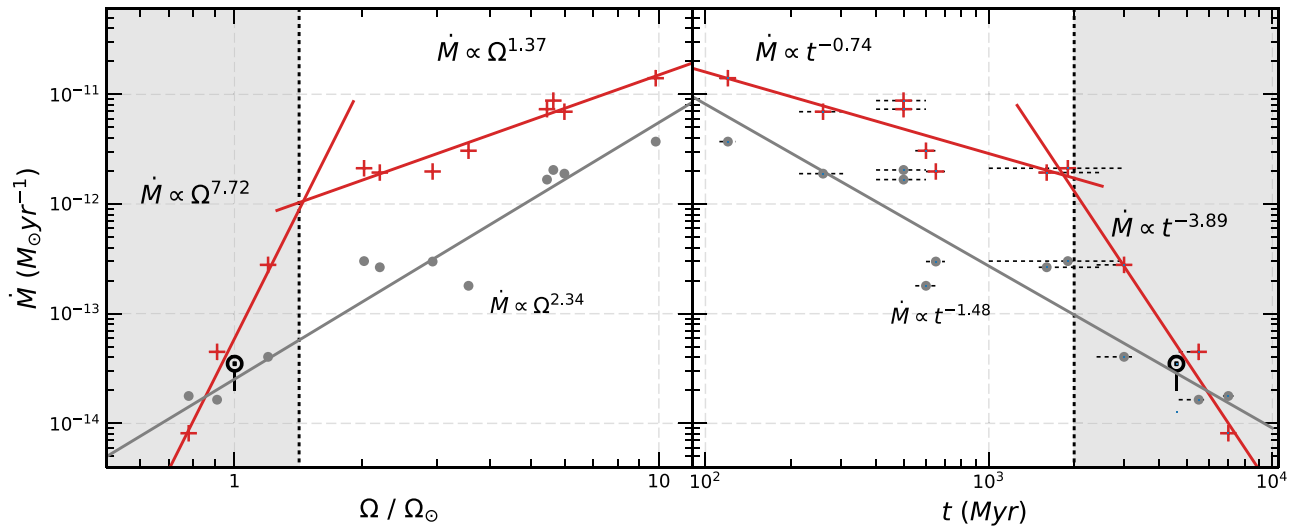


Figure A2. Plot similar to Fig. 2 with the resulting mass-loss rate from a linear fit in $T_{\text{cor}}-\Omega$ (Fig. A1) shown in grey. Other symbols represent the same as in Fig. 2. We can see this produces lower mass-loss rates in most cases, with the exception of 16Cyg A. The relation for each fit is shown beside the fitted line.

This paper has been typeset from a $\text{\TeX}/\text{\LaTeX}$ file prepared by the author.

The solar wind in time – II. 3D stellar wind structure and radio emission

D. Ó Fionnagáin¹★, A. A. Vidotto¹, P. Petit^{2,3}, C. P. Folsom^{2,3}, S. V. Jeffers⁴, S. C. Marsden⁵, J. Morin⁶, J.-D. do Nascimento, Jr^{7,8} and the BCool Collaboration

¹*School of Physics, Trinity College Dublin, College Green, Dublin 2, Ireland*

²*Institut de Recherche en Astrophysique et Planétologie, Université de Toulouse, UPS-OMP, F-31400 Toulouse, France*

³*IRAP, Université de Toulouse, CNRS, UPS, CNES, F-31400 Toulouse, France*

⁴*Institut für Astrophysik, Universität Göttingen, Friedrich-Hund-Platz 1, D-37077 Göttingen, Germany*

⁵*Centre for Astrophysics, University of Southern Queensland, Toowoomba, QLD 4350, Australia*

⁶*Laboratoire Univers et Particules de Montpellier, Université de Montpellier, CNRS, F-34095 Montpellier, France*

⁷*Dep. de Física, Universidade Federal do Rio Grande do Norte, CEP: 59072-970 Natal, RN, Brazil*

⁸*Harvard-Smithsonian Center for Astrophysics, Cambridge, MA 02138, USA*

Accepted 2018 November 12. Received 2018 November 2; in original form 2018 September 13

ABSTRACT

In this work, we simulate the evolution of the solar wind along its main-sequence lifetime and compute its thermal radio emission. To study the evolution of the solar wind, we use a sample of solar mass stars at different ages. All these stars have observationally reconstructed magnetic maps, which are incorporated in our 3D magnetohydrodynamic simulations of their winds. We show that angular-momentum loss and mass-loss rates decrease steadily on evolutionary time-scales, although they can vary in a magnetic cycle time-scale. Stellar winds are known to emit radiation in the form of thermal bremsstrahlung in the radio spectrum. To calculate the expected radio fluxes from these winds, we solve the radiative transfer equation numerically from first principles. We compute continuum spectra across the frequency range 100 MHz to 100 GHz and find maximum radio flux densities ranging from 0.05 to 2.2 μJy . At a frequency of 1 GHz and a normalized distance of $d = 10$ pc, the radio flux density follows $0.24 (\Omega/\Omega_{\odot})^{0.9} (d/[10\text{pc}])^{-2} \mu\text{Jy}$, where Ω is the rotation rate. This means that the best candidates for stellar wind observations in the radio regime are faster rotators within distances of 10 pc, such as κ^1 Ceti (0.73 μJy) and χ^1 Ori (2.2 μJy). These flux predictions provide a guide to observing solar-type stars across the frequency range 0.1–100 GHz in the future using the next generation of radio telescopes, such as ngVLA and Square Kilometre Array.

Key words: stars: solar-type – stars: winds, outflows – radio continuum: stars .

1 INTRODUCTION

Solar analogues are essential to our understanding of how our own Sun has evolved through its past and how it will evolve into the future. The rotational evolution of stars has a significant effect on the activity (Wright et al. 2011; Vidotto et al. 2014b), as rotation has been linked to activity markers such as coronal X-ray emission (Telleschi et al. 2005; Wright et al. 2011), chromospheric activity (e.g. Ca II, H α) (Lorenzo-Oliveira et al. 2018) and flaring rates (Maehara et al. 2017). The stellar dynamo is regulated by rotation and convection, which in turn generates the magnetic field causing stellar activity (Brun & Browning 2017). By virtue of this relationship between rotation and activity, the evolution of orbiting planets is directly affected, e.g. by high-energy stellar radiation incident

on their atmospheres (Owen & Mohanty 2016; Ribas et al. 2016). Stellar rotation has been shown to decrease with age (Skumanich 1972) following $\Omega \propto t^{1/2}$ for stars older than ~ 700 Myr (Gallet & Bouvier 2013). More recently, however, some deviation from this standardized age–rotation relationship has been observed at older ages (Van Saders et al. 2016), with some processes proposed to explain this behaviour (Metcalfe, Egeland & van Saders 2016; Beck et al. 2017; Booth et al. 2017; Ó Fionnagáin & Vidotto 2018).

The mechanism by which stars spin-down while traversing the main sequence is through angular momentum loss by their magnetized winds (e.g. Weber et al. 1967; Vidotto et al. 2014a; See et al. 2017b). Therefore, this indicates that the surface magnetic field of the star also evolves with time, as demonstrated with magnetic field observations analysed using the Zeeman–Doppler Imaging (ZDI) technique (Vidotto et al. 2014b; Folsom et al. 2016, 2018). ZDI is a method that allows for the reconstruction of the large-scale magnetic field of the stellar surface from a set of high-resolution

* E-mail: ofionnad@tcd.ie

spectropolarimetric data (Semel 1989; Brown et al. 1991; Donati et al. 1997), although it is insensitive to small-scale fields (Lang et al. 2014; Lehmann et al. 2018). See et al. (2017a,b) determined, from 66 ZDI-observed stars, that the magnetic geometry as well as angular momentum and mass-loss is correlated to Rossby number.¹ Other works have demonstrated that there is a link between all of stellar activity, magnetic strength and geometry, angular momentum loss, and stellar winds (Matt et al. 2012; Nicholson et al. 2016; Pantolmos & Matt 2017; Finley, Matt & See 2018).

Stellar angular momentum-loss depends upon how much mass is lost by their winds (Weber et al. 1967). Due to the tenuous nature of low-mass stellar winds, a direct measurement of their winds is difficult (e.g. Wood et al. 2005), but would prove extremely useful in the constraining of mass-loss rates and other global wind parameters. In this regard, the observations of radio emission from the winds of low-mass stars could provide meaningful constraints on wind density and mass-loss rate (Lim & White 1996; Güdel 2002; Villadsen et al. 2014; Fichtinger et al. 2017; Vidotto & Donati 2017). The wind is expected to have continuum emission in radio through the mechanism of thermal free-free emission (Panagia & Felli 1975; Wright, Barlow & Michael 1975). This emission is expected to be stronger for stars with denser winds and is also dependent on the density (n) gradient in the wind with radial distance, R : $n \propto R^{-a}$. The value of a is indirectly related to other stellar parameters such as the specific gravity, magnetic field, and rotation. When $a = 2$ this represents when the wind has reached terminal radial velocity, however, this is unrealistic in regions closer to the star where the wind is accelerating. Therefore, we expect stellar winds to exhibit gradients much steeper than when $a = 2$. We discuss this further in Section 4.

With this idea in mind, Güdel, Guinan & Skinner (1998) and Gaidos, Güdel & Blake (2000) observed various solar analogues. They could place upper limits on the radio fluxes from these objects, and so indirectly infer upper mass-loss rate constraints. All non-degenerate stars emit some form of radio emission from their atmospheres (Güdel 2002). Although different radio emission mechanisms dominate at different layers in their atmosphere and wind (Güdel 2002). For example, detecting coronal radio flares at a given frequency implies the surrounding wind is optically thin at those frequencies, allowing for placement of upper mass-loss limits. In addition, Güdel (2007) noted that thermal emission should dominate at radio frequencies as long as no flares occur while observing. The three dominant thermal emission mechanisms the author described are bremsstrahlung from the chromosphere, cyclotron emission above active regions, and coronal bremsstrahlung from hot coronal loops. These emission mechanisms must be addressed when attempting to detect the winds of solar-type stars at radio frequencies.

Observing these winds can become difficult as the fluxes expected from these sources is at the μJy level (see upper limits placed by Gaidos et al. 2000; Villadsen et al. 2014; Fichtinger et al. 2017), and can be drowned out by chromospheric and coronal emission as described in the previous paragraph. Villadsen et al. (2014) observed three low-mass stars, with positive detections for all three stars in the Ku band (centred at 34.5 GHz) of the VLA, and non-detections at lower frequencies. They suggested that the detected emissions originate in the chromosphere of these stars, with some contributions from other sources of radio emission. If emanating from the

chromosphere, these detections do not aid in constraining the wind. Fichtinger et al. (2017) more recently observed four solar-type stars with the VLA at radio frequencies, and provided upper limits to the mass-loss rates for each, ranging from 3×10^{-12} to $7 \times 10^{-10} M_{\odot} \text{ yr}^{-1}$, depending on how collimated the winds are. Bower et al. (2016) observed radio emission from the young star V830 Tau, with which Vidotto & Donati (2017) were able to propose mass-loss rate constraints between 3×10^{-10} and $3 \times 10^{-12} M_{\odot} \text{ yr}^{-1}$. Transient coronal mass ejections should also be observable, which would cause more issues in detecting the ambient stellar wind, but these events are expected to be relatively short and could also help in constraining transient mass-loss from these stars (Crosley et al. 2016).

To aid in the radio detection and interpretation of the winds of solar-type stars, we here quantify the detectability of the winds of six solar-like stars of different ages within the radio regime from 100 MHz to 100 GHz. We aim to study the effects ageing stellar winds have on different solar analogues along the main sequence, allowing us to constrain global parameters and quantify the local wind environment.

To do this, we conduct 3D magnetohydrodynamical simulations of winds of solar-type stars, investigating the main-sequence solar wind evolution in terms of angular-momentum loss rates (\dot{J}), mass-loss rates (\dot{M}), and wind structure. We then use the results of our simulations to quantify the detectability of the radio emission from the solar wind in time, that can help guiding and planning of future observations of solar-like winds. We present the sample of stars simulated and analysed in Section 2. Discussed in Section 3 is the stellar wind modelling and simulation results. Our models predict the evolution of \dot{J} , \dot{M} , and Φ_{open} of the solar wind through time, while also constraining the planetary environment surrounding the host stars. In Section 4 we demonstrate how we calculate radio emission for each star and the resulting emissions and flux densities expected. Section 5 we conclude on the results presented in this work.

2 STELLAR SAMPLE

Our sample of solar-like stars was selected so as to closely resemble to Sun in both mass and radius. They cover a range of rotation rates (from 4.8 to 27 d or 1 to 5.6 Ω_{\odot}) with ZDI reconstructed by Petit et al. (2008), do Nascimento, Jr. et al. (2016), and Petit et al. (in preparation) as part of the BCool collaboration. Gallet & Bouvier (2013, 2015) depict different age-rotation evolutionary tracks for a $1 M_{\odot}$ star, which converge at 800 Myr to the Skumanich law (Skumanich 1972). χ^1 Ori follows the fast rotator track, while the rest of our stars exist beyond the convergence point. We note that HD 190771 and HD 76151 exhibit faster rotation than the Skumanich law, which could be due to uncertainties in their ages. The stars in our sample are listed below, see also Table 1 for stellar parameters, and Fig. 1 for observed ZDI maps.

χ^1 Orion This star is both the youngest star and the fastest rotator we have simulated, with a rotation period of 4.8 d and an age of 0.5 Gyr (Vidotto et al. 2014b). This fast rotation should indicate a more active star than the slower rotators, which we see confirmed in the high-magnetic-field strengths. The large-scale magnetic geometry reconstructed with ZDI for this star displays a complex structure (Fig. 1), showing very un-dipolar like structure (Petit et al., in preparation). Note that the ZDI observations here include 10 spherical

¹Rossby number (Ro) is defined as the ratio between stellar rotation and convective turnover time (Noyes et al. 1984).

Table 1. Stellar parameters of our sample are shown on the left (mass, radius, rotation period, age, and distance) and specifics of the simulations are shown on the right (base density, base temperature, mass-loss rate, angular momentum-loss rate, open magnetic flux, and flux ratio between surface and open magnetic fluxes). Stellar parameters were compiled in Vidotto et al. (2014b). Distances are found using the Gaia DR2 database^a (Prusti et al. 2016; Brown et al. 2018) values for parallax.

Star	Observables						Simulation					
	M_* (M_\odot)	R_* (R_\odot)	P_{rot} (d)	Ω (Ω_\odot)	Age (Gyr)	d (pc)	n_0 (cm^{-3}) ($\times 10^8$)	T_0 (MK)	\dot{M} ($M_\odot \text{ yr}^{-1}$) ($\times 10^{-13}$)	\dot{J} (erg) ($\times 10^{30}$)	Φ_{open} (G cm) ($\times 10^{22}$)	f
χ^1 Ori	1.03	1.05	4.86	5.60	0.5	$8.84^{\pm 0.02}$	18.9	2.84	46.5	285	22.5	0.37
HD 190771	0.96	0.98	8.8	3.09	2.7	$19.02^{\pm 0.01}$	13.2	3.04	36.1	91.0	23.46	0.59
κ^1 Ceti	1.03	0.95	9.3	2.92	0.65	$9.15^{\pm 0.03}$	12.8	2.98	22.1	124	30.71	0.44
HD 76151	1.06	0.98	15.2	1.79	3.6	$16.85^{\pm 0.01}$	9.54	2.47	8.26	31.8	14.68	0.49
18 Sco	0.98	1.02	22.7	1.20	3.0	$14.13^{\pm 0.02}$	7.5	1.85	6.47	5.34	4.29	0.70
HD 9986	1.02	1.04	23	1.18	4.3	$25.46^{\pm 0.03}$	7.44	1.82	5.82	2.35	3.30	0.94
Sun Min	1.0	1.0	27.2	1	4.6	–	6.72	1.5	1.08	1.04	3.44	0.69
Sun Max	1.0	1.0	27.2	1	4.6	–	6.72	1.5	1.94	15.5	6.17	0.24

Note. ^a <https://gea.esac.esa.int/archive/>

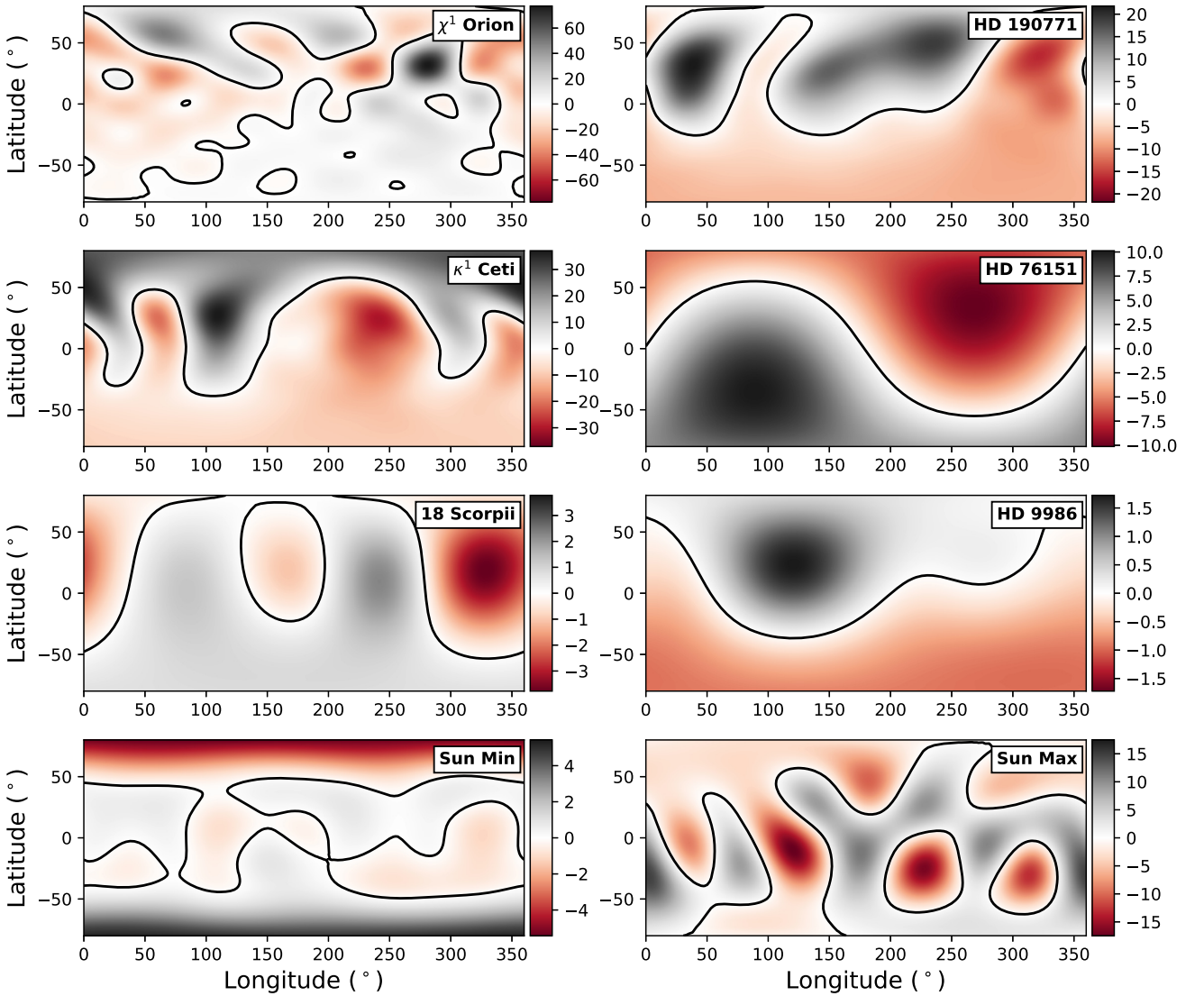


Figure 1. Radial surface magnetic fields of our stars. Each magnetic field is saturated at the maximum absolute value for each field respectively. Magnetic field contours are shown in Gauss. The maps are shown in latitude–longitude coordinates.

harmonic degrees, which is the most of all simulations. This star is the closest star in our sample at 8.84 pc.²

HD 190771 This star possesses an uncharacteristically short rotation period (8.8 d) for its commonly used age (2.7 Gyr, derived from isochrone fitting, Valenti & Fischer 2005). This fast rotation should indicate a more active star, which we see validated in the ZDI observations of the magnetic field at the stellar surface. We see one of the least dipolar fields in the sample, with large areas of strong magnetic field of both polarities in the northern hemisphere (Fig. 1). Note that polarity reversal has been observed to occur in the magnetic field of this star (Petit et al. 2009).

κ^1 **Ceti** is estimated to be the second youngest star in our selected sample, with an age of 0.65 Gyr (Rosén et al. 2016). The observed rotation period from photometry is 9.2 d (Messina & Guinan 2003; Rucinski et al. 2004, ground and space, respectively). The higher levels of activity in this star are apparent when we examine the ZDI map, with non-dipolar geometry and relatively strong B field ($B_{r,\max} \approx 35$ G, do Nascimento, Jr. et al. 2016). It is the second closest star in our sample (excluding the Sun), at a distance of 9.13 pc.²

HD 76151 has a rotation period of 15.2 d (Maldonado et al. 2010). The age of HD 76151 is estimated to be 3.6 Gyr (Petit et al. 2008). ZDI observations of HD 76151 present a strong dipolar field, with $B_{r,\max} \approx 10$ G, which is tilted to the axis of rotation by 30° (Petit et al. 2008). Considering the age of the star and the dipolar geometry of the magnetic field, we expect a slower wind than the faster, more magnetically active rotators (see also Pognan et al. 2018).

18 Scorpii is 3 Gyr old and possesses a rotation period of 22.3 d. It displays very quiescent behaviour, with a weak, largely dipolar magnetic field (Petit et al. 2008). It is the most similar solar twin for which we have surface magnetic field measurements, displaying very similar spectral lines to the Sun (Meléndez et al. 2014). Recently, many more solar twins have been identified (Lorenzo-Oliveira et al. 2018), however, these stars do not have magnetic field observations.

HD 9986 presents another off axis dipole, with a maximum field strength of 1.6 G and an age of 4.3 Gyr (Vidotto et al. 2014b). This is the weakest magnetic field of any star in the sample, Petit et al. (in preparation).

The Sun has a well documented cyclical behaviour, of which we take one map at the maximum of the cycle, and another map at the minimum of the cycle. Maps for the minima and maxima are taken at Carrington rotations 1983 and 2078, respectively, which were observed with SOHO/MDI in the years 2001 and 2008. We have removed the higher degree harmonics ($\ell \geq 5$) for both maps, so as to replicate the Sun as if observed similarly to the other slowly rotating stars in the sample (Vidotto 2016; Lehmann et al. 2018; Vidotto et al. 2018). We note that the Sun at maximum possesses a much more complex magnetic geometry than the solar minimum, including a stronger magnetic field (e.g. DeRosa, Brun & Hoeksema 2010).

3 WIND MODELLING

3.1 3D numerical simulations of stellar winds

We use the 3D MHD numerical code BATS-R-US to simulate the winds of our sample of stars. This code has been used frequently

in the past to study many magnetic astrophysical plasma environments (Powell et al. 1999; Tóth et al. 2005; Manchester et al. 2008; Vidotto et al. 2015; Vidotto 2017; Alvarado-Gómez et al. 2018). Here we use it to solve for eight parameters: mass density (ρ), wind velocity ($\mathbf{u} = \{u_x, u_y, u_z\}$), magnetic field ($\mathbf{B} = \{B_x, B_y, B_z\}$), and gas pressure P . The code numerically solves a set of closed ideal MHD equations representing, respectively, the mass conservation, momentum conservation, the induction equation, and the energy equation:

$$\frac{\partial \rho}{\partial t} + \nabla \cdot (\rho \mathbf{u}) = 0, \quad (1)$$

$$\frac{\partial (\rho \mathbf{u})}{\partial t} + \nabla \cdot \left[\rho \mathbf{u} \mathbf{u} + \left(P + \frac{B^2}{8\pi} \right) \mathbf{I} - \frac{\mathbf{B} \mathbf{B}}{4\pi} \right] = \rho \mathbf{g}, \quad (2)$$

$$\frac{\partial \mathbf{B}}{\partial t} + \nabla \cdot (\mathbf{u} \mathbf{B} - \mathbf{B} \mathbf{u}) = 0, \quad (3)$$

$$\frac{\partial \varepsilon}{\partial t} + \nabla \cdot \left[\mathbf{u} \left(\varepsilon + P + \frac{B^2}{8\pi} \right) - \frac{(\mathbf{u} \cdot \mathbf{B}) \mathbf{B}}{4\pi} \right] = \rho \mathbf{g} \cdot \mathbf{u}, \quad (4)$$

where the total energy density is given by

$$\varepsilon = \frac{\rho u^2}{2} + \frac{P}{\gamma - 1} + \frac{B^2}{8\pi}. \quad (5)$$

Here, \mathbf{I} denotes the identity matrix, and \mathbf{g} the gravitational acceleration. We assume that the plasma behaves as an ideal gas, that $P = nk_B T$, where $n = \rho / (\mu m_p)$ is the total number density of the wind, ρ representing the mass density, and μm_p denoting the average particle mass. We take $\mu = 0.5$, which represents a fully ionized hydrogen wind. We can also relate the pressure to the density, by assuming the wind is polytropic in nature, which follows the relationship: $P \propto \rho^\gamma$, where γ represents the polytropic index. This polytropic index implicitly adds heat to the wind as it expands, meaning we do not require an explicit heating equation in our model. We adopt $\gamma = 1.05$, which is similar to effective index found by Van Doorselaere et al. (2011) for the Sun, and to values used in the literature for simulating winds (Vidotto et al. 2015; Pantolmos & Matt 2017; Ó Fionnagáin & Vidotto 2018).

The free parameters of polytropic wind models, such as ours, are the base density (ρ_0) and temperature (T_0) of the wind. Here, we use the empirical model from Ó Fionnagáin & Vidotto (2018) that relates both the temperature and density of the wind base with the rotation of the star (see also Holzwarth & Jardine 2007; See et al. 2014; Johnstone et al. 2015a,b; Réville et al. 2016).

$$T_0 (\Omega < 1.4 \Omega_\odot) = 1.5 \pm 0.19 \left(\frac{\Omega_\star}{\Omega_\odot} \right)^{1.2 \pm 0.54} \text{ MK} \quad (6)$$

$$T_0 (\Omega > 1.4 \Omega_\odot) = 1.98 \pm 0.21 \left(\frac{\Omega_\star}{\Omega_\odot} \right)^{0.37 \pm 0.06} \text{ MK} \quad (7)$$

$$n_0 = 6.72 \times 10^8 \left(\frac{\Omega_\star}{\Omega_\odot} \right)^{0.6} \text{ cm}^{-3}. \quad (8)$$

To set the magnetic field vector, we use the radial component of the ZDI maps at the stellar surfaces (Fig. 1). At the initial state, we use a potential field source surface model (e.g. Altschuler & Newkirk 1969) to extrapolate the magnetic field into the grid, with the field lines becoming purely radial beyond $4 R_\star$. The code then numerically solves the MHD equations and allows the magnetic

²<https://gea.esac.esa.int/archive/>

field to interact with the wind (and vice versa), until it reaches a relaxed state.

Fig. 2 shows the structure of the winds, with open magnetic field lines displayed in grey and closed magnetic fields shown in red. We can see the field lines become much more structured and organized in the slower rotators with more dipolar fields, as opposed to the complex field lines of the faster rotators with less dipolar fields. Equatorial radial velocities are shown as a yellow-blue graded surface, with the radial velocities ranging from 300 to 580 km s⁻¹ at 0.1 au, near the outer boundary of our simulations. Shown in orange are the Alfvén surfaces, which denote where the poloidal wind velocity equals the Alfvén velocity ($u_{\text{pol}} = u_A = B/\sqrt{4\pi\rho}$). They display where the wind becomes less magnetically dominated and more kinetically dominated by the flowing wind. We see these Alfvén surfaces range from 2 to 6 R_{*} across our sample. Stars with very weak magnetic fields (e.g. 18 Sco, HD 9986) generally have smaller Alfvén surface radii.

3.2 Mass-loss rates (\dot{M}), angular momentum-loss rates (\dot{J}), and open magnetic flux (Φ_{open})

From our wind simulations we can calculate the mass-loss rate from each of the stars by integrating the mass flux through a spherical surface S around the star

$$\dot{M} = \oint_S \rho u_r \, dS, \quad (9)$$

where \dot{M} is the mass-loss rate, ρ is the wind density, u_r is the radial velocity, and S is our integration surface. In our simulations we see an overall decrease of \dot{M} with decreasing rotation rate, Table 1, which is consistent with the works of Cranmer & Saar (2011), Suzuki et al. (2013), Johnstone et al. (2015a,b), and Ó Fionnagáin & Vidotto (2018). We note that the mass-loss rate we find for the Sun is ~ 5 times larger than the observed value of $\sim 2 \times 10^{-14} M_{\odot} \text{ yr}^{-1}$. This is because of our choice of base density, which is three times higher than in Ó Fionnagáin & Vidotto (2018). We opted for a three times higher base density as we were unable to find a stable solution for the winds of a few stars in our sample. Ó Fionnagáin & Vidotto (2018) suggested that the angular-momentum loss for solar-type stars would drop off substantially for slow rotators, causing older solar-type stars to rotate faster than expected. This would explain the findings of Van Saders et al. (2016), who observed a set of ageing solar-like stars and discovered that they rotated at much faster rates than expected by the traditional Skumanich age–rotation relationship. In our previous work, Ó Fionnagáin & Vidotto (2018), we linked the anomalous fast rotation at older ages to the drop in mass-loss rates at older ages, and consequently, to a drop in the angular momentum-loss rate. Unfortunately, we could not verify this drop in angular momentum for slower rotators, as we do not have magnetic field maps for solar-mass stars that rotate much slower than the Sun. This lack in magnetic field maps in this regime can be explained observationally as detecting weak magnetic fields in slowly rotating stars is very challenging. Therefore, we compare mass-loss rates calculated here using the faster rotators. Fig. 3 shows the mass-loss rate (red points) and the fit to these points (red line) which follows the relationship

$$\dot{M} = 4.7(\pm 0.1) \times 10^{-13} \left(\frac{\Omega_{\star}}{\Omega_{\odot}} \right)^{1.4 \pm 0.2} M_{\odot} \text{ yr}^{-1}. \quad (10)$$

The fit to the faster rotators from Ó Fionnagáin & Vidotto (2018) (shown as a dotted black line), which possesses the power-law index of 1.4, agrees within the error to the power law index fit here

of 1.6 ± 0.2 . It is interesting that these mass-loss rates agree so well considering the base density of the 3D simulations is three times higher than in Ó Fionnagáin & Vidotto (2018). This suggests that the inclusion of a magnetic field in the 3D simulations would generate a much lower mass-loss rate than in the 1D simulations, given the same base densities. This is most likely due to closed magnetic regions, which act to hold in material, and reduce \dot{M} .

We also determine \dot{J} from our simulations as

$$\dot{J} = \oint_S \left[-\frac{\varpi B_{\phi} B_r}{4\pi} + \varpi u_{\phi} \rho u_r \right] dS, \quad (11)$$

where $\varpi = (x^2 + y^2)^{1/2}$, the cylindrical radius, B and u are the magnetic field and velocity components of the wind, and r and ϕ denote the radial and azimuthal components, respectively (Mestel 1999; Vidotto et al. 2014a). The integral is performed over a spherical surface (S) in a region of open field lines. From Fig. 3 we see a trend of decreasing \dot{J} towards slower rotating stars. We note that while the solar minimum simulation has a reasonable angular momentum loss rate, we find that the solar maximum simulation has a higher \dot{J} than expected (see e.g. Finley et al. 2018).

The magnetic field geometry and strength affect the wind in these simulations as it evolves, by establishing a pressure and tension against the ionized plasma. Here we calculate how much of the wind consists of open and closed field lines, by integrating the unsigned magnetic flux passing through a surface near the outer edge of our simulation domain, where all the field lines are open

$$\Phi_{\text{open}} = \oint_{S_{\text{sph}}} |B_r| \, dS. \quad (12)$$

The open flux of the wind, Φ_{open} , is relevant as regions of open flux the origin of the fast solar/stellar wind (Verdini et al. 2010; Réville et al. 2016; Cranmer, Gibson & Riley 2017). It is also related to how efficient the wind is at transporting angular momentum from the star (Réville et al. 2015). In Fig. 3 we see that across the rotation periods of our sample, open flux decreases as the stars spin-down. There is also a hint of an open flux plateau in the faster rotators. In Table 1, we also present the ratio f of open to unsigned surface magnetic field flux (Φ_{surf}), following the convention: $\Phi_{\text{surf}} = f\Phi_{\text{open}}$.

3.3 Wind derived properties at typical hot-Jupiter distances

From our simulations we can gather much information on the structure of the winds of solar-like stars. This aids us in the analysis of the wind evolution from young to older solar-type stars along the main sequence. It also impacts the study of exoplanet evolution, as exoplanets exist orbiting these stars, embedded in the stellar wind. The main components of the wind affecting exoplanets are magnetic pressure (for close in exoplanets) and ram pressure (for distantly orbiting exoplanets). There also exists a thermal pressure constituent to the wind, but this is usually much smaller than both of the previous pressures. In our case, at 0.1 au the ram pressure dominates as this is well above the Alfvén surface for each star. The ram pressure is given as

$$P_{\text{ram}} = \rho u_r^2. \quad (13)$$

Here we assume the orbit to be in the equatorial plane aligned with the rotation axis, but we note that this might not always be the case for hot Jupiters (Huber et al. 2013; Anderson, Storch & Lai 2016). We see from Fig. 4 that there can be large variations

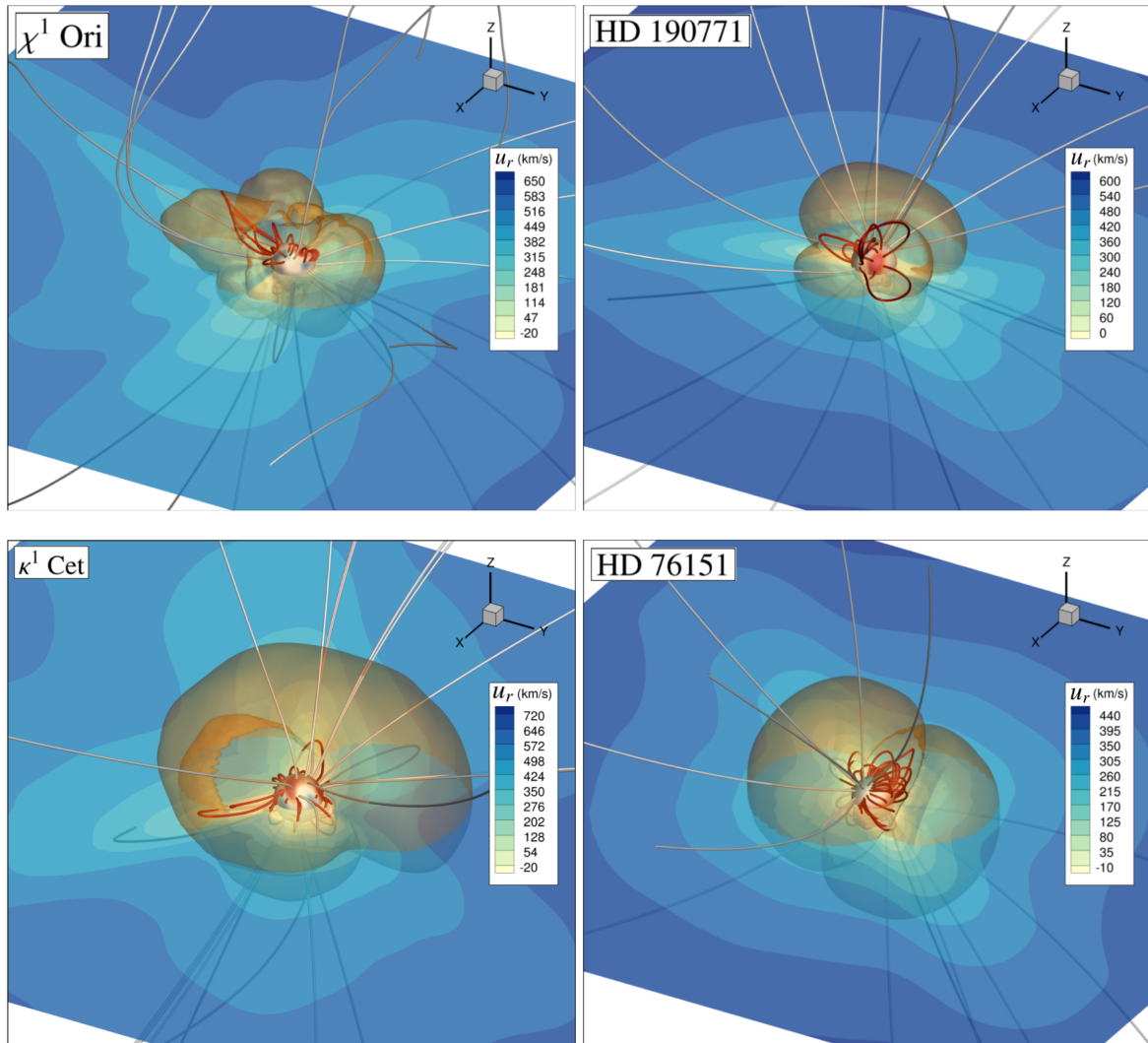


Figure 2. Steady state solutions for the simulated winds of the solar analogues. The translucent slice through the $z = 0$ plane shows the wind radial velocity (u_r). Open and closed magnetic field lines are shown as grey and red streamlines, respectively. Magnetic polarity is shown on the stellar surface as a red-blue diverging contour. The orange surface shows the Alfvén surface, where $u_r = u_A$, the Alfvén velocity. Note that the faster rotators have much less uniform, dipolar Alfvén surfaces, due to the less uniform magnetic fields topologically, at their surfaces.

in the ram pressure impinging upon an orbiting exoplanet at 0.1 au, both within a single orbit around a particular host star, and between each host star. From these, we infer the evolution of the planetary environment around a solar-like star as it evolves. We see that the Sun at minimum possesses the lowest ram pressure of any of the stars in our sample. We can compare the distribution of velocities for all of the stars by histogramming the velocities across a sphere of 0.1 au. This method can give insight into the structure of the wind, discerning uni-modal and multimodal wind structures (see Fig. 5). We observe that more complex and stronger fields lead to less uniform wind structures. We can see that the winds of 18 Sco, HD 9986, and the Sun at minimum display unimodality, while other stars such as χ^1 Ori and HD 190771 have a very skewed velocity distributions. The magnetic field strength and geometry seems to directly affect the wind structure even at these distances. This is discussed in Réville et al. (2016), who noted that the expansion of magnetic flux tubes can cause an acceleration in the wind.

4 RADIO EMISSION OF THE SOLAR WIND IN TIME

4.1 Radiative transfer model

It has long been established that the plasma of stellar winds emit at radio wavelengths through thermal free-free processes (Panagia & Felli 1975; Wright et al. 1975; Lim & White 1996). If this radio emission is observed, it could provide a way to detect the winds of low-mass stars directly, allowing an estimation of the wind density and temperature at that location in the wind. Constraining the density of the wind would allow a much better estimate on the mass-loss rate of the star, and by extension angular-momentum loss rates.

Analytical expressions for the radio emission calculation are commonly used in the literature (Panagia & Felli 1975; Wright et al. 1975; Lim & White 1996; Fichtinger et al. 2017; Vidotto & Donati 2017). For example, Panagia & Felli (1975) assumed a power law dependence of density with radial distance, such that

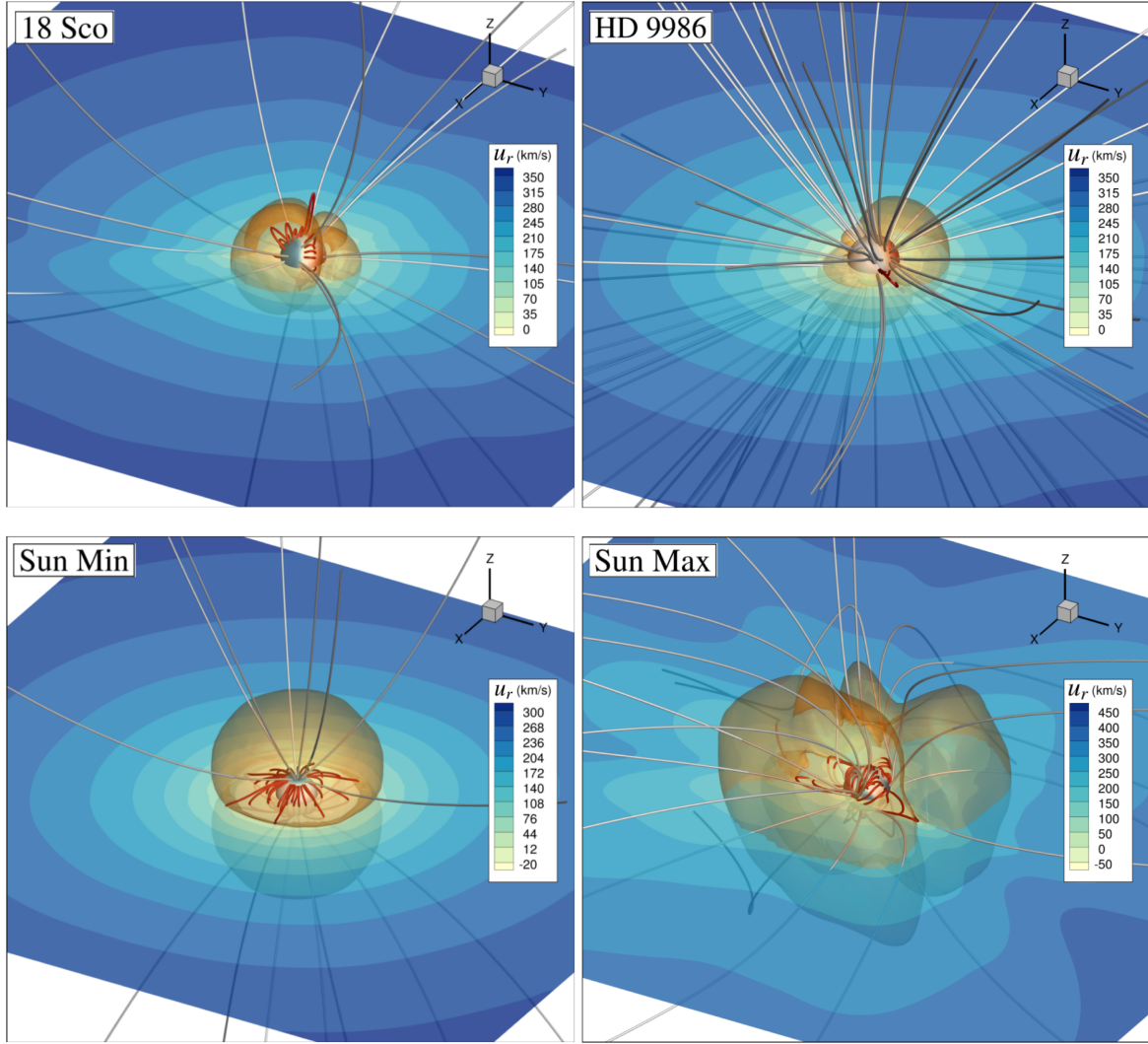


Figure 2. Continued.

$\rho \propto R^{-\alpha}$, which generates a radius dependence for radio flux density with frequency: $S_\nu \propto \nu^{\frac{-4.2}{2\alpha-1}+2}$. However, when R is small and the wind is still accelerating, this density dependence deviates from a power law. Thus, these power-law gradients can underestimate the density decay close to the star and overestimate it further from the star. This is discussed further in Appendix A. A similar approach is also used in defining the distance-dependence of the temperature of the wind. To overcome this, we perform the radio emission calculation from first principles, by solving the radiative transfer equation numerically (code available on GitHub: <https://github.com/ofionnad/radiowinds>; Ó Fionnagáin 2018). Using our 3D MHD simulations, we can use the exact density decay expected, which gives a more precise estimation of the wind emission.

Fig. 6 shows a schematic of our calculation grid, we divide the grid into equally spaced cells, each possessing a value of wind density and temperature. The illustration shows a red annulus around a magnetic star, outlining the expected radio emission from the wind (this is not expected to be spherically symmetric). Note that the actual number of cells used in calculations ($=200^3$) is much greater than depicted in Fig. 6. From this, we can calculate the thermal emission expected from these winds by solving the radiative

transfer equation,

$$I_\nu = \int_{-\infty}^{\tau'_{\max}} B_\nu e^{-\tau'} d\tau' \quad (14)$$

where I_ν denotes the intensity from the wind, B_ν represents the source function, which in the thermal case becomes a blackbody function, τ represents the optical depth of the wind, with τ' representing our integration coordinate across the grid. The optical depth of the wind depends on the absorption coefficient, α_ν , of the wind as

$$\tau_\nu = \int \alpha_\nu ds, \quad (15)$$

where s represents the physical coordinate along the line of sight, α_ν is described as (Panagia & Felli 1975; Wright et al. 1975; Cox & Pilachowski 2002),

$$\alpha_\nu = 3.692 \times 10^8 [1 - e^{-h\nu/k_B T}] Z^2 f_g T^{-0.5} \nu^{-3} n_e n_i \quad (16)$$

and the blackbody function is the standard Planck function.

$$B_\nu = \frac{2h\nu^3}{c^2} \frac{1}{e^{h\nu/k_B T} - 1}, \quad (17)$$

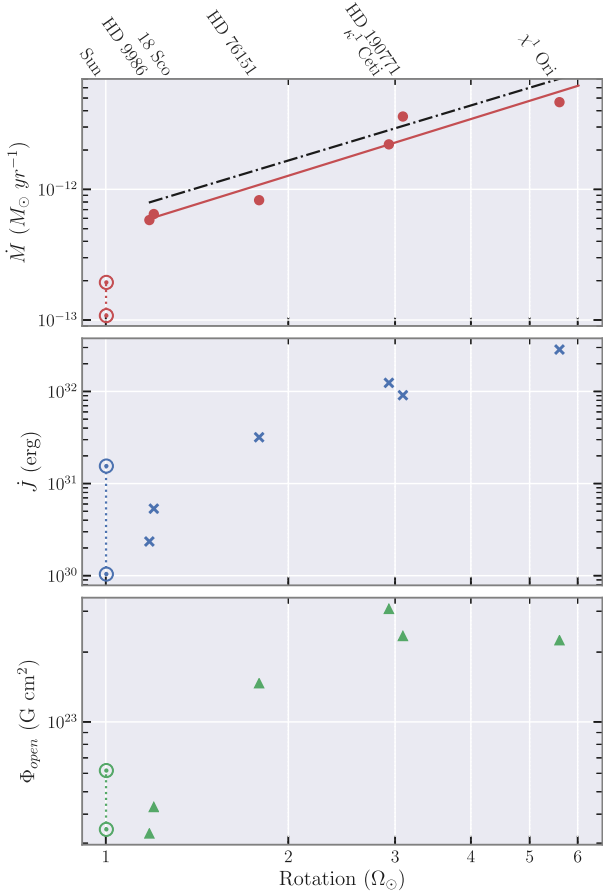


Figure 3. Top to bottom, the three panels above show the mass-loss rate, angular momentum-loss rate, and unsigned magnetic open flux from our sample of simulations. The stars are labelled at the top of the figure, with the solar simulations represented by the solar symbol (\odot), where activity maximum is always on top. In the top panel we include a fit to the data (red line, excluding the Sun) and compare this to the fast rotator fit as described in Ó Fionnagáin & Vidotto (2018) (black dashed line).

where ν is the observing frequency, h is Planck’s constant, k_B is Boltzmann’s constant, T is the temperature of the wind, Z is the ionic state of the wind (+1 for our ionized hydrogen wind), with n_e and n_i representing the electron and ion number densities of the wind. In our case we have the same number of ions and electrons, so this becomes simply n_i^2 . f_g is the gaunt factor which is defined as (Cox & Pilachowski 2002)

$$f_g = 10.6 + 1.9 \log_{10} T - 1.26 \log_{10} Z\nu. \quad (18)$$

4.2 Evolution of the radio emission with age

Using equations (14) or (17) we calculate 2D images for each frequency (cube of data) for the intensity and optical depth, across the plane of the sky, showing the intensity attributed to different regions of the wind, and the optical depth associated with it. This is represented in Fig. 7. Note that for comparison we calculate solar wind radio emission at a distance of 10 pc. We can see that the intensity of the emission increases as we increase the frequency, although it radiates from a much smaller region. This is due to the decrease in the optical depth with frequency and allows us to see further into the wind, to much denser regions giving rise to more emission. The optical depth of the wind will have a major impact on

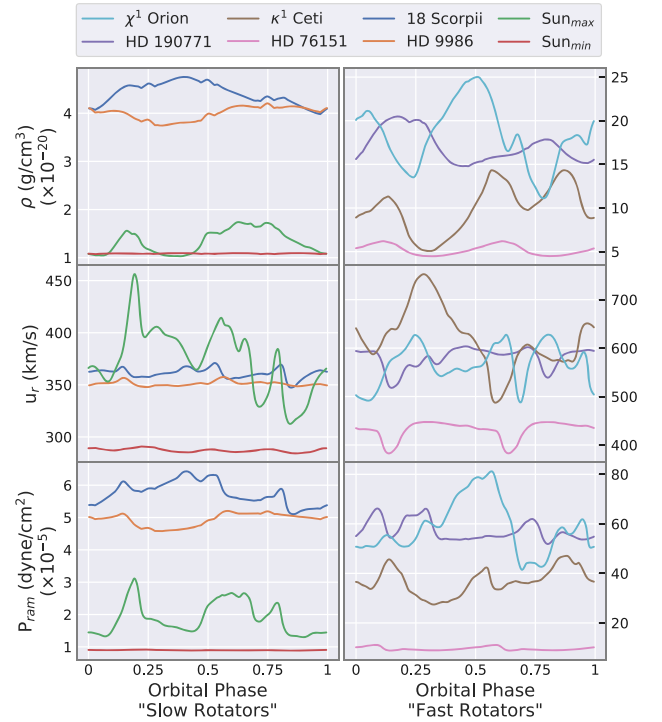


Figure 4. Top: Figure showing the density variations of the wind at the equator ($z = 0$ plane) for each star in our sample, at a distance of 0.1 au. Middle: The velocity variations of the wind at the equator at 0.1 au. Bottom: Calculated ram pressures of the wind at 0.1 au at the equator, using equation (13). The figures are split into slow (left) and fast (right) rotators so to conserve the visibility of variation across all winds. Note that the y-axes on the left and right have different scales. This figure is optimally viewed in colour.

the observations of these winds. Low optical depths allow emission from the low corona to escape and be detected, these regions are contaminated with other forms of radio emission, likely dominant, such as chromospheric emission and flaring. However, Lim & White (1996) suggest that we still can provide meaningful upper limits to the mass-loss rate of the star if a flare is detected as one must assume a maximum base density to the wind, therefore constraining mass-loss rates. From the intensity we can calculate the flux density (S_ν) of the wind as

$$S_\nu = \frac{1}{d^2} \int I_\nu dA = \frac{1}{d^2} \sum_{i,j} I_\nu \Delta i \Delta j, \quad (19)$$

where A is the area of integration, d is the distance to the object, and i and j denote the coordinates in our 2D image of I_ν values. Δi and Δj represent the spacing in our grid in the i and j directions. In this calculation we have assumed that the angle subtended by the stellar wind is small, therefore $d\Omega = dA/d^2$.

Table 2 shows the main results from our radio emission calculation, giving values for the expected flux density, from each star at 6 GHz. Fig. 8(a) shows the spectrum of each stellar wind for the range of frequencies 0.1–100 GHz. Our calculation uses actual density distribution in the simulated wind to find the optical depth and the flux density. We obtain a spectrum in the optically thick regime, leading to a power law fit which is related to the density gradient in the wind. Another result of using a numerical model is that the radio photosphere (R_ν), calculated at a distance where $\tau = 0.399$, is not spherical, but changes with the density variations in the wind, causing anisotropic emission, as evident from Fig. 7

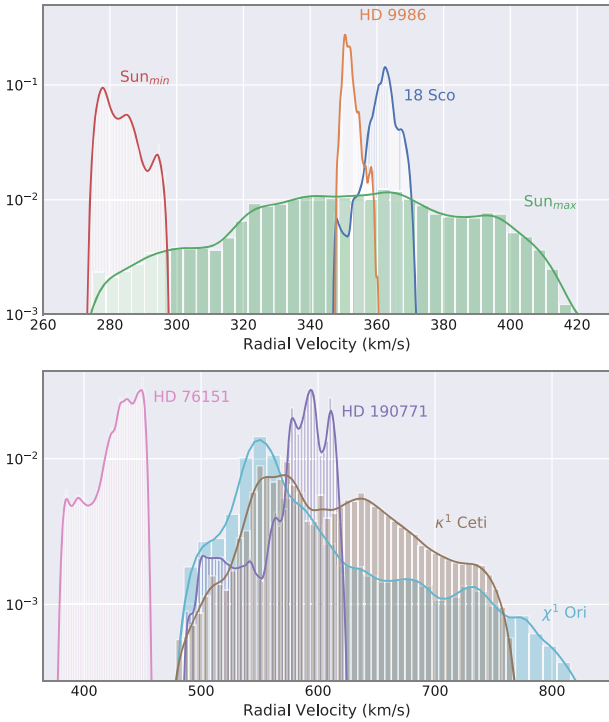


Figure 5. Velocity histogram for our stellar sample, allowing insight into the wind structure (e.g. Réville et al. 2016). Velocities are taken at a distance of 0.1 au, and split into slower rotators (top) and faster rotators (bottom). Note the different velocity scales on each panel. This histogram shows the normalized frequency of each velocity present in the wind at this distance. We can see that the winds of 18 Sco and HD 9986 are extremely unimodal, while other stars such as HD 190771 have a very skewed distribution of velocities. The magnetic field strength and geometry seems to directly affect the wind structure even at these distances. Bin size is selected using the Freedman–Diaconis rule.

(dashed contours). Note that these radio winds are not resolvable with current radio telescopes but should indicate how the radio photosphere in the wind changes with frequency, and the anisotropy of the specific intensity, I_ν , in the wind. We also provide a power-law fit to the optically thick regime of the radio emission (from 0.1 to 1 GHz) and note that it can vary quite significantly, depending on what range of frequencies is being fitted. In Table 2 we show the fit parameters we find according to

$$S_\nu = S_0 \nu^\phi. \quad (20)$$

Our radio calculations give an insight into the expected emissions from solar-type stars. We see that, at the appropriate sensitive frequencies for radio telescopes such as the VLA, the winds all exhibit similar spectrum shapes. Fig. 8(a) shows the spectrum for each star, using different colours as depicted in the legend. We show that the upper limits set by Fichtinger et al. (2017) (hereafter, F17) (black arrows) are consistent with our estimations of the wind emission for κ^1 Ceti: our values are three times lower than these upper limits. χ^1 Ori is detected by F17, but they attribute this emission to the chromosphere and other sources as the star was observed to flare during the observation epoch (we discuss detection difficulties further in Section 4.4). Indeed, Fig. 8(a) shows the detected emission occurs within the optically thin regime of the spectrum according to our models and at approximately 20 times higher flux density than we predict for the stellar wind emission. This supports the deduction that these detections are from other sources, and not the thermal

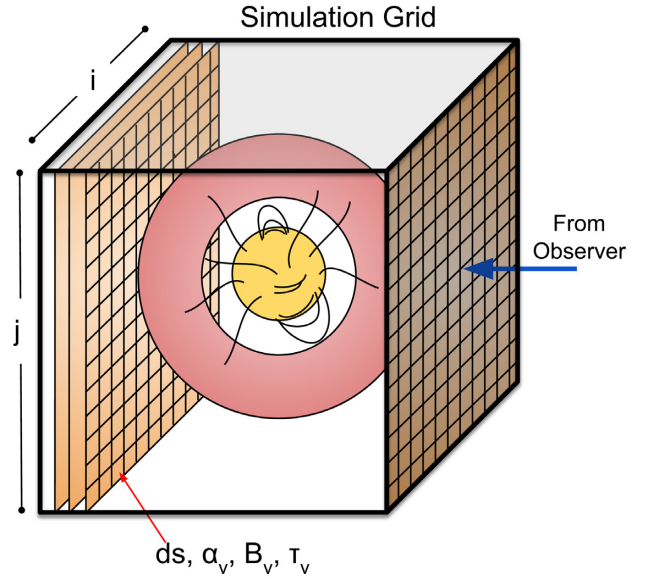


Figure 6. Schematic showing how the intensity is calculated from our grid. The red annulus around the star illustrates thermal radio emission regions from the wind, with a magnetic star at the centre of the diagram. From our wind simulation we create a grid of uniform discrete distances filled with variables including position (s), density (n), and temperature (T). From this we calculate values for the absorption coefficient (α , equation 16), the blackbody function (B_ν , equation 17), and the optical depth (τ_ν , equation 15) for each cell in our grid. We integrate along the line of sight from the observer to find the intensity using equation (14), and find flux density by integrating across i and j . We take the line of sight to be along the x axis for each star, which is not necessarily true, but adopted as such because it is assumed variability in the radio emission will not vary much depending on viewing angle or rotation axis.

wind. F17 estimated the thermal wind emission to possess a flux of 1.3 μJy at 10 GHz, which agrees quite well with our calculation of 0.77 μJy . If the emission seen at 100 μJy by F17 were coming from the stellar wind, our models would require a base density five times larger ($\approx 10^{10} \text{cm}^{-3}$). With this, we can actually infer that the mass-loss rate of χ^1 Ori is smaller than $2\text{--}3 \times 10^{-11} M_\odot \text{yr}^{-1}$, showing that even non-detections of stellar wind radio emission can still provide meaningful upper limits for the mass-loss rates. If we normalize the spectra shown in Fig. 8(a) to remove the distance dependence, upon which the spectrum relies very heavily, we see that the younger more rapidly rotating stars display a higher flux density than the more evolved stars. The Sun in this case would possess the weakest emission.

4.3 Evolution with magnetic cycle

In Fig. 8(a) we calculate the expected radio emission from our solar maximum and solar minimum simulations assuming a distance of 10pc (grey lines) to give an impression of the differences between the radio emission of the winds and the detectability of each star. We show that the thermal quiescent radio flux does not change substantially across a solar magnetic cycle. This is because the radio emission is heavily dependent on the density of the medium and both solar simulations have the same base density. The slight spectral differences, which occur mostly in the optically thick regime, are a consequence of the different magnetic fields causing different density gradients in the wind. For there to be substantial differences

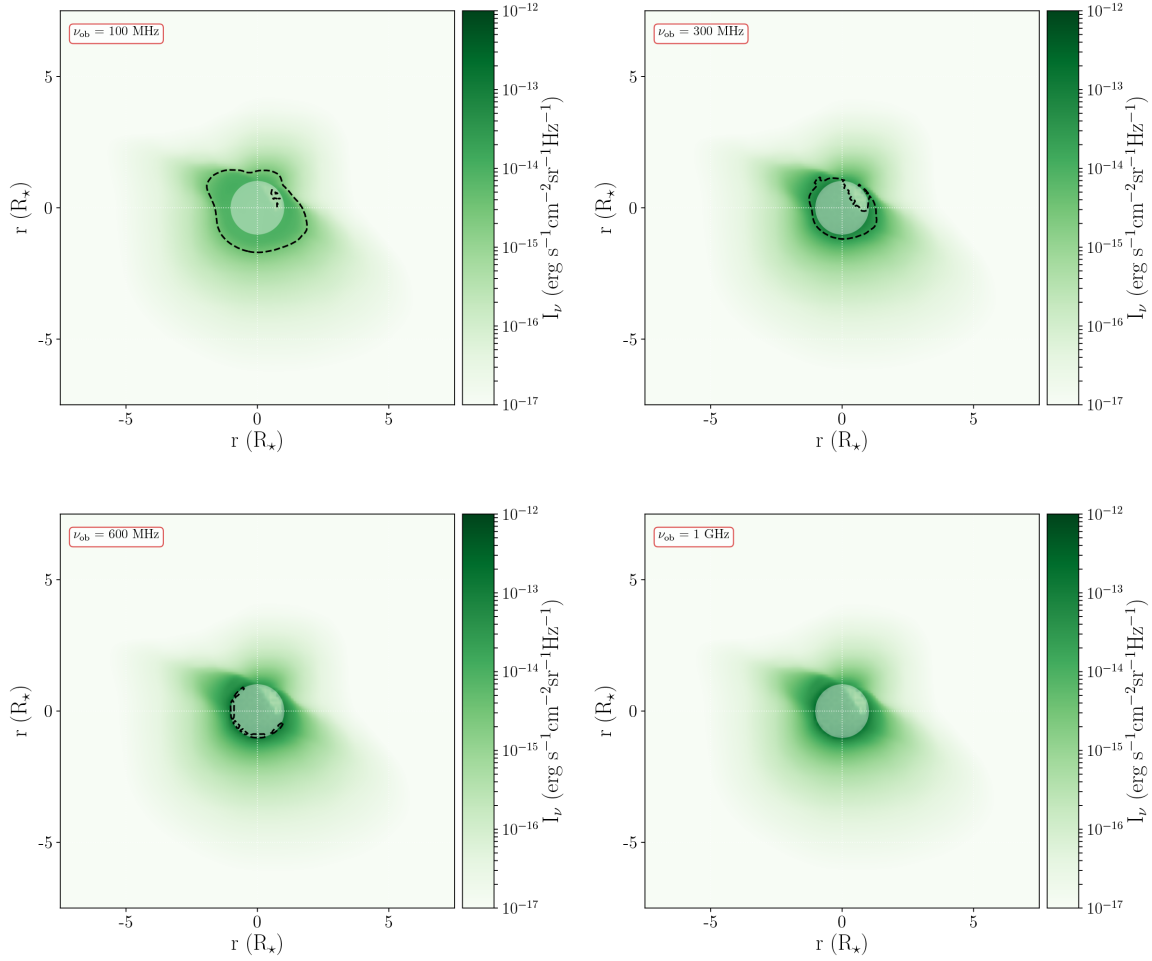


Figure 7. Example of intensity and optical depth for κ^1 Ceti at observing frequencies of 100 MHz (top left), 300 MHz (top right), 600 MHz (bottom left), and 1 GHz (bottom right). The green colour scale represents the intensity of emission from the wind, looking along the line of sight of our simulation grid. The dashed black contour represents the region where the wind becomes optically thick [according to Panagia & Felli (1975), $\tau = 0.399$]. We can see that the emission is anisotropic due to the anisotropy of the wind density and temperature. The intensity reaches a maximum in the thin regime, as we can see emission from the entire wind. The white circle denotes $R = 1 R_*$. There exists no contour in the bottom right plot as the wind is optically thin at 1 GHz. Plasma in front of the star still emits in radio, but we have excluded any contribution from behind the star along the line of sight.

Table 2. Predicted radio emission from our stellar wind models. Example fluxes at a frequency of 6 GHz are given ($S_{6\text{GHz}}$), in this case we find that all of the winds would be optically thin at this frequency. The power-law fit to the spectra was conducted between 0.1 and 1 GHz, giving the coefficient (S_0) and power index (ϕ). However, the spectral slope between these two frequencies varies substantially, tending to shallower slopes at higher frequencies. Depending on the fitting range, slopes can range from 0.6 to 1.5. All slopes tend to -0.1 in the thin regime. The final column gives the frequency at which each wind becomes optically thin (ν_{thin}).

Star	$S_{6\text{GHz}}$ (μJy)	S_0	ϕ	ν_{thin} (GHz)
χ^1 Ori	1.75	1.53	1.32	1.93
HD 190771	0.19	0.19	1.13	1.67
κ^1 Ceti	0.79	0.81	1.14	1.93
HD 76151	0.14	0.16	1.11	2.22
18 Sco	0.14	0.16	1.10	1.93
HD 9986	0.04	0.05	1.12	1.93
Sun max (10 pc)	0.22	0.26	1.21	2.10
Sun min (10 pc)	0.22	0.25	1.14	2.10

in thermal radio emission from a star displaying cyclic magnetic behaviour there would need to be a dramatic change in global density at the base of the wind. Note that the emission calculated here is quiescent wind emission and is the same in both the solar maximum and minimum cases. Non-thermal radio emission, such as 10.7 cm emission, is linked to solar activity and varies through the solar activity cycle (Solanki, Inhester & Schüssler 2006).

4.4 Detectability

The density at low heights in the stellar atmosphere is much higher than the stellar wind density. Radio emission from the lower atmosphere should dominate the emission in the optically thin regime of the stellar wind. This would most likely drown out any emission from the wind in the upper atmosphere and make detection of the wind impossible. However, as pointed out by Reynolds (1986), if the wind is entirely optically thin and emission is deduced to emanate from the lower stellar atmosphere, this can aid in placing limits on the stellar winds density and therefore the mass-loss rate of the star (cf. end of Section 4.2).

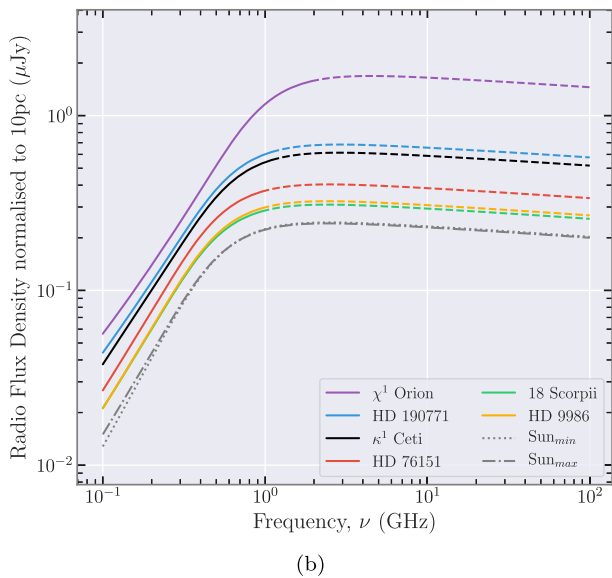
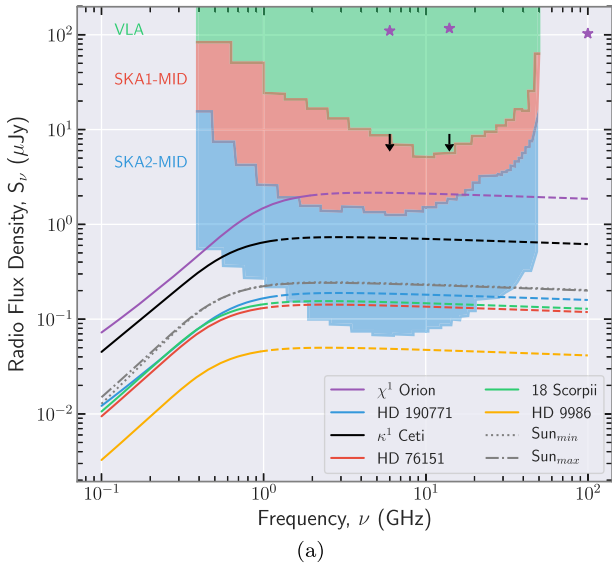


Figure 8. *Top:* We see that the radio spectra for each wind are very similar in shape. Differences in flux density are strongly affected by distance to the object. The dashed lines represent the optically thin part of each spectrum, and there are differences in where the emission becomes optically thin from star to star at the frequency ν_{thin} . The black arrows indicate the observational upper limits of κ^1 Ceti found by Fichtinger et al. (2017). From the same work we mark the chromospheric detections of χ^1 Ori (purple stars), using both VLA and ALMA, which is concluded to originate from chromospheric emission. Our results show this conclusion to be valid as we predict the wind to emit at much lower fluxes. Sensitivities of the current VLA and future SKA1-MID and SKA2-MID are included shaded in green, red, and blue, respectively (SKA sensitivities from Pope et al. 2018) and adjusted for 2 h integration time. *Bottom:* Here we normalized spectra in the top panel to a distance of 10 pc. This allows direct comparison of radio emission to an ageing solar wind. As the stars age and spin-down the radio emission decreases by an order of magnitude between 500 Myr and 4.6 Gyr.

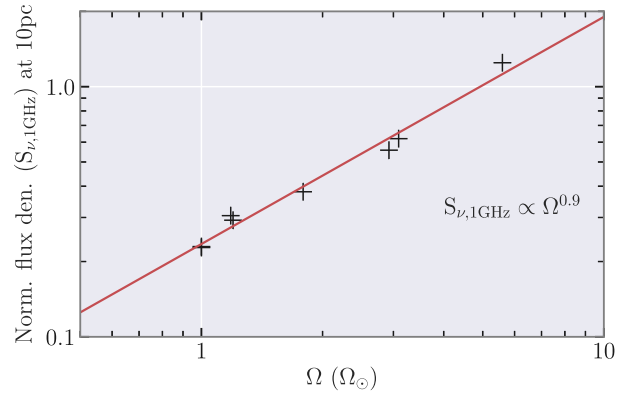


Figure 9. Normalized flux density at 1 GHz as a function of stellar rotation. We see a tight fit to this power law (see equation 21), with an almost linear dependence of stellar wind radio flux on stellar rotation at 1 GHz.

There have been many observations of solar-type low-mass stars in the radio regime (Güdel et al. 1998; Gaidos et al. 2000; Villadsen et al. 2014; Fichtinger et al. 2017), many of which have placed upper flux densities and mass-loss rates on the winds of these stars. Both Gaidos et al. (2000) and F17 used the VLA to observe a set of solar analogues, some of which overlap with the stars we have simulated here, placing tight constraints on the wind of κ^1 Ceti. Fig. 8(a) displays the sensitivity of the VLA (purple shade) given some typical observational parameters (2 h integration time, 128 MHz bandwidth) taken at central band frequencies. We show that the VLA is currently not sensitive enough to detect the winds simulated here. Villadsen et al. (2014) observed four nearby solar-like stars using the VLA (X, Ku, and Ka bands, at 10, 15, and 34.5 GHz centre frequencies, respectively). The authors find detections for all objects in the Ka band but can only provide upper limits to flux density for the other frequency bands. They conclude (similarly to F17) that all detections come from thermal chromospheric emission, and the upper limits set at lower frequencies infer rising spectra and so optically thick chromospheres at these frequencies.

In the future, upgrades to the existing VLA system (ngVLA, see Osten et al. 2018) could increase instrument sensitivity by a factor of 10. This increase in sensitivity means that stars simulated here such as χ^1 Ori and κ^1 Ceti would be detectable in their thin regime. The Square Kilometre Array (SKA) project is a future low-frequency radio telescope that will span a large frequency range. The expected sensitivity level of the future SKA1-MID and SKA2-MID telescopes (with a typical 2 h integration time³) are shown in Fig. 8(a), shaded in red and blue (sensitivities for SKA taken from Pope et al. 2018, but adjusted to account for a 2 h integration time). Given these sensitivities one could potentially directly detect the winds of χ^1 Ori and κ^1 Ceti using the SKA, below 1 GHz. This sensitivity level (sub- μ Jy) means other possible solar analogues not simulated here could also be detected, provided they are close enough. First light for SKA1-MID is expected after the mid 2020’s.

We show in Fig. 8(b) that the faster rotators emit more flux. In Fig. 9, we present the normalized flux density at 1 GHz and at a

³<https://astronomers.skatelescope.org/wp-content/uploads/2016/05/SKA-TEL-SKO-000002.03.SKA1SystemBaselineDesignV2.pdf>

distance of 10 pc as a function of rotation rate. We found that

$$S_{\nu, 1 \text{ GHz}} = 0.24 \left[\frac{\Omega}{\Omega_{\odot}} \right]^{0.9} \left[\frac{10 \text{ pc}}{d} \right]^2 \mu\text{Jy}. \quad (21)$$

Consequently, younger, rapidly rotating stars within a distance of 10 pc will be the most fruitful when observing thermal radio emission from stellar winds.

5 SUMMARY AND CONCLUSIONS

In this study, we presented wind simulations of eight solar analogues (including two of the Sun itself, from Carrington rotations 1983 and 2078) with a range of rotation rates and ages, using a fully 3D MHD code (Fig. 2). We selected a sample of solar-type stars and constrained the sample for which we had observations of their surface magnetic fields (Fig. 1). Other input parameters for our model include base temperatures and densities retrieved from semi-empirical laws scaled with rotation, equations (6)–(8) (Ó Fionnagáin & Vidotto 2018).

We demonstrated that the angular-momentum loss rate decreases steadily along with mass-loss rate over evolutionary time-scales (Fig. 3). Younger stars (≈ 500 Myr) rotating more rapidly ($P_{\text{rot}} \approx 5$ d) display \dot{J} values up to $\approx 10^{32}$ erg. The Sun (4.6 Gyr, $P_{\text{rot}} = 27.2$ d) alternatively exhibits a much lower \dot{J} at minimum $\approx 10^{30}$ erg, with significant variance of one order of magnitude over the solar magnetic cycle. The difference in solar \dot{J} from minimum to maximum is explained by the greater amount of Φ_{open} in the solar maximum case. Given that our solar maximum and minimum simulations differ, this incentivizes the monitoring of stars across entire magnetic cycles to deepen our understanding of stellar activity cycles (Jeffers et al. 2017, 2018). We found a similar declining rotation trend with \dot{M} with slower rotators losing less mass than their faster rotating counterparts. Our solar analogues display a \dot{M} ranging from 1×10^{-13} to $5 \times 10^{-12} M_{\odot} \text{ yr}^{-1}$.

We showed in Fig. 4 how the density, velocity, and ram pressures would vary for a hot Jupiter orbiting any of these solar-like stars at a distance of 0.1 au. We see that the sun at minimum provides the lowest ram pressures of the sample ($< 10^5 \text{ dyn cm}^{-2}$) while HD 190771 and χ^1 Ori display the highest ram pressures with a maximum $> 80 \times 10^{-5} \text{ dyn cm}^{-2}$. This is useful for any further studies on planetary environment within the winds of G-type stars, with the age and rotation of the host star indirectly playing a role in the final ram pressure impacting the planets and therefore upon atmospheric evaporation. We examined how the velocities of these stellar winds are distributed globally, by taking a histogram of velocities at a distance of 0.1 au, shown in Fig. 5. We showed that more magnetically active stars display less uniform density distributions and overall have a more complicated structure.

We developed a numerical tool for calculating thermal radio emission from stellar winds given a simulation grid, removing the need for analytical formulations that have been used in the past (Panagia & Felli 1975; Fichtinger et al. 2017; Vidotto & Donati 2017). This tool solves the radiative transfer equation for our wind models, which allowed us to derive radio flux densities, intensities, and spectra. We found emission around the μJy level with the winds staying optically thick up to 1–2 GHz. We compared our calculated flux densities with recent observations and found our predictions agree with the observational upper limits of κ^1 Ceti and χ^1 Ori (Gaidos et al. 2000; F17). Previous radio detections have been interpreted as originating in the chromospheres of solar-like stars and not their winds (Villadsen et al. 2014; F17), which is supported by our simulations.

The normalized radio flux density emitted from these stellar winds is found to relate to stellar rotation as $S_{\nu, 1 \text{ GHz}} \propto \Omega^{0.9}$. This indicates that desired observational targets are stars with fast rotation rates within a distance of 10 pc. We showed in Fig. 8(a) that more active close by stars like χ^1 Ori and κ^1 Ceti would be readily detectable with the next generation of radio telescopes such as SKA and ngVLA.

ACKNOWLEDGEMENTS

The authors wish to acknowledge the DJEI/DES/SFI/HEA Irish Centre for High-End Computing (ICHEC) for the provision of computational facilities and support. This work used the BATS-R-US tools developed at the University of Michigan Center for Space Environment Modeling and made available through the NASA Community Coordinated Modeling Center. DÓF wishes to acknowledge funding received from the Trinity College Postgraduate Award through the School of Physics. AAV acknowledges funding received from the Irish Research Council Laureate Awards 2017/2018. SJ acknowledges the support of the German Science Foundation (DFG) Research Unit FOR2544 ‘Blue Planets around Red Stars’, project JE 701/3-1 and DFG priority program SPP 1992 ‘Exploring the Diversity of Extrasolar Planets’ (RE 1664/18). We thank Jackie Villadsen and Joe Llama for their useful discussion on topics of stellar radio emission. The authors would like to thank our referee, Dr Jorge Zuluaga, for his valuable input on this work.

Software: BATS-R-US (Powell et al. 1999), RADIOWINDS (Ó Fionnagáin 2018), SCIPY (Jones et al. 2001), MATPLOTLIB (Hunter 2007), and TECPLOT and SEABORN (Waskom et al. 2018).

REFERENCES

- Altschuler M. D., Newkirk G., 1969, *Sol. Phys.*, 9, 131
 Alvarado-Gómez J. D., Drake J. J., Cohen O., Moschou S. P., Garraffo C., 2018, *ApJ*, 862, 93
 Anderson K. R., Storch N. I., Lai D., 2016, *MNRAS*, 456, 3671
 Beck P. G. et al., 2017, *A&A*, 602, A63
 Booth R. S., Poppenhaeger K., Watson C. A., Silva Aguirre V., Wolk S. J., Aguirre V. S., Wolk S. J., 2017, *MNRAS*, 471, 1012
 Bower G. C., Loinard L., Dzib S., Galli P. A. B., Ortiz-León G. N., Moutou C., Donati J.-F., 2016, *ApJ*, 830, 107
 Brown A. G. A., Vallenari A., Prusti T., de Bruijne J. H. J., Babusiaux C., Zurbach C., Zwitter T., 2018, *A&A*, 616, A1
 Brown S. F., Donati J.-F., Rees D. E., Semel M., 1991, *A&A*, 250, 463
 Brun A. S., Browning M. K., 2017, *Living Rev. Sol. Phys.*, 14, 4
 Cox A. N., Pilachowski C. A., 2002, *Allen’s Astrophysical Quantities*, Vol. 53. Springer, New York
 Cranmer S. R., Gibson S. E., Riley P., 2017, *Space Sci. Rev.*, 212, 1345
 Cranmer S. R., Saar S. H., 2011, *ApJ*, 741, 54
 Crosley M. K. et al., 2016, *ApJ*, 830, 24
 DeRosa M. L., Brun A. S., Hoeksema J. T., 2010, *Proc. Int. Astron. Union*, 6, 94
 do Nascimento J.-D., Jr. et al., 2016, *ApJ*, 820, L15
 Donati J.-F., Semel M., Carter B. D., Rees D. E., Cameron A. C., 1997, *MNRAS*, 291, 658
 Fichtinger B., Güdel M., Mutel R. L., Hallinan G., Gaidos E., Skinner S. L., Lynch C., Gayley K. G., 2017, *A&A*, 599, A127 (F17)
 Finley A. J., Matt S. P., See V., 2018, *ApJ*, 864, 125
 Folsom C. P., Petit P., Bouvier J., Morin J., Lèbre A., Donati J.-F., 2016, *MNRAS*, 10, 113
 Folsom C. P. et al., 2018, *MNRAS*, 474, 4956
 Gaidos E. J., Güdel M., Blake G. A., 2000, *Geophys. Res. Lett.*, 27, 501
 Gallet F., Bouvier J., 2013, *A&A*, 556, A36
 Gallet F., Bouvier J., 2015, *A&A*, 577, A98
 Güdel M., 2002, *ARA&A*, 40, 217

Güdel M., 2007, *Living Rev. Sol. Phys.*, 4, 3
 Güdel M., Guinan E. F., Skinner S., 1998, *PASP*, 154, 1041
 Holzwarth V., Jardine M., 2007, *A&A*, 463, 11
 Huber D. et al., 2013, *Science*, 342, 331
 Hunter J. D., 2007, *Comput. Sci. Eng.*, 9, 90
 Jeffers S. V., Saikia S. B., Barnes J. R., Petit P., Marsden S. C., Jardine M. M., Vidotto A. A., 2017, *MNRAS*, 471, L96
 Jeffers S. V. et al., 2018, *MNRAS*, 479, 5266
 Johnstone C. P., Güdel M., Brott I., Lüftinger T., 2015b, *A&A*, 577, A28
 Johnstone C. P., Güdel M., Lüftinger T., Toth G., Brott I., 2015a, *A&A*, 577, A27
 Jones E. et al., 2001., SciPy: Open Source Scientific Tools for Python, <http://www.scipy.org/>
 Lang P., Jardine M., Morin J., Donati J.-F., Jeffers S., Vidotto A. A., Fares R., 2014, *MNRAS*, 439, 2122
 Lehmann L. T., Jardine M. M., Mackay D. H., Vidotto A. A., 2018, *MNRAS*, 478, 4390
 Lim J., White S. M., 1996, *ApJ*, 462, L91
 Lorenzo-Oliveira D. et al., 2018, *A&A*, 619, A73
 Maehara H., Notsu Y., Notsu S., Namekata K., Honda S., Ishii T. T., Nogami D., Shibata K., 2017, *PASJ*, 69
 Maldonado J., Martínez-Arnáiz R. M., Eiroa C., Montes D., Montesinos B., 2010, *A&A*, 521, A12
 Manchester W. et al., 2008, *ApJ*, 684, 1448
 Matt S. P. S., MacGregor K. K. B., Pinsonneault M. M. H., Greene T. P. T., 2012, *ApJ*, 754, L26
 Meléndez J. et al., 2014, *ApJ*, 791, 14
 Messina S., Guinan E. F., 2003, *A&A*, 409, 1017
 Mestel L., 1999, *Stellar Magnetism*. Oxford Univ. Press, Oxford
 Metcalfe T. S., Egeland R., van Saders J., 2016, *ApJ*, 826, L2
 Nicholson B. A. et al., 2016, *MNRAS*, 459, 1907
 Noyes R. W., Hartmann L. W., Baliunas S. L., Duncan D. K., Vaughan A. H., 1984, *ApJ*, 279, 763
 Osten R. A., Crosley M. K., Güdel M., Kowalski A. F., Lazio J., Linsky J., Murphy E., White S., 2018, preprint ([arXiv:1803.05345](https://arxiv.org/abs/1803.05345))
 Ó Fionnagáin D., Vidotto A. A., 2018, *MNRAS*, 476, 2465
 Ó Fionnagáin D. (Version v0.0.5), Zenodo, 2018, ofionnad/radiowinds: Calculating Thermal Bremsstrahlung Emission from Stellar Wind
 Owen J. E., Mohanty S., 2016, *MNRAS*, 459, 4088
 Panagia N., Felli M., 1975, *A&A*, 39, 1
 Pantolmos G., Matt S. P., 2017, *ApJ*, 849, 83
 Petit P., Dintrans B., Morgenthaler A., Van Grootel V., Morin J., Lanoux J., Aurière M., Konstantinova-Antova R., 2009, *A&A*, 508, L9
 Petit P. et al., 2008, *MNRAS*, 388, 80
 Pognan, Q., Garraffo, C., Cohen, O., Drake, J., 2018, *ApJ*, 856, 53
 Pope B. J. S., Withers P., Callingham J. R., Vogt M. F., 2018, preprint ([arXiv:1810.11493](https://arxiv.org/abs/1810.11493))
 Powell K. G., Roe P. L., Linde T. J., Gombosi T. I., De Zeeuw D. L., 1999, *J. Comp. Phys.*, 154, 284
 Prusti T. et al., 2016, *A&A*, 595, A1
 Reynolds S. P., 1986, *ApJ*, 304, 713
 Ribas I. et al., 2016, *A&A*, 596, A111
 Rosén L., Kochukhov O., Hackman T., Lehtinen J., 2016, *A&A*, 593, A35
 Rucinski S. M. et al., 2004, *PASP*, 116, 1093
 Réville V., Brun A. S., Matt S. P., Strugarek A., Pinto R. F., 2015, *ApJ*, 798
 Réville V., Folsom C. P., Strugarek A., Brun A. S., 2016, *ApJ*, 832, 145
 See V., Jardine M., Vidotto A. A., Petit P., Marsden S. C., Jeffers S. V., do Nascimento J. D., 2014, *A&A*, 570, A99
 See V. et al., 2017a, *MNRAS*, 466, 1542
 See V. et al., 2017b, *MNRAS*, 466, 1542
 Semel M., 1989, *A&A*, 225, 456
 Skumanich A., 1972, *ApJ*, 171, 565
 Solanki S. K., Inhester B., Schüssler M., 2006, *Rep. Prog. Phys.*, 69, 563
 Suzuki T. K., Imada S., Kataoka R., Kato Y., Matsumoto T., Miyahara H., Tsuneta S., 2013, *PASJ*, 65, 98
 Telleschi A., Güdel M., Briggs K., Audard M., Ness J., Skinner S. L., 2005, *ApJ*, 622, 653
 Tóth G. et al., 2005, *J. Geophys. Res.*, 110, A12226

Valenti J. A., Fischer D. A., 2005, *A&AS*, 159, 141
 Van Doorselaere T., Wardle N., Zanna G. D., Jansari K., Verwichte E., Nakariakov V. M., 2011, *ApJ*, 727, L32
 Van Saders J. L., Ceillier T., Metcalfe T. S., Aguirre V. S., Pinsonneault M. H., García R. A., Mathur S., Davies G. R., 2016, *Nature*, 529, 181
 Verdini A., Velli M., Matthaes W. H., Oughton S., Dmitruk P., 2010, *ApJ*, 708, L116
 Vidotto A., 2017, *EPJ Web Conf.*, 160, 05011
 Vidotto A. A., 2016, *MNRAS*, 459, 1533
 Vidotto A. A., Donati J.-F., 2017, *A&A*, 602, A39
 Vidotto A. A., Fares R., Jardine M., Moutou C., Donati J.-F. F., 2015, *MNRAS*, 449, 4117
 Vidotto A. A., Jardine M., Morin J., Donati J. F., Opher M., Gombosi T. I., 2014a, *MNRAS*, 438, 1162
 Vidotto A. A., Lehmann L., Jardine M., Pevtsov A., 2018, *MNRAS*, 12, 1
 Vidotto A. A. et al., 2014b, *MNRAS*, 441, 2361
 Villadsen J., Hallinan G., Bourke S., Güdel M., Rupen M., 2014, *ApJ*, 788, 112
 Waskom M. et al., 2018, *mwaskom/seaborn*: v0.9.0 (July 2018),
 Weber E. J. E. E. J., Davis, Leverett J., Davis L., Jr., Davis, Leverett J., 1967, *ApJ*, 148, 217
 Wood B. E., Müller H.-R., Zank G. P., Linsky J. L., Redfield S., 2005, *ApJ*, 628, L143
 Wright A. E., Barlow M. J., Michael J., 1975, *MNRAS*, 170, 41
 Wright N. J., Drake J. J., Mamajek E. E., Henry G. W., 2011, *ApJ*, 743, 48

APPENDIX A: EFFECTS OF DENSITY AND ITS GRADIENT ON RADIO EMISSION

Many previous analytical works have shown the strong dependence of thermal free–free radio emission on density gradients in the wind (Panagia & Felli 1975; Wright et al. 1975; Lim & White 1996). We show in Fig. A1 how the flux density spectrum for κ^1 Ceti would change given a density gradient that follows $n \propto R^{-2}$ (green line), and in addition one that has a constant temperature (red line). Both of these models have a base density three times less than the original spectrum (blue line). We see that this slower density decay has a dramatic affect on the shape of the spectrum in the optically thick regime. The density gradient for our simulation varies across the grid, but in nearly all cases it is much steeper than $n \propto R^{-2}$. The

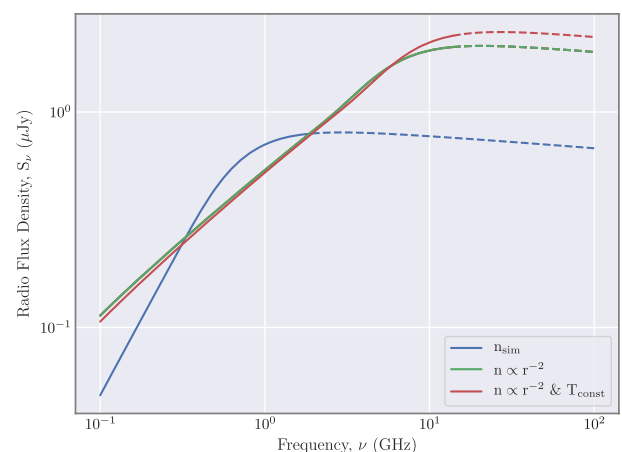


Figure A1. The blue line shows the same spectrum for κ^1 Ceti as shown in Fig. 8(a). The green line represents the same grid, with the same temperature gradient, but with a density that falls off with R^{-2} . The base density for this green line is also a factor of 3 smaller than the blue line. The red line represents the same scenario as the green line but with a constant temperature across the grid. Here we can see the huge impact density gradient has on flux density and spectrum shape.

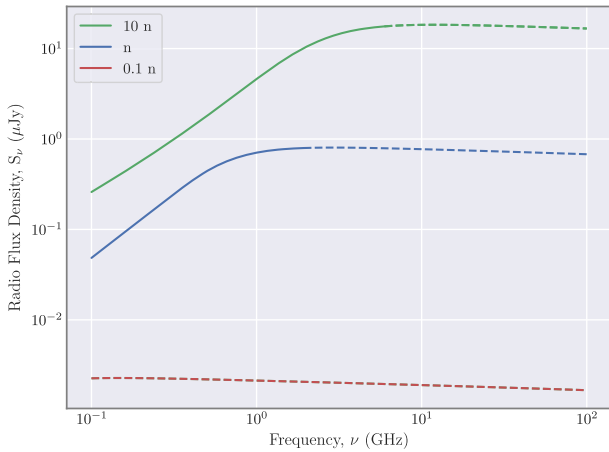


Figure A2. The blue line shows the same spectrum for κ^1 Ceti as shown in Fig. 8(a). The green line represents the same density structure with 10 times the original density, and the red line represents the original density divided by a factor of 10. The dashed portion of each line represents where the wind becomes optically thin. We see in the low-density case that the entire wind is optically thin and emission is very low as there is an extremely tenuous wind. For the high-density case we see much higher fluxes, and the wind is optically thick for most of the observing frequencies in our range.

steeper decay of density causes the emission to be lower across all frequencies. The temperature gradient has a minimal effect on spectrum shape compared to the density.

Fig. A2 shows how the density of the wind will affect the overall emission, changing where the wind becomes optically thick/thin, and the increase/decrease in the flux density. This is relevant to observations because, if two or more detections are made at different frequencies and follow the optically thin power law of $\propto \nu^{-0.1}$, then we can assume the wind is thin and therefore constrain the value for density in the wind. In the low-density case the entire wind is optically thin and emission is very low as there is an extremely tenuous wind. For the high-density case we see much higher fluxes, and the wind is optically thick for most of the observing frequencies in our range.

This paper has been typeset from a $\text{\TeX}/\text{\LaTeX}$ file prepared by the author.

Circumstellar environment of 55 Cancri

The super-Earth 55 Cnc e as a primary target for star–planet interactions[★]

C. P. Folsom¹, D. Ó Fionnagáin², L. Fossati³, A. A. Vidotto², C. Moutou¹, P. Petit¹, D. Dragomir^{4,★★}, and J.-F. Donati¹

¹ IRAP, Université de Toulouse, CNRS, UPS, CNES, 31400 Toulouse, France
e-mail: cfolsom@irap.omp.eu

² Trinity College Dublin, College Green, Dublin 2, Ireland

³ Space Research Institute, Austrian Academy of Sciences, Schmiedlstrasse 6, 8042 Graz, Austria
e-mail: luca.fossati@oeaw.ac.at

⁴ Department of Physics and Kavli Institute for Astrophysics and Space Research, MIT, Cambridge, MA 02139, USA

Received 25 November 2019 / Accepted 8 December 2019

ABSTRACT

Context. 55 Cancri hosts five known exoplanets, most notably the hot super-Earth 55 Cnc e, which is one of the hottest known transiting super-Earths.

Aims. Because of the short orbital separation and host star brightness, 55 Cnc e provides one of the best opportunities for studying star–planet interactions (SPIs). We aim to understand possible SPIs in this system, which requires a detailed understanding of the stellar magnetic field and wind impinging on the planet.

Methods. Using spectropolarimetric observations and Zeeman Doppler Imaging, we derived a map of the large-scale stellar magnetic field. We then simulated the stellar wind starting from the magnetic field map, using a 3D magneto-hydrodynamic model.

Results. The map of the large-scale stellar magnetic field we derive has an average strength of 3.4 G. The field has a mostly dipolar geometry; the dipole is tilted by 90° with respect to the rotation axis and the dipolar strength is 5.8 G at the magnetic pole. The wind simulations based on this magnetic geometry lead us to conclude that 55 Cnc e orbits inside the Alfvén surface of the stellar wind, implying that effects from the planet on the wind can propagate back to the stellar surface and result in SPI.

Key words. stars: individual: 55 Cnc – stars: magnetic field – stars: late-type – stars: winds, outflows – planetary systems – planet–star interactions

1. Introduction

The 55 Cnc system is one of the most relevant systems for understanding planets with masses or radii in between those of Earth and Neptune. This mass-radius regime, which is characterised by a large variety of bulk densities, is not found in the solar system, but yet constitutes the largest population of known exoplanets.

55 Cnc (G8V) hosts five known exoplanets, most notably the close-in super-Earth 55 Cnc e ($M_p = 8.37 \pm 0.38 M_\oplus$, $R_p = 1.92 \pm 0.08 R_\oplus$, $P_{\text{orb}} = 18$ h). This exoplanet offers one of the best opportunities for detailed characterisation of a super-Earth thanks to two key properties: at $V \approx 6$, the host star is the third brightest star known to host a transiting planet; and because of the high planetary temperature, there is a high planet–star flux contrast, making the planetary emission well detectable at optical and infrared (IR) wavelengths.

Observations suggest that 55 Cnc and 55 Cnc e (also called “planet e”) may be an up-scaled analogue of the Jupiter-Io system (Demory et al. 2016a). This would imply the presence of a significant exosphere surrounding the planet and plasma flowing from the planet towards the star, following the stellar magnetic field lines. *Spitzer* Space Telescope observations conducted at 4.5 μm indicate the dayside thermal emission of the planet varied

by about 300% between 2012 and 2013; temperatures ranged between 1300 and 3000 K (Demory et al. 2016b). This can be explained assuming that the planetary lithosphere is partially molten, particularly on the dayside.

The Microvariability and Oscillations of Stars telescope (MOST) satellite observations (Winn et al. 2011; Dragomir et al. 2014) show variability in the visible that could be linked to the IR variability. The MOST phase curve in 2012 shows a smaller amplitude than in 2011, and the former is comparable to the IR phase curve. This has led to suggestions that there is opaque material in the visible and IR, such as grains of dust coupled to hot plasma, similar to Io (Krüger et al. 2003). The grey behaviour of dust could provide the same opacity both in the visible and IR.

More recently, Ridden-Harper et al. (2016) detected absorption at the position of the CaII H&K resonance lines, which may be connected with the exosphere of planet e. This 4.9σ detection was achieved only for one of the four datasets, suggesting temporal variability in the optical depth of the material surrounding the planet.

Reconciling these properties would require the presence of azimuthally inhomogeneous circumstellar material and/or of a large exosphere made of ions and charged dust particles similar to Io (Krüger et al. 2003), which could contribute to a variable grey opacity along the line of sight through diffusion of stellar light. The large-scale structure of the circumstellar material appears to remain stable for days or weeks (Demory et al. 2016b), which would likely require a large-scale stellar magnetic field for support.

[★] Based on observations obtained at the Telescope *Bernard Lyot* (USR5026) operated by the Observatoire Midi-Pyrénées, Université de Toulouse (Paul Sabatier), Centre National de la Recherche Scientifique of France.

^{★★} Hubble Fellow.

A large stellar magnetic field would also be able to connect the star and planet, creating chromospheric hotspots. Again, we find an analogy with the Io-Jupiter system, in which observations indicate the existence of auroral hotspots in Jupiter at the footpoints of magnetic field lines connecting Io to Jupiter (Bhardwaj & Gladstone 2000). Therefore, detecting the presence of a significant magnetic field on 55 Cnc would support the idea that this system is a scaled-up version of the Jupiter-Io system. Examining the stellar magnetic and wind properties would also clarify the likelihood of magnetic star-planet interactions (SPIs).

We present the detection and characterisation of the stellar surface magnetic field of 55 Cnc and model its stellar wind. This paper follows an earlier unsuccessful search for a magnetic field for 55 Cnc by Marcy (1984) using Zeeman broadening. From our simulations, we propose that 55 Cnc e should be a primary target for detecting SPIs, and instrumentation available in the near future may indeed lead to such a detection.

2. Zeeman Doppler imaging

To detect and characterise the magnetic field of 55 Cnc, we observed the star using the Narval spectropolarimeter at the Pic du Midi Observatory in France. Narval includes a polarimeter module connected by fibre to a high resolution ($R \sim 65\,000$) échelle spectrograph (3700–10 500 Å). Observations were made in Stokes V mode, providing both total intensity (Stokes I) and circularly polarised (Stokes V) spectra. Data were reduced using the LIBRESPLIT pipeline (Donati et al. 1997) in the version built for Narval.

We obtained 20 observations of 55 Cnc on ten nights between March 1 and April 21, 2017. Two consecutive observations were obtained on each night to allow the possibility of co-adding observations. Magnetic detections were obtained reliably in single observations, therefore co-adding was not needed. A total exposure time of 3600 s (as a sequence of four 900 s sub-exposures) was used.

To detect Zeeman splitting in Stokes V , we used least squares deconvolution (LSD; Donati et al. 1997; Kochukhov et al. 2010). This is a cross-correlation technique that produces pseudo-average line profiles with greatly reduced noise. We used the line mask for a 5000 K star from Folsom et al. (2018a), a normalising wavelength of 650 nm, a normalising Landé factor of 1.195, and the code of Donati et al. (1997). We obtained magnetic detections in the V LSD profiles (Fig. 1) on all nights except for April 10, and those non-detections appear to be due to the rotation phase of the star.

We characterised the magnetic field strength and geometry of 55 Cnc using Zeeman Doppler imaging (ZDI; e.g. Donati et al. 2006). The ZDI technique uses a regularised fitting procedure to model the rotationally modulated Stokes V LSD profiles and infer the simplest magnetic geometry needed to reproduce the profiles. We used the ZDI code of Folsom et al. (2018a), following the analysis procedure of Folsom et al. (2018b). The $v \sin i$ of 55 Cnc is poorly constrained since it is below the resolution of Narval. We inferred an equatorial velocity of 1.24 km s^{-1} , using the interferometric radius of $0.943 \pm 0.010 R_{\odot}$ from von Braun et al. (2011; confirmed by Ligi et al. 2016), and the rotation period of $38.8 \pm 0.05 \text{ d}$ from Bourrier et al. (2018), which is within 3σ of $40.7 \pm 0.7 \text{ d}$ from Hempelmann et al. 2016. To constrain the intrinsic line profile shape we fit the line in Stokes I with a Voigt profile, broadened by this upper limit on $v \sin i$, and found a Gaussian width of 2.32 km s^{-1} and a Lorentzian width of 0.81 (2.84 km s^{-1}) (cf. Folsom et al. 2018b).

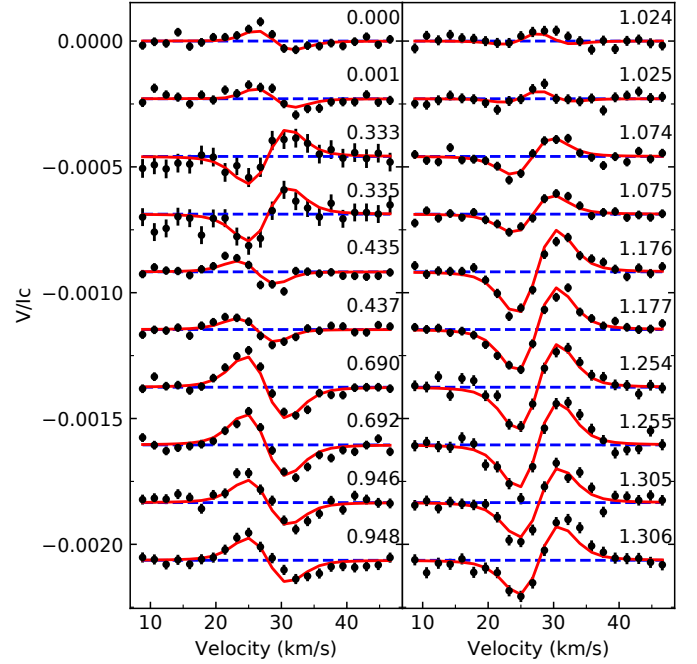


Fig. 1. Stokes V profiles via LSD of 55 Cnc (black points), labelled by rotation cycle for a 39-day period shifted vertically for clarity. The dashed lines indicate zero and solid lines are the best-fit ZDI model profiles.

Using the above equatorial velocity and intrinsic line widths, we constrained the inclination of the stellar rotation axis (i) via ZDI to fit the Stokes V profile variability. This was done by fitting ZDI models with a wide range of inclinations and looking for values that provided the best fit. We find $i > 80^\circ$ with a 1σ confidence (and $i > 65^\circ$ at a 3σ confidence), with the most likely values near 90° . Bourrier et al. (2018) find an orbital inclination for 55 Cnc e of $83.59^{+0.47}_{-0.44}$, thus our rotation inclination is consistent with the stellar rotation axis and planet orbital axis being aligned.

We re-derived the rotation period using ZDI fitting of the LSD profiles, as was done by Folsom et al. (2018b) and found $39.0 \pm 0.3 \text{ d}$, which is in good agreement with Bourrier et al. (2018). We searched for surface differential rotation via ZDI, as in Folsom et al. (2018b), but find no strong evidence for it. We find that $d\Omega$ (the difference in angular frequency between the pole and equator) is $< 0.065 \text{ rad day}^{-1}$ at a 3σ confidence level, and that this parameter covaries strongly with rotation period. The uncertainty is based on variations in χ^2 for models computed with different period and $d\Omega$ but the same entropy, as in Folsom et al. (2018b). This result implies that differential rotation, if at all present, is not anomalously strong in this star compared to other stars of this spectral type. The specific value of $d\Omega$ within this uncertainty range has a minimal impact on the magnetic map, changing field strengths and how poloidal or axisymmetric the field is by less than 2%. Our data span only 1.3 rotation cycles, further complicated by the low $v \sin i$, which likely explains the lack of evidence for differential rotation in the data.

The final magnetic map is presented in Fig. 2 and corresponding line profile fits are in Fig. 1 for $i = 90^\circ$, $P = 39.0 \text{ d}$, and $d\Omega = 0 \text{ rad d}^{-1}$. We find an average unsigned large-scale field of 3.4 G . The large-scale field we reconstruct is dominantly poloidal (99% of the magnetic energy, as calculated from B^2), and most of that poloidal field is in the dipole (79% energy) and quadrupole (19% energy) components. The strength of the

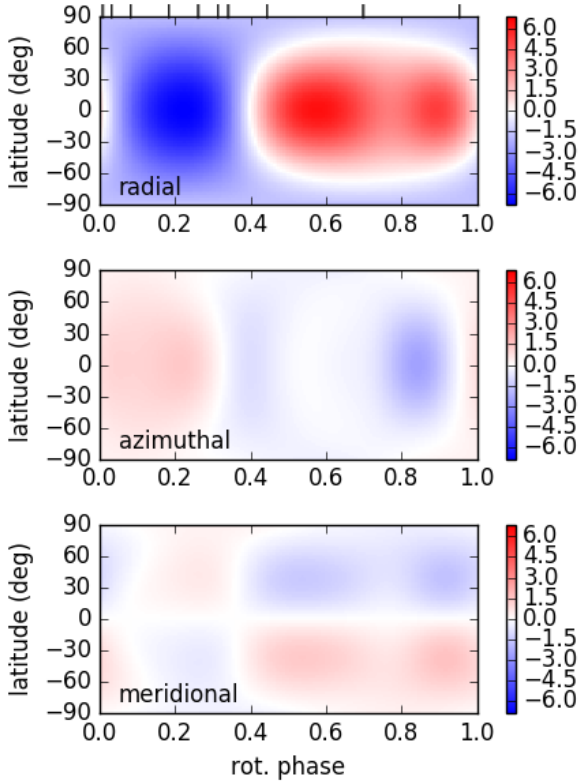


Fig. 2. Magnetic map of 55 Cnc from ZDI. The radial, azimuthal, and meridional components of the magnetic field are presented in units of G. The ticks above the *top panel* indicate phases in which observations were obtained.

dipolar component, at the magnetic pole, is 5.8 G. The magnetic field we find is dominantly non-axisymmetric (94% energy, $m \neq 0$), although that may be biased because the stellar inclination is near 90° .

To investigate the impact of an unexpectedly large error in the inclination, we computed a magnetic map with $i = 60^\circ$, and found the map was largely unchanged. The axisymmetry of the poloidal component is virtually unchanged, while the dipolar axisymmetry increases by 5%. We derive the same poloidal fraction, although 4% of the poloidal energy shifts from the dipole to the quadrupole and octopole components.

As the inclination approaches 90° , ZDI (like regular Doppler imaging) suffers from north-south “mirroring” effects. More precisely, in terms of spherical harmonics, components where $l + m$ is an odd number, i.e. where $B(\theta, \phi) = -B(\pi - \theta, \phi)$, are not constrained when $i = 90^\circ$ and thus are forced to zero by the regularisation. Most notably that includes the axisymmetric dipole component ($l = 1, m = 0$), therefore there is likely some magnetic field to which our observations are not sensitive. The phase sampling of the observations between 0.5 and 1.0 is relatively coarse, which likely lowers the resolution of the magnetic map in that hemisphere. However, for the stellar wind near planet e and beyond, only the most large-scale features (lowest degree spherical harmonic) dominate (e.g. [Jardine et al. 2017](#)).

3. Stellar wind around 55 Cnc

We used the numerical modelling tool BATS-R-US ([Powell et al. 1999](#)) to simulate the stellar wind of 55 Cnc. This code has been used to simulate astrophysical plasma environments ([Tóth et al. 2005](#); [Manchester et al. 2008](#); [Vidotto et al. 2015](#);

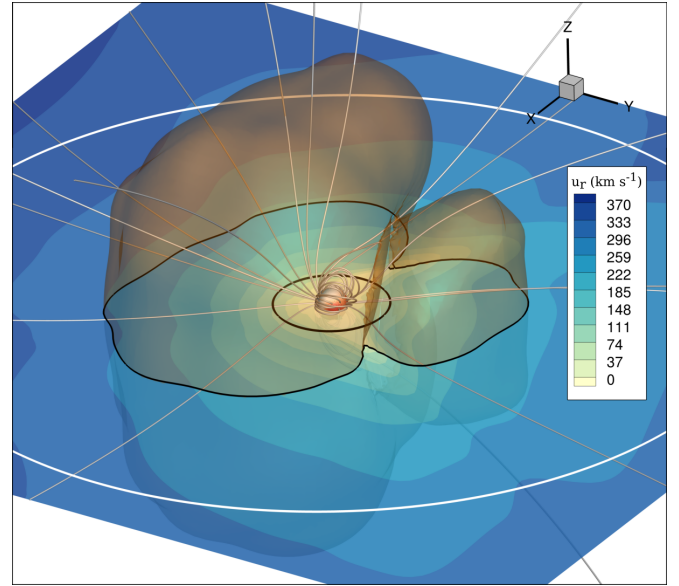


Fig. 3. Three-dimensional MHD simulation of 55 Cnc. Wind velocity is shown as a slice at the $z = 0$ plane and extends to $30 R_*$. The Alfvén surface is shown in orange; its intersection with the orbital plane of the planets is highlighted with a thick black line. Open magnetic field lines are shown in grey and closed magnetic field lines are shown in red. The orbits of 55 Cnc e and b are represented in black and white respectively.

[Alvarado-Gómez et al. 2018](#)), and in this work we used the version from [Vidotto et al. \(2015\)](#), more details can be found in that paper). The BATS-R-US tool solves the set of closed, ideal magnetohydrodynamic (MHD) equations for mass, momentum, and energy conservation, and the magnetic induction equation. The code solves for eight parameters: mass density (ρ), velocity ($\mathbf{u} = \{u_x, u_y, u_z\}$), magnetic field ($\mathbf{B} = \{B_x, B_y, B_z\}$), and gas pressure (P). We assume that the plasma behaves as an ideal gas, hence $P = nk_B T$, where $n = \rho / (\mu m_p)$ is the total number density of the wind, where μm_p denotes the average particle mass. We take $\mu = 0.5$, which represents a fully ionised hydrogen wind. Pressure is related to density in the wind by the polytropic relation: $P \propto \rho^\gamma$, where γ is the polytropic index. Through the polytropic index, heating is implicitly added to the wind. We adopt $\gamma = 1.05$, similar to values used in the literature ([Vidotto et al. 2015](#); [Réville et al. 2015](#); [Ó Fionnagáin & Vidotto 2018](#)). Including the polytropic index, this model contains three free parameters; the remaining two are the base density (ρ_0) and base temperature (T_0) of the wind. For this simulation we used $\rho_0 = 10^{-16} \text{ g cm}^{-3}$ and $T_0 = 1 \text{ MK}$. We simulated the stellar wind in a grid that extends to $30 R_*$ in each direction. Our simulation has a range of resolutions from 0.019 – $0.625 R_*$. We find that 55 Cnc is losing mass at a rate of $2.2 \times 10^{-14} M_\odot \text{ yr}^{-1}$, similar to the solar mass-loss rate of $2 \times 10^{-14} M_\odot \text{ yr}^{-1}$, and angular momentum at a rate of $8.2 \times 10^{29} \text{ erg}$.

Figure 3 shows the output of our simulation, where the black and white circles represent the orbits of planets e and b at 3.5 and $26.2 R_*$, respectively. Extracting values from the wind at these orbits allows us to investigate the environment surrounding these planets. Table 1 shows the values of the stellar wind properties averaged over one planetary orbit for each of the known planets. As some of the planets are outside the domain of our simulation, we perform an extrapolation of the wind values at planets c, f, and d. While planet e is impacted by a much slower wind, the wind still imparts a higher ram pressure upon planet e than upon

Table 1. Stellar wind local properties around the known 55 Cnc planets averaged over one planetary orbit.

Orbital wind properties	“e”	“b”	“c”	“f”	“d”	Reference
Orbital period (days)	0.74	14.7	44.4	262	4825	Baluev (2015)
Semi-major axis (au)	0.0154	0.1134	0.2373	0.7708	5.957	Bourrier et al. (2018)
Semi-major axis (R_{\star})	3.52	25.85	54.10	175.74	1358.17	Bourrier et al. (2018)
Stellar wind density (g cm^{-3})	4.5×10^{-19}	7.7×10^{-22}	1.4×10^{-22}	1.2×10^{-23}	1.7×10^{-25}	This work
Velocity (km s^{-1})	87.5	343.0	384.5	384.5	384.5	This work
Velocity incl. orbital motion (km s^{-1})	244.1	349.4	388.9	385.9	384.6	This work
Ram pressure ($10^{-7} \text{ dyn cm}^{-2}$)	313.1	8.69	2.06	0.27	0.008	This work
Temperature (10^6 K)	1.08	0.837	0.761	0.666	0.528	This work
Magnetic field (nT)	5021	39.02	7.04	0.56	0.007	This work

planet b, owing to the much higher wind density closer to the star.

Figure 3 shows that planet e orbits entirely within the Alfvén surface of the wind of 55 Cnc. This means that the wind is magnetically dominated around this planet. Being in a sub-Alfvénic regime means that planet e has a direct connection to the star; in the sub-Alfvénic regime, the planet can generate Alfvén wings, which can couple to the star and carry electromagnetic energy towards the star (e.g. Saur et al. 2013; Fischer & Saur 2019). This scenario has ramifications for the SPI, as we discuss in the next section. An important factor to keep in mind is that the size of the Alfvén surface depends on the stellar magnetic field and wind base density. Although the stellar magnetic field is tied to the observations, the density is a free parameter in our model. Thus, we performed two additional sets of simulations, with three times larger and three times smaller base density. These choices affect, for example, the mass-loss rate of the stellar wind, but in all three scenarios we explored, the orbit of planet e remains entirely within the Alfvén surface.

4. Star–planet interactions induced by planet 55 Cnc e

It has been suggested that close-in planets could enhance stellar activity via SPI, which would be able to generate induced-chromospheric hotspots in the host star (Cuntz et al. 2000; Cuntz & Shkolnik 2002). Potential signatures of SPI in the form of anomalous chromospheric emission modulated by a planet has been reported for a few systems, such as in the case of HD 179949 (Shkolnik et al. 2008; Fares et al. 2012) and HD 189733 (Cauley et al. 2018). However, not all close-in planets can generate induced emission in their host stars (Shkolnik et al. 2005, 2008; Miller et al. 2012, 2015). One possible suggestion is that if the planet orbits beyond the Alfvén surface, information from a potential star-planet magnetic reconnection event would be prevented from propagating towards the star. Given the sub-Alfvénic orbit of 55 Cnc e, we investigate in this work the potential sites of generation of chromospheric hotspots caused by SPI. Figure 4 shows a set of 100 magnetic field lines that intercept planet e as it orbits around the star. If chromospheric hotspots can be formed as a result of “magnetic SPI” (i.e. through magnetic reconnection or Alfvén wings; Neubauer 1980, Ip et al. 2004), the footpoints of the connecting lines would tell us where and when such hotspots would appear.

Figure 4 shows that the magnetic field lines linking the planet to the star are a combination of open lines and closed loops. These closed magnetic loops cause the SPI-related

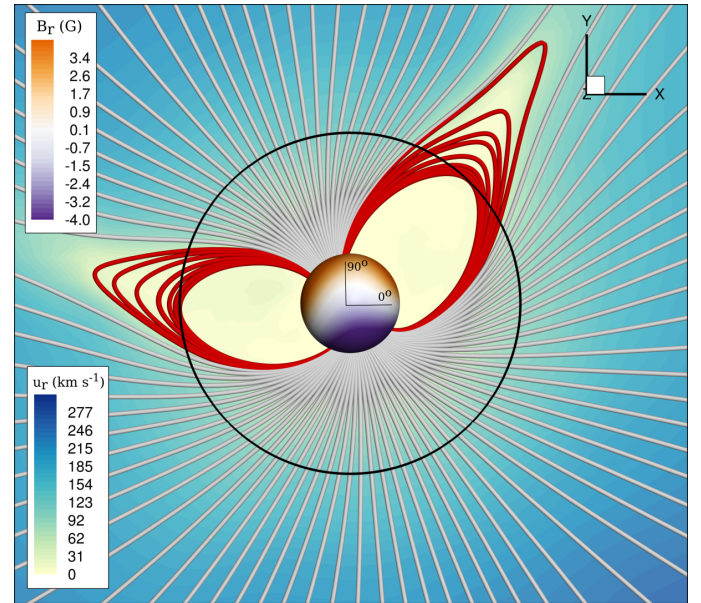


Fig. 4. Stellar magnetic field lines that intercept planet e as it orbits around the star (black circle). Stellar rotation axis is perpendicular to this orbital plane. The red field lines correspond to closed field regions. The top colour bar shows magnetic field strength (purple-orange) and bottom colour bar shows the stellar wind velocity (yellow-blue).

chromospheric spots on the star to move differently from the planetary orbit; large jumps occur where the planet moves from one branch of the closed loop to another. This phase lag and jumping effect is evident from Fig. 5 (see also predictions by McIvor et al. 2006). In fact, Fig. 5 shows that the footpoints move from lagging behind the planet orbit to ahead of it. Furthermore, for the closed loops, it is expected that the SPI occurs at both footpoints of the loop, unless that loop extends beyond the Alfvén surface. Recently, Strugarek et al. (2019) show a similar effect in the case of Kepler-78, where the magnetic topology of the host star can greatly affect the transient nature of SPI. Although their simulations do not explain the amplitude of enhanced activity observed by Moutou et al. (2016), in stars with stronger magnetic fields (e.g. HD 179949; Fares et al. 2012) the effect may be more detectable.

As the observed magnetic field of 55 Cnc is largely described by a dipole tilted by 90° to the rotation axis, all of the magnetic field lines that intersect with the planetary orbit lie within the equatorial plane. This is specific to the case of 55 Cnc and to the epoch of ZDI observation. For other planetary systems and/or

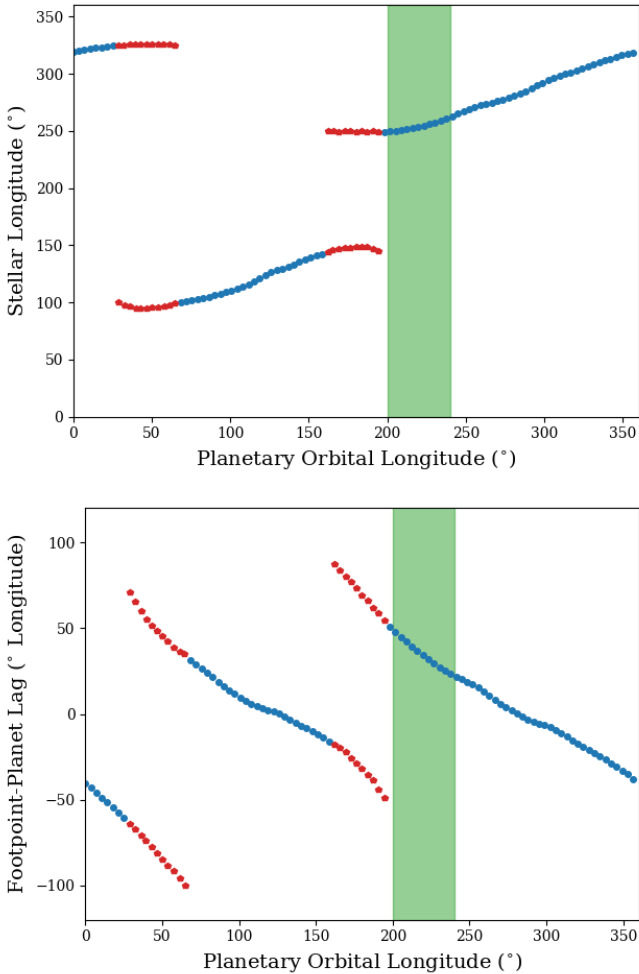


Fig. 5. *Top:* longitude of the footpoint on the stellar surface vs. the longitude of the planetary orbit, as defined in Fig. 4. Footpoints of open (closed) magnetic field lines are shown in blue (red). *Bottom:* phase lag (difference in longitudes between footpoint and subplanetary point) vs. the orbital longitude of the planet. The green region indicates the location during planetary transit.

different observing epochs, the magnetic field footpoints may lie above/below the equator, and this is dependent on the large-scale stellar magnetic field geometry. The magnetic field is essential for identifying the theoretical period of modulation for magnetic SPI. An aligned dipole generates a modulation at the synodic period (0.73 d for 55 Cnc e), while a dipole tilted at 90° generates a modulation of half the synodic period. The visibility of magnetic footpoints are also modulated by the stellar rotation period. For 55 Cnc, because the field is not purely dipolar, the distribution of footpoints on the stellar surface is not symmetric about the rotation axis; the branch of footpoints of positive polarity (Fig. 4) occupies a smaller range of stellar longitudes than that of negative polarities. This can also be seen in the top panel of Fig. 5, in which we see that the branch of footpoints above 180° of stellar longitude lasts longer than the footpoints below 180° . An additional phase lag between the planet and induced stellar activity may be present as a consequence of the time it takes the Alfvén waves to travel to the star (Strugarek et al. 2019). For 55 Cnc, however, this travel time lag is less than 10% of the orbital period.

Because the inclination of the rotation axis of 55 Cnc is near 90° , we cannot strongly constrain the axisymmetric dipolar

component of the magnetic field. Unfortunately, this limitation is intrinsic to any Stokes V observations and additional observations will not simply resolve it. Depending on how strong an unseen $m = 0$ dipole is, this could change the position of hotspots on the surface of the star, mostly in latitude, as the connectivity between the stellar magnetic field and planet could change. In terms of wind modelling, adding a dipolar component with $m = 0$ to the magnetic map of 55 Cnc derived in this work would imply an Alfvén surface that is larger than that we computed. In this case, an unseen axisymmetric dipolar component would only reinforce our results that 55 Cnc e orbits inside the Alfvén surface, strengthening possible SPI.

5. Summary and discussion

To summarise, we have used spectropolarimetric observations of 55 Cnc to detect the stellar magnetic field and mapped the large-scale magnetic field using ZDI, finding largely a tiled dipolar field. This magnetic map was used as input for a 3D MHD simulation of the stellar wind, and the properties of the wind at the positions of the known planets were estimated. We found that 55 Cnc e orbits entirely within the Alfvén surface of the stellar wind, which implies magnetic field lines connect planet e to the star, allowing for magnetic SPIs. Using these simulations, we estimated the possible position of chromospheric hotspots due to this interaction, and found they would be offset in phase from the planet’s orbital position and that apparent activity due to SPI may be modulated with a period close to twice the orbital or synodic period. Recently, Sulis et al. (2019) detected a stellar flux modulation in phase with the orbital period of planet e. Furthermore, the amplitude of this modulation appears to be directly related to stellar activity, indicating that this could be caused by magnetic interaction occurring as a consequence of the planet lying entirely within the Alfvén surface of the star. Assuming the interpretation of the observation by Sulis et al. (2019) in terms of SPI is correct, the possible apparent discrepancy in the timing of the modulation between the observation and the model prediction may be caused by the fact that the photometric and spectropolarimetric observations have been obtained more than two years apart: within this time, the geometry and strength of the stellar magnetic field may have changed.

Ideally, contemporaneous observations of different activity proxies would be able to better characterise any signature of SPI. Additionally, future spectropolarimetric observations of the system would also allow us to investigate whether the large-scale field is varying with time, and how. In particular, we would be able to further investigate the axisymmetric component, given that we found that the magnetic field is dominantly non-axisymmetric. New spectropolarimetric observations over a longer time period would also allow us to further constrain the level of differential rotation on 55 Cnc. In our analysis, it appears that differential rotation is not exceptionally strong in this star. Thanks to its high photometric precision, the CHEOPS mission will be able to follow the amplitude of the photometric modulation, which would be particularly powerful when combined with contemporaneous spectropolarimetric monitoring (e.g. Fares et al. 2017).

Acknowledgements. A.A.V., D.Ó.F., C.P.F. acknowledge joint funding received from the Irish Research Council and Campus France through the Ulysses funding scheme. The authors acknowledge the DJEI/DES/SFI/HEA Irish Centre for High-End Computing (ICHEC) for the provision of computational facilities and support. This work used the BATS-R-US tools developed at the University of Michigan Center for Space Environment Modeling and made available through the NASA Community Coordinated Modeling Center. D.Ó.F. acknowledges

funding received from the Trinity College Postgraduate Award. D.D. acknowledges NASA Hubble Fellowship (HST-HF2-51372.001-A). A.A.V. acknowledges funding received from the Irish Research Council Laureate Awards 2017/2018 and from the European Research Council (ERC) under the European Union's Horizon 2020 research and innovation programme (grant agreement No 817540, ASTROFLOW). J.F.D. acknowledges funding from the European Research Council (ERC) under the H2020 research & innovation programme (grant agreement #740651 NewWorlds).

References

- Alvarado-Gómez, J. D., Drake, J. J., Cohen, O., Moschou, S. P., & Garraffo, C. 2018, *ApJ*, **862**, 93
- Baluev, R. V. 2015, *MNRAS*, **446**, 1493
- Bhardwaj, A., & Gladstone, G. R. 2000, *Rev. Geophys.*, **38**, 295
- Bourrier, V., Dumusque, X., Dorn, C., et al. 2018, *A&A*, **619**, A1
- Caulley, P. W., Shkolnik, E. L., Llama, J., Bourrier, V., & Moutou, C. 2018, *AJ*, **156**, 262
- Cuntz, M., & Shkolnik, E. 2002, *Astron. Nachr.*, **323**, 387
- Cuntz, M., Saar, S. H., & Musielak, Z. E. 2000, *ApJ*, **533**, L151
- Demory, B.-O., Gillon, M., de Wit, J., et al. 2016a, *Nature*, **532**, 207
- Demory, B.-O., Gillon, M., Madhusudhan, N., & Queloz, D. 2016b, *MNRAS*, **455**, 2018
- Donati, J.-F., Semel, M., Carter, B. D., Rees, D. E., & Collier Cameron, A. 1997, *MNRAS*, **291**, 658
- Donati, J.-F., Howarth, I. D., Jardine, M. M., et al. 2006, *MNRAS*, **370**, 629
- Dragomir, D., Matthews, J. M., Winn, J. N., & Rowe, J. F. 2014, *IAU Symp.*, **293**, 52
- Fares, R., Donati, J. F., Moutou, C., et al. 2012, *MNRAS*, **423**, 1006
- Fares, R., Bourrier, V., Vidotto, A. A., et al. 2017, *MNRAS*, **471**, 1246
- Fischer, C., & Saur, J. 2019, *ApJ*, **872**, 113
- Folsom, C. P., Bouvier, J., Petit, P., et al. 2018a, *MNRAS*, **474**, 4956
- Folsom, C. P., Fossati, L., Wood, B. E., et al. 2018b, *MNRAS*, **481**, 5286
- Hempelmann, A., Mittag, M., Gonzalez-Perez, J. N., et al. 2016, *A&A*, **586**, A14
- Ip, W.-H., Kopp, A., & Hu, J.-H. 2004, *ApJ*, **602**, L53
- Jardine, M., Vidotto, A. A., & See, V. 2017, *MNRAS*, **465**, L25
- Kochukhov, O., Makaganiuk, V., & Piskunov, N. 2010, *A&A*, **524**, A5
- Krüger, H., Geissler, P., Horányi, M., et al. 2003, *Geophys. Res. Lett.*, **30**, 2101
- Ligi, R., Creevey, O., Mourard, D., et al. 2016, *A&A*, **586**, A94
- Manchester, W., Vourlidas, A., Toth, G., et al. 2008, *ApJ*, **684**, 1448
- Marcy, G. W. 1984, *ApJ*, **276**, 286
- McIvor, T., Jardine, M., & Holzwarth, V. 2006, *MNRAS*, **367**, L1
- Miller, B. P., Gallo, E., Wright, J. T., & Dupree, A. K. 2012, *ApJ*, **754**, 137
- Miller, B. P., Gallo, E., Wright, J. T., & Pearson, E. G. 2015, *ApJ*, **799**, 163
- Moutou, C., Donati, J. F., Lin, D., Laine, R. O., & Hatzes, A. 2016, *MNRAS*, **459**, 1993
- Neubauer, F. M. 1980, *J. Geophys. Res.*, **85**, 1171
- Ó Fionnagáin, D., & Vidotto, A. A. 2018, *MNRAS*, **476**, 2465
- Powell, K. G., Roe, P. L., Linde, T. J., Gombosi, T. I., & De Zeeuw, D. L. 1999, *J. Comp. Phys.*, **154**, 284
- Réville, V., Brun, A. S., Strugarek, A., et al. 2015, *ApJ*, **814**, 99
- Ridden-Harper, A. R., Snellen, I. A. G., Keller, C. U., et al. 2016, *A&A*, **593**, A129
- Saur, J., Grambusch, T., Duling, S., Neubauer, F. M., & Simon, S. 2013, *A&A*, **552**, A119
- Shkolnik, E., Walker, G. A. H., Bohlender, D. A., Gu, P. G., & Kürster, M. 2005, *ApJ*, **622**, 1075
- Shkolnik, E., Bohlender, D. A., Walker, G. A. H., & Collier Cameron, A. 2008, *ApJ*, **676**, 628
- Strugarek, A., Brun, A. S., Donati, J. F., Moutou, C., & Réville, V. 2019, *ApJ*, **881**, 136
- Sulis, S., Dragomir, D., Lendl, M., et al. 2019, *A&A*, **631**, A129
- Tóth, G., Sokolov, I. V., Gombosi, T. I., et al. 2005, *J. Geophys. Res.*, **110**, A12226
- Vidotto, A. A., Fares, R., Jardine, M., Moutou, C., & Donati, J.-F. 2015, *MNRAS*, **449**, 4117
- von Braun, K., Boyajian, T. S., ten Brummelaar, T. A., et al. 2011, *ApJ*, **740**, 49
- Winn, J. N., Matthews, J. M., Dawson, R. I., et al. 2011, *ApJ*, **737**, L18

λ Andromedae: A solar wind proxy post-main sequence

D. Ó Fionnagáin^{1†}, A. A. Vidotto¹, P. Petit², C. Neiner³, W. Manchester IV⁵,
C. Folsom²

¹*School of Physics, Trinity College Dublin, College Green, Dublin 2, Ireland*

²*IRAP, Université de Toulouse, CNRS, UPS, CNES, 14 Avenue Edouard Belin, 31400, Toulouse, France*

³*LESIA, Paris Observatory, PSL University, CNRS, Sorbonne University, Université de Paris, 5 place Jules Janssen, 92195 Meudon, France*

⁵*Department of Climate and Space Sciences and Engineering, University of Michigan, Ann Arbor, MI48109, USA*

Accepted XXX. Received YYY; in original form ZZZ

ABSTRACT

λ Andromedae (λ And) is a proxy for an evolved Sun. Its wind has been detected in the past through radio observations, it is known to possess a hot corona from X-ray spectroscopy, and it has evolved off the main sequence becoming a sub-giant star. We use spectropolarimetric observations to determine the surface magnetic field of this solar mass star through the Zeeman-Doppler Imaging (ZDI) technique. This provides us with important constraints for simulating the wind of this sub-giant. Although much older than our Sun, having evolved off the main sequence, this star exhibits a much stronger large-scale magnetic field — $B_{\max} = 60$ G. To investigate the wind of λ And, we simulate two stellar wind scenarios: a “hot wind”, which uses a polytropic formulation and a “cold wind”, which uses a wave-driven formulation. From our simulations we calculate the thermal bremsstrahlung expected from the wind of λ And and compare this to radio observations. These observations allow us to place a constraint on the base density of the wind of λ And, thus providing a way to constrain mass-loss rate *a posteriori*. From our most compatible simulation, we predict a radio flux density of 0.89 mJy at 4.5 GHz, which agrees with radio observations. The same simulation indicates that λ And exhibits $\dot{M} = 2.91 \times 10^{-9} M_{\odot} \text{ yr}^{-1}$. This value for mass-loss rate in λ And is much larger than previous estimates, but agrees much better with the evolving mass-loss rate trend for evolved solar-mass stars.

Key words: stars: winds, outflows – stars: magnetic field – stars: late-type – stars: solar-type

1 INTRODUCTION

Stellar atmospheres are highly dynamic environments that change on timescales varying from milliseconds (e.g. flares) to giga-years (e.g. spin-down). We examine the long timescale evolution of solar-type stars by simulating the wind of λ Andromedae, to infer the future evolution of our Sun. This G8 IV type star has a mass of $1.0 \pm 0.2 M_{\odot}$, a radius of $7.0 \pm 0.7 R_{\odot}$, a rotation rate of 54 days, and exists at a distance of 24.2 pc (Table 1). It is a well studied star with X-ray (Audard et al. 2003; Drake et al. 2011), EUV (Baliunas et al. 1984; Dupree et al. 1996; Sanz-Forcada et al. 2003), optical (Frasca et al. 2008), interferometric imaging (Parks et al. 2015), and radio observations (Bath & Wallerstein 1976; Bowers & Kundu 1981; Lang et al. 1985). This makes λ And a good candidate for an old solar proxy, as we can draw physical constraints from past observations. Cool stars that have evolved off the main sequence can be split into three distinct groups based on their coronae (formerly two groups, dividing line from Linsky & Haisch 1979; Drake & Linsky 1986); sun-like stars with hot coronae, warm/weak coronal

stars, and cold stars without coronae (Linsky & Haisch 1979; Ayres et al. 2003; Cranmer & Winebarger 2019). Simply by placing λ And on a HR-diagram we know that, while somewhat evolved with a radius of $7.0 R_{\odot}$, it has not yet lost its hot corona (Figure 1). Additionally, X-ray observations show that λ And fits into the hot corona category as its spectrum shows hot line formations (Linsky & Haisch 1979; Drake et al. 2011). Ortolani et al. (1997) showed that the coronal temperature should exist around 0.9 keV (≈ 10.4 MK), while Sanz-Forcada et al. (2003) found that during quiescence, the plasma temperature is closer to 7.9 MK. As a broad rule, stars in the ‘Hot Corona’ region tend to have mass-loss rates $10^{-10} M_{\odot} \text{ yr}^{-1}$ and terminal velocities of $\approx 100 \text{ km s}^{-1}$. Stars to the right of this divide, with ‘No Corona’, usually show mass-loss rates of $< 10^{-8} M_{\odot} \text{ yr}^{-1}$, and terminal velocities of $< 40 \text{ km s}^{-1}$ (Drake & Linsky 1986; O’Gorman et al. 2018). Figure 1 shows a roughly smooth transition between these two scenarios however, giving rise to an intermediate ‘Hybrid’ scenario, where the stars show signs of weak/warm coronae, perhaps giving rise to partially ionising winds, and having a combination of wind driving mechanisms.

Müller et al. (2001) and Wood et al. (2002) derived a mass-loss rate for λ And indirectly through Ly- α absorption of excess neutral

† E-mail: ofionnad@tcd.ie

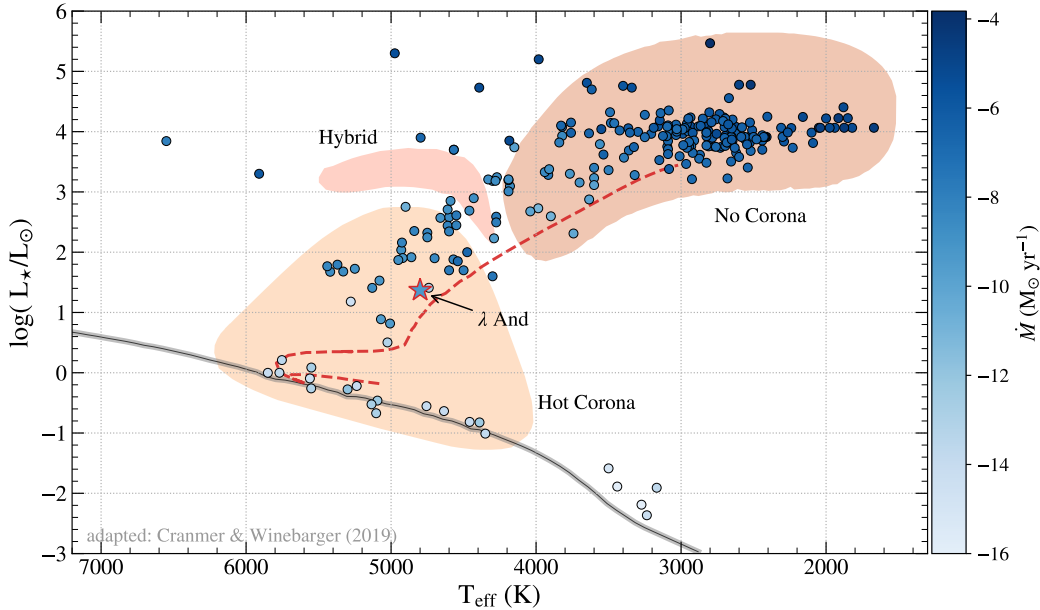


Figure 1. This is an adapted figure from Cranmer & Winebarger (2019). It shows the evolution of stellar mass-loss rates as low-mass stars evolve off the main sequence and become red giants. We contextualise the evolution of λ And, shown over-plotted (red outlined star symbol). We see that although λ And has begun to expand, it is still a sub-giant and retains its hot corona. Stellar mass-loss rate is shown as a blue scale. The grey line shows the zero-age main sequence, with filled regions shown for stars presenting hot corona, no corona, and a hybrid wind scenario (Linsky & Haisch 1979; Ayres et al. 2003). The dashed red line shows the $1 M_{\odot}$ evolutionary track from Drake et al. (2011).

^a *Stellar data—priv. comm., S. Cranmer, Jan 2020.*

Table 1. Physical parameters of λ And from Drake et al. (2011)

$M (M_{\odot})$	$R (R_{\odot})$	$\log(L_{\star}/L_{\odot})$	$T_{\text{eff}} (K)$	$P_{\text{rot}} (d)$	$d (pc)$
1.0 ± 0.2	7.0 ± 0.7	1.37	4800	54	24.2 ± 0.3

hydrogen build-up between the stellar wind and the astrosphere. They found a mass-loss rate of $2 \times 10^{-15} M_{\odot} \text{ yr}^{-1}$ (Wood 2018), they found a mass-loss rate (\dot{M}) of $2 \times 10^{-13} M_{\odot} \text{ yr}^{-1}$ and $10^{-13} \dot{M}_{\odot}$ respectively, although they claim the detection is uncertain. More recent work suggested an even lower mass-loss rate of $2 \times 10^{-15} M_{\odot} \text{ yr}^{-1}$. This is unexpectedly low compared to the previously mentioned mass-loss rates for post-main sequence stars, and is a much lower mass-loss rate per unit surface area than the Sun itself.

A particularly promising technique to constrain low-mass stellar winds is to use radio observations of the thermal bremsstrahlung from the ionised winds (Panagia & Felli 1975; Wright et al. 1975; Lim & White 1996; Villadsen et al. 2014; Fichtinger et al. 2017; Vidotto & Donati 2017; Ó Fionnagáin et al. 2019). While stars along the main sequence possess winds too tenuous to detect with current instrumentation, the increased mass-loss rates of the more evolved low-mass stars provide a more attainable target (eg. O’Gorman et al. 2017). There have been many radio observations of λ And, Bath & Wallerstein (1976); Bowers & Kundu (1981); Lang et al. (1985) all presented detected radio flux densities ranging from 0.84 – 65 mJy across the frequency range 2 – 8 GHz. We use the Bowers & Kundu (1981) and Lang et al. (1985) value of ≈ 0.85 mJy at 4.5 – 5 GHz, as a benchmark for our work presented here, as they are at similar observation frequencies and their observed flux densities agree with each other.

We present the first surface magnetic field observations of λ And and detect a strong magnetic field for such an evolved star. These observations, carried on the Narval spectropolarimeter,

allow us to constrain the surface magnetic field of λ And. These derived surface magnetic fields can constrain the lower boundary of the 3D magnetohydrodynamic wind simulations that we run. Usually, we see a decay in magnetic field strength as solar-type stars evolve, as their activity decreases along with their rotation (Skumanich 1972; Vidotto et al. 2014b; Booth et al. 2020), however, this sub-giant star seems to have a relatively strong large-scale magnetic field compared to the Sun. The exact process through which this star would reach this stage in its evolution with such a magnetic field are yet unknown. Potential reasons are that it began with a much stronger dynamo in its past than anticipated, or perhaps the secondary companion had some effect on the primary star at a point in the past. λ And differs from the Sun as it is a RS Canum Venaticorum (RS CVn) variable, meaning it is a variable binary system and it is comparatively metal-poor (Drake et al. 2011). For the purposes of this work, we assume the binarity of this system will not effect our results, as the variability on this star is most likely due to stellar rotation or strong magnetic activity (Drake et al. 2011), and not caused by the orbit of the binary system, as is the typical case for classical RS CVn stars. We do not include the effects of different metal abundances on the stellar wind and stellar evolution, but the effects of which have been examined in other works (Suzuki 2018).

In this work we employ two 3D MHD wind models, using BATS-R-US (Powell et al. 1999; Sokolov et al. 2013; Van Der Holst et al. 2014), including the stellar magnetic field, with which we aim to more accurately replicate the observed radio flux. We provide two cases for the stellar wind, a “hot” and “cold” case. As stars become older they cool significantly, this cooling means they no longer have a hot corona to drive their stellar winds in the form of thermal acceleration. Despite this, the mass-loss rate of these stars dramatically increases by many orders of magnitude (see Figure 1). Therefore it is expected in these cool evolved scenarios, the wind

is driven by waves, predominantly Alfvén waves. It is also possible that winds form some sort of hybrid wind, with characteristics from both a coronal driven hot wind, and cold wave-drive wind. In this work our hot and cold models include a polytropic thermally driven wind and an Alfvén wave driven wind respectively. We use these two different models to find which one better reproduces the radio observations of λ Andromedae.

In Section 2 we discuss the spectropolarimetric observations of the star and the results from Zeeman Doppler Imaging. Section 3 details the different models that we use to simulate the stellar wind of λ And. In Sections 4 and 5 we discuss the results of our simulations, the global parameters of the wind, the calculated radio emissions and how they compare to the observations. We conclude and summarise the work conducted in this paper in Section 6.

2 OBSERVED SURFACE MAGNETIC FIELDS

λ And was observed with the NARVAL high resolution spectropolarimeter installed on the Bernard Lyot Telescope (TBL, Pic du Midi Observatory, France, Aurière 2003) in the frame of the BritePol program (Neiner et al. 2017). The circular polarization mode of Narval was used to acquire the data, providing a simultaneous measurement of Stokes V and Stokes I over a wavelength domain extending from 370 nm to 1 μ m at a spectral resolution of about 65,000.

Each Stokes V sequence consists of 4 sub-exposures of 56 seconds each, obtained with different azimuthal angles of the half wave Fresnel rhombs in the polarimetric module (Semel et al. 1993). A Null polarization spectrum was also computed for each observation by destructively combining the 4 sub-exposures. This allows to check for any spurious signal in Stokes V that may have been produced by variable weather conditions, instrumental issues or non-magnetic stellar variations such as pulsations.

The full set of BritePol observations consisted in 6 measurements obtained in December 2013, 1 in January 2014, and 19 from August to October 2016. Our magnetic model was restricted to the 2016 data, as the permanent evolution of surface features on cool active stars similar to λ And prevents us from combining data obtained over more than a few weeks (see e.g. Petit et al. 2004a for the active subgiant primary of the RS CVn system HR 1099). We also removed from this time series the observation obtained on Aug 10, as the LSD method (see paragraph below) led to an abnormal outcome for this specific spectrum. The subset selected here offers a good basis for tomographic mapping, with a dense set of observations spread over most of one stellar rotation (assuming a period of 54 d, Drake et al. 2011). All data used in this article are publicly available in the PolarBase data base (Petit et al. 2014).

Our set of Stokes V spectra do not exhibit any line signatures, which is typical of the relatively small amplitude of Zeeman signatures recorded in most cool active stars. As usually done in this situation, we make use of the Least-Square Deconvolution method (LSD hereafter, Donati et al. 1997) to extract an average, pseudo line profile of enhanced signal-to-noise ratio. To do so, we adopt a list of lines produced by a photospheric model (Kurucz 1993) with stellar parameters close to those of λ And ($T_{\text{eff}} = 4800 \pm 100$ K and $\log g = 2.75 \pm 0.25$, Drake et al. 2011). We impose for the LSD pseudo-line profiles an equivalent wavelength of 650 nm, and an equivalent Landé factor of 1.21. The outcome is a time-series of Stokes I and Stokes V pseudo line profiles, with the systematic detection of a polarised signature at the radial velocity of the line (Appendix A).

The surface magnetic field geometry was calculated with the

Zeeman-Doppler Imaging (ZDI) technique (Semel 1989), using the spherical harmonics expansion proposed by Donati et al. (2006), and the latest python implementation of Folsom et al. (2018a). In this framework, the stellar surface is paved with rectangular pixels linked to a local line model. Following Folsom et al. (2018b), the local Stokes I line profile takes the form of a Voigt profile weighted according to a projection factor and linear limb darkening coefficient (taken equal to 0.73, Claret 2004). Each local line profile is also Doppler shifted according to the local radial velocity produced by stellar rotation, assuming $v \cdot \sin i = 7.3 \text{ km.s}^{-1}$ (Massarotti et al. 2008). The local Stokes V line profile is computed from the local Stokes I profile and the local longitudinal field using the weak field approximation (where Stokes V is proportional to the first derivative of Stokes I). The global Stokes I and V profiles obtained after integrating over the visible stellar hemisphere are then Doppler shifted to follow the radial velocity variations produced by the orbital motion of the target. Our ZDI model includes spherical harmonics modes up to $\ell = 15$, as no noticeable improvement of the Stokes V fit is obtained when further increasing this number. The best ZDI model is obtained for an inclination angle equal to $71 \pm 2^\circ$, which is consistent (within uncertainties) with the estimate of Donati et al. (1995) (60^{+30}_{-10}). The sets of synthetic Stokes I and V profiles obtained with this ZDI procedure are illustrated in Appendix A.

The resulting magnetic geometry is plotted in Figure 2. Several magnetic spots are recovered and most of them are located near the equator (in both the radial and azimuthal field components). The maximum (local) field strength is equal to 83 G, while the average field strength is equal to 21 G. Most of the magnetic energy is reconstructed in the poloidal field component (64%), and most of the poloidal field is observed in low order spherical harmonics components, with about 78% of the poloidal magnetic energy in modes with $\ell \leq 3$. The low latitude azimuthal field forms a unipolar ring (of positive polarity), as already observed in several cool, evolved stars (e.g. Donati et al. 2003; Petit et al. 2004a,b). We note that the rotation phases where the azimuthal field strength is large also have a strong radial field strength (around phase 0.2, and also between phases 0.6 and 0.9).

The reduced χ^2 obtained by the ZDI inversion is equal to 1.9, showing that our simple magnetic model cannot fully reproduce the shape of the observed Stokes V pseudo profiles. We assume here a solid rotation of the stellar surface, and this assumption is often the main limitation of ZDI models of cool stars, since the surface is expected to be differentially rotating. Following the procedure of Petit et al. (2002), we searched for a progressive distortion of the magnetic geometry under the influence of a solar or anti-solar surface shear. This search was inconclusive, likely because our data set does not cover more than one rotation period. Another possible limiting factor is the continuous appearance and disappearance of magnetic spots, and the relatively large timespan of our data (slightly less than 2 months) is possibly responsible for some significant intrinsic evolution of the magnetic pattern. To compare the surface magnetic field of λ And with the magnetic survey for evolved stars of Aurière et al. (2015), we have computed longitudinal field (B_l) values (Rees & Semel 1979) for every observation included in the ZDI analysis. The maximal longitudinal field strength throughout the time series is $|B_l|_{\text{max}} = 13.7 \pm 0.4$ G, in good agreement with $|B_l|_{\text{max}}$ values reported by Aurière et al. (2015) at similar rotation periods. We therefore suggest that, although λ And is a member of a close binary system, the observed surface magnetic field strength is not noticeably influenced by the tidal interaction between the primary and its low-mass companion.

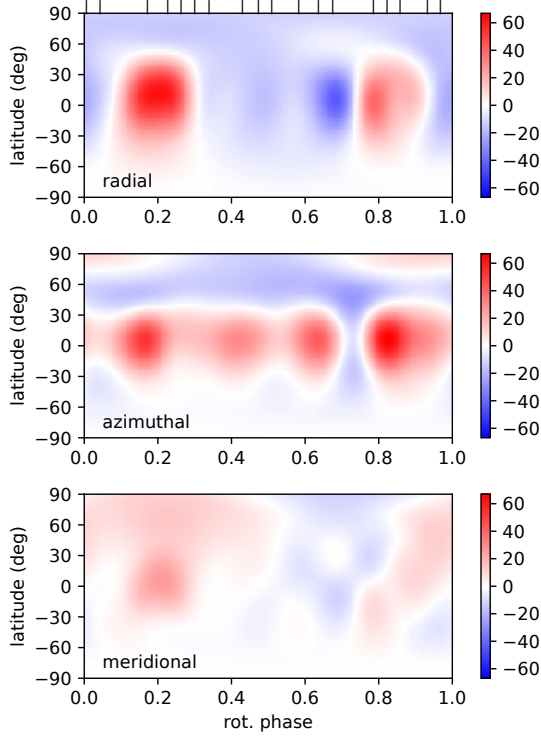


Figure 2. Large scale magnetic field geometry of λ And, as reconstructed with the ZDI method. From top to bottom, the three panels show the radial, azimuthal and meridional components of the photospheric magnetic field (in Gauss). The observed rotational phases are shown as vertical ticks above the radial field map.

3 RED GIANT STELLAR WIND MODELS

We use two separate implementations of the BATS-R-US code, the ‘hot’ polytropic wind model, as described in Vidotto & Donati (2017); Ó Fionnagáin et al. (2019) and the ‘cold’ two-temperature AWSOM model which is defined in Van Der Holst et al. (2014). As evolved type stars possess cool extended atmospheres, we expect that they are wave driven (predominantly Alfvén waves), which drive wind acceleration through turbulent dissipation. This concept has been used for evolved stars frequently in the past (Hartmann & MacGregor 1980; Vidotto & Jatenco-Pereira 2006; Suzuki 2007; Airapetian et al. 2010; Cranmer & Saar 2011; Van Der Holst et al. 2014; Yasuda et al. 2019). For a star such as λ And, it is possible that as it moves towards the hybrid area of Figure 1, the wind combines both thermal acceleration and wave driving. Therefore we carry out simulations of both cases to compare to observations. We summarise the essential equations to both models below:

3.1 Hot wind model

In this model, the inner boundary of the simulation begins in the corona of the star. We assume a polytropic index which drives the wind of the star by supplying energy to the wind. The polytropic index in the solar wind has been measured as $\Gamma = 1.1$ (Van Doorselaere et al. 2011), and many numerical solar wind simulations use $1 < \Gamma < 1.15$ (Keppens & Goedbloed 1999; Matt et al. 2012; Johnstone et al. 2015a,b), here we adopt a value of $\Gamma = 1.05$. BATS-R-US solves for 8 parameters in this case: mass density (ρ), wind veloc-

ity ($\mathbf{u} = \{u_x, u_y, u_z\}$), magnetic field ($\mathbf{B} = \{B_x, B_y, B_z\}$), and gas pressure P . The equations that govern this model are shown below.

$$\frac{\partial \rho}{\partial t} + \nabla \cdot (\rho \mathbf{u}) = 0, \quad (1)$$

$$\frac{\partial(\rho \mathbf{u})}{\partial t} + \nabla \cdot \left[\rho \mathbf{u} \mathbf{u} + \left(P + \frac{B^2}{8\pi} \right) \mathbf{I} - \frac{\mathbf{B}\mathbf{B}}{4\pi} \right] = \rho \mathbf{g}, \quad (2)$$

$$\frac{\partial \mathbf{B}}{\partial t} + \nabla \cdot (\mathbf{u}\mathbf{B} - \mathbf{B}\mathbf{u}) = 0 \quad (3)$$

$$\frac{\partial \varepsilon}{\partial t} + \nabla \cdot \left[\mathbf{u} \left(\varepsilon + P + \frac{B^2}{8\pi} \right) - \frac{(\mathbf{u} \cdot \mathbf{B})\mathbf{B}}{4\pi} \right] = \rho \mathbf{g} \cdot \mathbf{u}, \quad (4)$$

where the total energy density is given by:

$$\varepsilon = \frac{\rho u^2}{2} + \frac{P}{\gamma - 1} + \frac{B^2}{8\pi} \quad (5)$$

Here, \mathbf{I} denotes the identity matrix, and \mathbf{g} the gravitational acceleration. We assume that the plasma behaves as an ideal gas, that $P = n_{\text{cor}} k_B T$, where $n_{\text{cor}} = \rho / (\mu m_p)$ is the total number density of the wind. ρ represents the mass density, k_B is the Boltzmann constant, and μm_p denotes the average particle mass. We take $\mu = 0.5$, which represents a fully ionised hydrogen wind. Polytropic index aside, the other free parameters are base coronal density, base coronal temperature, and base magnetic field. For this model we use $n_{\text{cor}} = 2.5 \times 10^{10} \text{ cm}^{-3}$ and $T_{\text{cor}} = 1 \text{ MK}$. The base magnetic field is constrained using ZDI observations, of which we only include the radial field component, B_r , in our simulations, which are thoroughly described in Section 2. Note that all parameters here equate to coronal values, as this is where the bottom of this simulation begins. We use a Cartesian grid, with the minimum resolution of $0.01 R_\star$ and a maximum resolution of $0.3 R_\star$, totalling 622672 blocks, or 3.98×10^7 cells. (Figure B1).

3.2 Cold wind model

We use the SC (solar corona) module of the AWSOM code to simulate our cold wind scenario. This module of the SWMF framework has been used previously to simulate the Alfvén wave driven wind of the Sun (Sokolov et al. 2013; Van Der Holst et al. 2014; Meng et al. 2015; Oran et al. 2017; Gombosi et al. 2018) and other stars (Alvarado-Gómez et al. 2018, 2019). In this model an Alfvén wave flux is assumed to be propagating from the base of the wind. Source terms are included to account for the dissipation of these waves through turbulence and reflection, which is converted into pressure that drives the stellar wind. The equations that differ from the polytropic model described in Section 3.1 are the momentum equation, which includes separated electron (P_e) and ion pressures (P_i), and the additional pressure from the Alfvén waves (P_A)

$$\frac{\partial(\rho \mathbf{u})}{\partial t} + \nabla \cdot \left[\rho \mathbf{u} \mathbf{u} + \left(P_i + P_e + P_A + \frac{B^2}{8\pi} \right) \mathbf{I} - \frac{\mathbf{B}\mathbf{B}}{4\pi} \right] = \rho \mathbf{g}. \quad (6)$$

The energy equations for electrons and ions become

$$\begin{aligned} \frac{\partial \varepsilon_i}{\partial t} + \nabla \cdot \left[\mathbf{u} \left(\varepsilon_i + P_i + \frac{B^2}{8\pi} \right) - \frac{(\mathbf{u} \cdot \mathbf{B})\mathbf{B}}{4\pi} \right] \\ = -(\mathbf{u} \cdot \nabla)(P_e + P_A) + \frac{N_i k_B}{\tau_{ei}} (T_e - T_i) + Q_i - \rho \mathbf{g} \cdot \mathbf{u} \end{aligned} \quad (7)$$

$$\begin{aligned} \frac{\partial}{\partial t} \left(\frac{P_e}{\gamma - 1} \right) + \nabla \cdot \left(\frac{P_e}{\gamma - 1} \mathbf{u} \right) + P_e \nabla \cdot \mathbf{u} \\ = -\nabla \cdot \mathbf{q}_e + \frac{N_i k_B}{\tau_{ei}} (T_i - T_e) - Q_{rad} + Q_e \end{aligned} \quad (8)$$

where ε_i represents the energy for the ions, according to Equation (5). $T_{e,i}$ and $n_{e,i}$ denote electron and ion temperatures and densities respectively. We employ the equation of state $P_{e,i} = n_{e,i} k_B T_{e,i}$ and the adiabatic index is $\gamma = 5/3$. \mathbf{q}_e represents the electron heat transport which transitions smoothly from collisional (Spitzer & Härm 1953) to collisionless (Hollweg 1978) heat flux so that the Spitzer-Härm collisional form dominates near the star, and the Hollweg collisionless form dominates further out in the wind. Q_e and Q_i are the heating functions for electrons and ions respectively and are partitioned forms of turbulent dissipation by Alfvén waves (Chandran et al. 2011). Q_{rad} is the radiative cooling and is defined as

$$Q_{rad} = \Lambda N_e N_i, \quad (9)$$

where Λ is the radiative cooling rate from CHIANTI v9.0 (Dere et al. 2019). The Alfvén wave dissipation, reflection and propagation are governed by the wave energy density equations

$$\frac{\partial w_{\pm}}{\partial t} + \nabla \cdot [(\mathbf{u} \pm \mathbf{V}_A) w_{\pm}] + \frac{w_{\pm}}{2} (\nabla \cdot \mathbf{u}) = \mp \mathcal{R} \sqrt{w_- w_+} - \xi_{\pm} w_{\pm} \quad (10)$$

where w_{\pm} represents the wave energy densities for waves parallel (+) and anti-parallel (-) to the magnetic field. $\mathbf{V}_A = \mathbf{B}/\sqrt{4\pi\rho}$ is the Alfvén velocity, \mathcal{R} is the wave reflection rate, and ξ is the dissipation rate. The dissipation rate is

$$\xi_{\pm} = \frac{2}{L_{\perp}} \sqrt{\frac{w_{\mp}}{\rho}} \quad (11)$$

where L_{\perp} is the transverse correlation length of the Alfvén waves perpendicular to \mathbf{B} . As in Hollweg (1986), $L_{\perp} \propto \sqrt{B}$, with the proportionality constant (ℓ) set as an adjustable parameter of the model. The reflection rate \mathcal{R} depends on the ratio of energy densities of parallel and anti-parallel waves, and the Alfvén velocity. A thorough description of this entire model can be found in Van Der Holst et al. (2014).

The model requires values to be set for the free parameters, which range from the chromospheric density (n_{chr}), chromospheric temperature (T_{chr}), Alfvén wave Poynting flux (S_A), and the damping proportionality constant (ℓ). These physical parameters do not have direct constraints from observations although we can limit some of these parameters *a posteriori*. For example, selecting a base density that is too large could cause an unrealistically high mass-loss rate and the estimated radio emission could exceed observed levels (see Section 5). For our cold wind scenario, we ran a number of simulations varying these base parameters, shown in Table 2. We began these simulations with an equatorial dipolar magnetic field of $B_{eq} = 30$ G. This is a similar magnetic field strength to the average and maximum magnetic fields found in the ZDI map of λ And (Figure 2). Additionally, we ran a set of simulations using the ZDI map for the cold wind scenario, three of which are shown in Table 2: C1, C2, and C3.

Contrary to the hot wind simulation, the cold wind simulations reach a quasi-steady state. This occurs as the heating depends on the dissipation of Alfvén waves, which in turn depends on the magnetic field geometry and strength, the simulations tend to reach a point where they oscillate. In these cases, an average of the states is taken for the simulation parameters.

The SC module in the Alfvén wave-driven model uses a 3D spherical grid, with radial stretching from 1-30 R_{\star} . It also employs

adaptive mesh refinement (AMR), adding extra refinement to the volume surrounding the current sheet. Radial stretching and AMR are quite efficient, increasing the resolution near the star and in required locations, without significantly increasing the number of cells in the simulation. The AMR is turned on for a single timestep after 100 timesteps to add refinement to the current sheet, which is the region where the magnetic field changes polarity and is susceptible to magnetic reconnection and high currents, which could cause issues in simulations without AMR. Our simulation mesh has $r_{min,max} = 0.0003, 1.25 R_{\star}$ and $\phi/\theta_{min,max} = 0.025, 1.5 R_{\star}$, resulting in an average of 45k blocks, and 4.3×10^6 cells (Figure B1).

3.3 Mass and angular momentum losses

From our wind simulations we can calculate the mass-loss rate from each of the stars by integrating the mass flux through a spherical surface S around the star

$$\dot{M} = \oint_S \rho u_r dS, \quad (12)$$

where \dot{M} is the mass loss rate, ρ is the wind density, and u_r is the radial velocity. We also determine angular momentum-loss rate from our simulations as

$$j = \oint_S \left[-\frac{\varpi B_{\phi} B_r}{4\pi} + \varpi u_{\phi} \rho u_r \right] dS \quad (13)$$

where B and u are the magnetic field and velocity components of the wind, $\varpi = (x^2 + y^2)^{1/2}$, the cylindrical radius, and r and ϕ denote the radial and azimuthal components respectively (Mestel 1999; Vidotto et al. 2014a). Both mass-loss and angular momentum-loss are calculated from our simulations.

3.4 Radio modelling

Stellar winds emit thermal bremsstrahlung as they are composed of ionised plasma. Initially, the calculated radio flux from these winds was done analytically (Panagia & Felli 1975; Wright et al. 1975; Lim & White 1996), but with 3D simulations, it has become possible to do this calculation numerically (Moschou et al. 2018; Cohen et al. 2018; Ó Fionnagáin et al. 2019). From our simulations we can calculate the expected radio flux density by analysing the particle density and temperature structure in the wind. We use the Python package *RadioWinds* Ó Fionnagáin (2018) to calculate the thermal radio emission from the wind of λ And. We can calculate the thermal emission expected from these winds by solving the radiative transfer equation,

$$I_{\nu} = \int_0^{\tau'_{max}} B_{\nu} e^{-\tau_{\nu}} d\tau' \quad (14)$$

where I_{ν} denotes the intensity from the wind, B_{ν} represents the source function, which in the thermal case becomes a blackbody function, τ_{ν} represents the optical depth of the wind, with τ' representing our integration coordinate across the grid. The optical depth of the wind depends on the absorption coefficient, α_{ν} , of the wind as

$$\tau_{\nu} = \int \alpha_{\nu} ds, \quad (15)$$

where s represents the physical coordinate along the line of sight, α_{ν} is described as (Panagia & Felli 1975; Wright et al. 1975; Cox & Pilachowski 2002),

$$\alpha_{\nu} = 3.692 \times 10^8 [1 - e^{-h\nu/k_B T}] Z^2 f_g T^{-0.5} \nu^{-3} n_e n_i \quad (16)$$

Table 2. Summary of our simulations. In the case of the cold model we have many iterations of the winds as we are varying the input Poynting flux (S_A) of the Alfvén waves and the proportionality constant for wave damping (ℓ) for different base wind densities. All cold simulations here possess a base temperature of 50,000 K, with a 1 MK base temperature for the hot wind scenario as its base begins embedded in the corona. Each lettered simulation denotes a different base density (n_{base}). The fiducial Poynting flux is $S_0 = 37 \text{ W m}^{-2}\text{G}^{-1}$ and fiducial damping length $\ell_0 = 1.5 \times 10^5 \text{ m T}^{0.5}$.

Simulation Input					Simulation Output				
Sim	B field	$n_{\text{base}} \text{ cm}^{-3}$	$S_A [\text{W m}^{-2}\text{T}^{-1}]$	$\ell [\text{m T}^{0.5}]$	$v_{\text{max}} [\text{km s}^{-1}]$	$T_{\text{max}} [\text{MK}]$	$\dot{M} [M_{\odot} \text{ yr}^{-1}]$	$\dot{J} [\text{erg}]$	$\Phi_{\text{radio}} [\text{mJy}]$
A0	Dipole		S_0	ℓ_0	700	5.8	4.7×10^{-12}	3.1×10^{34}	0.005
A1	Dipole	1.5×10^{10}	$10 S_0$	ℓ_0	930	11	3.9×10^{-11}	1.1×10^{35}	0.011
A2	Dipole		S_0	$7 \ell_0$	817	6.6	4.1×10^{-12}	3.0×10^{34}	0.004
A3	Dipole		$S_0 / 10$	$7 \ell_0$	405	3.37	5.6×10^{-13}	1.6×10^{34}	0.004
B0	Dipole	1.5×10^{12}	S_0	$7 \ell_0$	765	5.7	3.7×10^{-12}	3.2×10^{34}	0.007
B1	Dipole		S_0	$253 \ell_0$	977	4.9	2.0×10^{-12}	2.5×10^{34}	0.008
C0	Dipole		S_0	$253 \ell_0$	497	4.4	1.9×10^{-11}	3.7×10^{34}	0.014
C1	ZDI	1.5×10^{13}	S_0	$253 \ell_0$	590	2.9	1.2×10^{-11}	9.8×10^{33}	0.014
C2	ZDI		$30 S_0$	$7 \ell_0$	619	4.3	1.7×10^{-10}	4.5×10^{34}	0.030
C3	ZDI		$S_0 / 10$	$253 \ell_0$	527	2.1	1.7×10^{-12}	3.0×10^{33}	0.007
D0	Dipole	1.5×10^{14}	S_0	$253 \ell_0$	765	5.6	4.0×10^{-12}	3.1×10^{34}	0.014
D1	Dipole		$S_0/10$	$253 \ell_0$	292	1.7	2.7×10^{-12}	1.8×10^{34}	0.013
Z0	ZDI	2.5×10^{101}	—	—	456	1.0	2.91×10^{-9}	2.2×10^{35}	0.890

and the blackbody function is the standard Planck function.

$$B_{\nu} = \frac{2h\nu^3}{c^2} \frac{1}{e^{h\nu/k_B T} - 1} \quad (17)$$

where ν is the observing frequency, T is the temperature of the wind, h is Planck's constant, Z is the ionic state of the wind, and n_e and n_i represent the electron and ion number densities of the wind. From the intensity we can calculate the flux density (S_{ν}) of the wind as,

$$S_{\nu} = \frac{1}{d^2} \int I_{\nu} d\Omega \quad (18)$$

where d is the distance to the star, and Ω is the solid angle.

4 POST-MS WINDS FROM MHD SIMULATIONS

As presented in Section 1, we have observational constraints on the wind of λ And that we use here to constrain the free parameters of our model. For example, the location λ And on the H-R diagram provides loose constraints on mass-loss rates based on studies of other evolved low-mass stars: 10^{-11} – $10^{-9} M_{\odot} \text{ yr}^{-1}$ (see Figure 1, Linsky & Haisch 1979; Cranmer & Winebarger 2019). It is possible that λ And is transitioning from a hot corona to no corona implying it could have a “hybrid” wind, with mixed characteristics of the hot coronal winds and the cool wave-driven winds. However, the X-ray observations point more strongly towards λ And still showing signs of a hot corona (Ortolani et al. 1997; Sanz-Forcada et al. 2004; Drake et al. 2011), with maximum coronal temperatures of 7–10 MK. While giants more evolved than λ And usually possess winds with low terminal velocities ($< 40 \text{ km/s}$ Drake & Linsky 1986; O’Gorman et al. 2018), the presence of a hot corona is likely to lead to moderate terminal wind velocities (≈ 300 – 400 km s^{-1}), and mass-loss rates of 10^{-11} – $10^{-9} M_{\odot} \text{ yr}^{-1}$ (Linsky & Haisch 1979; Drake & Linsky 1986). The aforementioned mass-loss rate derived from comparison to neighbour stars in the HR diagram, however, is at odds with the mass-loss rate derived in astrophysical observations, which can be as low as $2 \times 10^{-15} M_{\odot} \text{ yr}^{-1}$ and as high as $1 \times 10^{-13} M_{\odot} \text{ yr}^{-1}$ (Wood 2018; Müller et al. 2001).

The several orders of magnitude differences in the mass-loss rates of λ And derived so far in the literature has led to us to use a different approach to constrain the wind of λ And, using radio observations. Radio emission from stellar winds provide us a direct detection of the wind (Bath & Wallerstein 1976; Bowers & Kundu 1981; Lang et al. 1985; Panagia & Felli 1975; Wright et al. 1975), which limits the density adopted in our simulations and, consequently, the mass-loss rate (Vidotto 2017; Ó Fionnagáin & Vidotto 2018; Ó Fionnagáin et al. 2019). In the particular case of λ And there are detections of 0.86 mJy at 4.5 GHz (Bowers & Kundu 1981) and 0.84 mJy at 5 GHz (Lang et al. 1985), with older observations finding even higher radio flux from this source of 65 mJy at 5 GHz and 20 mJy at 8.1 GHz (Bath & Wallerstein 1976). In this paper, we will use the more recent observations for comparison. Here, we aim to find a wind solution that matches as many of these constraints as possible, using our two numerical models. We take two separate approaches in this work to simulate the wind of λ And Section 3. Our first approach, the hot wind model, begins at the base of the corona, with the thermal pressure and polytropic index determining wind acceleration and energy deposition. Our second approach, the a cold wind model, begins at the chromosphere, with wind acceleration and heating determining by Alfvén wave dissipation. Our input parameters for our simulations are shown in Table 2, detailing the base wind density, base magnetic field (either the ZDI map or a dipolar field), the Poynting flux and damping length coefficient. The latter two parameters do not apply to the hot wind scenario. We derive some indicative output parameters of the simulations in Table 2, the most important of which are the mass-loss rate and radio flux density.

As can be seen in the last row of Table 2, we find quite an agreeable solution for the wind of λ And for our hot wind scenario using the BATS-R-US polytropic model. Our derived radio flux density of 0.89 mJy at a frequency of 4.5 GHz is very similar to the observed values of 0.86 mJy at 4.5 GHz and 0.84 mJy at 5 GHz (Lang et al. 1985; Bowers & Kundu 1981). We will present more details of our radio emission calculation in Section 5. The simulation temperature and wind velocity are shown in Figure 3. This polytropic simulation displays a mass-loss rate of 2.9×10^{-9}

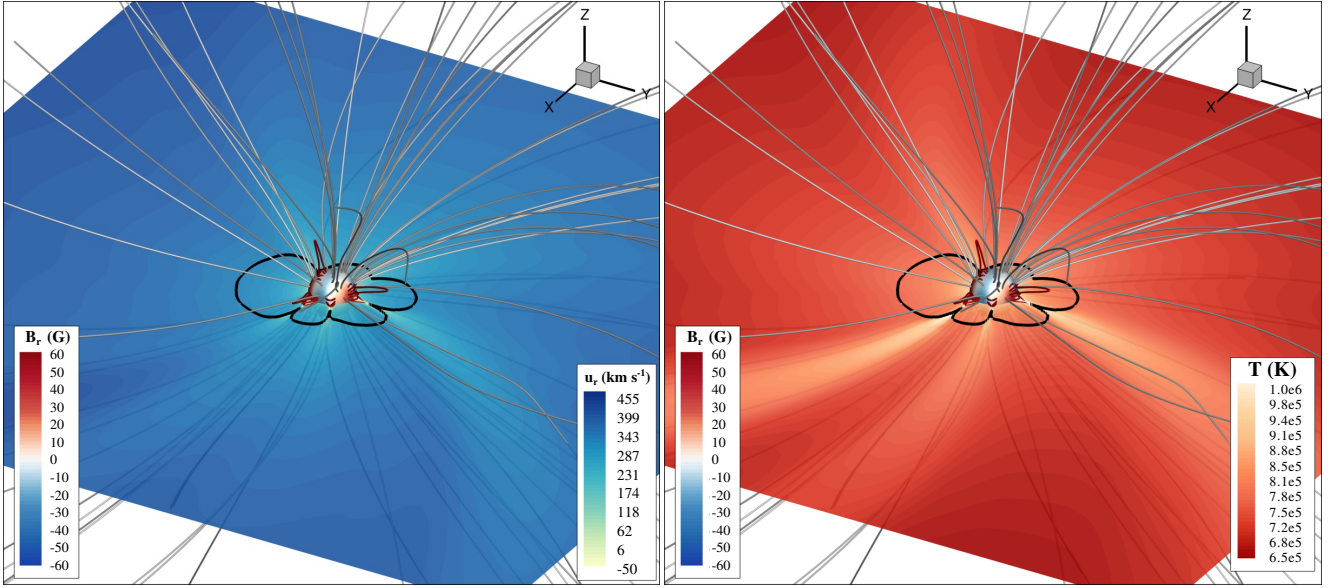


Figure 3. Result of our “hot” wind, a thermally driven, polytropic, 3D MHD simulation. *Left:* Wind velocities displayed along the equatorial plane (yellow-blue) *Right:* Wind temperatures displayed along the equatorial plane (orange-red). In both plots, surface magnetic fields are displayed in blue-red. Closed magnetic field lines are red, open magnetic field lines are grey. The Alfvén surface intersection with the x-y plane is shown as a black line.

$\dot{M}_{\odot} \text{ yr}^{-1}$ or 1.3×10^5 times the solar mass-loss rate. This value is much greater than astrospheric estimates ($2 \times 10^{-15} - 10^{-13} M_{\odot} \text{ yr}^{-1}$, Müller et al. 2001; Wood 2018, even though our terminal wind velocities ($\approx 400 \text{ km s}^{-1}$) agree with the one adopted by these authors. Our mass-loss rate is more in line with the mass-loss rates of neighbour stars in the HR diagram (Figure 1). We also computed the angular-momentum loss from λ And, which amounts to $2.2 \times 10^{35} \text{ erg}$. While we have no good age estimates for λ And, other than it is more evolved than the Sun, it has a much stronger spin-down rate than the Sun $\approx 2 \times 10^5 J_{\odot}$ (where $J_{\odot} = 10^{29} - 10^{30} \text{ erg}$ Finley et al. 2018). It was previously believed that stellar rotation followed a simple power law with age (Skumanich 1972), and this seems to hold true for main-sequence stars, but more recently it has been found that evolved stars do not follow this relationship (Van Saders et al. 2016; Booth et al. 2017; Ó Fionnagáin et al. 2019; Metcalfe & Egeland 2019). More research into the complex relationship of stellar rotation, age and their activity is needed for evolved stars before we can accurately say what is happening here.

Note that our polytropic wind model is unable to reproduce the high temperatures seen in X-ray observations. Similarly to the Sun, it is believed that X-ray emission originates in small-scale magnetic field, likely due to reconnection events (Priest 2003; Aschwanden 2004; Shibata & Magara 2011; Lehmann et al. 2018). The X-ray emission is larger inside regions of closed field lines, with X-ray dark regions along open magnetic field lines, along which the solar wind propagates. Given that our simulations only account for the large scale magnetic field, it is not surprising that our simulations do not reach the largest temperatures observed in the closed corona.

Our second model, using the AWSOM code, results in relatively similar wind velocities, as can be seen in Table 2, and a much cooler wind structure outside of magnetic loop regions. An example of a cold wind model with a ZDI map at the lower boundary is shown in Figure 4, and another one with a dipolar field as the lower boundary condition is shown in Figure 5. Since the AWSOM code usually can not find a truly steady-state solution, we average the global variables over 1000 timesteps at the end of the simula-

Table 3. Compiled list of radio observations for λ And. We show each flux density (mJy) for observing frequencies (GHz).

ν [GHz]	Φ_{radio} [mJy]	Ref.
2.72	< 15	
5	65	Bath & Wallerstein (1976)
8.1	20	
5	0.84	Lang et al. (1985)
4.5	0.86	Bowers & Kundu (1981)

tion. Table 2 shows a compilation of the AWSOM models we ran. For our simulations we varied the Poynting flux (S_A), the damping length (ℓ), and the base wind density (n_{chr}). S_A alters the amount of energy the Alfvén waves begin with at the base of the simulation, which can then be dissipated into the wind. ℓ changes the damping length of the waves, increasing this value will cause the dissipation of energy to be much more extended, a small ℓ value will cause much of the energy to be deposited lower in the wind, near the chromosphere. The base density plays a large role in the final wind structure as many physical processes depend heavily on the density structure. The wave dissipation (Equation (11)), and particularly the radiative cooling (Equation (9)) have strong dependencies on density, and subsequently have strong consequences for the density structure in the wind. Suzuki et al. (2013) (Figure 5 within) have shown how increasing input Poynting flux at the stellar surface can change the transition region height, and also cause a significant reduction in density with height in the wind. We see a similar effect in our simulations, which is consequential for our predicted radio flux densities. Our cold wind models all have substantially smaller radio fluxes than what is observed, as can be seen in Table 2. We will detail these results in Section 5. We also note that while the hot wind solution discussed above does not present the high temperatures seen in X-ray observations of hot coronal lines, the cold wind solutions produce much hotter, albeit confined, regions within closed magnetic loops. Therefore the cold wind scenarios produce hotter maximum temperatures as can be seen in Table 2. This is in better agreement

with X-ray-derived temperatures from observations than that of the hot wind model. However, we have not directly computed the X-ray luminosities from our simulations—through radiative transfer methods like our work in Section 5 for radio emissions—therefore we can only say that our maximum temperatures from our simulations are similar to derived temperatures from observations, and not conclude anything about X-ray luminosity itself.

Our cold-wind models produce much lower mass-loss rates than our hot wind models. The largest mass-loss rate from our cold wind models is $1.9 \times 10^{-10} M_{\odot} \text{ yr}^{-1}$, which is still one order of magnitude less than our hot wind model. The lowest mass-loss rates calculated come from the **A4** model, with $5.6 \times 10^{-13} M_{\odot} \text{ yr}^{-1}$. This is one order of magnitude larger than the currently accepted solar mass-loss rate. We find it difficult to constrain this value for these simulations as these winds do not produce similar radio flux density to the observed values (see Section 5). The cold wind model produces slightly lower angular momentum-loss rates than the hot wind model. It is worth noting here that the use of either the ZDI magnetic field, or a dipole, does not dominate the global wind parameters such as mass-loss rate and angular momentum-loss rate. These seem to be mostly dominated by the Poynting flux and damping length parameters.

Figures 3 to 5 show the Alfvén surfaces (the surface where the wind velocity equals the Alfvén velocity) as black contours. While the Alfvén surfaces in the hot wind (**Z0**) and cold wind (**C1**) models are relatively small, we see that the Alfvén surface is quite extended in the dipolar model **D1** ($\approx 30 R_{\star}$). The surface is so large ($\sim 30 R_{\star}$) that it extends beyond the orbit of the secondary star. In this case, interesting effects can take place in the system. Perturbations caused by an orbiting companion could travel downwind through plasma waves, allowing this information to reach the base of the wind and modifying the wind structure globally. This is similar to the physical processes seen in the cases of exoplanets orbiting in sub-Alfvénic regions (Strugarek et al. 2019; Folsom et al. 2020). We ignore the companion star in this work and assume that the companion is not actively affecting the stellar wind, which might not be true, in the simulation case **D1**, for example. Of course in our other simulations the Alfvén surface is much less extended, in which case, we expect the companion not to affect the stellar wind.

5 RADIO EMISSION FROM THE WIND OF λ AND

In Section 1 we discussed that stellar winds can be constrained or detected through radio observations. This thermal radio emission scales with the wind plasma density squared ($\propto n^2$), which means the tenuous winds of low-mass main sequence stars remain mostly undetectable for current radio telescopes. However, in the case of solar-mass red giants their winds are much denser due to an increase in mass-loss rate, allowing these winds to be readily detected at radio wavelengths. Observations show a radio flux density of $\sim 0.8 \text{ mJy}$ at 4.5–5 GHz (Bowers & Kundu 1981; Lang et al. 1985).

We describe the equations for calculating our simulations predicted radio flux density in Section 3.4. In the case of our hot wind scenario we find an agreeable radio flux of 0.89 mJy at a frequency of 4.5 GHz. This is close to the observed value for Bowers & Kundu (1981) and Lang et al. (1985). The radio intensity of this wind model is shown in Figure 6 (Left). We can see that there seems to be quite an extended region of specific radio intensity, outside of the optically thick region, shown by the dashed contour. It is from outside the optically thick barrier that the emitted radio flux can escape. The geometry of the optically thick region, including its size, is

determined almost exclusively by the density structure of the wind. We find that in the case of the cold wind simulations, the density structure results in radio flux densities that are very low and do not agree with observations.

In the case of the Alfvén driven wind, none of our simulations reached the required level of radio flux to reproduce the observations (see Table 2). The largest radio flux of any of the cold wind simulations was the **C2** case, which possesses a very dense chromospheric boundary condition of $1.5 \times 10^{13} \text{ cm}^{-3}$. The wave-driven wind, due to the cold inner regions that are almost isothermal, causes a strong exponential density decay with distance. We found that increasing the base density further does not necessarily increase the radio flux, as the density drops off in a more rapid fashion than the lower base density cases. This happens as the high density near the star causes this region to become hydrostatic-like, leading to an exponential decay in wind density. The higher base density, being so confined near the star, does not contribute much to the emitted radio flux density at 4.5 GHz as the wind is optically thick out to $\approx 2 R_{\star}$. As a result of the exponential decay, outside this optically thick region, the wave-driven winds display much lower density than the thermally driven polytropic wind, resulting in lower radio flux densities.

This is more easily illustrated in Figure 7, which shows the averaged equatorial density profile for the three plotted simulations in Figures 3 to 5. The hot wind model (shown in blue) begins with a lower base density, but with a mostly r^{-2} dependency on distance. The cold wind models however, produce an exponential decay in density up to $\approx 2 R_{\star}$, at which point, they have a much lower density than the hot wind scenario. This results in much lower radio intensity in the optically thin region shown in Figure 6.

6 SUMMARY & CONCLUSIONS

We present observations of the surface magnetic field of λ Andromedae, a solar mass G8 IV star, along with simulations of its stellar wind. In our simulations, we describe two wind models and compare those to radio and X-ray observations of λ And.

BritePol spectropolarimetric observations from August to October 2016 of λ And were obtained and used to derive a surface magnetic field through ZDI. We found a magnetic field that exhibits mostly low order spherical harmonics (78% are $\ell \leq 3$), with most of the magnetic energy in the poloidal component. The geometry of the field is tilted at 90° with respect to the rotation axis. We found a maximum local magnetic field of $B_{r,\text{max}} = 83 \text{ G}$, with an average of $B_{r,\text{avg}} = 21 \text{ G}$ (Figure 2). This is a relatively strong compared to the solar magnetic field, considering the evolved state of λ And.

Using the ZDI magnetic map, we carried out simulations using two different models: a hot wind model and a cold wind model. We include here a single hot polytropic wind case, for which we find results that are agreeable with previous radio observations. In the cold wave-drive model, we run a set of simulations varying the input parameters of Poynting flux (S_A) and damping length (ℓ). We find that increasing Poynting flux consistently results in hotter, faster stellar winds, while damping length has a more complicated relationship to wind velocity and temperature, with shorter damping lengths depositing more energy near the star.

Our hot wind model agrees very well with previous radio observations of λ Andromedae. We find a radio flux density of 0.89 mJy at 4.5 GHz. We have shown our cold wind implementation struggled to reach the same level of radio emission, which we attribute to exponential density decay in the lower atmosphere of our simulations, suggesting a hydrostatic-like region near the star. This

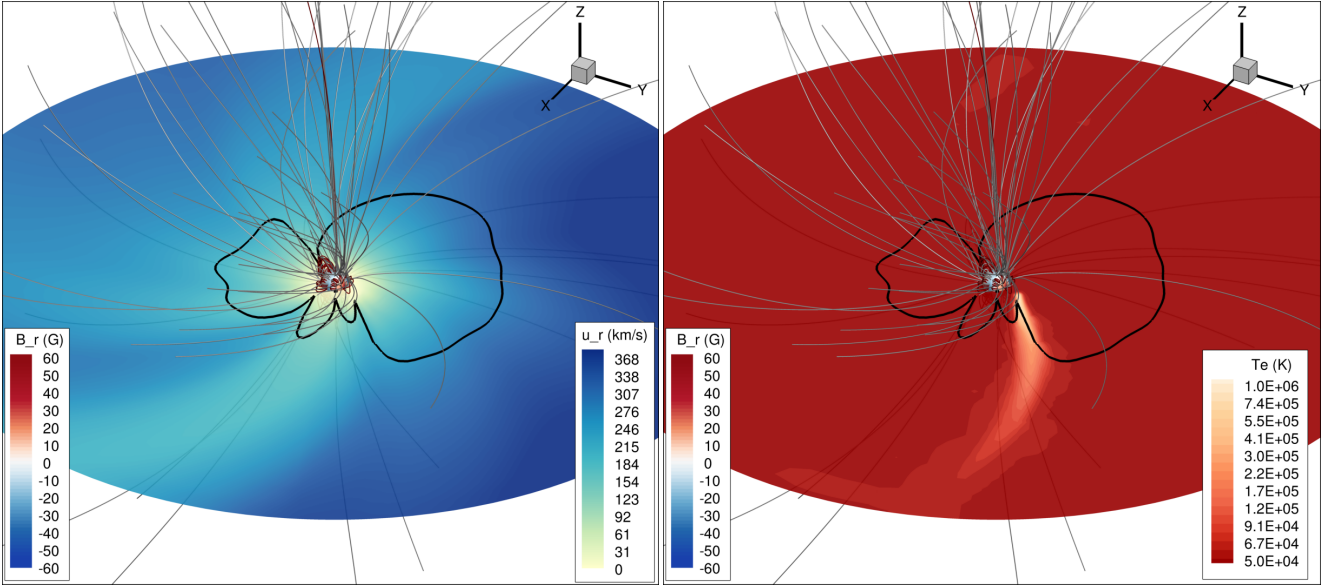


Figure 4. Model C1, one of the “cold” wind, Alfvén wave-driven, 3D MHD simulations, with the ZDI map set as the inner boundary for the magnetic field. *Left:* Wind velocities displayed along the equatorial plane (yellow-blue) *Right:* Wind temperatures displayed along the equatorial plane (orange-red). In both plots, surface magnetic fields are displayed in blue-red. Closed magnetic field lines are red, open magnetic field lines are grey. The Alfvén surface intersection with the x-y plane is shown as a black line.

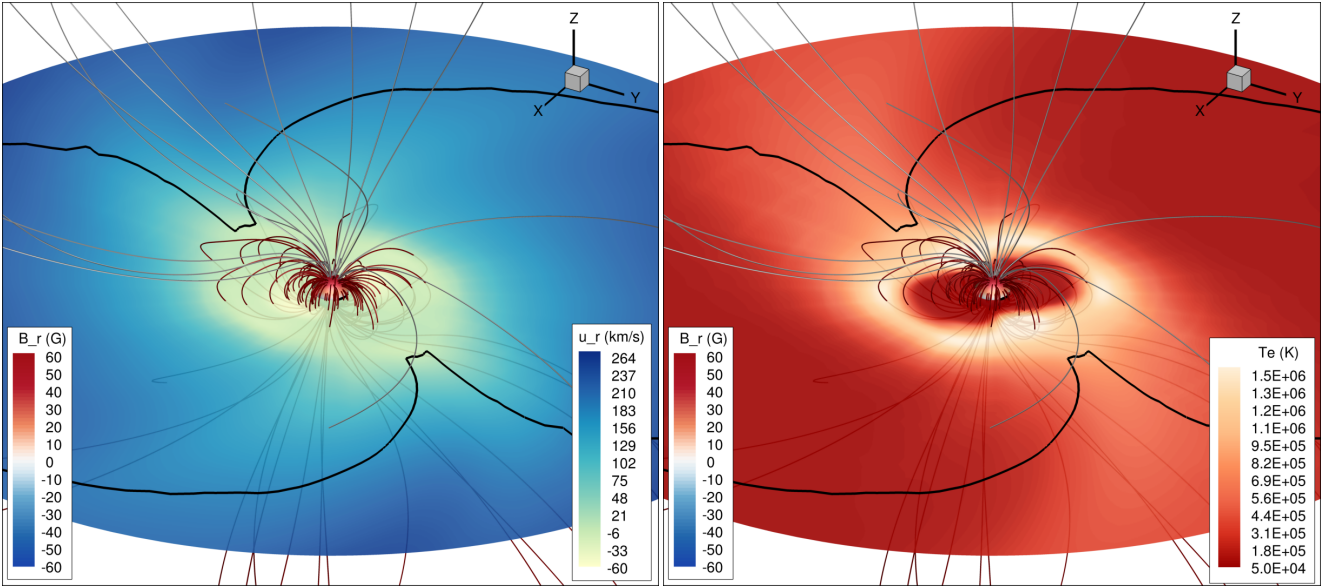


Figure 5. Model D1, one of the “cold” wind, Alfvén wave-driven, 3D MHD simulations, with a dipolar field of $B_{\text{dip,max}} = 60G$. *Left:* Wind velocities displayed along the equatorial plane (yellow-blue) *Right:* Wind temperatures displayed along the equatorial plane (orange-red). In both plots, surface magnetic fields are displayed in blue-red. Closed magnetic field lines are red, open magnetic field lines are grey. The Alfvén surface intersection with the x-y plane is shown as a black line.

steep density declivity causes the highest density regions to be obscured from the observer by the opaque wind. This agreement with radio observations allows us to place confident constraints on the stellar mass-loss rate.

The mass-loss rate of our hot wind model is $2.91 \times 10^{-9} M_{\odot} \text{yr}^{-1}$. This result are in line with general trends in evolved low-mass stellar mass-loss rates (see Figure 1). The cold wind model produces lower mass-loss rates overall, with a high of $1.7 \times 10^{-10} M_{\odot} \text{yr}^{-1}$ and a low of 5.6×10^{-13} , still much larger than the current accepted solar mass-loss rate. Our hot wind simulation displays a strong spin-down

rate of $\dot{J} = 2.2 \times 10^{35} \text{ erg}$. Our cold wind model maximum spin-down rate is similar at $\dot{J} = 1.1 \times 10^{35} \text{ erg}$ for a dipolar magnetic field, and $\dot{J} = 4.5 \times 10^{34} \text{ erg}$ for the observed surface magnetic field. As there is no consensus on low-mass stellar spin-down rates for stars older than our Sun, it is difficult to place these spin-down rates in a solar evolutionary context, but these angular momentum-loss rates are much larger than current accepted values for \dot{J}_{\odot} .

The maximum temperatures we find exist in our cold wind simulations ($T_{\text{max}} = 11 \text{ MK}$; model A1), but are notably confined to small regions in the wind. We see a maximum temperature of 1

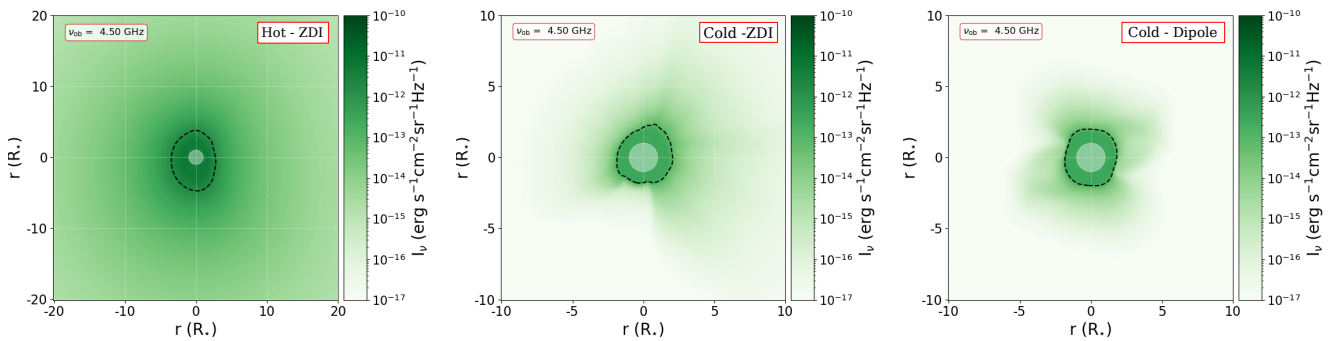


Figure 6. Radio intensities of the hot wind, cold wind with a ZDI map, and cold wind with a dipole, respectively, shown in Figures 3 to 5. Plots from the cold wind models is zoomed in to $R \in [-10, +10]$ to display more detail. It is very evident from these plots that the density decay in the Alfvén wave driven winds has a significant effect on the radio flux density emitted from the wind.

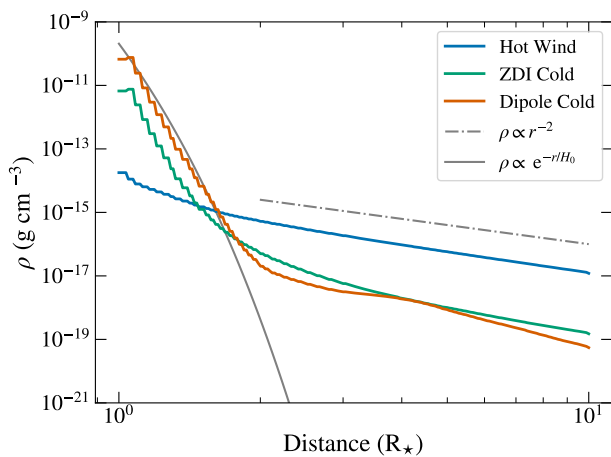


Figure 7. In this plot we show the averaged density around the equator of 3 simulations shown in blue (Figure 3), green (Figure 4), and orange (Figure 5) respectively. The wave-driven cold wind scenarios display hydrostatic behaviour close to the stellar surface and we see an exponential decay with a scale height of $0.05 R_\star$. Gray lines show examples of r^{-2} (dot-dash) and exponential decay (solid).

MK in our hot wind model, which is markedly below the derived temperatures from X-ray observations. This is due to the lack of small-scale magnetic field in these simulations. It is generally accepted that the small-scale field, which can produce strong local magnetic fields, produces the hottest plasma, which emits hot X-ray lines. The ZDI technique is not sensitive to these small-scale fields, and so they are excluded from our simulation. Furthermore, the stellar winds emanate from open field regions, whereas it is the closed field regions that produce this hot plasma.

Overall, we expect the wind of λ Andromedae to be most similar to our hot wind scenario. Assuming the hottest coronal regions arise from the small-scale magnetic field, it is not surprising we do not see this in our hot wind model. Importantly, the hot wind model provides very good agreement with observed radio flux densities, strengthening the support for our derived mass-loss rate. Simulating the winds of sub-giant solar-type stars seems to be adequately described by using polytropic models to produce global wind parameters. However, we expect that this is not the case for stars further along the red giant branch which possess no corona at all. Our hot wind model constrains the mass-loss rate of

λ Andromedae to $1.3 \times 10^{-10} M_\odot \text{ yr}^{-1}$, within the expected range of mass-loss rates for a stars of a similar ilk.

ACKNOWLEDGEMENTS

DOF and AAV would like to acknowledge funding from the European Research Council (ERC) under the European Union’s Horizon 2020 research and innovation programme (grant agreement No 817540, ASTROFLOW). The authors wish to acknowledge the SFI/HEA Irish Centre for High-End Computing (ICHEC) for the provision of computational facilities and support. This work used the BATS-R-US tools developed at the University of Michigan Center for Space Environment Modeling and made available through the NASA Community Coordinated Modeling Center.

REFERENCES

- Airapetian V., Carpenter K. G., Ofman L., 2010, *ApJ*, **723**, 1210
 Alvarado-Gómez J. D., Drake J. J., Cohen O., Moschou S. P., Garraffo C., 2018, *ApJ*, **862**, 93
 Alvarado-Gómez J. D., Garraffo C., Drake J. J., Brown B. P., Oishi J. S., Moschou S. P., Cohen O., 2019, *ApJ*, **875**, L12
 Aschwanden M. J., 2004, *Physics of the Solar Corona. An Introduction*
 Audard M., Güdel M., Sres A., Raassen A. J. J., Mewe R., 2003, *A&A*, **398**, 1137
 Aurière M., 2003, in Arnaud J., Meunier N., eds, *EAS Publications Series* Vol. 9, EAS Publications Series. p. 105
 Aurière M., et al., 2015, *A&A*, **574**, A90
 Ayres T. R., Brown A., Harper G. M., 2003, *ApJ*, **598**, 610
 Baliunas S. L., Guinan E. F., Dupree A. K., 1984, *ApJ*, **282**, 733
 Bath G. T., Wallerstein G., 1976, *PASP*, **88**, 759
 Booth R. S., Poppenhaeger K., Watson C. A., Silva Aguirre V., Wolk S. J., Aguirre V. S., Wolk S. J., 2017, *MNRAS*, **471**, 1012
 Booth R. S., Poppenhaeger K., Watson C. A., Silva Aguirre V., Stello D., Bruntt H., 2020, *MNRAS*, **491**, 455
 Bowers P. F., Kundu M. R., 1981, *AJ*, **86**, 569
 Chandran B. D. G., Dennis T. J., Quataert E., Bale S. D., 2011, *J* 10.1088/0004-637X/743/2/197
 Claret A., 2004, *A&A*, **428**, 1001
 Cohen O., Moschou S.-P., Gloer A., Sokolov I., Mazeh T., Drake J., Garraffo C., Alvarado-Gomez J., 2018
 Cox A. N., Pilachowski C. A., 2002, *Allen’s Astrophysical Quantities*. Vol. 53, Springer New York, doi:10.1007/978-1-4612-1186-0
 Cranmer S. R., Saar S. H., 2011, *ApJ*, **741**, 54
 Cranmer S. R., Winebarger A. R., 2019, *ARA&A*, **57**, 157

- Dere K. P., Del Zanna G., Young P. R., Landi E., Sutherland R. S., 2019, *ApJS*, **241**, 22
- Donati J.-F., Henry G., Hall D., 1995, *A&A*, **293**, 107
- Donati J.-F., Semel M., Carter B. D., Rees D. E., Cameron A. C., 1997, *MNRAS*, **291**, 658
- Donati J. F., et al., 2003, *MNRAS*, **345**, 1145
- Donati J.-F., et al., 2006, *MNRAS*, **370**, 629
- Drake S. A., Linsky J. L., 1986, *AJ*, **91**, 602
- Drake J. J., Ball B., Eldridge J. J., Ness J.-U. U., Stancliffe R. J., 2011, *Astronomical Journal*, **142**, 144
- Dupree A., Brickhouse N., Hanson G., 1996, in *Astrophysics in the Extreme Ultraviolet*. Springer, pp 141–145
- Fichtinger B., Güdel M., Mutel R. L., Hallinan G., Gaidos E., Skinner S. L., Lynch C., Gayley K. G., 2017, *A&A*, **599**, A127
- Finley A. J., Matt S. P., See V., 2018, *ApJ*, **864**, 125
- Folsom C. P., et al., 2018a, *MNRAS*, **474**, 4956
- Folsom C. P., et al., 2018b, *MNRAS*, **481**, 5286
- Folsom C. P., Fionnagáin D. Ó., Fossati L., Vidotto A. A., Moutou C., Petit P., Dragomir D., Donati J. F., 2020, *A&A*, **633**, A48
- Frasca A., Biazzo K., Taş G., Evren S., Lanzafame A. C., 2008, *A&A*, **479**, 557
- Gombosi T. I., van der Holst B., Manchester W. B., Sokolov I. V., 2018, *Living Rev. Sol. Phys.*, **15**, 4
- Hartmann L., MacGregor K. B., 1980, *ApJ*, **242**, 260
- Hollweg J. V., 1978, *Reviews of Geophysics and Space Physics*, **16**, 689
- Hollweg J. V., 1986, *J. Geophys. Res.*, **91**, 4111
- Johnstone C. P., Güdel M., Lüftinger T., Toth G., Brott I., 2015a, *A&A*, **577**, A27
- Johnstone C. P., Güdel M., Brott I., Lüftinger T., 2015b, *A&A*, **577**, A28
- Keppens R., Goedbloed J. P., 1999, *A&A*, **343**, 251
- Kurucz R. L., 1993, SYNTH spectrum synthesis programs and line data
- Lang K., Willson R., Pallavicini R., 1985, [10.1007/978-94-009-5420-5_38](https://doi.org/10.1007/978-94-009-5420-5_38), pp 267–270
- Lehmann L. T., Jardine M. M., Mackay D. H., Vidotto A. A., 2018, *MNRAS*, **478**, 4390
- Lim J., White S. M., 1996, *ApJ Letters*, **462**, L91
- Linsky J. L., Haisch B. M., 1979, *ApJ*, **229**, L27
- Massarotti A., Latham D. W., Stefanik R. P., Fogel J., 2008, *AJ*, **135**, 209
- Matt S. P. S., MacGregor K. K. B., Pinsonneault M. M. H., Greene T. P. T., 2012, *ApJ*, **754**, L26
- Meng X., Van der Holst B., Tóth G., Gombosi T. I., 2015, *MNRAS*, **454**, 3697
- Mestel L., 1999, *Stellar magnetism*. Oxford University Press
- Metcalfe T. S., Egeland R., 2019, *ApJ*, **871**, 39
- Moschou S.-P., Sokolov I., Cohen O., Drake J. J., Borovikov D., Kasper J. C., Alvarado-Gomez J. D., Garraffo C., 2018
- Müller H.-R., Zank G. P., Wood B. E., 2001, *ApJ*, **551**, 495
- Neiner C., Wade G. A., Marsden S. C., Blazère A., 2017, in *Second BRITE-Constellation Science Conference: Small Satellites - Big Science*. pp 86–93 ([arXiv:1611.03285](https://arxiv.org/abs/1611.03285))
- Ó Fionnagáin D., 2018, [10.5281/ZENODO.1476578](https://doi.org/10.5281/ZENODO.1476578)
- Ó Fionnagáin D., Vidotto A. A., 2018, *MNRAS*, **476**, 2465
- Ó Fionnagáin D., et al., 2019, *MNRAS*, **483**, 873
- O’Gorman E., Harper G. M., Vlemmings W., 2017, *A&A*, **599**, A47
- O’Gorman E., Coughlan C. P., Vlemmings W., Varenus E., Sirothia S., Ray T. P., Olofsson H., 2018, pp 1–9
- Oran R., Landi E., van der Holst B., Sokolov I. V., Gombosi T. I., 2017, *ApJ*, **845**, 98
- Ortolani A., Maggio A., Pallavicini R., Sciortino S., Drake J. J., Drake S. A., 1997, *A&A*, **325**, 664
- Panagia N., Felli M., 1975, *A&A*, **39**, 1
- Parks J., et al., 2015, [arXiv preprint arXiv:1508.04755](https://arxiv.org/abs/1508.04755)
- Petit P., Donati J.-F., Collier Cameron A., 2002, *MNRAS*, **334**, 374
- Petit P., et al., 2004a, *MNRAS*, **348**, 1175
- Petit P., et al., 2004b, *MNRAS*, **351**, 826
- Petit P., Louge T., Théado S., Paletou F., Manset N., Morin J., Marsden S. C., Jeffers S. V., 2014, *PASP*, **126**, 469
- Powell K. G., Roe P. L., Linde T. J., Gombosi T. I., De Zeeuw D. L., 1999, *Journal of Computational Physics*, **154**, 284
- Priest E. R., 2003, *Advances in Space Research*, **32**, 1021
- Rees D. E., Semel M. D., 1979, *A&A*, **74**, 1
- Sanz-Forcada J., Brickhouse N. S., Dupree A. K., 2003, *ApJS*, **145**, 147
- Sanz-Forcada J., Favata F., Micela G., 2004, *A&A*, **416**, 281
- Semel M., 1989, *A&A*, **225**, 456
- Semel M., Donati J. F., Rees D. E., 1993, *A&A*, **278**, 231
- Shibata K., Magara T., 2011, *Living Reviews in Solar Physics*, **8**, 6
- Skumanich A., 1972, *ApJ*, **171**, 565
- Sokolov I. V., et al., 2013, *ApJ*, **764**, 23
- Spitzer L., Härm R., 1953, *Physical Review*, **89**, 977
- Strugarek A., Brun A. S., Donati J. F., Moutou C., Réville V., 2019, *ApJ*, **881**, 136
- Suzuki T. K., 2007, *ApJ*, **659**, 1592
- Suzuki T. K., 2018, *PASP*, **70**, 1
- Suzuki T. K., Imada S., Kataoka R., Kato Y., Matsumoto T., Miyahara H., Tsuneta S., 2013, *PASP*, **65**, 98
- Van Der Holst B., Sokolov I. V., Meng X., Jin M., Manchester W. B., Tóth G., Gombosi T. I., 2014, *ApJ*, **782**, 81
- Van Doorselaere T., Wardle N., Zanna G. D., Jansari K., Verwichte E., Nakariakov V. M., 2011, *ApJ*, **727**, L32
- Van Saders J. L., Ceillier T., Metcalfe T. S., Aguirre V. S., Pinsonneault M. H., García R. A., Mathur S., Davies G. R., 2016, *Nature*, **529**, 181
- Vidotto A., 2017, *EPJ Web of Conferences*, **160**, 05011
- Vidotto A. A., Donati J.-F., 2017, *A&A*, **602**, A39
- Vidotto A. A., Jatenco-Pereira V., 2006, *ApJ*, **639**, 416
- Vidotto A. A., Jardine M., Morin J., Donati J. F., Opher M., Gombosi T. I., 2014a, *MNRAS*, **438**, 1162
- Vidotto A. A., et al., 2014b, *MNRAS*, **441**, 2361
- Villadsen J., Hallinan G., Bourke S., Güdel M., Rupen M., 2014, *ApJ*, **788**, 112
- Wood B. E., 2018, in *Journal of Physics Conference Series*. p. 012028 ([arXiv:1809.01109](https://arxiv.org/abs/1809.01109)), [doi:10.1088/1742-6596/1100/1/012028](https://doi.org/10.1088/1742-6596/1100/1/012028)
- Wood B. E., Muller H., Zank G. P., Linsky J. L., 2002, *ApJ*, **574**, 412
- Wright A. E., Barlow M. J., Michael J., 1975, *MNRAS*, **170**, 41
- Yasuda Y., Suzuki T. K., Kozasa T., 2019, *ApJ*, **879**, 77

APPENDIX A: ZDI ADJUSTMENT OF STOKES I AND V LSD PSEUDO-PROFILES

APPENDIX B: SIMULATION GRIDS

This paper has been typeset from a $\text{\TeX}/\text{\LaTeX}$ file prepared by the author.

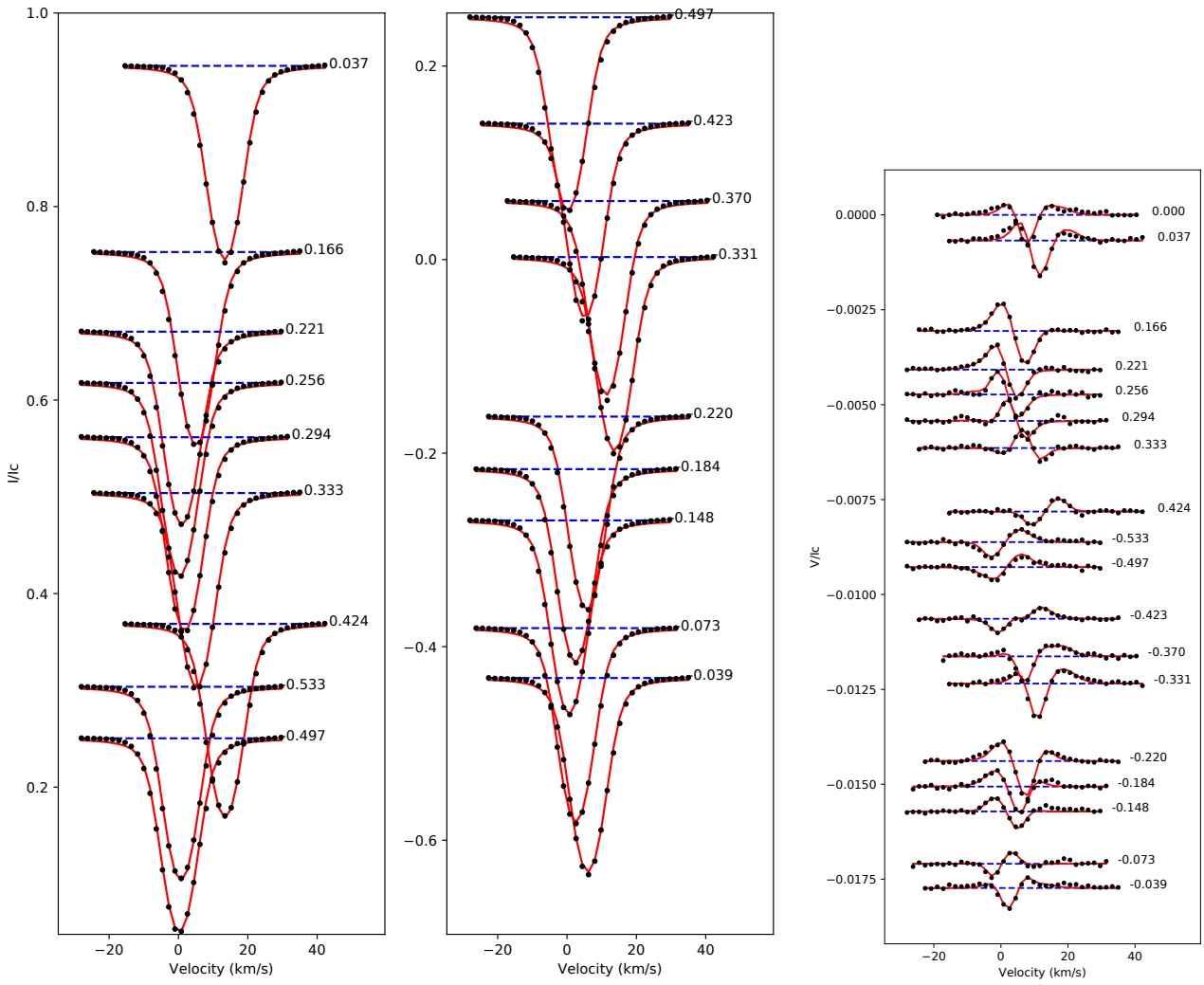


Figure A1. *Left & Middle:* Stokes I LSD pseudo-profiles of λ And (black points), over-plotted with the set of synthetic Stokes I profiles produced by the ZDI model (red line). The profiles are vertically shifted for display clarity. The dashed blue lines show the continuum level, and the phases of observation are indicated on the right of every profile. *Right:* The same figure but for Stokes V profiles.

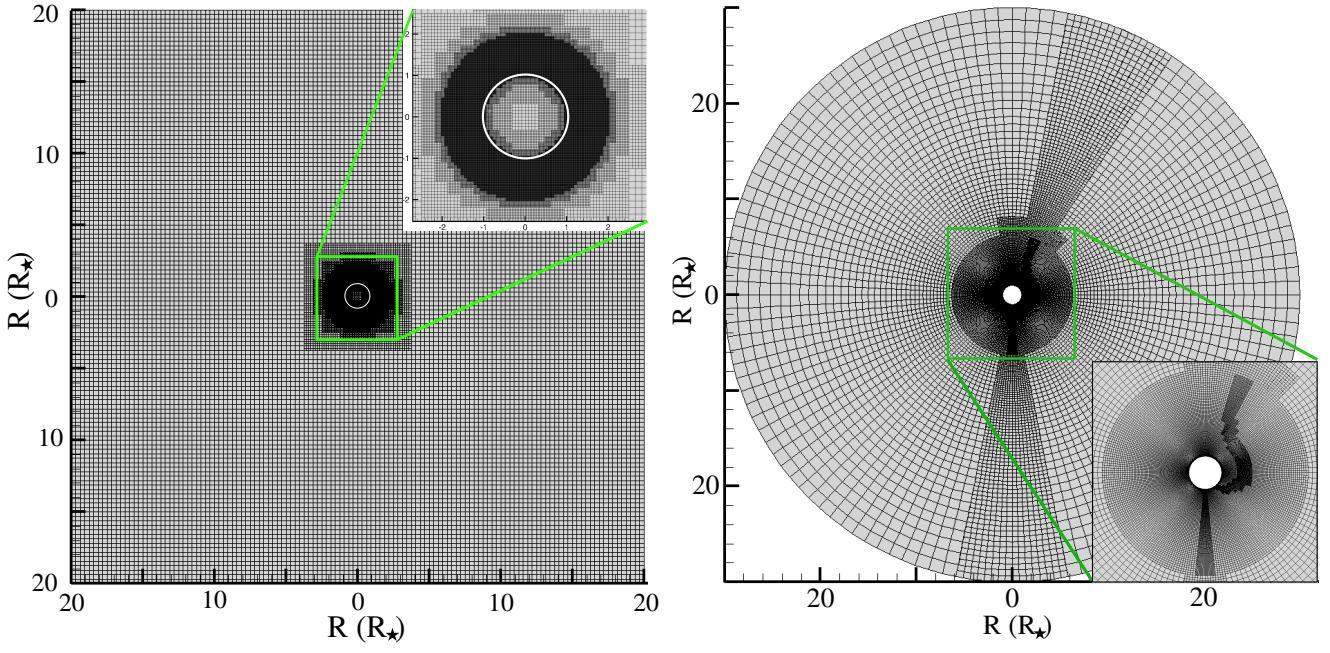


Figure B1. *Left:* Simulation mesh from our hot wind scenario. *Right:* Simulation mesh from our cold wind scenario. This simulation included adaptive mesh refinement, leading to non-uniform refinement close to the star.